Arctic Sea Ice Dynamics: Drift and Ridging in Numerical Models and Observations

Arktische Meereisdynamik: Drift und Presseis-rückenbildung in numerischen Modellen und Beobachtungsdaten

Torge Martin

Arctic Sea Ice Dynamics: Drift and Ridging in Numerical Models and Observations

Arktische Meereisdynamik: Drift und Presseis-rückenbildung in numerischen Modellen und Beobachtungsdaten

Torge Martin

This logo was created by the author for the 'open ship' day of RV Polarstern in June 2005.

Torge Martin

Alfred-Wegener-Institut für Polar- und Meeresforschung

Postfach 12 01 61

27515 Bremerhaven

Germany

Contents

II   Observations of Pressure Ridges
or: Both sides of the story   85

III   Numerical Modelling of Pressure Ridges
or: From the small scale to the large scale   115

Contents

Abstract

The Arctic sea ice cover is constantly in motion driven by the wind and ocean currents. The transport of freshwater and latent heat is associated with the ice drift. Furthermore, the drift causes deformation of the sea ice cover under compressive and shear forces and pressure ridges form. Ridges in turn affect the momentum and—to a minor degree—the heat exchange between sea ice and atmosphere and ocean because they strongly increase the local surface roughness and thickness of the ice. Therefore, the sea ice drift and deformation interact with the climate system and its changes, and it is a key issue to both the remote-sensing and modelling community to provide products of good quality. The present thesis splits into three parts: a study of modelled and observed drift estimates, an analysis of sea ice ridge quantities derived from laser altimeter and airborne electromagnetic measurements and an investigation of different numerical algorithms for the representation of ridges in a large-scale sea ice model.

The study of sea ice drift focuses on the comparison of different sea ice-ocean coupled models and the validation with buoy and remote-sensing data of the period 1979–2001 on the basis of monthly averages. According to drift speed distributions the group of models, which matches best the observations, has a mode at drift speeds around 0.03 m s^{-1} and a short tail towards higher speeds. However, there are also models with much larger drift speeds. In general, all models are capable of producing realistic drift pattern variability although differences are found between models and observations. Reasons for these differences are manifold and lie in discrepancies of wind stress forcing as well as sea ice model characteristics and sea ice-ocean coupling.

The investigation of sea ice ridges is based on Arctic-wide in situ measurements of the period 1995–2005 which include different sea ice roughness regimes. While sail density is found to emphasise local deformation events sail height features a large-scale, positive gradient from the Siberian shelf seas towards the Lincoln Sea, where sails of up to 10 m height were found. However, regionally averaged sail heights are found to vary little between 1.1 m and 1.6 m. Rather large ratios of 10 sails per keel and 1:6.3 m for sail height to keel depth are derived. Linear relationships are determined for sail to keel density and sail height to keel depth. Furthermore, functional relationships of sail height and level ice thickness are found.

Three different approaches to the simulation of pressure ridge formation are introduced and tested in idealised experiments and for realistic Arctic condi-

tions. Simulations are evaluated with airborne laser profiles of the sea ice surface roughness. The main characteristics of the respective ridging algorithms are: (1) a prognostic derivation of deformation energy from which ridge parameters are deduced, (2) a redistribution function, transforming level ice to a second, ridged ice category, combined with a stochastic simulation of ridge quantities, and (3) prognostic equations for ridge density and height resulting in the formation of ridged ice volume. The model results show that the ridge density is mainly related to the sea ice drift whereas the mean sail height relates to the parent ice thickness. Most deformation occurs at coastlines. In general, all of the three algorithms produce realistic distributions of ridges. Finally, the second ridging scheme is regarded to be most appropriate for climate modelling while the third scheme is found to be advantageous for short-term sea ice forecasting.

Zusammenfassung

Die Meereisdecke des Arktischen Ozeans befindet sich in ständiger Bewegung angetrieben von Wind und Ozeanströmung. Damit einher geht der Transport von Süßwasser und latenter Wärme. Die Deformation der Eisdecke ist eine weitere Folge der Eisdrift und tritt unter der Einwirkung von Druck- und Scherkräften auf, die Presseisrücken bilden. Diese Eisrücken beeinflussen den Impuls- und – in geringerem Maße – den Wärmeaustausch zwischen Atmosphäre, Meereis und Ozean, weil sie zu einer Verstärkung der lokalen Oberflächenrauhigkeit und Eisdicke führen. Meereisdrift und -deformation wechselwirken mit dem Klimasystem und dessen Veränderungen. Deshalb ist es für Fernerkundler und Modellierer entscheidend, Produkte von hoher Qualität zu erzeugen. Die vorliegende Arbeit gliedert sich in drei Abschnitte: eine Studie über beobachtete und modellierte Eisdrift, eine Analyse über Presseisrückenparameter, die mit Hilfe von hubschraubergestützten Laseraltimeter- und Elektromagnetikmessungen gewonnen wurden, und eine Untersuchung verschiedener numerischer Algorithmen, die die Darstellung von Eisrücken in großskaligen Meereismodellen ermöglichen.

Die Meereisdriftstudie geht hauptsächlich auf den Vergleich unterschiedlicher Meereis-Ozean-Modelle anhand von Monatsmitteln und deren Validierung mit Bojen- und Fernerkundungsdaten über den Zeitraum 1979–2001 ein. Gemäß den Häufigkeitsverteilungen der Driftgeschwindigkeiten ist die Gruppe von Modellen, die Verteilungen mit Modalwerten von $0{,}03\,\mathrm{m\,s^{-1}}$ und einer rasch abfallende Flanke zu hohen Geschwindigkeiten hin aufweisen, den Beobachtungen am ähnlichsten. Es gibt jedoch einige Modelle, die zu deutlich höheren Driftgeschwindigkeiten neigen. Im Allgemeinen geben alle Modelle die räumliche Verteilung der Eisdrift in der Arktis realistisch wieder, obwohl Unterschiede zu den Beobachtungsdaten auftreten. Die Gründe für diese Abweichungen sind vielfältig und in den unterschiedlichen Windantrieben, Meereismodelleigenschaften und Meereis-Ozean-Kopplungen zu finden.

Die Untersuchung der Presseisrücken stützt sich auf arktisweite Messungen aus den Jahren 1995–2005, die verschiedene Eisrauhigkeitsregime mit einschließen. Während die Segeldichte lokale Deformationsereignisse hervorhebt, weist die Segelhöhe einen großskaligen, positiven Gradienten auf, der sich von den sibirischen Schelfmeeren bis zur Lincolnsee erstreckt, in der Segelhöhen von bis zu 10 m gemessen wurden. Regionale Mittelwerte der Segelhöhe variieren jedoch nur leicht zwischen diesen Gebieten von 1,1 m bis 1,6 m. Aus den Messungen wurden vergleichsweise große Verhältnisse von 10 Segeln pro Kiel

und 1:6,3 m zwischen Segelhöhe und Kieltiefe abgeleitet. Lineare Beziehungen für die Segel- zu Kieldichte und Segelöhe zu Kieltiefe konnten nachgewiesen werden. Es wurde auch ein funktionaler Zusammenhang zwischen der Segelhöhe und der ursprübglichen Eisdicke gefunden.

Drei verschiedene Ansätze zur Simulation der Presseisrückenbildung werden vorgestellt und in idealisierten Experimenten sowie unter realistischen arktischen Bedingungen getestet. Die Simulationen werden mit Hilfe von hubschraubergestützten Laserprofilen der Meereisrauhigkeit evaluiert. Die Haupteigenschaften der jeweiligen Presseisrückenalgorithmen sind: (1) eine prognostisch berechnete Deformationsenergie aus der Eisrückenparameter abgeleitet werden, (2) eine Umverteilungsfunktion, die undeformiertes Eis in eine Eiskategorie für deformiertes Eis verlagert und mit einem stochastischem Modell zur Presseisrückengenerierung gekoppelt ist, und (3) prognostische Gleichungen für Rückendichte und -höhe die wiederum die Dicke des deformierten Eises bestimmen. Die Modellergebnisse zeigen, dass die Rückendichte in direkter Beziehung zur Eisdrift steht, während die Segelhöhe der Dickenverteilung undeformierten Eises folgt. Die meisten Presseisrücken werden entlang der Küsten gebildet. Im Allgemeinen produzieren alle drei Rückenalgorithmen realistische Presseisrückenverteilungen. Letztlich wird der zweite Algorithmus als optimal für die Verwendung in Klimamodellen bewertet und der dritte als vorteilhaft für Meereisvorhersagemodelle angesehen.

Chapter 1

Introduction

"Saturday, April, 6th [1895]. Two a.m., $-11.4°$ Fahr. $(-24.2°C$.) [at approximately $86°$ N and $96°$ E]. The ice grew worse and worse. Yesterday it brought me to the verge of despair, and when we stopped this morning I had almost decided to turn back. I will go on one day longer, however, to see if the ice is really as bad farther northwards as it appears from the ridge, 30 feet [~ 10 m] in height, where we are encamped. We hardly made 4 miles yesterday. Lanes, ridges, and endless rough ice, it looks like an endless moraine of ice-blocks; and this continual lifting of the sledges over every irregularity is enough to tire out giants. Curious this rubble-ice. For the most part it is not so very massive, and seems as if it had been forced up somewhat recently, for it is incompletely covered with thin, loose snow, through which one falls suddenly up to one's middle. And thus it extends mile after mile northwards, while every now and then there are old floes, with mounds that have been rounded off by the action of the sun in the summer—often very massive ice."

Fridtjof Nansen [1898]
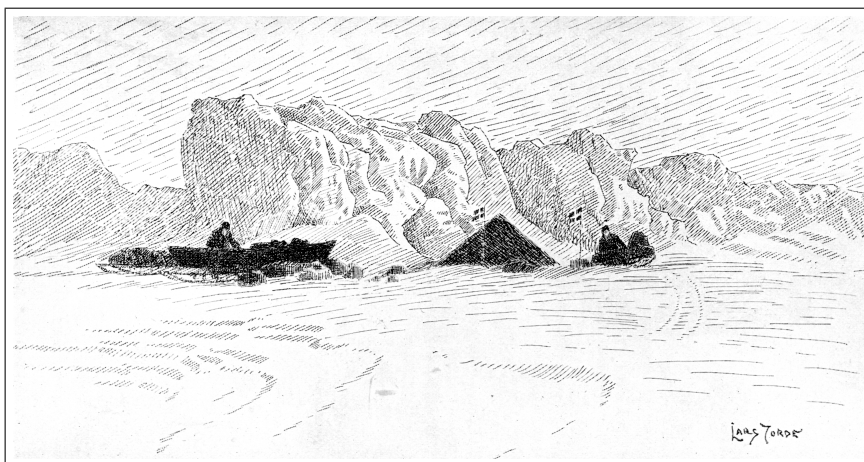
Figure 1.1: Large pressure ridges at Nansen's northernmost camp at 86 ° 13.6' N, 8 April, 1895. [from *Nansen*, 1898, by *Lars Jorde*, from a Photograph]

Fridtjof Nansen's report on the Norwegian Polar Expedition from 1893 to 1896 [*Nansen*, 1898] gives a detailed view of the characteristics of the Arctic sea ice cover which is still valid after more than 100 years. Of particular note is his description of the deformation events of the pack ice in which his ship *Fram* was frozen and the enormous problems he and is companion Hjalmar Johansen encountered because areas of endless numbers of pressure ridges hindered their way across the ice towards the North Pole. They had to abandon their intention to reach the north pole on foot because of the pathless and inhospitable Arctic sea ice cover. Nansen reached his northern-most position on April, 8th: 86° 13.6' N and about 95° E. A drawing of their northernmost camp shows the impressive size of the sea ice ridges they found (Figure 1.1).

This study focusses on the state-of-the-art observation and modelling of these ridges, which are as much a feature of the Arctic as a hundred years ago.

1.1 The Arctic

The Arctic is geographically defined as the region north of 66° 33' N: the Arctic Circle (see Figure 1.2). The 10 °C isotherm in July or the treeline are further limits[a]. The Arctic Ocean is a mediterranean sea enclosed by the land masses of Europe and Asia (together also known as Eurasia), and North America. It covers an area of $15.551{\cdot}10^6$ km^2 or $9.541{\cdot}10^6$ km^2 depending upon which marginal seas are included[b] [*Jacobsson*, 2002]. The Arctic Ocean has an average depth of 1361 m with a maximum depth of 5260 m located along the Gakkel Ridge of the Eurasian basin [*Jacobsson*, 2002]. The surrounding marginal seas are shelf seas and are divided from the central Arctic Ocean by the individual edges of the continental slope. Namely these are (from Europe eastward) the Barents, Kara, Laptev, East Siberian, Chukchi, Beaufort and Lincoln seas (Figure 1.2). The water depth does not exceed 200 m in any of these areas, and Laptev and East Siberian seas are found to be the shallowest with mean depths of only 48 and 58 m respectively [*Jacobsson*, 2002]. Off the flat shelves the topography of the ocean bottom is marked by fault-block ridges, plains of the abyssal zone, ocean deeps, and basins (Figure 1.3). The Arctic Ocean is linked to the North Atlantic

---

[a]Definitions of "the Arctic" and further information are provided by the *Arctic Monitoring and Assessment Programme* (AMAP, `http://www.amap.no`), which is one of five Working Groups of the Arctic Council.

[b]The *International Hydrographic Organization* (IHO, `http://www.marine.gov.uk/iho.htm`) regards the Norwegian, Greenland, Iceland and Labrador seas as well as the Baffin and Hudson bays and the passages of the Canadian Archipelago as parts of the Arctic Ocean. The expression "Arctic Ocean" as used in the present study is based on the division of *Jacobsson* [2002] that includes only the central Arctic basin and the adjacent shelf seas and yields in the smaller area given. All following values relate to this "interior" Arctic Ocean.
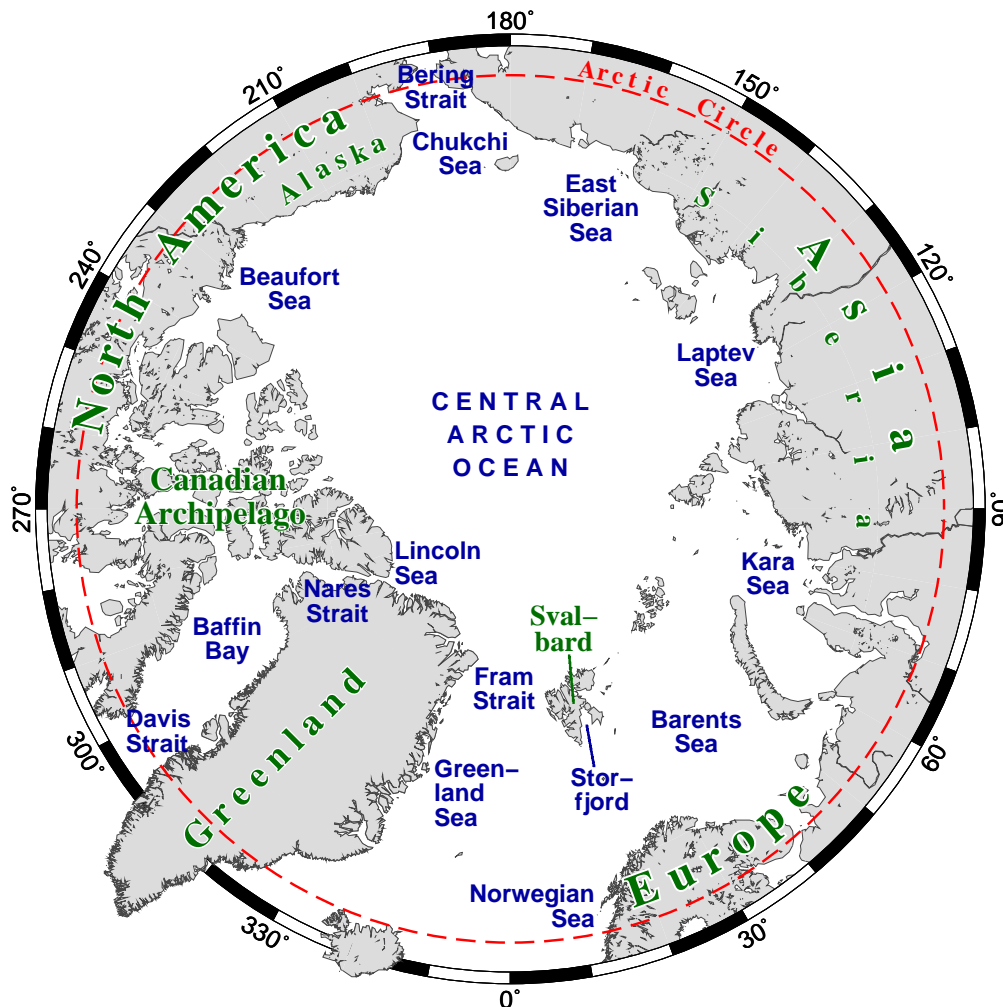
Figure 1.2: Map of the Arctic Ocean and its marginal seas.

by the Fram Strait and Barents Sea east of Greenland and by the passages of the Canadian Archipelago and Davis Strait west of Greenland. There is only one rather small connection to the Pacific Ocean: the Bering Strait.

The Arctic, as one of the earth's polar regions, is characterised by special climate conditions. The surface temperature depends strongly on the incoming solar radiation which has a prominent annual cycle in the polar regions. In the Arctic the sun does not set during the polar day and does not rise during the polar night. The polar day lasts 24 hours (June 21st) at the Arctic Circle and half a year at the geographic North Pole. The same holds for the polar night which is on December 21st at the Arctic Circle. This means that large parts of the Arctic experience long time spans of darkness in which the incoming solar radiation does not compensate for the outgoing thermal longwave radiation. This results in surface air temperatures (SAT) of $-30\,°$C or less. These low air temperatures in turn cause a cooling of the upper oceanic layer that finally results in the formation of sea ice. This oceanic ice cover is one of the most prominent charac-
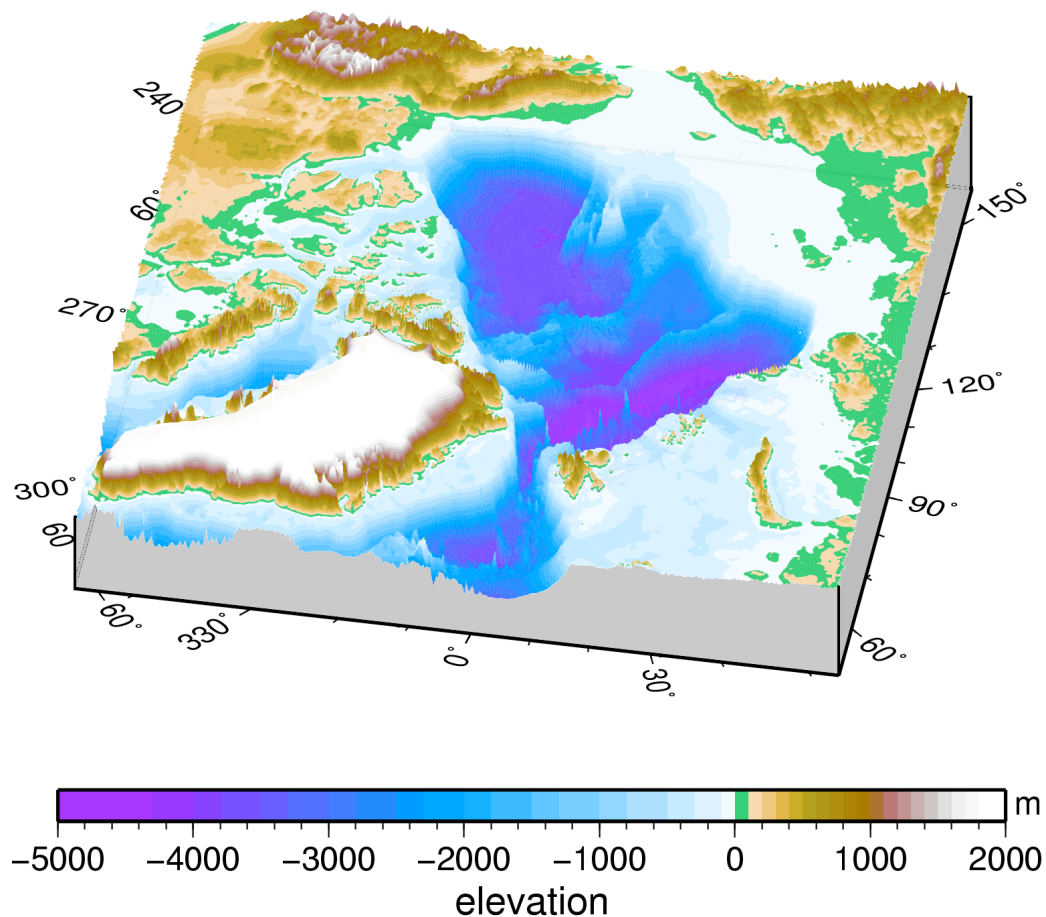
Figure 1.3: Bathymetry of the Arctic Ocean and topography of surrounding land masses. Elevations of the ETOPO2 data set are shown, which are provided by the *National Geophysical Data Center* (NGDC) and available at `http://www.ngdc.noaa.gov/mgg/geodas/geodas.html`

teristics of the Arctic Ocean and differentiates this marine area from subpolar regions. During summer the direct solar radiation causes melting and evaporation, which results in surface air temperatures of about $+10\,°C$ and a layer of low clouds or mist. These latter condensates decrease the amount of incoming shortwave radiation while reflecting outgoing longwave radiation back down to the surface.

The temperature gradient between pole and equator causes the polar vortex, a cyclone spanning the entire Arctic in the middle and upper troposphere ($\sim$3–10 km) and stratosphere. It is most intense during winter when the temperature gradient is strongest and hinders the exchange of air masses between the mid-latitudes and the Arctic. Mass and energy exchange are controlled by turbulent processes, particularly planetary waves which cause cyclic breakdowns of the vortex. The areas south of the vortex are characterised by frontal cyclones in the lower troposphere which move eastward and are associated with the polar jet stream. This jet stream is located at the periphery of the vortex, where the

pressure and temperature gradients are strongest between the inner side of the polar vortex and the outer subpolar region, and it is vertically centred at about 200 hPa.

During winter the Arctic sea level pressure (SLP) pattern is characterised by a high pressure system over the northern Asian continent, the Siberian High, which can form a high pressure ridge towards North America. Its stability is due to the large land mass which produces a cold continental climate during winter. Another high, located over Greenland, is caused by the underlying large glacial mass and is therefore a stable year-round feature. Low pressure systems enter the Arctic mainly from the North Atlantic (Iceland Low) via the Greenland Sea as well as the Norwegian and Barents seas [*Serreze et al.*, 1993; *Serreze*, 1995; *Brümmer et al.*, 2000]. Within the Arctic, cyclone activity is strongest over the Kara Sea and—less frequent—over the Laptev Sea as well as over Baffin Bay [*Serreze et al.*, 1993; *Serreze*, 1995; *Brümmer et al.*, 2000]. Fewer cyclones enter from the Pacific Ocean (Aleutian Low) during the winter season because the Beaufort High forms a strong pressure barrier [*Serreze and Barry*, 1988; *Zhang et al.*, 2004]. During summer, cyclones are weaker by 5–10 hPa but generally have a longer life-time and protrude much farther into the Arctic [*Serreze and Barry*, 1988; *Serreze et al.*, 1993; *Zhang et al.*, 2004]. In the above regions cyclonic activity weakens in summer, but increases over Siberia, the Canadian Archipelago and the central Arctic itself [*Serreze et al.*, 1993]. In these latter regions cyclolysis dominates during summer time [*Serreze*, 1995]. Centres of cyclogenesis in the Arctic periphery change from the Atlantic sector in winter to the Pacific sector in summer and while cyclones are generated over the sea in the Atlantic they form over land in the Pacific sector [*Zhang et al.*, 2004]. In general, cyclones transport warm air into the Arctic and hence may cause melting even in winter time. An increase in the number and intensity of cyclones entering the Arctic has been observed during the second half of the 20th century and can be related to climate warming [*McCabe et al.*, 2001; *Zhang et al.*, 2004].

The water masses of the Arctic Ocean originate mainly in the Atlantic (79%) with only a small contribution from the Pacific Ocean (19%) [*AMAP*, 1998]. River run-off amounts to 2% of the entire water mass, which is a large contribution compared to other oceans. Outflow paths are through the Fram Strait continuing in the East Greenland Current (75%) and through the Canadian Archipelago (25%) [*AMAP*, 1998]. The Arctic Ocean is markedly stratified at 50–150 m below its mixed layer of 30–50 m thickness [*Carmack*, 2000]. This halocline layer is very complex and its character varies throughout the Arctic Ocean. In a simplified approach it consists mainly of Atlantic water and with a Pacific halocline layer formed above it in the western Arctic Ocean only, as the Pacific water is less saline at 32.7 ± 1 compared to 35 ± 0.05 for Atlantic-derived water [*Schlosser et al.*,

2000]. Below this layer various components of Atlantic water occupy the water column down to about 1600 m [*Carmack*, 2000]. This water enters the Arctic Ocean via two main pathways: through the Fram Strait in the West Spitsbergen Current and over the Barents Sea shelf. Within the Arctic the Atlantic Current circulates anti-clockwise and follows the basin topography. The current splits up into several branches that flow parallel to the main sea floor ridges towards the North American continental shelf. Below 1600 m the Arctic Deep Water is found.

The strong stratification within the upper layers (above 200 m depth) of the central Arctic Ocean results in low vertical diffusion rates, prevents winter convection and deepening of the surface mixed layer below 50 m, and insulates the warm Atlantic layer located below the halocline. These are essential preconditions for a year-round ice covered ocean. Current oceanographic interest is focussed on the freshwater balance of the mixed and halocline layers, and on the spreading of new properties and changing of driving mechanisms in the Atlantic layer.

1.2   Sea ice in general

Sea ice is frozen ocean and thus has to be clearly distinguished from other basic ice types formed of freshwater: land ice, lake ice and river ice [*WMO*, 1989].

Sea ice is often subdivided into two simple categories depending on its age: first-year and multi-year ice. Multi-year ice is defined as ice that survives one or more melting seasons. The two categories have different characteristics: salt content and its vertical distribution in the ice, crystal structure and layers, and total thickness. Furthermore, layers of snow-ice and superimposed ice as well as sediments may help to identify former surfaces in older sea ice that may also have experienced deformation. Snow-ice develops from refrozen snow and sea water when the snow load on top of an ice floe is heavy enough to force the ice under the water level and cause flooding at the interface of ice and snow. Superimposed ice is refrozen freshwater from snow melt on an ice floe.

Another important distinction is made for stationary sea ice: Typically the pack ice is afloat and drifting. Along shore lines, however, so-called fast ice can occur. Fast ice is sea ice that is attached to the shore or shallow sea bottom areas and hence not able to move with the normal pack ice. Fast ice often has a flat surface and is only deformed at its grounding points. The fast ice edge forms an advanced coastline and areas of open water—leads and polynyas—or intense deformation commonly occur along this edge.

Sea ice is an important component of the global climate system. For example, its bright surface reflects most of the incoming solar radiation, in contrast

to the dark ocean. Sea ice formation and melt are processes that have large-scale implications on the oceanic thermohaline circulation because they affect deep ocean convection. Sea ice is also of importance because it acts as an insulator between atmosphere and ocean hindering the direct exchange of heat, moisture, momentum, and gases and aerosols.

The main physical parameters describing the large-scale sea ice cover are concentration, thickness and drift. These parameters are described in the following sections together with examples of related physical processes, observed variability and their implications for climate change.

1.2.1 Concentration

Sea ice concentration is defined as ice covered area per unit area and hence ranges between zero and unity. It is also called ice compactness or coverage, and is expressed as a percentage. The ice concentration can be changed thermodynamically by refreezing of open water or lateral melting of ice. Dynamic processes may also change the ice covered area per unit area: strong winds may open up the closed ice cover forming so-called leads or polynyas or may close areas of open water. Dynamic processes can also cause the ice floes to break into smaller blocks that pile up, resulting in consumption of ice area.

Ice concentration is usually given for a defined area like a grid cell or pixel. From these single estimates the ice area and extent of a certain region can be derived. The ice area is the sum of the single cell/pixel areas multiplied by the particular ice concentration estimates. In contrast, ice extent is a binary value, i.e. a single cell/pixel counts either as ice covered or ice free depending on a threshold of ice concentration, which ranges usually between 15 and 30%[c]. Hence the total ice area of a region is always smaller than or equal to the ice extent. The same threshold is often used to determine a distinct ice edge in the continuous decrease of ice concentration in the marginal ice zone (MIZ). The ice extent, however, can be derived more easily and with a higher accuracy from satellite observations than the absolute ice area [*W. Meier*, pers. comm.].

The total Arctic sea ice area changes with season from a mean value of circa $14 \cdot 10^6$ km^2 in winter (March) to $7 \cdot 10^6$ km^2 in summer (September) [*Bjørgo et al.*, 1997; *Johannessen et al.*, 2004] (see Figure 1.4). For a long period, from 1900 to 1970, the sea ice extent, estimated from ship and aircraft observations, showed no significant variation beside this annual cycle [*Walsh and Chapman*, 2001]. Only in the summer record were significant departures from the mean found in two maxima at around 1915 and 1950. This rather constant behaviour changed

---

[c]More information can be found at the National Snow and Ice Data Center web page `http://nsidc.org/seaice/data/terminology.html`.
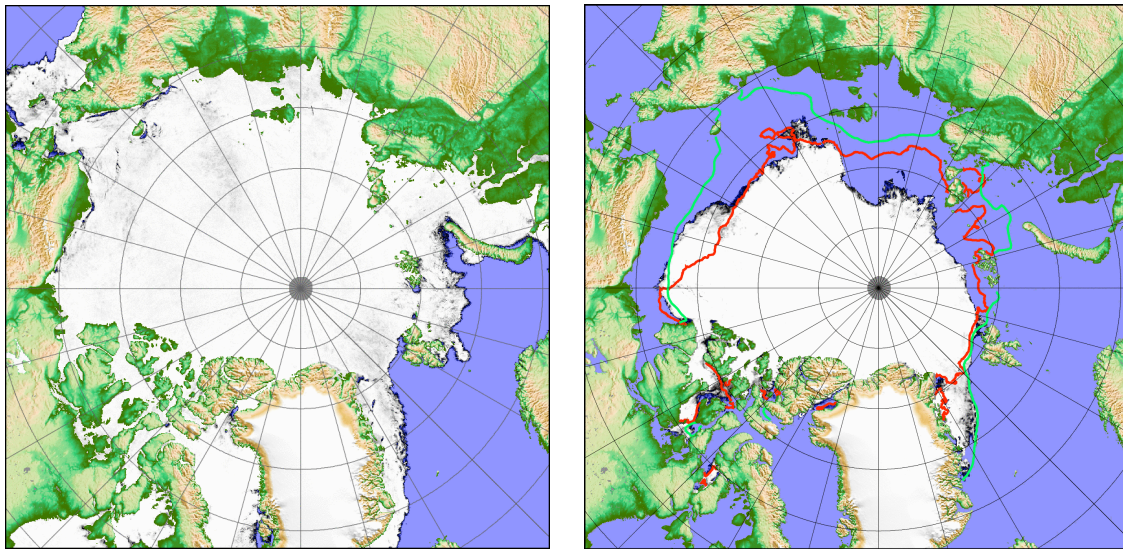
Figure 1.4: Seasonal variation of the Arctic sea ice cover; concentration and extent of (**left panel**) March 2006 and (**right panel**) September 2005 as derived from AMSR-E satellite observations. The right panel further shows the long-term retreat of the Arctic summer sea ice cover. Isolines of the mean ice extent (threshold is 50% ice concentration) of the periods 1979–1982 and 2002–2005 are drawn in green and red respectively. [from `http://www.seaice.de`, courtesy of *L. Kaleschke*]

in the 1970s. Affected by the Arctic climate warming [*Chapman and Walsh*, 1993; *Johannessen et al.*, 2004] the extent of the Arctic sea ice cover has shrunk by roughly 2.8–4.5% per decade [*Bjørgo et al.*, 1997; *Cavalieri et al.*, 1997; *Parkinson et al.*, 1999] in the last 30 years. In each year since 2000 a new record September minimum in ice extent occurred [*Serreze et al.*, 2003; *Stroeve et al.*, 2005; *NSIDC*, 2005]. The decrease in sea ice extent is associated with an increasing duration of the summer melt season of 8% per decade [*Smith*, 1998]. Although the sea ice retreat is strongest in summer, the negative trend is independent of season [*Walsh and Chapman*, 2001]. However, the winter ice cover was found to be comparatively stable until recently, when a considerable decline in ice area was also recorded for the winter season [*Meier et al.*, 2005; *Comiso*, 2006]. The massive multi-year ice has even been reduced by 7–9% per decade [*Johannessen et al.*, 1999; *Comiso*, 2002]. Though this ice type is more persistent against melting than the thinner first-year ice, changes in the Arctic ice drift pattern (see below) have lead to a major and persistent net loss of older ice ($\geq$10 years) with a trend of -4.2% yr^{-1} in the period 1989–2003 [*Rigor and Wallace*, 2004; *Belchansky et al.*, 2005]. More recently, a doubled decrease in multi-year ice area of 14% between 2005 and 2006, most prominent in the Eurasian part of the Arctic Ocean, was observed [*Nghiem et al.*, 2006]. Hence, dynamic processes play a large role, amplifying climate feedback processes that have been initiated thermodynamically and accelerating their progression [*Comiso and Parkinson*,

2004]. Those climate model experiments which are forced by observed CO_2 concentrations predict a further retreat of the Arctic sea ice cover of roughly 15% within the next 50 years [*Vinnikov et al.*, 1999]. Hence, the negative trend is expected to be a stable feature with major implications for the Arctic and also global climate.

The connection between sea ice cover and climate change is strong because the global sea ice area accounts for more than a quarter of the total cryospheric surface and contributes to short positive feedback cycles, intensifying, for example, existent natural variations and also global warming. Sea ice that is thicker than 10 cm has a high albedo α of 0.7 [*Perovich*, 1996], i.e. it reflects 70% of the incoming solar radiation, whereas the open ocean absorbs about 90% of this energy. Falling snow accumulates on top of the large solid surface offered by the sea ice cover and intensifies the surface albedo to 0.75–0.85 [*Perovich*, 1996]. Therefore sea ice has a cooling effect on the heat budget of polar regions. This means that the observed increase of air temperature in the Arctic of about 0.5 °C per decade within the last 25 years causes not only the retreat of the snow and ice cover but is also amplified by the diminished ice cover which allows the ocean to absorb more incoming solar radiation and results in a further temperature rise, accelerating the ice melt [*Comiso and Parkinson*, 2004]. A further contribution to sea ice melt is a decrease in surface albedo which is caused by the formation of melt ponds in summer ($\alpha = 0.15$–0.45 [*Fetterer and Untersteiner*, 1998]) as well as the sedimentation of natural and anthropogenic aerosols ($\alpha = 0.4$–0.6 [*Light et al.*, 1998]). Arctic-wide remote sensing results show an average summer albedo of 0.5–0.7 decreasing by up to 50% towards the ice edge in the Arctic marginal seas [*Laine*, 2004]

The sea ice-albedo feedback mechanism is a positive feedback cycle which in general supports sea ice growth as well as reduction. However, regarding present climate change it plays a major role as a sea ice diminishing factor. A decrease in surface albedo results in an increased uptake of solar radiation by the sea ice, which causes ice melt and a further decrease of the albedo [*Ebert and Curry*, 1993]. *Curry et al.* [1995] show that the ice-albedo feedback is much more complex and, for example, ice thickness and melt pond coverage play opposing roles. Moreover the authors state that the feedback mechanism needs to be viewed separately for the marginal ice zone and the internal pack ice. The ice-albedo feedback is even independent of variations in external forcing because the surface albedo is directly linked to the ice characteristics, i.e. once triggered and passing a state of seasonal equilibrium this feedback mechanism may account for the observed massive sea ice loss since 1989 [*Lindsay and Zhang*, 2005]. Satellite observations confirm this strong connection showing parallel negative trends in ice concentration and surface albedo of the Arctic sea ice

cover [*Comiso*, 2001; *Laine*, 2004].

1.2.2 Thickness

Sea ice is three-dimensional and having considered its areal extent, the ice thickness is now discussed. The heat transport in ocean and atmosphere and the heat exchange between them is mainly due to turbulent fluxes. Sea ice acts as an insulator for heat exchange between atmosphere and ocean because sea ice is a rigid material and thus, already a thin sea ice layer interrupts the turbulent heat exchange. In "solid" sea ice conductive fluxes are responsible for heat exchange. However, sea ice is not completely solid. Because the solid ice and salt crystals are accompanied by liquid brine pockets and air bubbles, which both make the ice porous, it resembles a mushy layer instead. Thus the thermal conductivity of the ice is a combination of that of the single components of this mushy layer. The brine pockets are thermal reservoirs because they retain latent heat during melting and freezing processes inside the ice floe. In long brine channels even convection can occur affecting the total heat flux through the ice. This complex structure of sea ice is ultimately responsible for the great differences in sensible heat flux between open ocean (up to 450 W m^{-2} over wintertime polynyas [*Andreas and Cash*, 1999]) and young sea ice (as low as 10 W m^{-2} if ice thickness exceeds 1 m [*Maykut*, 1978]) respectively and the atmosphere. The heat flux is not immediately shut down with the onset of sea ice growth. During winter there is a strong temperature difference of 20–30 °C between the oceanic mixed layer, which is at the freezing point (−1.86 °C), and the colder atmospheric surface layer above. Under these extreme conditions 10 cm of sea ice would mean a reduction of 20–50% in the sensible heat flux and an ice thickness of 40 cm reduces the flux by one order of magnitude (model approach: *Maykut* [1978]; measurements: *Lüpkes et al.* [2004]; [*A. B. Heide*, pers. comm.]).

Already in 1890 *J. Stefan* stated that the growth of sea ice by thermodynamic processes depends on the actual ice thickness itself [*Wadhams*, 2000]

$$\frac{\partial H}{\partial t} \propto \frac{T_b - T_s}{H} \tag{1.1}$$

where H is the actual ice thickness and T_s and T_b the temperature of the ice at its surface and bottom. Due to the low thermal conductivity of sea ice its thermodynamic growth is limited. As shown in Figure 1.5 the average thickness of the Arctic sea ice cover undergoes not only seasonal variations but grows asymptotically towards a limit. This equilibrium ice thickness H_{eq} can be estimated from the ice-ocean heat flux Q_w [*Eicken*, 2003]:

$$H_{eq} = \frac{\lambda_i(T_b - T_s)}{Q_w} \tag{1.2}$$
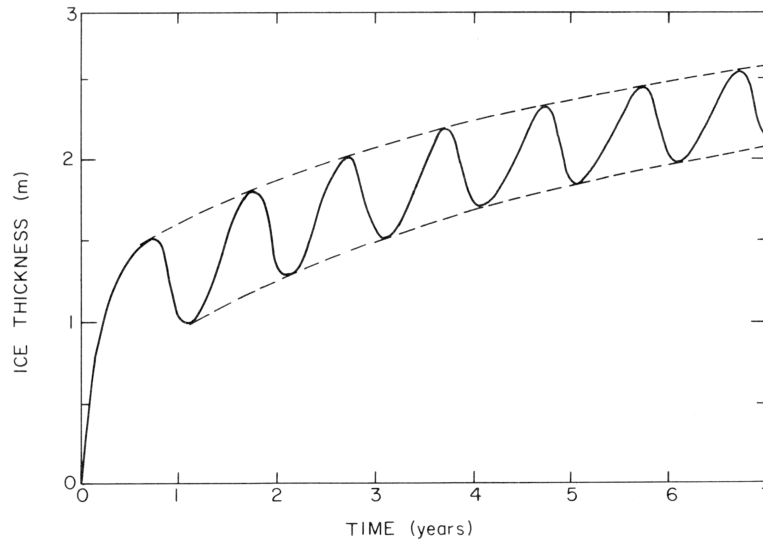
Figure 1.5: The thermodynamic growth of sea ice thickness is limited by the oceanic heat flux and the thermal conductivity of the ice. [from *Maykut*, 1986, Fig. 11]

The thermal conductivity of the ice λ_i is a function of the salinity and the temperature of the ice and generally ranges between 1.0 and 2.5 W m^{-1}K^{-1} [*Untersteiner*, 1961; *Yen*, 1981; *Maykut*, 1986]. The vertical temperature difference between the ice underside and its surface $T_b - T_s$ differs throughout the year between -34° and 0°C with an average of -18.6°C [*Maykut and Untersteiner*, 1971]. The average Arctic ice-ocean heat flux is 2–5 W m^{-2} [*Maykut*, 1986; *Maykut and McPhee*, 1995; *Krishfield and Perovich*, 2005]. Seasonal variability is strong and the winter flux of less than 1.5 W m^{-2} is negligible compared to summer values of up to 40–60 W m^{-2} on single days in July and August (monthly means amount to half of these) *Maykut and McPhee* [1995]; *Steele and Boyd* [1998]; *Krishfield and Perovich* [2005]. During summer, leads allow the oceanic mixed layer to be heated directly by solar radiation, which accounts for 75% of the annual variability in ice-ocean heat flux[*Krishfield and Perovich*, 2005]. *Krishfield and Perovich* [2005] further derived an overall trend for this heat flux of 0.2 W m^{-2}decade^{-1} for the period 1979–2002 and found the strongest interannual variability in the Beaufort Sea. The Arctic equilibrium ice thickness resulting from these values can not be reached within a single growth season [*Eicken*, 2003]. Accounting for more complex relationships than Equation (1.2) represents, *Maykut and Untersteiner* [1971] calculated the equilibrium ice thickness to be 2.5–3 m in the Arctic Ocean with a one-dimensional thermodynamic sea ice and snow layer model (see Figure 1.5). They found that oceanic heat flux and snow thickness have the greatest influence on ice thickness. The thermal conductivity of the snow layer is smaller than that of sea ice by one order of magnitude [*Sturm et al.*, 2002].

However, sea ice thickness does not only grow thermodynamically but also
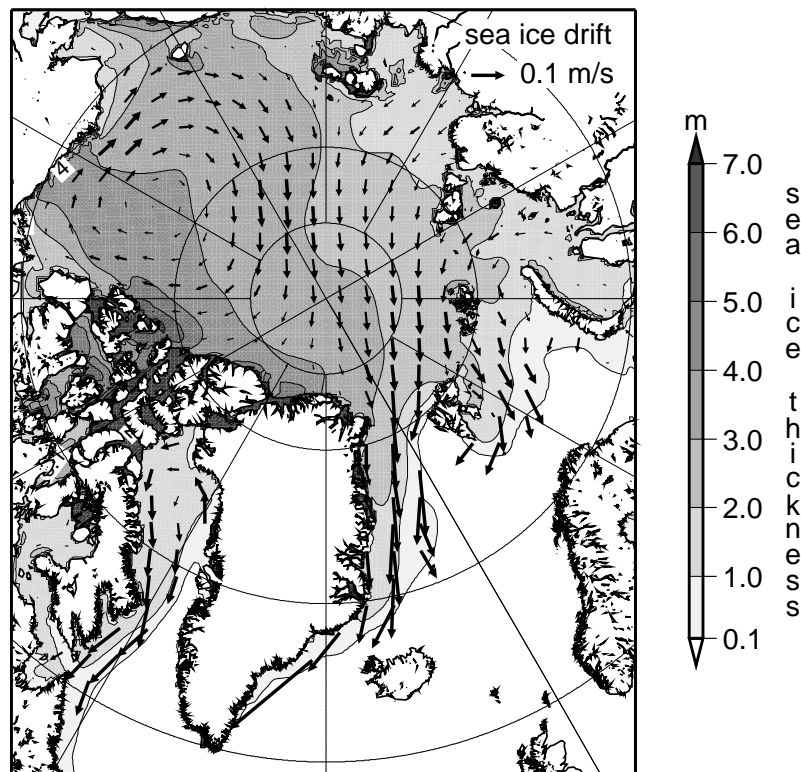
Figure 1.6: Typical winterly sea ice thickness distribution (contours) and drift pattern (vectors) of the Arctic Ocean from a sea ice model.

by dynamic deformation processes. The formation of pressure ridges—structures of piled up ice blocks that will be introduced in detail in Section 1.3—causes ice thicknesses that exceed the equilibrium thickness reached by pure thermodynamic growth. The thermodynamic regime always drives the ice towards the equilibrium thickness. At the ice-ocean interface the heat flux balance consists of only two fluxes: the oceanic heat flux and the conductive heat flux. Melting occurs when the former dominates and freezing when the latter is larger. Because the conductive heat flux depends on the vertical temperature gradient it is not only related to the temperature difference between ice surface and bottom but also to the ice thickness. Thus melting may occur at the deepest point of ridges, in which ice blocks are pressed well below the draft of flat, level ice floes, even in winter time while the undeformed ice next to it still grows. Hence, the equilibrium ice thickness is not only an upper limit of thermodynamic growth, it represents the average ice thickness that results from the external conditions for the sea ice system.

As already indicated in the previous paragraph, sea ice can be split into different thickness classes. In numerical sea ice models a common classification is to distinguish between undeformed/level ice and deformed/ridged ice. The thickness of level ice is due to thermodynamic growth only. All newly formed ice belongs automatically to this class. As soon as the ice becomes deformed,

it changes to the deformed ice class. Deformed ice can still thicken thermodynamically, but the larger ice thickness results in a reduced conductive heat flux and hence smaller growth rates. The ice thickness also affects the ice strength and thus the deformation process itself.

In Figure 1.6 the typical ice thickness distribution is shown. The Arctic sea ice cover features a positive gradient from the Eurasian shelf seas towards the coastline of Greenland and the Canadian Archipelago. Thicker ice may also reach into the Beaufort Sea under certain conditions. The Arctic-wide mean ice thickness of 2–3.5 m as well as its spatial distribution currently experience extreme changes. Measurements with different sounding systems have shown a decrease in ice thickness of ∼42% (1.3 m) from the 1960s and early 1970s to the mid 1990s [*Rothrock et al.*, 1999] and of 22.5% between 1991 and 2001 [*Haas*, 2004b]. A comparison of various model results and observational data showed a general agreement with these measurements, indicating a trend in ice thickness decrease of 0.6–1 m within the period 1987–1997 [*Rothrock et al.*, 2003]. The most intense change in the sea ice cover is reported for the Eurasian part of the Arctic Ocean [*Rothrock et al.*, 1999; *Nghiem et al.*, 2006].

Model results of *Lindsay and Zhang* [2005] show a decrease in mean ice thickness of 43% (1.31 m) within the 16 year period of 1988–2003. While the level ice thickness has a negative trend during the entire simulation period 1948–2003, the ridged ice features a positive trend until 1988 followed by a negative trend which is stronger than that of the level ice for the rest of the simulated period [*Lindsay and Zhang*, 2005, Fig. 3]. This observation leads the authors to the conclusion that possibly a tipping-point is passed and the Arctic ice-ocean system entered a new era of thinning sea ice, which is dominated by internal thermodynamic processes related to the positive ice-albedo feedback rather than external forcing. However, *Krishfield and Perovich* [2005] state that the increase of the ice-ocean heat flux over the last two decades would explain the decrease in ice thickness detected by *Rothrock et al.* [2003] considering the equilibrium ice thickness calculations of a one-dimensional model of *Maykut and Untersteiner* [1971]. When considering these purely thermodynamic reasons for ice loss, one should not forget the influence of dynamic processes. The Arctic has lost most of its thick multi-year ice in the last decade due to changes in large-scale ice motion [*Belchansky et al.*, 2005].

1.2.3   Drift

Sea ice is not a stationary cover of the ocean. Ice floes are afloat and their motion is forced by wind and ocean currents. Under free drift conditions, i.e. internal ice interactions are negligible, the geostrophic wind accounts for more than
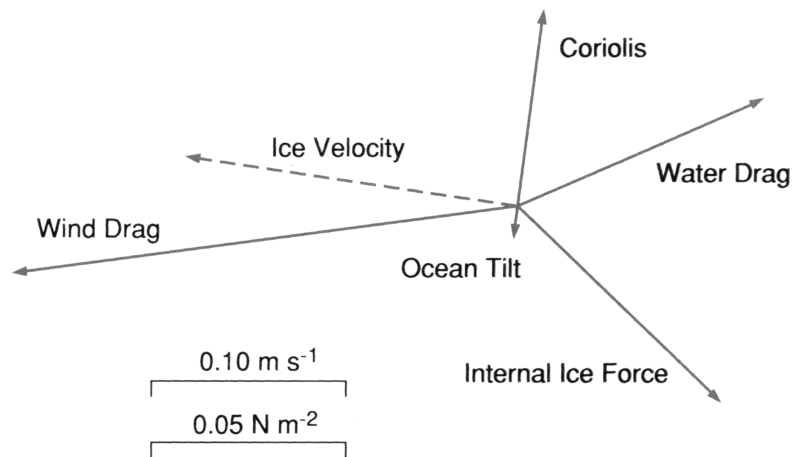
Figure 1.7: Schematic diagram of the momentum balance of sea ice for winter conditions based on wind and water stress measurements. The internal force is derived as a residual and the resulting ice velocity is shown as a dashed line. [from *Hibler and Flato*, 1992, Fig. 12.1]

70% of the variance of ice drift velocity [*Thorndike and Colony*, 1982]. *Kimura and Wakatsuchi* [2000] found for the winter half year that the ice drifts almost parallel ($\pm 10°$) to the geostrophic wind and that the drift speed amounts to 0.3–2% of the wind speed featuring values of about 2% in the absence of strong ocean currents [see also *Thorndike and Colony*, 1982; *Vinje*, 1985]. The authors further showed that a wind factor of about 1% is typical for the central Arctic Ocean and that it drops below 0.5% in the North of Greenland and the Canadian Archipelago, where sea ice is thickest and most compact, and along the Siberian coastline, where fast ice occurs. Beside the strong impact of the wind, ocean stress and the internal interactions of the ice also contribute to the balance of forces acting on sea ice and are approximately equal in magnitude (see Figure 1.7). The oceanic stress counteracts the wind forcing, except in cases of weak winds. Internal forces develop when the ice experiences pressure, e.g. near steep shore lines or in semi-enclosed bays as well as in the case of a very compact ice cover. Measurements have shown that these can be of the same order of magnitude as the wind and ocean stresses [*Leppäranta*, 1980]. Further contributors such as the tilt of the ocean surface, the Coriolis force, inertia and steady current terms are one order of magnitude smaller [*Hibler and Flato*, 1992]. Sea ice reacts quickly to changes in the local wind and thus reflects features like cyclones very well. In a model, sea ice reaches a steady drift state within an hour after a wind forcing is applied [*Hibler and Flato*, 1992]. The rapid reaction of the ice to the wind field leads the drift track of single ice floes to exhibit the randomness of "a drunkard's walk" [*Colony and Thorndike*, 1985]. This means that the movement of pack ice is not regular and different states of motion are observable: divergence, convergence and shear motion may be observed.
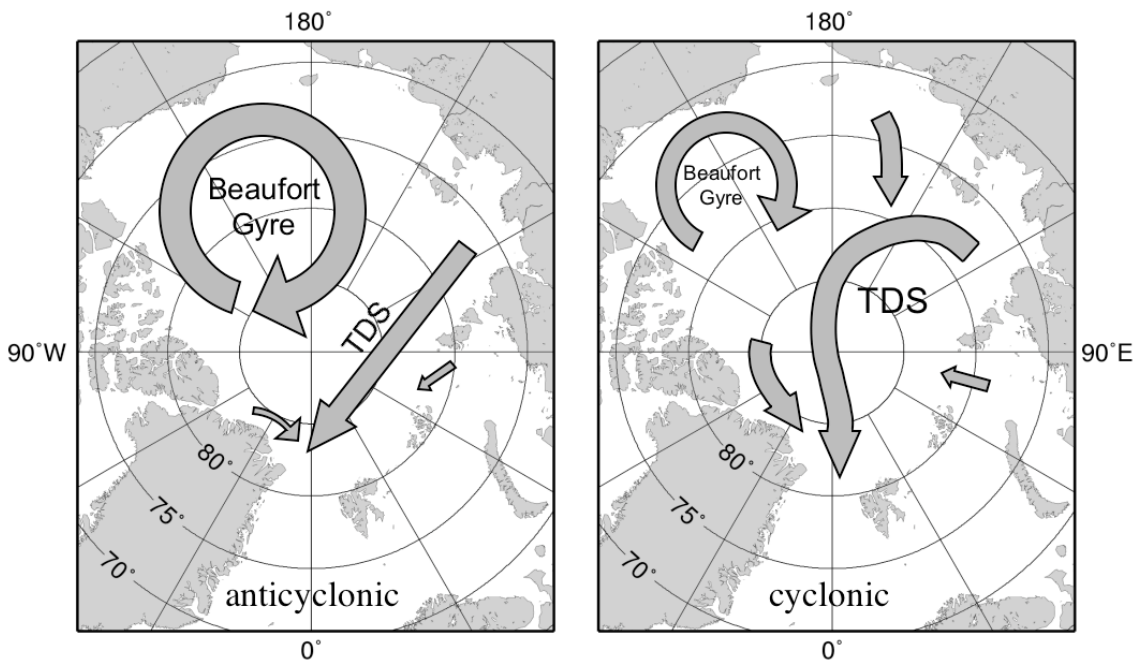
Figure 1.8: Schematics of the anticyclonic and cyclonic sea ice drift regimes that are most prominent in the Arctic Ocean and alternate on a seasonal scale as well as dominate each for 5–7 year periods. Thickness of arrows corresponds roughly to the strength of the respective feature, i.e. the associated ice volume transport.

In the Arctic the mean field of sea ice motion features two main patterns: the Beaufort Gyre and the Transpolar Drift Stream (TDS). The Beaufort Gyre is an anticyclonic gyre typically covering the Beaufort Sea and parts of the central Arctic Ocean between the East Siberian Sea and the North Pole (see Figure 1.6). The stream of sea ice that exits out of the Laptev and East Siberian seas and then crosses the central Arctic Ocean towards the Fram Strait is called the TDS. Further contributions to the TDS stem from the Beaufort Gyre, mainly comprising multi-year ice, and from the Kara Sea, where some of the first year ice exits towards the central Arctic and some flows to the Barents Sea. The strength of these two main patterns plays a dominant role in the age distribution of Arctic sea ice. The recirculation of ice in the Beaufort Gyre may cause residence times of more than 10 years in the western Arctic whereas the ice will not become older than 5 years in the eastern Arctic if advected in the shorter TDS pathway [*Rigor and Wallace*, 2004; *Belchansky et al.*, 2005]. The extent and strength of the Beaufort Gyre and TDS change due to variability in atmospheric pressure patterns. Although the Arctic sea ice drift field does not necessarily feature either of these patterns, monthly or annual averages are commonly separated into two wind-driven drift regimes named anticyclonic and cyclonic respectively for discussion [*Gudkovich*, 1961]. On a seasonal scale the anticyclonic regime dominates during winter and the cyclonic regime is found during the few months

of Arctic summer [*Proshutinsky et al.*, 2002]. However, multi-annual drift composites feature both of these regimes, which are found to recur every 5–7 years [*Proshutinsky and Johnson*, 1997]. The anticyclonic regime is characterised by a strong Beaufort Gyre covering large parts of the Arctic Ocean and a straight TDS (see Figure 1.8, left panel). The modelled drift pattern shown in Figure 1.6 is an example of the anticyclonic regime. In the cyclonic regime the Beaufort Gyre is weakened and retreats into the Beaufort Sea with its centre closer to the Canadian or Alaskan coasts. The TDS then has a cyclonic bend and covers a larger area than in the anticyclonic case (see Figure 1.8, right panel). It is important to notice that the main source regions of sea ice transported towards the Fram Strait differ in the two regimes. During a cyclonic phase more thick, multi-year ice from the central Arctic Ocean and from north of Greenland and the eastern Canadian Archipelago are transported towards the Fram Strait. Thus, the export of ice into the Greenland Sea is amplified in these years—leading to a strong decrease in the total Arctic sea ice volume—whereas during anticyclonic phases more ice recirculates within the Beaufort Gyre [*Proshutinsky et al.*, 2002; *Martin and Martin*, 2006].

Investigations of satellite-derived estimates and buoy drift measurements have shown that the two drift regimes can be related to the North Atlantic Oscillation (NAO)[d] and Arctic Oscillation (AO)[e] [*Kwok*, 2000; *Rigor et al.*, 2002]. *Cavalieri and Häkkinen* [2001] confirmed the assumption of *Proshutinsky and Johnson* [1997] that the two drift regimes result from changes in the strength and extent of the Icelandic Low and the Siberian High. The authors state that the Siberian High extends across the central Arctic and forms a high pressure ridge between the Asian and North American continents during the anticyclonic regime and that the Icelandic Low stretches into the Barents and Kara seas in the cyclonic phase which is also characterised by a weakened Siberian High. Furthermore, the cyclonic regime phases are associated with strong de-

---

[d] The North Atlantic Oscillation (NAO) describes the variation of the atmospheric mass above the North Atlantic caused by the simultaneous intensification (positive phase) or weakening (negative phase) of the Icelandic low and Azores high pressure areas. The signal is strongest during the winter months December–March. *Hurrell* [1995] defined the NAO index as the normalised sea level pressure (SLP) difference between the two observation stations in Stykkisholmur, Iceland and Lisboa, Portugal. The sea ice export through the Fram Strait is found to be strongly correlated with the NAO after its shift in 1978 [*Hilmer and Jung*, 2000].

[e] The Arctic Oscillation (AO) is defined as the leading empirical orthogonal function of the wintertime SLP field of the northern hemisphere. The AO is associated with strong fluctuations at the 50 hPa level and corresponds to a surface signature of modulations in the strength of the polar vortex aloft. The derivation of the AO index is based upon the leading principle component of monthly means of wintertime (November–April) SLP anomalies. Geostrophic height anomalies of opposing sign have been observed between the polar region north of 65 ° N and a subpolar ring centred at 45 ° N. [*Thompson and Wallace*, 1998, 2000; *Deser*, 2000]

creases in the total Arctic sea ice volume [*Martin and Martin*, 2006]. The regime phases also correlate with variations in the liquid freshwater content of the Arctic Ocean [*Proshutinsky et al.*, 2002].

The drift of sea ice plays an important role in the climate system. On local scales, deformation, which occurs under convergent or shear motion, increases the ice thickness and changes the surface roughness, providing a larger working surface for the atmospheric and oceanic drag. Moreover the formation of leads and polynyas due to convergent or shear drift immediately affects the oceanic heat balance [*Perovich and Maykut*, 1990; *Maykut and McPhee*, 1995] and the subsequent formation of new ice in winter results in a salt uptake by the ocean as salt is released during the freezing process. The average salinity of the Arctic mixed layer amounts to 30–34 *Tomczak and Godfrey* [1994]; *Schlosser et al.* [2000] whereas young sea ice has a bulk salinity of less than 15 being halved within six months and further reduced in multi-year ice which has a salinity of only 0–4 [*Weeks*, 1998]. Thus sea ice can be regarded as freshwater and has again an impact on the ocean when it is melting. Sea ice can also be regarded as a storage vessel of freshwater and latent heat—because freezing is an exothermic process—and thus to retain signals beyond the annual cycle. Sea ice drift then effects a transport of these properties and adds large-scale importance to these processes: Most sea ice does not melt where it forms. The shelf seas of the Arctic Ocean are the main sea ice production areas; specifically the Laptev, Kara and East Siberian seas with ice export rates of 430 km^{3}yr^{-1}, 250 km^{3}yr^{-1} and 150 km^{3}yr^{-1} respectively [*Alexandrov et al.*, 2000; *Martin and Martin*, 2006]. Consequently, salty and hence dense water is formed on the shelves. Dense surface waters in turn drive oceanic deep convection. The ice is transported across the Arctic Ocean and departs into the North Atlantic Ocean. Most of it melts in the Greenland and Norwegian seas (a net import of 3200 km^{3}yr^{-1} on average is calculated by *Hilmer et al.* [1998]). The low-density melt water has a stabilising effect on the oceanic stratification[f]. With its implications for the formation of deep water sea ice and its volume export out of the Arctic Ocean are of significance to the climate system and to global climate change.

---

[f] Extremely large sea ice export events cause a pooling of fresher-than-normal waters at the ocean surface and can be linked to the so-called Great Salinity Anomalies (GSA) *Dickson et al.* [1988]; *Aagaard and Carmack* [1989]; *Häkkinen* [1998]; *Hilmer et al.* [1998]; *Belkin et al.* [1998]. The GSA have a damping effect on the deep convection which normally takes place during winter in the Greenland and Labrador seas. As one of the driving mechanisms the deep convection is an important contributor to the global thermohaline circulation.

1.3   A first view on ridges

1.3.1   The nature of deformed sea ice

As already mentioned in Section 1.2.3 the sea ice cover is not stationary. Its motion results in opening, closing and deformation of the cover. Two of the three states of sea ice motion, convergence and shear, may deform the ice cover, if the motion can not be compensated by lead closing. Depending on the actual ice thickness there are two main kinds of deformation: rafting and ridging.

Rafting takes place when the ice is thin and elastic enough that it does not break under pressure so that floes slide on top of each other intact. In a special case, finger rafting, fractures occur perpendicular to the interacting edges and one or both floes split into fingers or fork like lamellae that subsequently intertwine. With growing floe thickness the ice becomes less elastic and one or both floes may break—to form a ridge—before the frontal area of one floe can slide as a whole beneath the other and pressure is released into rafting. *Parmeter* [1975] found that the critical thickness at which ridging begins to occur depends on material properties, such as temperature and porosity of the ice, and hence is predictable. The maximum ice thickness at which rafting can occur is estimated to range between 5 and 25 cm [*Parmeter*, 1975; *Richter-Menge and Jones*, 1993]. This agrees with the study of *Weeks and Kovacs* [1970] in which deformation at an ice thickness of 15 cm on average is described as a transitional state between finger rafting, rafting and ridging.

In the case of ridging, piled up ice blocks form a line along the original fracture zone (Figure 1.9)[g]. This process has characteristics known from plate tectonics and bent sea ice floes as well as subduction zones often filled with water can be found in front of newly formed ridges (see Figure 1.10, left panel). The ice blocks in ridges are of order of magnitude of 0.1–1 m in diameter and their thickness corresponds to that of the level ice from which they originate, the so-called parent ice (Figures 1.11a and 1.11b). A ridge separates into a sail above the water-level and a keel below. Measurements have shown a general dependence between these two parts. *Timco and Burden* [1997] reviewed the results of 112 first-year and 64 multi-year single ridge measurements and found ratios of 4.4 (first-year) and 3.3 (multiyear) between keel depth and sail height. Extreme values observed so far record a maximum height of 10 m and depth of more than 40 m [*Wadhams*, 2000]. Typical sail heights in the Arctic average 1–2 m. *Tucker et al.* [1984] found that the maximum sail height $H_{s_{max}}$ of a ridge reached during a deformation event depends on the parent ice thickness H_l. The same relation-

---

[g] Though the photographs presented in Figures 1.9 and 1.10 (left panel) have been taken during a campaign on Baltic sea ice near Hailuoto, Finland in 2004 the newly formed ridges are in principle also typical for Arctic first-year sea ice.

Figure 1.9: New pressure ridges piled up along the fast ice edge.

ship holds for the maximum keel depth $H_{k_{max}}$, though a different coefficient is obtained by *Melling and Riedel* [1996]:

$$H_{s_{max}} = 5.24\sqrt{H_l} \quad \text{and} \quad H_{k_{max}} = 16\sqrt{H_l}\,. \tag{1.3}$$

Hopkins [1998] confirmed these findings with a two-dimensional particle model for single ridge evolution (see his Figure 5), while *Amundrud et al.* [2004] found a factor of 20 for the upper envelope of their keel draft data. *Tucker et al.* [1984] mention a factor of 3.71 for a best fit regression curve of all sail height data. As only newly formed ridges have been investigated by the authors this shows that not all sails necessarily reach their maximum height. The same holds for the keels and is due to a lack of level ice or an early decrease in the forcing of the deformation process. Assuming a keel of triangular shape (Figure 1.11b)

Figure 1.10: Left panel: New ridges are blocky and very inhomogeneous. The deformation process of sea ice floes resembles plate tectonics and subduction zones in front of ridges can be found (black arrow). **Right panel:** The surface of weathered ridges becomes smooth and the interior consolidated (white arrow).
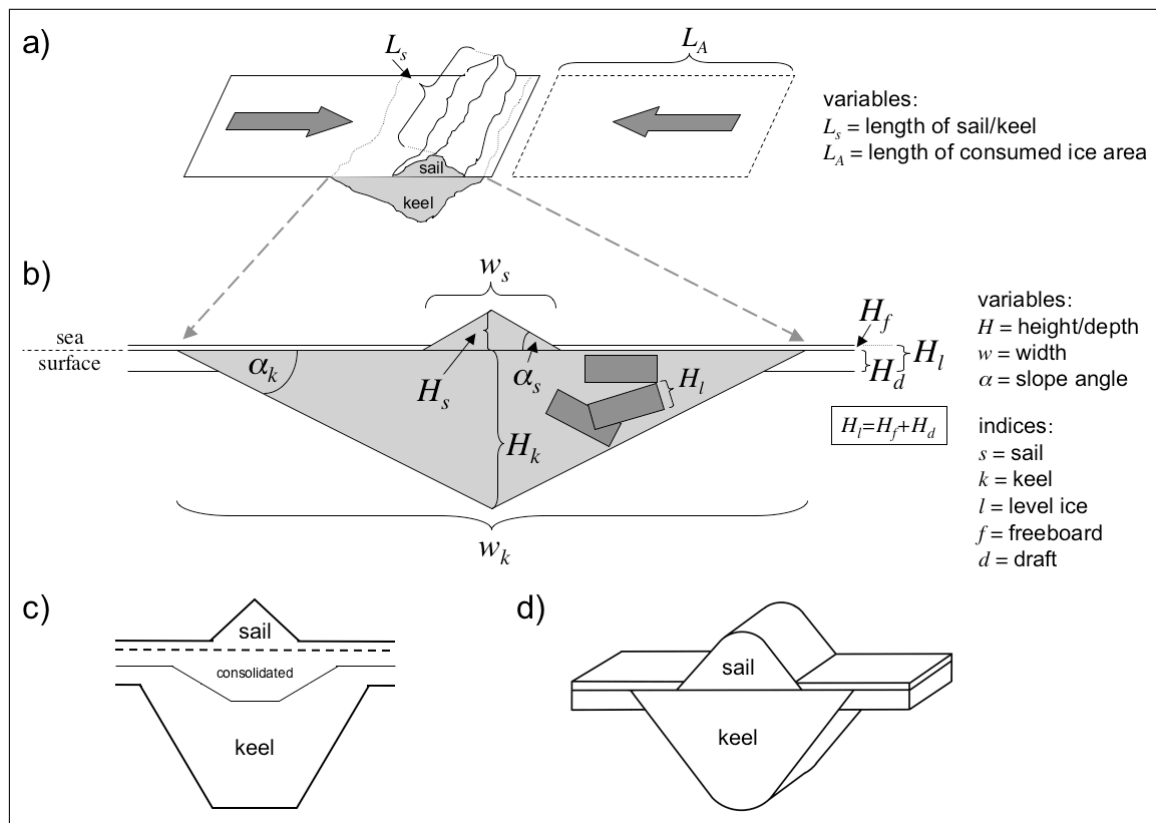
Figure 1.11: (**a**) Schematic of the formation and shape of a typical pressure ridge. Convergent drift pushes two ice floes into each other and blocks, which have previously formed level ice of length L_A, are piled up. (**b**) Geometric cross-sectional model of a pressure ridge following the common triangular shape. Variables that are used in the main text are declared. The proportions of sail and keel are true to scale according to average values from *Timco and Burden* [1997]. (**c**) Alternative trapezoid keel shape after *Timco and Burden* [1997, Fig. 2]. Ice blocks and water in voids may refreeze to a massive consolidated layer in the centre of the ridge. (**d**) Alternative Gaussian sail and keel shape after *Steiner et al.* [1999, Fig. 3].

Amundrud et al. [2004] showed that a ridge of maximum draft incorporates at least 560 m of level ice (corresponding to L_A in Figure 1.11a) and that only a quarter of their observed floes was large enough to provide this ice area.

Another common measure for the characterisation of ridges is the slope angle of the flanks of sail and keel. Here, idealised flanks are viewed as straight inclined planes. Slope angles of sails are observed between $14\,^\circ$ and $30\,^\circ$ with an average of $24\,^\circ$ for first-year and $17\,^\circ$ for multi-year ridges, whereas keel slopes range between $16\,^\circ$ and $55\,^\circ$ with means of $33\,^\circ$ and $24\,^\circ$ for newly formed and weathered ridges respectively [*Kovacs*, 1971; *Weeks et al.*, 1971; *Wadhams*, 1978, 2000]. These values are highly variable and depend on the sample size as well as the location of observation [*Timco and Burden*, 1997].

The large range of these parameters gives a good impression of the very com-

plex structure ridges have in reality (Figure 1.9). For example, a keel is not always attached to one sail or sail and keel are not centred on top of each other. This is particularly likely for older ridges. Ridges are very inhomogeneous. Due to their blocky formation they contain voids, which are at first filled with air (sail) or sea water (keel) and may later fill up with snow or refreeze respectively. Thus, the formerly loose blocks freeze solid into a so-called consolidated layer at the intersection of sail and keel, stabilising the deformed floe area (see Figure 1.10, right panel). Nevertheless, approximating the cross-sectional shape of a ridge with a triangle for the sail centred above an inverted one for the keel (Figure 1.11b) is a common approach in ridge observation [*Timco and Burden*, 1997, Fig. 16] and modelling [*Lensu*, 2003a]. Describing the keel shape as a trapeze (Figure 1.11c) instead of a triangle takes into account that a keel continues to grow laterally perpendicular to the ridge length axis once the maximum depth is reached *Hopkins* [1998].

Following the *WMO* [1989] there are three more types of ice deformation worth mentioning: fracturing, hummocking and shore ice ride up. Fracturing describes the first step in ice deformation, when ice is under pressure and deforms permanently with the first occurrence of a rupture. In contrast, hummocks are comparable to ridges. They consist of blocks or larger tilted floe pieces but do not have a longitudinal extension because they form when ice experiences pressure from more than one side rather than developing along a fracture line. Finally, the shore ice ride up refers to the case of sea ice being pushed onto land or structures. A deformation feature not listed in the *WMO* [1989] chart is rubble. A rubble field is an area of randomly scattered and tilted ice blocks which has a relatively constant thickness compared to the triangular cross-sectional shape of a ridge. In the case of strong, long-lasting pressure ridges can form so-called clusters, i.e. no level ice is found between them, and consequently, the structure of single ridges can merge in a rubble field. Often rubble is not viewed as an independent deformation feature but is interpreted as an initiating [*Parmeter*, 1975] or finalising [*Hopkins*, 1998] stage of ridging. The ablation of deformational features is known as weathering. This process leads to an increased compactness of the features and eliminates their irregularities. A Gaussian cross-sectional shape may describe these rounded ridges best (see Figure 1.11d). Besides the *WMO* [1989] nomenclature, weathered sails/keels are also known as hummocks/bummocks.

1.3.2 Techniques of ridge measurements

Measurements of sea ice pressure ridges can be performed at different scales. Beginning with in situ techniques sail height and freeboard respectively are

measured with levelling devices well-known from geodetic surveying. The thickness of a ridge is measured directly by drilling either with an auger or a hot water drill [e.g. *Nortala-Hoikkanen et al.*, 1994]. The size of voids in between the blocks of the ridge, i.e. the porosity of the ridge, can also be derived from these drill hole observations, along with block thickness and slope angles. Keel parameters are much more difficult to access either by divers or with sonar (sound navigation and ranging) instruments. In situ methods give high spatial resolution of individual ridges but are limited in number owing to logistical constrains. *Timco and Burden* [1997] compiled results of 176 single ridge measurements from different Arctic regions and the Baltic Sea.

Remote sensing techniques offer the opportunity to cover a larger area of deformed sea ice and to record parameters from a number of ridges which is statistically more significant. Sea ice surface roughness observations can be performed with airborne laser (light amplification by stimulated emission of radiation) instruments. These allow the derivation of ridge statistics [e.g. *Ketchum*, 1971] though low frequency aircraft movements need to be removed first [*Hibler*, 1972]. Upward-looking sonar (ULS) instruments can be attached to the top of oceanographic moorings [e.g. *Melling et al.*, 1995; *Fissel et al.*, 2004]. An ULS may also be mounted on a submarine which is capable of diving across the entire Arctic Ocean. The derivation of ridge statistics from under-ice profiles recorded with ULS is described for example by *Wadhams and Davy* [1986]. A more recent approach applies autonomous underwater vehicles (AUVs) for under ice sonar observations [*Wadhams et al.*, 2004].

Another new technique for ridge measurements is an airborne instrument that combines an electromagnetic device (EM) for ice underside detection and a laser for surface elevation, the EM bird [*Haas*, 2004a]. Although other efforts have been made to record ice surface and underside profiles at the same time and location [e.g. *Wadhams*, 1980] these campaigns lacked real contemporaneity because the individual instruments were not mounted on the same device as is the case for the EM bird. Sail and keel data collected with the EM bird are used in the present study.

The disadvantage of the above remote sensing instruments is a lack of information about keel width because the crossing angle of the instrument beam and ridge is unknown. For the ULS technique this problem is solvable using additional side-scan sonars. These allow not only the derivation of the keel width but also the detection of the slope angles and orientation of the ridge [*Davis and Wadhams*, 1995]. For airborne measurements the same can be achieved with a side scan laser though this instrument is still in a test phase [*S. Hendricks*, pers. comm.].

Satellite-based remote sensing of equivalent pressure ridge quantities is not

yet operational because processing methods for the recorded backscatter data is still under development. The main problem is to distinguish between different characteristics of the sea ice surface that all cause similar backscatter intensities, i.e. to distinguish between small-scale roughness at the cm-scale and large ridges or rubble fields [*W. Dierking*, pers. comm.].

The present study focusses on sail height and keel depth proportions as well as ridge density. The latter is also known as ridge frequency and is defined as the number of ridges per km. This set of parameters is found to be a good interface between ridge measurements and numerical modelling for comparison and derivation of parameterisations. They are also important for navigation in ice-covered seas and can be related directly to other important parameters, for example the atmospheric drag over sea ice [e.g. *Garbrecht et al.*, 2002].

1.3.3   Ridging in a sea ice model

Three different concepts of pressure ridge modelling need to be distinguished: (1) the formation process of a single ridge is studied, for example with a discrete element model that resolves single ice plates [e.g. *Hopkins*, 1998]; (2) the ridging process is considered as an abstract deformation scheme, which is used to redistribute ice between thickness categories, rather than being resolved in all its complexities [e.g. *Flato and Hibler*, 1991, 1995]; (3) a prognostic description of ridge quantities in an Arctic-wide sea ice model in which ridging is viewed as an individual process affecting the sea ice thickness and momentum balance [*Steiner et al.*, 1999; *Martin*, 2006, and the present study].

In this study a dynamic-thermodynamic continuum model is applied similar to those that are routinely used in coupled climate simulations. In such models the sea ice component often contains an over-simplified parameterisation of dynamic ice growth. The ice concentration variable is artificially restricted to unity and, consequently, the actual ice thickness increases because the mean ice thickness remains unchanged. This aspect will be discussed in more detail later in the present study. Ridges are rarely simulated explicitly in Arctic-wide sea ice models. Because of the mismatch in length scales between common Arctic-wide model grids (10–100 km) and ridges (10–1000 m) single deformation features are not resolved. Hence, ridging is a subscale process that needs to be parameterised. In an effort to find a new, realistic parameterisation for the description of ridge formation with all its implications for the sea ice cover, three different pressure ridge models are compared in this study. The models are based on the works of *Steiner et al.* [1999], *Harder and Lemke* [1994] and *Lensu* [2003a].

The derivation of ridge quantities in an Arctic-wide sea ice model has the ad-

vantage that related processes and causes of climate change in the Arctic, for example the formation of fast ice, changes in atmospheric and oceanic drag or the ratio of deformed and total ice volume, may be determined in more detail. The changing distribution of deformed ice in the Arctic Ocean is a good indicator of Arctic sea ice regime changes and plays an important role in the explanation of these changes [e.g. *Lindsay and Zhang*, 2005].

1.4 Motivation and aims of this study

The motivation for the present study is twofold: First, pressure ridges are a prominent feature of the sea ice cover affecting the physical system of sea ice at various levels and, second, ridges are great obstacles for shipping on sea ice covered oceans. The deformation of the sea ice cover results in an increase in the thickness of the ice, i.e. ridges store a large part of the total Arctic sea ice volume. This deformed ice volume can also be interpreted as a kind of memory to the ice cover because, for example, storm events during winter causing deformation influence the melt rate, which depends on the ice thickness, during the subsequent summer. Furthermore, the surface roughness of ice floes is increased by ridging. A deformed floe offers the drag performed by wind and ocean currents a larger working area and hence ridging has an effect on the momentum balance and the effective drift speed of sea ice. Finally, estimates of sea ice surface roughness give another opportunity to compare models and remote sensing data so that large-scale models can be validated.

The second reason for this study is the development and validation of a ridging algorithm for application in a numerical model that is appropriate for sea ice forecasting. In this context the study is part of the *European Union* (EU) project *Ice Ridging Information for Decision Making in Shipping Operations* (IRIS)[h]. While the Scandinavian participants focussed on Baltic Sea modelling, the investigations here relate to high Arctic regions. The overall aim and achievement of the IRIS project was to develop pressure ridge algorithms that allow ridging parameters to be obtained from state of the art sea ice models and to verify these model estimates with simultaneous air-borne and ground measurements. Therefore, the present study focusses not only on ridge modelling but also considers ridge measurements. For this purpose sea ice surface laser

---

[h] Scientific partners of the IRIS project were: Helsinki University of Technology, Ship Laboratory, Finland; Alfred Wegener Institute, Germany; Finnish Institute of Marine Research, Finland; Information Technology, Technical Research Centre of Finland; Kvaerner Masa-Yards, Arctic Research Centre, Finland; Swedish Meteorological and Hydrological Institute, Sweden; The Scottish Association of Marine Science, United Kingdom. (http://www.tkk.fi/Units/Ship/Research/Iris/Public/)

profiles over an eleven year period (1995–2005) were available and, moreover, 100% simultaneously recorded sea ice surface and underside profiles from four campaigns in 2003–2005 are investigated for the first time with respect to sail and keel parameters.

The challenge in sea ice pressure ridge modelling is to find an equilibrium between applying limiting parameterisations and allowing the physical processes to develop freely in the model. Parameterisations are necessary to describe sub-scale processes in a model and offer a possibility to prevent unrealistic simulation results. Moreover, model output variables need to be chosen that enable a comparison with measurement data. Here, ridge density and height are preferred in agreement with the IRIS partners. The present study includes a comparison of three different approaches to ridge modelling in order to test their suitability for the project aims, i.e. sea ice forecasting for shipping operations and Arctic change studies. Such an application-oriented comparison has not been performed before.

In order to gain realistic results and substantial insight into the different ridge algorithms a hierarchy of realisations of an Arctic-wide dynamic-thermodynamic sea ice model (SIM) is applied in this study. First, a discussion of simulated sea ice drift estimates is presented including results from the SIM in ocean-coupled and uncoupled modes. On long time scales of years to decades, the interannual variability of the ocean has important implications for sea ice drift variations. However, the uncoupled SIM is found to perform well and is suitable for the development and validation of ridge algorithms, not least because the wind has a much stronger impact than the ocean on short time scales of days to weeks typical for forecast computations [*Thorndike and Colony*, 1982]. The uncoupled SIM computes faster and thus saves time during ridge model development. Simulation runs of the uncoupled SIM are performed for an Arctic-wide comparison of individual ridge model results and observational data. During ridge algorithm development a further simplification of the SIM is applied: As ridge formation is a purely dynamic process the different ridging algorithms are first tested with thermodynamic processes turned off in the SIM.

1.5   Outline

The present study is divided into three main parts. In combination they provide the central thread: the implementation and validation of pressure ridge algorithms in an Arctic-wide numerical sea ice model (SIM). The first part begins with the presentation of the dynamic-thermodynamic sea ice model in Chapter 2, which will later form the basis for the ridge modelling experiments. For the modelling of deformation processes the model needs to have sea ice drift

velocity estimates of good quality. Hence, in Chapter 3, results from the SIM are compared to estimates from other sea ice models and observations with respect to the spectrum of drift speeds and the resemblance of drift patterns. This chapter includes a wide discussion of possible reasons for deviations between models (Section 3.6) and an inspection of the effects of these differences on the sea ice transport through the Fram Strait (Section 3.7).

Part II focusses on ridge measurements and aims not only at presenting results from airborne ridge observations but also at giving a clue as to what the ridge algorithms are expected to reproduce. Chapter 4 includes an overview of contributing campaigns and data processing techniques used as well as the results of simultaneous sea ice surface and underside ridge measurements with special respect to modelling applicability.

Finally, in Part III, three different ridging algorithms are introduced, tested in idealised experiments and applied to realistic Arctic conditions . Chapter 5 gives an overview of the different states of sea ice motion (Section 5.1) which are responsible for the deformation, and the meaning of "ridging schemes" as these are applied to some state-of-the-art regional climate models for polar regions (Section 5.3). In Chapter 6, the underlying ideas and the implementation of the three different approaches to ridge modelling are explained. Results of sensitivity studies with idealised forcing and topography of all three algorithms are presented in Chapter 7. These successful tests allow an application of the algorithms to realistic Arctic conditions on an Arctic-wide model grid (Chapter 8). The distributions of ridges in the Arctic as resulting from each of the algorithms is presented in Section 8.2 and the validation of the model results with observations from Chapter 4 is discussed in Section 8.3.

Each of the three main parts ends with an individual summary which emphasises the most important investigations made and results achieved. In the final Chapter 9 overall conclusions are drawn and an outlook for subsequent investigations and the next steps in ridging related modelling is presented.

Part I

Foundations for
Pressure Ridge Modelling
or: The discovery of slowness

Chapter 2

A large-scale sea ice model

In this chapter the physical quantities and processes that are necessary to describe the sea ice cover itself, and its formation and reduction in a numerical large-scale sea ice model are presented along with the relevant equations. The sea ice quantities are affected by their environment, which is characterised by the state of the oceanic mixed layer below the ice and the atmospheric conditions above.

Sea ice forms a thin, insulating layer between atmosphere and ocean. The horizontal length scales of the sea ice cover are larger than the vertical scale $dx \simeq dy >> dz$ by three to four orders of magnitude. Hence, the sea ice cover offers a large working surface for interactions with its environment. As a sea ice model is not intended to describe the entire climate system, external forcing needs to be provided in the form of atmospheric and oceanic parameters. These may be inferred from observations or results of atmosphere, ocean or fully coupled models. Usually the forcing values are averaged in space or time, or both. Instead of external forcing fields another numerical model that computes atmospheric or oceanic quantities may be coupled to the sea ice model.

The starting point of this study is a dynamic-thermodynamic sea ice model with viscous-plastic rheology. The dynamics are based on the fundamental work of *Hibler* [1979]. The thermodynamic part of the model is based upon the zero-layer approach of *Semtner* [1976] for heat conduction within the sea ice layer and heat exchange to the atmosphere and ocean is considered according to the studies of *Parkinson and Washington* [1979] and *Lemke* [1987] respectively. The model also includes a prognostic snow layer after *Owens and Lemke* [1990]. The present model was implemented and configured for the Arctic Ocean by *Harder* [1996].

Extensive studies of the quality of the applied rheology in the Sea Ice Model Intercomparison Project (SIMIP) [*Kreyscher*, 1998; *Kreyscher et al.*, 2000], and of the simulated sea ice area, thickness and drift [*Hilmer*, 2001; *Martin*, 2003] have proven the model to be a valuable instrument in understanding the Arctic sea

ice cover and its variability. The ice export from the Arctic Ocean into the Nordic Seas and the North Atlantic has been investigated by *Harder et al.* [1998] and *Hilmer et al.* [1998]. *Hilmer and Jung* [2000] found a close relationship between the NAO and the Fram Strait ice export. The long-term trend in the total Arctic sea ice volume has been discussed by *Hilmer and Lemke* [2000]. *Martin and Martin* [2006] calculated sea ice transports within the Arctic Ocean and showed a relationship between ice volume variations and ice drift regimes. A precursory version of the model used in the present study can be found in *Lieser* [2004], where the model was applied to assimilation of ice concentration observations and sea ice forecasting.

In the present study a hierarchy of realisations of the primary sea ice model is applied. The model described in this chapter is run in three different modes: a coupled mode together with an ocean model, in an uncoupled mode and uncoupled without thermodynamics. The different model realisations were chosen to match the requirements of the individual numerical experiments. The particular model specifications, grid layout and forcing data is described with the corresponding experiment in Chapters 3, 7 and 8. In the following the physics of the primary sea ice model are described.

2.1 Prognostic variables

The ice concentration, mean ice thickness and ice motion are commonly derived prognostically in large-scale sea ice models.

The mass of a layer of sea ice per unit horizontal cross-sectional area is $m_i = \rho_i h$ where ρ_i is the density of sea ice, which is considered to be uniform in space and time, and h is the ice volume per unit horizontal cross-sectional area. h is also known as mean ice thickness and equals the actual ice thickness H weighted by the ice concentration A:

$$h = AH. \tag{2.1}$$

The ice concentration A is the area of ice covered ocean per unit horizontal cross-sectional area and hence has a defined co-domain of $[0, 1]$. The mean ice thickness h is thus the thickness of the sea ice layer when its mass is considered to be equally distributed over the entire area such that $A = 1$, i.e. $h \leq H$. Then the ice mass per unit volume or partial ice density is given by $\tilde{\rho}_i = \rho_i A$ [*Gray and Morland*, 1994].

A first step towards a sea ice model is to apply the conservation of ice mass. The ice mass within a defined area is conserved when the partial ice density satisfies the well-known conservation equation

$$\frac{\partial \tilde{\rho}_i}{\partial t} + \nabla_3 \cdot (\tilde{\rho}_i \, \vec{u}_3) = 0 \tag{2.2}$$

where t stands for time and $\nabla_3 = (\partial/\partial x, \partial/\partial y, \partial/\partial z)$ denotes the three-dimensional Nabla-operator and $\vec{u}_3 = (u, v, w)$ is the ice drift velocity in the three dimensional space expressed in cartesian coordinates x, y and z. From Equation (2.2) the evolution equation of ice concentration A can be deduced by substituting $\tilde{\rho}_i$ with $A\rho_i$ and integrating vertically between ice bottom z_b and surface z_s

$$H\frac{\partial A}{\partial t} + H\,\nabla \cdot (A\,\vec{u}) + A\,(w_s - w_b) = 0\,. \tag{2.3}$$

Here, the Nabla-operator ∇ and the drift velocity $\vec{u}$ are reduced to the x and y dimensions and H is the physical ice thickness given by $z_s - z_b$. In a large-scale sea ice model the sea ice cover is commonly assumed to be two-dimensional and the vertical component of the ice velocity is neglected, i.e. the term $A(w_s - w_b)$ is cancelled . The problems that arise from this approximation are discussed in Chapter 5 in detail. Furthermore, the ice mass is not necessarily conserved within the layer. It may change due to phase changes of the frozen water at the floe edges. These processes are expressed in a source and sink term S_A on the right hand side of the evolution equation of ice concentration, which is finally

$$\frac{\partial A}{\partial t} + \nabla \cdot (A\,\vec{u}) = S_A\,. \tag{2.4}$$

The sea ice drift velocity $\vec{u}$ is derived from the momentum balance (see Section 2.2). The individual contributions to the source term S_A are presented in Section 2.3.

The volume flow $\tilde{q}_s$ per unit horizontal cross-sectional area at the surface of an arbitrarily shaped ice floe is determined from the difference between the normal speed u_n of a surface particle along the surface normal $\vec{n}_s$ and the shift of the entire ice floe in the same direction $\tilde{q}_s = u_n - \vec{u}_3 \cdot \vec{n}_s$ [*Gray and Morland*, 1994]. The surface of the ice floe is defined as $z - z_s(x, y, t) \equiv 0$ and its total temporal change is thus expressed by

$$\frac{\partial z_s}{\partial t} + \vec{u} \cdot \nabla z_s - w_s = \tilde{q}_s \tag{2.5}$$

where w_s is the vertical component of the motion of the entire ice floe at its surface [*Gray and Morland*, 1994]. An equivalent relationship holds for the ice floe bottom:

$$\frac{\partial z_b}{\partial t} + \vec{u} \cdot \nabla z_b - w_b = \tilde{q}_b\,. \tag{2.6}$$

Substracting Equation (2.6) from Equation (2.5) yields the evolution of the actual ice thickness H

$$\frac{\partial H}{\partial t} + \vec{u} \cdot \nabla H - (w_s - w_b) = \tilde{q}_s - \tilde{q}_b\,. \tag{2.7}$$

However, in the present large-scale sea ice model the mean ice thickness $h = A H$ is chosen instead of H to be the second conserved quantity, besides

ice concentration, utilised to describe the sea ice layer. The evolution equation of the mean ice thickness is derived by multiplying the evolution equation (2.7) of the actual ice thickness with A and adding the new equation to the evolution equation (2.3) of ice concentration; this also eliminates all terms related to vertical velocity components.

$$\frac{\partial h}{\partial t} + \nabla \cdot (h\,\vec{u}) = S_h \qquad (2.8)$$

The term S_h on the right hand side reflects the thermodynamic sources and sinks of the ice volume, including descriptions of the surface and bottom ice fluxes $\tilde{q}_s$ and $\tilde{q}_b$, and is discussed in Section 2.3.

The present sea ice model also includes a prognostic snow layer. The evolution equation of the mean snow thickness h_s corresponds to that of the mean ice thickness and is given by

$$\frac{\partial h_s}{\partial t} + \nabla \cdot (h_s\,\vec{u}) = S_{h_s} \,. \qquad (2.9)$$

This additional snow layer has direct implications only for the thermodynamic processes in the sea ice model.

The sea ice model as applied in the past and presented in this chapter includes only one ice class or type. The set of evolution equations presented above distinguishes between open water ($h = 0$) and an ice cover with a certain prognostic thickness ($h > 0$). The dynamics of the model rely only on this mean ice thickness, but for the thermodynamic calculations seven artificial ice thickness levels are considered (see Section 2.3). The model was changed with respect to its ice classes for the present study. Changes are documented in Chapter 6.

2.2   Dynamics, kinematics and rheology

Kinematics describe the movement of objects in space in terms of distance, speed and acceleration considering neither its causes nor results. In contrast dynamics are about the changes in motion due to the impact of forces. Finally, rheology connects kinematics and dynamics.

As this study focusses on the description of deformation it calls for a close look at the model's dynamics, kinematics and rheology in order to prepare for the discussion of deformation schemes in Chapter 5 and the presentation of ridging algorithms in Chapter 6.

Momentum balance

The evolution equations introduced above include the ice drift velocity $\vec{u}$ which is calculated from the momentum balance [*Hibler*, 1979]

$$m_i \left(\frac{\partial \vec{u}}{\partial t} + \vec{u} \cdot \nabla \vec{u} \right) = \vec{\tau}_a + \vec{\tau}_w - m_i \, f \, \vec{k} \times \vec{u}_3 - m_i \, g \, \nabla H_{tilt} + \vec{F}_{int} \, . \qquad (2.10)$$

On the right hand side of this equation the atmospheric stress $\vec{\tau}_a$ and the oceanic stress $\vec{\tau}_w$ are listed followed by the Coriolis force and the sea surface tilt force. Last but not least the internal ice forces $\vec{F}_{int}$ are part of the momentum balance. All components are of unit force per unit horizontal cross-sectional area. As the sea ice layer dynamics are regarded only in horizontal dimensions Equation (2.10) is the vertical integrated form of the complete three-dimensional momentum balance and thus does not contain components of the z-dimension.

The stresses occurring at the ice surface and underside depend on the wind $\vec{u}_a$ and ocean velocity $\vec{u}_w$ respectively as well as on the ice drift velocity $\vec{u}$. Both stresses are determined from quadratic formulations following the propositions of *McPhee* [1975] and *Hibler* [1979]. The impact of the wind is given by

$$\begin{aligned} \vec{\tau}_a &= \rho_a \, c_a | \vec{u}_a - \vec{u} | \, \left[(\vec{u}_a - \vec{u}) \, \cos \phi_a + \vec{k} \times (\vec{u}_a - \vec{u}) \, \sin \phi_a \right] \\ &\simeq \rho_a \, c_a \, | \vec{u}_{10m} | \, \vec{u}_{10m} \end{aligned} \qquad (2.11)$$

with the density of air $\rho_a = 1.3$ kg m^{-3}. The atmospheric drag coefficient c_a of $2.2 \cdot 10^{-3}$ is supported by the observations of *Overland and Colony* [1994]. The derivation of the atmosphere-ice stress $\vec{\tau}_a$ is simplified because the ice drift speed $|\vec{u}|$ is two orders of magnitude smaller than the wind speed $|\vec{u}_a|$ [*Thorndike and Colony*, 1982] and thus is negligible. The model is forced with the wind velocity at 10 m height, $\vec{u}_{10m}$, which is assumed to resemble the surface wind and hence the turning angle ϕ_a, observable for wind velocities at different heights within the Ekman layer, can be set to zero. This is not the case for the ocean currents, because the model is forced with geostrophical currents, so that the stress at the ice underside is determined from

$$\vec{\tau}_w = \rho_w \, c_w \, | \vec{u}_w - \vec{u} | \, \left[(\vec{u}_w - \vec{u}) \, \cos \phi_w + \vec{k} \times (\vec{u}_w - \vec{u}) \, \sin \phi_w \right] \qquad (2.12)$$

where the density of sea water $\rho_w = 1026$ km m^{-3} and the oceanic drag coefficient $c_w = 5.5 \cdot 10^{-3}$ [*McPhee*, 1980]. Here, a turning angle ϕ_w of 25 ° between the ice-ocean stress $\vec{\tau}_w$ and the undisturbed ocean velocity below the mixed layer relative to the ice velocity $(\vec{u}_w - \vec{u})$ is applied [*McPhee*, 1975, 1979; *Overland and Davidson*, 1992]. The atmospheric drag coefficient is actually derived from the ratio $c_a/c_w = 0.4$ [*Harder et al.*, 1998]. Atmospheric and oceanic forcing fields are described in detail with the various experiments presented in this study. The

impact of using different approaches for the derivation of the atmospheric drag and the effect of different ocean velocity fields on the ice drift are discussed in Chapter 3.

The Coriolis force is a pseudo force that needs to be considered when moving objects are described in a rotating reference system. The Coriolis parameter $f = 2\Omega \sin \varphi$ varies with latitude φ and its maximum value is twice the angular speed of the earth $\Omega = 7.29 \cdot 10^{-5} \mathrm{s}^{-1}$. In Equation (2.10) only the horizontal component of the Coriolis force is considered, which is defined by the cross product of the unit vector in the z-direction, $\vec{k} = (0, 0, 1)$, and the horizontal components of the ice drift $\vec{u}$, because the sea ice model includes no vertical motion of the ice.

The gravitational force is considered by the surface tilt force, where ∇H_{tilt} is the sea surface tilt, which in this study is determined from the ocean velocity using the geostrophic equation $g \nabla H_{tilt} = -f \vec{k} \times \vec{u}_w$. It represents the acceleration an ice floe gains when it slides down a tilted ocean surface, where the slope refers to the elevation from a surface of equal geopotential.

The internal forces are most important for sea ice deformation and the ridging approaches presented in Chapter 6. These forces are described as the divergence of the stress tensor σ

$$\vec{F}_{int} = \nabla \cdot \boldsymbol{\sigma} \,. \tag{2.13}$$

Here, the stress takes the unit of force per unit length because the sea ice cover is considered to be a two-dimensional continuum [*Rothrock*, 1975]. The description of the stress tensor σ itself requires an explanation of the ice kinematics first.

Kinematics

The gradient of the sea ice drift $\nabla \vec{u}$ is a tensor of rank two and splits up into a symmetric and an antisymmetric component. The former is the deformation rate $\dot{\varepsilon}$, describing deformation free from rotation, and the latter, the vorticity Ω, describes rotation free from deformation.

$$\dot{\varepsilon}_{ij} = \frac{1}{2} \left(\frac{\partial u_i}{\partial x_j} + \frac{\partial u_j}{\partial x_i} \right) \tag{2.14a}$$

$$\Omega_{ij} = \frac{1}{2} \left(\frac{\partial u_i}{\partial x_j} - \frac{\partial u_j}{\partial x_i} \right) \,. \tag{2.14b}$$

Here $i, j \in \{1, 2\}$, which holds for the rest of Section 2.2. $\dot{\varepsilon}$ is also known as the strain rate tensor[a] and plays an important role in the deformation schemes

---

[a] Strain is displacement per unit length and thus dimensionless. Strain in the direction of the displacement is named normal strain and strain directed perpendicular to the displacement direction is shear strain. Strain rate is the rate of strain per unit time $\dot{\varepsilon} \equiv d\varepsilon/dt$ and hence has unit s^{-1}. [*Mellor*, 1986]

discussed later in Chapter 5.

$$\dot{\boldsymbol{\varepsilon}} = \begin{pmatrix} \dfrac{\partial u}{\partial x} & \dfrac{1}{2}\left\{\dfrac{\partial u}{\partial y} + \dfrac{\partial v}{\partial x}\right\} \\ \dfrac{1}{2}\left\{\dfrac{\partial u}{\partial y} + \dfrac{\partial v}{\partial x}\right\} & \dfrac{\partial v}{\partial y} \end{pmatrix} = \begin{pmatrix} \dot{\varepsilon}_{11} & \dot{\varepsilon}_{21} \\ \dot{\varepsilon}_{12} & \dot{\varepsilon}_{22} \end{pmatrix}. \tag{2.15}$$

The components $\dot{\varepsilon}_{11}$ and $\dot{\varepsilon}_{22}$ are referred to as the normal strain rates and $\dot{\varepsilon}_{12} = \dot{\varepsilon}_{21}$ as the shear strain rates.

A tensor of rank two like $\dot{\boldsymbol{\varepsilon}}$ has two invariants, e.g. its principal components. For the calculation of invariants please see Appendix C.1. There is agreement on the following two invariants to describe the deformation rate of sea ice [*Leppäranta*, 1998]:

$$\dot{\varepsilon}_I = \dot{\varepsilon}_{11} + \dot{\varepsilon}_{22} \tag{2.16a}$$

$$\dot{\varepsilon}_{II} = \sqrt{(\dot{\varepsilon}_{11} - \dot{\varepsilon}_{22})^2 + 4\dot{\varepsilon}_{12}^2}. \tag{2.16b}$$

The first invariant $\dot{\varepsilon}_I$ is a measure of expansion or compression of a planar element and is shape-invariant. The term $\dot{\varepsilon}_I$ equals the divergence of ice motion. In contrats, the term $\dot{\varepsilon}_{II}$ describes area-invariant motion. This is also known as shear and $\dot{\varepsilon}_{II}$ equals twice the rate of shear (see Appendix C.1).

A measure of the total rate of deformation of a planar element is the absolute value of the deformation rate $\dot{\boldsymbol{\varepsilon}}$:

$$|\dot{\boldsymbol{\varepsilon}}| = \sqrt{\dot{\varepsilon}_I^2 + \dot{\varepsilon}_{II}^2}, \tag{2.17}$$

and the deformation angle θ reflects the ratio of convergence and shear contributing to the total deformation:

$$\tan\theta = \frac{\dot{\varepsilon}_{II}}{\dot{\varepsilon}_I}. \tag{2.18}$$

The deformation angle is particularly useful for illustrating the different states of deformation and the transitions between them. Moreover, $|\dot{\boldsymbol{\varepsilon}}|$ and $\tan\theta$ are utilised to define a polar coordinate system for expressing the horizontal strain rate (see Chapter 5 and Appendix C.2).

Rheology

In order to link kinematics with dynamics a rheology $\boldsymbol{\sigma} = \boldsymbol{\sigma}(\dot{\boldsymbol{\varepsilon}})$ is needed. Different kinds of rheologies are characterised by the way the interrelation between the stress tensor[b] $\boldsymbol{\sigma}$ and the strain rate tensor $\dot{\boldsymbol{\varepsilon}}$ is assumed. In the model described here the constitutive law

$$\sigma_{ij} = 2\eta\dot{\varepsilon}_{ij} + \left((\zeta - \eta)\dot{\varepsilon}_I - \frac{P}{2} \right)\delta_{ij} \tag{2.19}$$

---

[b] Stress is force per area and therefore has unit kg m^{-1}s^{-2}. Normal stresses are produced by tensile or compressive forces that act perpendicular to the surface of a cubic element. Shear stresses are caused by tangential forces that act parallel to the element's surface. [*Mellor*, 1986]
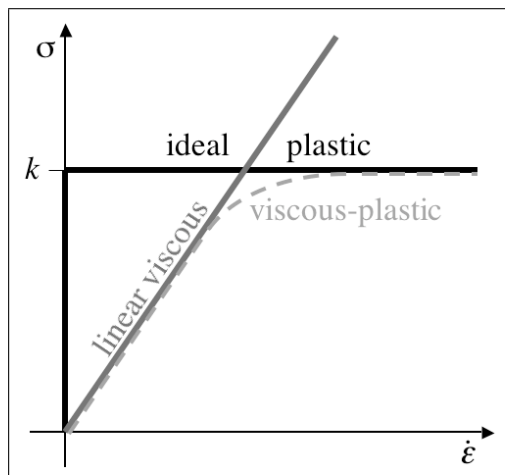
Figure 2.1: Schematic of different mechanical behaviour approximations for sea ice [after *Hibler*, 1979; *Mellor*, 1986].
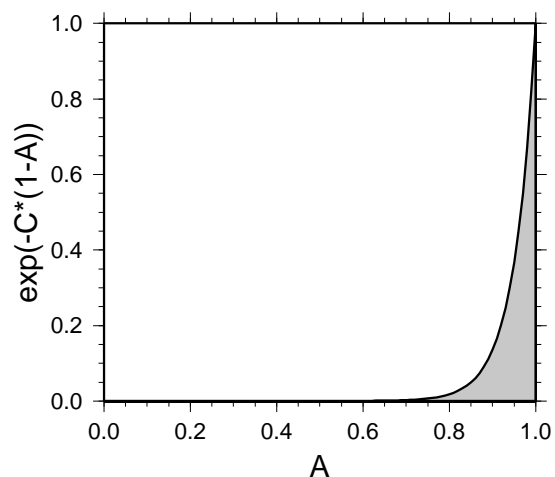
Figure 2.2: Exponential relationship of ice strength P and ice concentration A (see Equation (2.22)); $C^* = 20$.

of *Hibler* [1979] is applied that describes a viscous-plastic behaviour of sea ice.

Following the description of *Mellor* [1986] linear or Newtonian viscosity means that the stress σ is proportional to the strain rate $\dot{\varepsilon}$. The coefficient of proportionality is called the viscosity and has dimension kg m^{-1}s^{-1}. When the material behaves ideally plastically or rigid-plastically, there is no strain in the material until a certain yield stress k is reached ($\sigma < k$, $\varepsilon = 0$). Then the material strains indefinitely ($\sigma = k$, $\varepsilon \to \infty$). In the present model a combined rheology is used: sea ice is assumed to react viscous-plastically to applied stress following a non-linear viscous relationship between stress and strain rate (see Figure 2.1) [*Hibler*, 1979].

In Equation (2.19) ζ and η denote the bulk and shear viscosity respectively, and P is the ice strength. While the constitutive law (2.19) describes generally a non-linear, viscous, compressible fluid, the following definition of both viscosities and ice strength determine the either viscous or plastic behaviour of sea ice as known from AIDJEX[c] results.

$$\zeta = P/(2\Delta_{\dot{\varepsilon}}) \tag{2.20}$$

$$\eta = \zeta/e^2 \tag{2.21}$$

$$P = P^*h\exp\left(-C^*(1-A)\right)r_p(\Delta_{\dot{\varepsilon}}) \tag{2.22}$$

$$\text{with } \Delta_{\dot{\varepsilon}} = \sqrt{\dot{\varepsilon}_I^2 + e^{-2}\dot{\varepsilon}_{II}^2} \tag{2.23}$$

where $e = 2$ is the eccentricity of the elliptical yield curve (see Equation (2.26)

---

[c]The *Arctic Ice Dynamics Joint Experiment* (AIDJEX) was a milestone in the field of sea ice mechanics. Between 1970 and 1976 intensive field and modelling studies were performed adressing questions of the interrelation of large-scale sea ice deformation, stress states, ice morphology and heat balance. [*Untersteiner*, 1980]

and fig), $P^* = 1.5 \cdot 10^4 \, \mathrm{Nm^{-2}}$ is the ice strength parameter and $C^* = 20$ is the ice concentration parameter. A realistic range for C^* is 10–100. The exponential increase of the ice strength P with growing ice compactness expressed by Equation (2.22) is demonstrated in Figure 2.2. The term $\Delta_{\dot\varepsilon}$ is a kinematic measure of the total deformation of the sea ice cover.

Hibler [1979] stated that the definition of the viscosities—first of all the bulk viscosity ζ in Equation (2.20)—has the disadvantage that the viscosities become infinite for very small strain rates. Therefore he introduced a maximum bulk viscosity. Though this allows the shear stresses to converge to zero for very small strain rates the normal stresses converge to $-P/2$. However, a corresponding force that would result in a creeping divergent flow of the actual stationary ice cover is not observed in reality [*Hibler*, 1979; *Harder*, 1996]. Thus, in the present study the approach of *Harder* [1996] is applied, introducing a regime function $r_p(\delta_{\dot\varepsilon})$ as an addition to the derivation of the ice strength P (see Equation (2.22))

$$r_p(\Delta_{\dot\varepsilon}) = \frac{\Delta_{\dot\varepsilon}}{\Delta_{\dot\varepsilon} + \Delta_{min}} \, . \tag{2.24}$$

Because of the functional relationship between the viscosities and the ice strength P the regime function also affects both viscosities in a manner equivalent to the suggestion of the original scheme of *Hibler* [1979]. The advantage of the new scheme, which adjusts the ice strength for small strain rate values, is that now also the normal stresses converge to zero for very small strain rates. The parameter $\Delta_{min} = 5 \cdot 10^{-9} s^{-1}$ [*Kreyscher*, 1998] determines the rheological regime of the sea ice model. The regime function allows a gliding transition between linear-viscous ($\Delta_{\dot\varepsilon} < \Delta_{min}$) and ideal-plastic behaviour ($\Delta_{\dot\varepsilon} \geq \Delta_{min}$). With increasing values of Δ_{min} the ice tends towards the purely non-linear viscous regime.

The flow rule for sea ice as defined by the functional relationships (2.19)–(2.23) is based upon the assumptions that (1) sea ice is isotropic on the horizontal length scale of the model, (2) the effective tensile strength of the ice is small under all states of deformation, whereas the compressive strength is substantial under convergence, and (3) stresses are relatively independent of strain rate magnitude [*Hibler*, 1979].

According to the defined symmetry of $\dot\varepsilon$ the stress tensor $\boldsymbol{\sigma}$ is also symmetric and hence it is transformable towards the principle axes, which equal those of $\dot\varepsilon$. After *Rothrock* [1975] a pair of invariants of $\boldsymbol{\sigma}$ are given by

$$\sigma_I = \frac{1}{2}(\sigma_1 + \sigma_2) = \frac{1}{2}(\sigma_{11} + \sigma_{22}) = \zeta \, \dot\varepsilon_I - \frac{P}{2} \tag{2.25a}$$

$$\sigma_{II} = \frac{1}{2}(\sigma_2 - \sigma_1) = \sqrt{\eta^2(\dot\varepsilon_{11} - \dot\varepsilon_{22})^2 + \eta^2 4\dot\varepsilon_{12}^2} = \eta \, \dot\varepsilon_{II} \tag{2.25b}$$

where σ_1 and σ_2 are the principle stresses, which can be derived analogously to the principle strain rates (see Appendix C.1). The stress invariants of Equa-
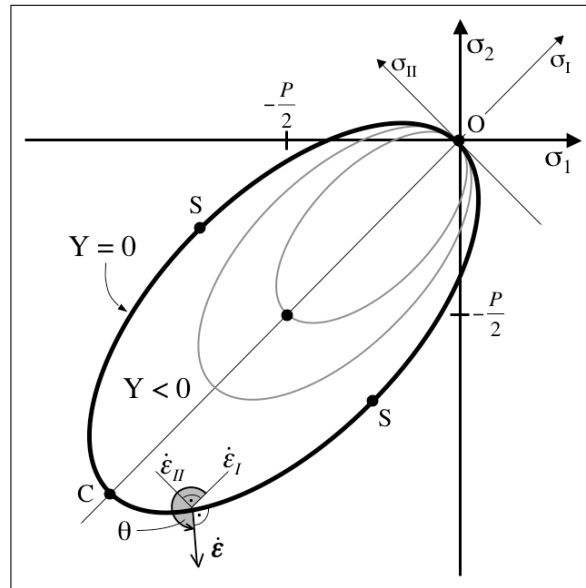
Figure 2.3: Schematic of the elliptical yield curve (see Equation (2.26)) [after *Rothrock*, 1975; *Hibler*, 1979]. Smaller ellipses indicated by grey lines illustrate the yield curve behaviour due to a reduced ice strength P that is adjusted to cases of small strain rates (Equations (2.22) and (2.24)). Stress states corresponding to pure shear motion and isotropic compression are marked with 'S' and 'C' respectively. All ellipses pass through the origin 'O', which means that under divergence all stresses equal zero.

tion (2.25) give a different description of the rheological relationship of Equation (2.19). σ_I describes negative pressure during convergent drift and σ_{II} is the maximum shear stress [*Rothrock*, 1975]. These principle components span a two-dimesional space of possible states of stress (see Figure 2.3). For a material that follows plastic behaviour during deformation, interior stresses are bound to a yield curve. The yield curve used in this model stems from *Hibler* [1979], and is of elliptical shape with an eccentricity of $e = 2$:

$$Y\left(\frac{\sigma_I}{P}, \frac{\sigma_{II}}{P}\right) = \left(2\frac{\sigma_I}{P} + 1\right)^2 + \left(2e\frac{\sigma_{II}}{P}\right)^2 - 1 = 0. \qquad (2.26)$$

If the stress is smaller than the outer limit given by the yield curve, the ice will behave viscously ($Y < 0$). When stresses reach the limit ($Y = 0$), the ice breaks, i.e. it behaves plastically, and stress is released. The angle θ of Equation (2.18) is the angle between the x-axis of the reference coordinate system and the normal $\dot{\varepsilon}$ of the yield curve (see Figure 2.3) [*Rothrock*, 1975]. The application of the regime function (Equation (2.24)) causes stresses to be positioned on an ellipse also in the viscous case, though these ellipses are smaller than the ellipse of the plastic yield stresses, because the ice strength is reduced to the same extent as the bulk and shear viscosities for very small deformation rates [*Harder*, 1996].

2.3   Thermodynamics

The evolution equations (2.4), (2.8) and (2.9) of the main scalar variables of the model feature local source and sink terms S. These mainly describe thermodynamic processes that are defined by the interaction of atmosphere, ocean and sea ice.

The thermodynamic part of the sea ice model follows the work of *Parkinson and Washington* [1979] regarding the atmospheric heat flux and the exchange processes between atmosphere and ice or ocean. Sea ice and snow cover are assumed to have no heat capacity and hence exhibit a linear temperature profile according to the zero-layer model of *Semtner* [1976]. The underlying ocean is represented by a one-dimensional mixed layer model after *Lemke* [1987] and *Lemke et al.* [1990] without horizontal exchange.

Energy balance

Sea ice growth ($\partial h / \partial t > 0$) or decay ($\partial h / \partial t < 0$) is controlled by the heat exchange of the sea ice cover with the atmosphere Q_a and ocean Q_w:

$$Q_a + Q_w + \rho_i \, L_i \, \frac{\partial h}{\partial t} = 0 \tag{2.27}$$

where the density of sea ice is $\rho_i = 910 \, \text{kg m}^{-3}$ and the specific latent heat $L_i = 3.34 \cdot 10^5 \, \text{J kg}^{-1}$. At each time the loss or gain of energy in the oceanic mixed layer is balanced by the latent heat released due to freezing or consumed by melting of sea ice. For example, a net heat loss to the atmosphere of $35.2 \, \text{W m}^{-2}$ relates to an ice thickness growth rate of 1 cm per day.

Following the zero-layer approach of *Semtner* [1976] the energy balance (2.27) can be evaluated separately for the ice surface and ice underside because the sea ice layer is assumed to have no heat capacity. Thus the conductive heat fluxes at the ice surface and underside have the same magnitude $|Q_c|$, but they are directed opposingly. At the surface the sum of atmospheric heat flux Q_a and conductive heat flux through the ice Q_c determines the change of ice thickness with time

$$\left(\frac{\partial h}{\partial t} \right)_a = - \frac{Q_a + Q_c}{\rho_i \, L_i} \ . \tag{2.28}$$

At the ice surface only melting is allowed, but there is no reservoir for melting water besides the oceanic mixed layer, i.e. formation of fresh water melt ponds and their refreezing are not considered.

Freezing and melting at the ice underside are determined by the difference of the oceanic heat flux Q_w and the conductive heat flux of the ice Q_c.

$$\left(\frac{\partial h}{\partial t} \right)_w = - \frac{Q_w - Q_c}{\rho_i \, L_i} \tag{2.29}$$

If the heat flux from the ocean is larger than the conductive heat flux of the ice ($Q_w > Q_c$) basal melting will occur. In contrast $Q_w < Q_c$ causes freezing. In the case that the grid cell is not entirely ice-covered ($A < 1$) the ocean exchanges heat directly with the atmosphere, and new ice may be formed in the grid cell.

In the following the derivation of the individual heat fluxes to the atmosphere, in the ice and from the ocean are described.

Atmosphere The atmospheric heat flux Q_a is determined by the budget of incoming ($\downarrow$) and outgoing ($\uparrow$) shortwave (R_{SW}) and longwave (R_{LW}) radiation, and the turbulent fluxes of sensible (Q_s) and latent (Q_l) heat

$$Q_a = R_{SW}^{\downarrow} + R_{SW}^{\uparrow} + R_{LW}^{\downarrow} + R_{LW}^{\uparrow} + Q_s + Q_l \,. \tag{2.30}$$

The incoming shortwave and longwave radiation are prescribed by external forcing. The calculation of the incoming shortwave radiation follows an empirical equation derived by *Zillman* [1972] for cloud free conditions and a cloudiness correction proposed by *Laevastu* [1960] [see also *Parkinson and Washington*, 1979]. The incoming shortwave radiation also determines its outgoing counterpart $R_{SW}^{\downarrow} = \alpha\, R_{SW}^{\uparrow}$. The ratio α is called albedo and represents the reflectivity of the ice, snow or ocean surface. Its value differs for varying surface characteristics (see Table 2.1). The tremendous difference in albedo between open ocean (0.1) and ice or snow (0.7–0.8) is most important for the energy balance of the oceanic mixed layer and climatic feedback cycles—e.g. a larger ice area reflects more incoming radiation and causes cooling, which leads again to more ice.

The calculations for incoming and outgoing longwave radiation are based upon the Stefan-Boltzman law. The incoming longwave radiation is parameterised from $R_{LW}^{\downarrow} = \epsilon_a\, \sigma_B\, T_a^4$ and includes the Stefan-Boltzmann constant $\sigma_B = 5.67 \cdot 10^{-8}\, \mathrm{Wm^{-2}K^{-4}}$ as well as the surface air temperature T_a (in K) at 2 m height. The emissivity of the air in the infrared spectrum ϵ_a is determined by the empirical relation $\epsilon_a = 0.765 + 0.22\, A_c^3$ [*König-Langlo and Augstein*, 1994], which

surface	albedo α
open water	0.10
melting ice w/o snow ($T_s \geq 0\,°\mathrm{C}$)	0.68
ice w/o snow ($T_s < 0\,°\mathrm{C}$)	0.70
melting snow ($T_s \geq 0\,°\mathrm{C}$)	0.77
snow ($T_s < 0\,°\mathrm{C}$)	0.81

Table 2.1: Albedo values applied in the sea ice model for different surface characteristics. T_s is the surface temperature of the ice.

bulk formulae parameters	symbol	value
surface air density	ρ_a	$1.3\,\text{kg m}^{-3}$
specific heat capacity of air	c_p	$1004\,\text{J kg}^{-1}\text{K}^{-1}$
specific latent heat of evaporation	L_e	$2.50{\cdot}10^6\,\text{J kg}^{-1}$
specific latent heat of sublimation	L_s	$2.83{\cdot}10^6\,\text{J kg}^{-1}$
exchange coefficient for sensible heat	C_s	$1.75{\cdot}10^{-3}$
exchange coefficient for latent heat	C_l	$1.75{\cdot}10^{-3}$

Table 2.2: Parameters used in the bulk formulae of Equations (2.31) and (2.32).

depends on the cloud coverage $A_c \in [0, 1]$. The outgoing longwave radiation is given as $R_{LW}^{\uparrow} = \epsilon_s\,\sigma_B\,T_a^4$ with a surface emissivity $\epsilon_s = 0.99$.

The turbulent fluxes are derived by the the bulk formulae after *Smith* [1988]:

$$Q_s = \rho_a\,c_p\,C_s\,|\vec{u}_a|\,(T_a - T_s) \quad \text{and} \tag{2.31}$$

$$Q_l = \rho_a\,L\,C_l\,|\vec{u}_a|\,(q_a - q_s). \tag{2.32}$$

Both fluxes depend on the surface wind speed $\vec{u}_a$ usually given at 10 m height. The sensible heat flux is determined by the temperature difference between ice (T_s) and atmosphere (T_a). The air temperature is again given at 2 m height. Similarly, the difference between the specific humidity of the air at 2 m height q_a and that at the ice surface q_s determines the latent heat flux. Here, the air mass directly at the ice surface is assumed to be always saturated and q_s is set accordingly. The value of the specific latent heat of fusion L is different for evaporation over open water and for sublimation over ice (see Table 2.2).

Sea ice   The zero-layer model of *Semtner* [1976] is based upon the assumption that the ice layer has no heat capacity. Thus the ice features a constant vertical conductive heat flux and a linear temperature profile. The temperature gradients of the ice and the snow layer differ because their thermal conductivities $\kappa_i = 2.17\,\text{Wm}^{-1}\text{K}^{-1}$ and $\kappa_s = 0.31\,\text{Wm}^{-1}\text{K}^{-1}$ deviate. The conductive heat flux through the ice and snow cover Q_c is defined by

$$Q_c = \frac{\kappa_i\,\kappa_s}{h\,\kappa_s + h_s\,\kappa_i}\,A\,(T_b - T_s). \tag{2.33}$$

At the surface the ice temperature T_s is restricted to the freezing temperature of fresh water ($T_s \leq 0\,°\text{C}$). Likewise the bottom temperature of the ice T_b is assumed to equal the freezing temperature of sea water T_f, which is set to the constant value of $-1.86\,°\text{C}$ (valid for a salinity of 34). The main implication of Equation (2.33) is that Q_c decreases with increasing ice (or snow) thickness h.

Ocean   As stated above the sea ice model is applied in various modes: stand-alone and coupled to an ocean model, in this study. Correspondingly,

the oceanic heat flux Q_w is provided directly by the ocean model in the second case, where the coupling of ocean and sea ice model follows the work of *Hibler and Bryan* [1987]. In the uncoupled mode the oceanic heat fluxes are provided as climatological monthly means from the same ocean model *Karcher et al.* [2003] to the sea ice model. The one-dimensional oceanic mixed layer model described by *Lemke* [1987]; *Lemke et al.* [1990] is thus applied only in a simplified version with a constant mixed layer depth restricted to ≤ 30 m. Nevertheless, this simplified mixed layer acts as a heat storage for the sea ice model. Furthermore, the simplification of the original mixed layer model leads to a convergence of the coupled and uncoupled sea ice model results, and hence enhances the comparability of these components of the model hierarchy used.

Source and sink terms of prognostic variables

Ice thickness   In order to derive the total change in ice volume the atmospheric and the oceanic components of Equations (2.28) and (2.29) have to be added

$$S_h = \left(\frac{\partial h}{\partial t}\right)_a + \left(\frac{\partial h}{\partial t}\right)_w .$$

(2.34)

The atmospheric part is treated so that the snow cover h_s melts first and then any remaining energy is used to decrease the ice thickness. The only source of snow thickness is the precipitation rate (times ice concentration) in the case of $T_s < 0$. The balance of the prognostic snow layer, the derivation of S_{h_s} of Equation (2.9), follows the ideas of *Owens and Lemke* [1990].

As expressed by Equation (2.33) the conductive heat flux depends strongly on the ice thickness. However, the model values are means over a distinct area, in which the real ice thickness may vary drastically. Thus the mean ice thickness h is split up into seven artificial ice levels of different thickness H_n by $H_n = \frac{1}{7}(2n-1)h/A$ with integer $n \in [1,7]$. This algorithm is based upon the assumption that ice thicknesses H_n are equally distributed between zero and $2h/A$ with a lower limit of $H_n \geq 5$ cm.

Flooding   Sea ice growth can be increased by a very thick snow layer on top. A heavy snow layer is able to gradually push the ice-snow interface under the water level, which is also described by a negative freeboard of the floe and results in flooding. The snow below the water level is infiltrated by sea water and freezes into so-called snow-ice. Snow-ice may consist of two components: frozen snow (meteoric ice) and frozen infiltrated sea water (sea ice). The simple approach of *Fischer* [1995], which takes advantage of the buoyancy of sea ice, is applied here: The total sea water displacement h_d by ice and snow cover is calculated. If this displacement is larger than the ice volume h, i.e. the freeboard is negative, the new ice volume will be derived by $h = h_d$. Then the prior snow

volume is reduced by the equivalent of the snow-ice mean thickness. Flooding is more common on Antarctic than Arctic sea ice because Antarctic sea ice is predominantly found at lower latitudes where the precipitation rate is higher. However, its use for Arctic sea ice models is recommended by *Lieser* [2004] especially for the model spin up in order to avoid unrealistic snow thickness on thin ice .

Ice concentration   Sources and sinks of ice concentration A are split into a freezing and a melting rate, F_h and M_h respectively:

$$S_A = \frac{1-A}{h_0} \, F_h + \frac{A}{2h} \, M_h - Q_A \tag{2.35}$$

where $F_h = \max(S_h, 0)$ and $M_h = \min(S_h, 0)$. The lead closing parameter $h_0 = 1.0$ specifies the closing rate of the ice cover after leads have opened. In addition to the thermodynamic process of melting the ice concentration may also be reduced dynamically by the opening of leads. This is expressed in the term Q_A, which will be presented in the next section.

2.4   Lead opening and land-fast ice schemes

Lead opening   Shear motion causes not only deformation but also lead opening. This creation of open water is represented by Q_A in Equation (2.35), defined as

$$Q_A = \frac{1}{2} \left(\Delta_{\dot\varepsilon} - |\dot\varepsilon_{11} + \dot\varepsilon_{22}| \right) \exp\left(-C^*(1-A) \right) \tag{2.36}$$

after *Hibler* [1980, Appendix A], *Hibler* [1984], *Flato and Hibler* [1991] and *Harder and Lemke* [1994]. It can easily be shown that this part of Equation (2.35) is only active under shear conditions. In the case of pure divergence or convergence ($\dot\varepsilon_{11} = \dot\varepsilon_{22} \neq 0, \dot\varepsilon_{12} = 0$), total deformation $\Delta_{\dot\varepsilon} = |\dot\varepsilon_{11} + \dot\varepsilon_{22}|$ and hence $Q_A = 0$. In contrast pure shear is characterised by $\dot\varepsilon_{11} = \dot\varepsilon_{22} = 0$ and $\dot\varepsilon_{12} \neq 0$, and Q_A amounts to half the rate of shear strain ($0.5 \, \dot\varepsilon_{12}$). Moreover, it can easily be shown that $Q_A \geq 0$ in all cases. Note that this shear-generated open water is in addition to the divergent generation of open water which is already parameterised by $A \nabla \cdot \vec{u}$ in Equation (2.4). The term Q_A and its application will be discussed again in Chapter 5 and Section 6.3.

Fast ice   Sea ice that is attached to the shore line or grounded in near shore regions is called (land-)fast ice. This ice type is usually rather flat and undergoes little deformation. Ridges may only occur along the shore or locally in shallow areas. For drifting sea ice the fast ice edge forms an advanced shore line and heavy ridging occurs during onshore wind events along this edge. Summer melt, strong offshore winds or a combination of both lead to a break-up of the fast ice, turning it into normal drifting sea ice.

Lieser [2004] included a fast ice scheme in the sea ice model: In coastal regions where mean water depths fall below 15 m the drift ice contained in the related model grid cell will be classified as fast ice if the mean ice thickness h exceeds a tenth of the water depth. This means numerically that the respective grid cell is excluded from the grid mask entering the drift calculations. Fast ice, however, may still change thermodynamically owing to the same processes as the drift ice in the model. This simple approach was shown to work well when compared to observations along the Siberian coast [*Lieser*, 2004].

Though being suitable on short time scale model runs, model test computations on decadal scales showed an accumulation of ice in areas of fast ice, i.e. melting alone does not lead to a complete disintegration of the fast ice during the summer months. Hence, fast ice is now reconverted to drift ice during the summer months July to September in order to account for the typical dynamic break up of the fast ice areas [*Flato and Brown*, 1996]. This simple approach solves the problem of unrealistic ice thickness due to the fast ice scheme.

2.5   Forcing

A model that does not describe the entire (climate) system needs external forcing at its boundaries. The forcing varies with the complexity of the model. The boundary conditions are thus chosen to match the particular requirements of the three different model realisations used in this study: ice-ocean coupled, stand-alone sea ice and sea ice dynamics only. In the following, general forcing specifications are briefly described which hold for all experiments and can be considered standard for the above sea ice model. Individual variations are emphasised in the description of the particular model experiments.

Atmospheric boundary conditions are represented by the wind velocity at 10 m height, the air temperature at 2 m height, the dew point temperature, the relative air humidity, precipitation and cloud coverage. These parameters are mainly derived from reanalysis data sets provided by the *National Centers for Environmental Prediction/National Center for Atmospheric Research* (NCEP/NCAR) [*Kalnay et al.*, 1996; *Kistler et al.*, 2001] or the *European Centre for Medium-Range Weather Forecast* (ECMWF). Oceanic forcing fields are horizontal currents and vertical heat fluxes of the undisturbed surface layer, i.e. from right below the mixed layer. These data are taken from the coupled ice-ocean realisation of the present model, the North-Atlantic-and-Arctic-Ocean-Sea-Ice-Model (NAOSIM) [*Karcher et al.*, 2003], where the oceanic part is of *Modular Ocean Model* (MOM) type.

The forcing data differ in their temporal and spatial variability. Representing the highest variability and thus changing with each time step of the model the

wind velocity and air temperature are prescribed at daily resolution. All other parameters are prescribed as climatological, averaged fields.

2.6 Model domain and numerics

A sea ice model consists not only of physical equations but also of the grid within which the equations are discretised. The grid also defines the horizontal resolution and the geographical domain in which the sea ice cover is simulated. The spatial resolution is limited due to the continuum assumption[d] which is a basis for the sea ice model presented. The time step is then chosen according to the Courant-Friedrich-Lewy (CFL) condition [*Courant et al.*, 1928]. The Courant number C_{cfl}

$$C_{cfl} = \frac{u\Delta t}{\Delta x} \tag{2.37}$$

reflects the advective length scale. In order to achieve numerical stability, $C_{cfl} < \frac{1}{2}$ is necessary. While usually a small Δx is desired, an adequately small Δt is often the limiting factor because of the increase in computational time[e].

The model equations are solved on a regular grid with rectangular grid cells. Here, the Arakawa B grid [*Mesinger and Arakawa*, 1976] is used. That means that the vector variables are shifted by $\frac{1}{2}\Delta x$ in both directions compared to the scalar variables, and both components of the vector variables are located on the same node (see Figure 2.4). This grid arrangement was chosen because terms in equations with cross-relations between x and y components, like the Coriolis term in the momentum balance, can be computed more accurately.

In order to solve the physical equations on the grid the method of finite differences is applied [see *Stössel and Owens*, 1992; *Hibler*, 1979, Appendix A], i.e. partial derivatives are transformed into fractions of finite differences

$$\frac{\partial u}{\partial x} = \frac{u(x+\Delta x) - u(x)}{\Delta x} - \mathcal{O}(\Delta x) \tag{2.38}$$

where $\mathcal{O}(\Delta x)$ denotes the truncation error of the Taylor series expansion that is of first order in this forward scheme. In contrast to *Hibler* [1979] a modified upstream scheme following the study of *Smolarkiewicz* [1983] is applied to solve

---

[d] The continuum assumption implies that the typical length scale of the elements of the modelled material, i.e. the size of the sea ice floes (10^0–10^3 m), is much smaller than the grid spacing (here ~ 28 km), so that the number of elements represented by each grid cell is large enough to assume isotropic behaviour of the material. At `http://widget.ecn.purdue.edu/~meapplet/java/continuum/Index.html` an illustrative application demonstrates the interaction of grid size and length scale of the material of interest.

[e] An application showing the interplay of the time increment and grid spacing regarding numerical stability and computation time can be found at `http://itg1.meteor.wisc.edu/wxwise/kinematics/barotropic.html`.
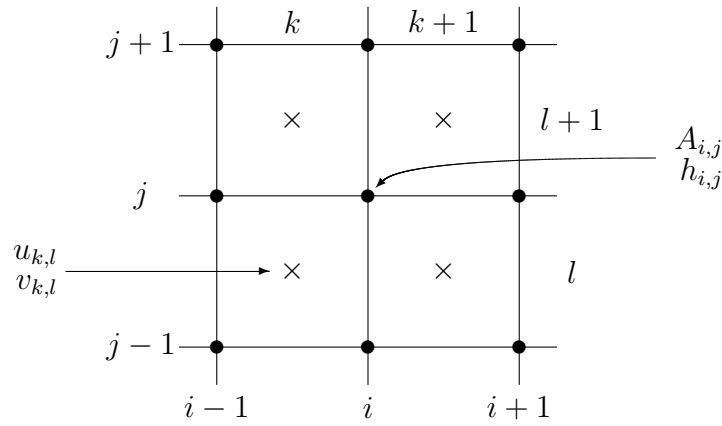
Figure 2.4: The Arakawa B arrangement of variabels on a regular grid. The positions for scalar variables are labelled with indices i and j and marked with a '•', and those of both vector components bear labels k and l as well as the mark '×'. For the consecutive numbering of the indices $i = k$ and $j = l$ holds true.

the advection term in the evolution equations [*Harder*, 1996]. This method is found to be advantageous because the model is numerically stable without explicit diffusion and physical quantities that are positive definite can not become negative for numerical reasons. For derivatives with respect to time only one forward-in-time step (explicit Euler) is necessary. The momentum balance is computed with a "four-colour" relaxation scheme [*Fritzsch*, 2001; *Lieser*, 2004].

Chapter 3

Validation of modelled sea ice drift estimates

3.1   Introduction

The spatial redistribution of sea ice is an important process in the climate system. The movement of sea ice forms leads and polynyas, ridges and rubble. Thus it has an essential impact on the growth rates and thickness of sea ice, and also on the heat and momentum exchange between ocean and atmosphere. Sea ice drift affects also the total sea ice volume and the position of the ice edge driving ice from the interior pack to outer regions where it melts. Due to the sea ice motion, freezing and melting occur at different locations and thus significantly modify the effect of these processes on the oceanic salt balance. Hence the quality of modelled sea ice drift estimates is an important aspect to be clarified before the sea ice model, which is described in the previous chapter, is used to study various ridging algorithms.

For this study results of five different sea ice-ocean models that all take part in the Arctic Ocean Model Intercomparison Project (AOMIP)[a] have been collected. Additional experiments with the coupled and uncoupled versions of the sea ice model described in Chapter 2 are included. Observational sea ice drift data from two satellite products, namely from *Fowler* [2003] and *Ezraty and Piollé* [2004], and buoys [*Ortmeyer and Rigor*, 2004] are used to validate the model results. Besides ice concentration—and related variables like ice area and extent—sea ice drift is the only variable that has been routinely measured from satellites since the late 1970s. Measurements of sea ice drift have much improved through better methods to derive drift speed from moving patterns between successive satellite images and through the introduction of microwave

---

[a]For further information refer to the project homepage at `http://fish.cims.nyu.edu/project_aomip/overview.html`.

imagery [*Emery et al.*, 1997; *Maslanik et al.*, 1998]. The comparison focusses on the period of overlap of satellite observations and AOMIP model results from 1979 to 2001 and 1992 to 2001 respectively.

The chapter begins with the introduction of the observational data sets, followed by a description of the AOMIP model specifications and experimental setup. Then general differences between models and observations are presented as histograms of drift speed and deviation angle of drift direction. Maps of sea ice drift patterns are produced for different meteorological regimes. A detailed discussion on possible reasons for observed differences between modelled and observational data succeeds. Finally a closer look on Fram Strait ice export rates, which are affected by the differences in drift velocity, is provided. Large parts of this chapter are published in *Martin and Gerdes* [2007] as a contribution to AOMIP.

3.2   Observational data sets

The used sea ice drift observations include two satellite products that cover the periods 1979–2001 and 1992–2001 respectively. Data for the longer period are provided by the National Snow and Ice Data Center (NSIDC). Namely, the monthly mean gridded fields of the Polar Pathfinder Project [*Fowler*, 2003] are used. These sea ice drift vector fields are a composite of daily drift computed from Advanced Very High Resolution Radiometer (AVHRR), Scanning Multi-channel Microwave Radiometer (SMMR), Special Sensor Microwave/Imager (SSM/I) satellite images and buoys of the International Arctic Buoy Program (IABP). The product has a spatial resolution of 25 km and is projected on the Equal-Area Scalable Earth (EASE) grid, which covers the entire Arctic. A second satellite derived drift product is obtained from the French ERS Processing and Archiving Facility (CERSAT), which is part of the French Research Institute for Exploitation of the Sea (IFREMER). Here, a merged product of Quick Scatterometer (QuikSCAT) and SSM/I derived sea ice drift vector fields [*Ezraty and Piollé*, 2004] is chosen. These fields are projected on a grid that is oriented exactly as NSIDC's SSM/I-12.5km-grid but with a spatial resolution of 62.5 km and covering the central Arctic only. The monthly means are a composite of the 3-day or 6-day products in this case. The NSIDC and CERSAT products differ in the way sea ice drift is treated before public release. The NSIDC offers a sea ice drift field constructed by including non-satellite information and readily interpolated at all grid nodes. Daily NSIDC data are available. The CERSAT product, on the other hand, contains drift estimates only at those locations, where satellite information is available and the estimates have passed certain filter routines. Thus, CERSAT provides data, which is closer to the raw measurements but con-
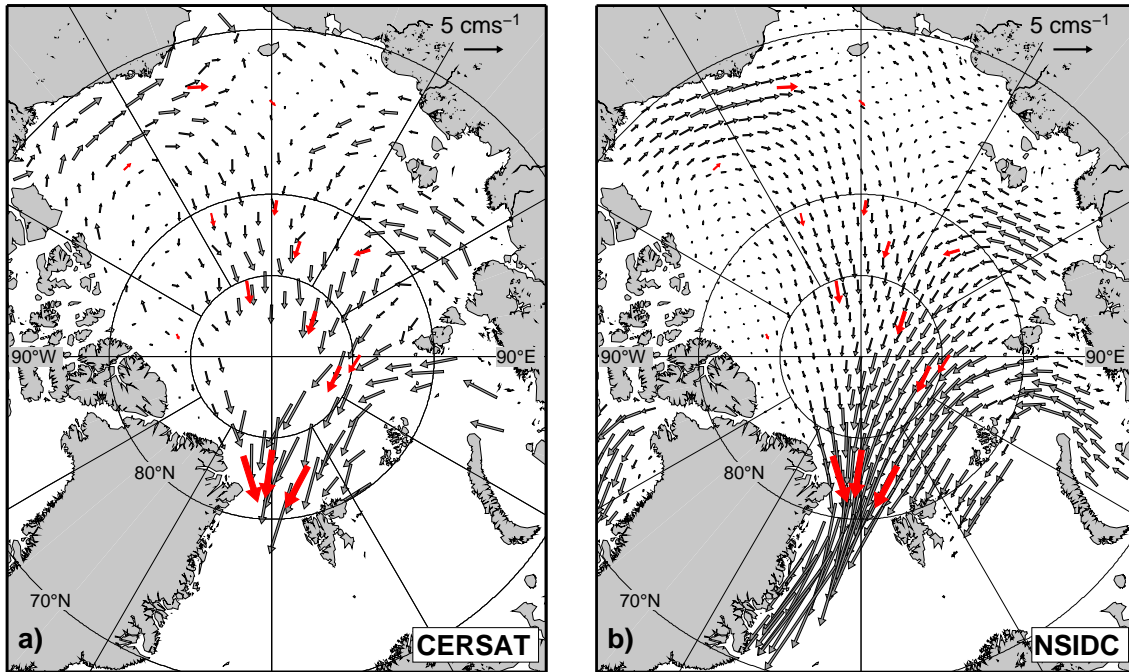
Figure 3.1: Maps of the Arctic sea ice drift field as represented in (**a**) observational data from CERSAT and (**b**) from NSIDC. An average of winter 1994/95 (November–April) is shown and both data sets have been reduced for clarity. Additionally, red vectors mark the mean drift of buoys of the IABP that fully cover the same period.

tains more gaps compared to the NSIDC product. From both these data sets we include only those monthly averaged data points in our investigation that were compiled from at least 25 of 30 days (80% temporal data coverage). Due to the selection of the sources for the drift derivation, the CERSAT data are only available during the winter season, October to April. Passive microwave radiometers are sensitive to the columnar atmospheric water content and sea ice/snow surface melting that restricts the retrieval of reliable drift estimates to the period from October to April [*Kwok et al.*, 1998; *Maslanik et al.*, 1998].

The satellite derived sea ice drift data are not direct observations and are afflicted with considerable uncertainty. Therefore we additionally included monthly mean drift estimates that we derived from raw position data of single buoys of the IABP [*Ortmeyer and Rigor*, 2004]. Although the buoy data set has a rather poor spatial coverage, 20–30 buoys with a spacing of 300–600 km are available each year [*Rigor et al.*, 2002], it represents the most exact drift measurements that are accessible at the moment. The standard error of the buoy positions that are derived with the Argos satellite system is less than 300 m [*Rigor et al.*, 2002]. Buoy position data are provided since 1979 mainly in 12 h intervals. We were able to calculate between 50 (first half of the 1980s) and 300 (first half of the 1990s) monthly drift estimates for each year. In the period 1979–2001 most estimates are from October (380) and least from January (240).
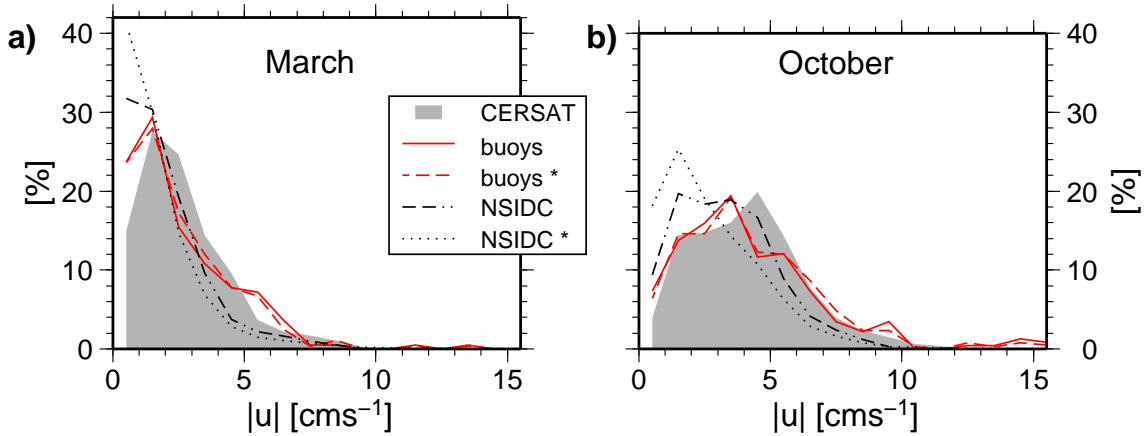
Figure 3.2: Histograms of observed sea ice drift speed for (**a**) March and (**b**) October of the interior Arctic. The CERSAT data of the period 1992–2001 are shown in grey shade. Additionally drift speed distributions are presented for two NSIDC based data sets, one corresponds to the CERSAT data locations and time period (NSIDC) and a second, that includes all grid nodes within the interior Arctic and spans the full time period 1979–2001 (NSIDC *). Furthermore, equivalent data from the IABP buoys of the period 1992–2001 (buoy) and 1979–2001 (buoy *) are incorporated. Percentage values of the ordinate correspond to histogram bins along the abscissa with a bin width of $1\,\mathrm{cm\,s^{-1}}$ beginning at $0\,\mathrm{cm\,s^{-1}}$. Lines of linear interpolation between bin values are shown instead of stairs-step diagrams for clarity reasons. The legend applies for both panels.

The spatial coverage of the buoys is densest in the central Arctic Ocean and in the Beaufort Sea but sparse in the Eurasian marginal seas.

Different sea ice drift products from satellite observations show differences that are manifest in the modal ice speed and speed distribution, expressed in a histogram, as well as the drift pattern. The latter is shown in Figure 3.1 for the winter mean of 1994/95, which stands out for its large Fram Strait ice export [*Vinje et al.*, 1998]. The NSIDC and CERSAT data sets agree on a spatially confined Beaufort Gyre, a cyclonic drift field extending from the Laptev Sea, and a broad Transpolar Drift Stream. Mean drift vectors compiled from buoy positions at the beginning and end of that winter support this pattern. To investigate the speed distribution characteristics we apply histograms of monthly averaged speed at the end of the winter (March) and summer season (October). In March, when the Arctic sea ice cover is closed and small speeds prevail, the differences between the data sets are comparatively small (Figure 3.2a). The modal speeds of all three observational data sets agree within a narrow range of 0.5–1.5 $\mathrm{cm\,s^{-1}}$. During October, after the melting season, the ice cover is less dense and the ice is able to move faster and more freely. This characteristic is more expressed in the CERSAT and buoy data. Due to its selection criteria the CERSAT data does not cover the entire Arctic at each time step and mainly coastal data is rare. Thus, small speeds are underrepresented, as can be seen in

Figure 3.2b in comparison with the distribution of all NSIDC data of October. This "coastal factor" is conceivably also the reason for the better match of the buoy drift estimates and the CERSAT data, even though the NSIDC data set incorporates buoy data. Moreover, under loose ice conditions a buoy represents the drift of a single ice floe rather than a mean drift of an area of 10^2–10^3 km^2, which is the typical grid cell or pixel size of model and satellite products.

3.3   Model data sets

From the AOMIP coordinated-analysis experiment [*Holloway et al.*, 2007] monthly mean sea ice drift results were provided from five different sea ice-ocean coupled models of the following institutions: National Aeronautics and Space Administration (NASA) Goddard Space Flight Center (GSFC) in Greenbelt, Maryland, USA; Institute of Ocean Science (IOS) in Sydney, British Columbia, Canada; Naval Postgraduate School (NPS) in Monterey, California, USA, University of Washington (UW) in Seattle, Washington, USA, and from the Alfred Wegener Institute the coupled version of the sea ice model described in Chapter 2 (hereafter referred to as AWI). The sea ice dynamics are all based on *Hibler* [1979] except those of the NPS model. The latter uses the elastic-viscous-plastic (EVP) rheology of *Hunke and Dukowicz* [1997]. Although all other models use the viscous-plastic rheology of the original Hibler model individual implementations differ in details. Parameters that affect sea ice dynamics like the strength of the ice vary among the models (see Table 3.1). The models also differ in the individual ocean components (AWI and IOS use the Modular Ocean Model

model	ice strength $P^*[10^4\,\text{N}\,\text{m}^{-2}]$	lead closing parameter $h_0[\text{m}]$	ice thickness mean [m]	std [m^2]
AWI	1.5	0.5	1.5	1.14
GSFC	1.0 *	0.25	1.2	1.72
IOS	2.0	0.3	2.1	1.50
NPS	2.75	0.5	1.7	1.14
UW	2.75	0.5	1.2	0.72

Table 3.1: Participating models and some of their sea ice parameters. Ice strength is a parameter of the *Hibler* [1979] model that enters the calculation of compression and shear strength of the ice. The lead closing parameter h_0 determines the demarcation between lateral and basal freezing. The mean and standard deviation (std) of ice thickness is calculated for the whole Arctic Ocean area including all marginal seas and Barents Sea for the period 1979–2001. *This value holds for 3.3 m of ice thickness h ($P^* = 3 \cdot 10^3 h$).*

(MOM), GSFC uses the Princeton Ocean Model (POM), NPS and UW use the Parallel Ocean Program model (POP)) and the coupling of sea ice and ocean models. The main atmospheric forcing components, wind velocity and surface air temperature, are specified for all AOMIP models to be the same.

3.3.1   The AOMIP wind forcing

The atmospheric forcing is prescribed in detail within AOMIP although some groups deemed small deviations from the protocol necessary. The sea ice drift is strongly depending on the wind forcing. Here, the surface wind is calculated from the sea level pressure (SLP) data of the National Centers for Environmental Prediction (NCEP) / National Center for Atmospheric Research (NCAR) reanalysis data (Kalnay et al., 1996) as follows: first the geostrophic wind u_g is derived

$$\vec{k} \times \vec{u}_g = -\frac{1}{f \rho_a} \nabla p_a \tag{3.1}$$

where $\vec{k}$ is the vertical unit vector, f the Coriolis parameter, ρ_a the air density and p_a the atmospheric pressure at sea level. Then the geostrophic wind is retarded by a factor of 0.8 ($u_g < 15.0$ m s^{-1}) or 0.7 (else) and turned by 30° ($u_g < 15.0$ m s^{-1}) or 20° (else) to the left in order to calculate the surface wind u_a. The wind stress is finally derived from

$$\vec{\tau}_a = \rho_a c_a |\vec{u}_a| \vec{u}_a \tag{3.2}$$

and the oceanic stress from

$$\vec{\tau}_w = \rho_w c_w |\vec{u} - \vec{u}_w| (\vec{u} - \vec{u}_w) \tag{3.3}$$

with drag coefficients c_a for atmosphere-sea ice or atmosphere-ocean and c_w for sea ice-ocean interaction respectively (see Table 3.2). In the GSFC and NPS model, however, a simplified atmospheric drag coefficient c_w of $1.1 \cdot 10^{-3}$ independent from the wind speed is applied (compare Table 3.2) and in the IOS

parameter	symbol	value
air density	ρ_a	$1.3 \, kg \, m^3$
sea water density	ρ_w	$1025 \, kg \, m^3$
air drag coeff.	c_a	$(1.1 + 0.04 u_a) \cdot 10^{-3}$
ocean drag coeff.	c_w	$5.5 \cdot 10^{-3}$

Table 3.2: Prescribed AOMIP parameters that are used in the derivation of the dynamic forcing; u_a is the surface wind speed given in $m \, s^{-1}$.

model, however, wind stress values from the NCEP/NCAR reanalysis were used directly. The GSFC model differs further in the oceanic drag, where a description after *Mellor and Kantha* [1989] is used instead.

3.3.2   Forcing of additional model experiments

The study includes two additional model runs from the hierarchy of AWI sea ice models introduced in Chapter 2. For AOMIP the sea ice-ocean coupled version is used (NAOSIM). In order to investigate the impact of different wind forcings an additional experiment is performed, hereafter referred to as AWI 10m-wind. In this experiment the wind velocity at 10 m height provided by the NCEP/NCAR reanalysis is used to derive the wind stress according to the algorithm described in Section 2.2. In the NAOSIM the coupling of the ocean and sea ice model follows the approach of *Hibler and Bryan* [1987]. For the calculation of the ocean-ice stress a four-days cumulative mean of the ocean velocity is computed from values of the second vertical layer of the ocean model which is centred at a depth of 15 m.

Another experiment is performed applying the uncoupled sea ice model (SIM). The atmospheric forcing is treated the same way as with the AWI 10m-wind experiment. The lack of a full ocean model requires to prescribe oceanic forcing as a boundary condition to the SIM. The ocean currents and heat fluxes used originate from a NAOSIM run covering the period 1979–1992 [*Karcher et al.*, 2003] resembling the AWI 10m-wind experiment and are merged to long-term monthly means. The ocean currents entering the preparation of the SIM forcing are of the same ocean model layer as those used for the calculation of the ice-ocean stress in coupled mode. The SIM ice-ocean stress is finally derived from Equation (2.12).

3.4   General differences of drift velocities

In order to present the main differences in drift speed among models and observations histograms are found to be the most concise illustration method. Seasonal histograms for the period 1979–2001 are shown in Figure 3.3. Drift speeds below 0.5 cm s^{-1} have been discarded. This speed bin would otherwise dominate the speed distribution in some models. Almost all of the corresponding data stem from grid points that are very close to land or from semi-enclosed bays. Satellite data for those regions are usually not available or prone to large errors such that validation of those model results is not possible with current data. Furthermore, the geometry of the models differs for reasons that are independent of the sea ice dynamics (e.g. horizontal resolution and related choices
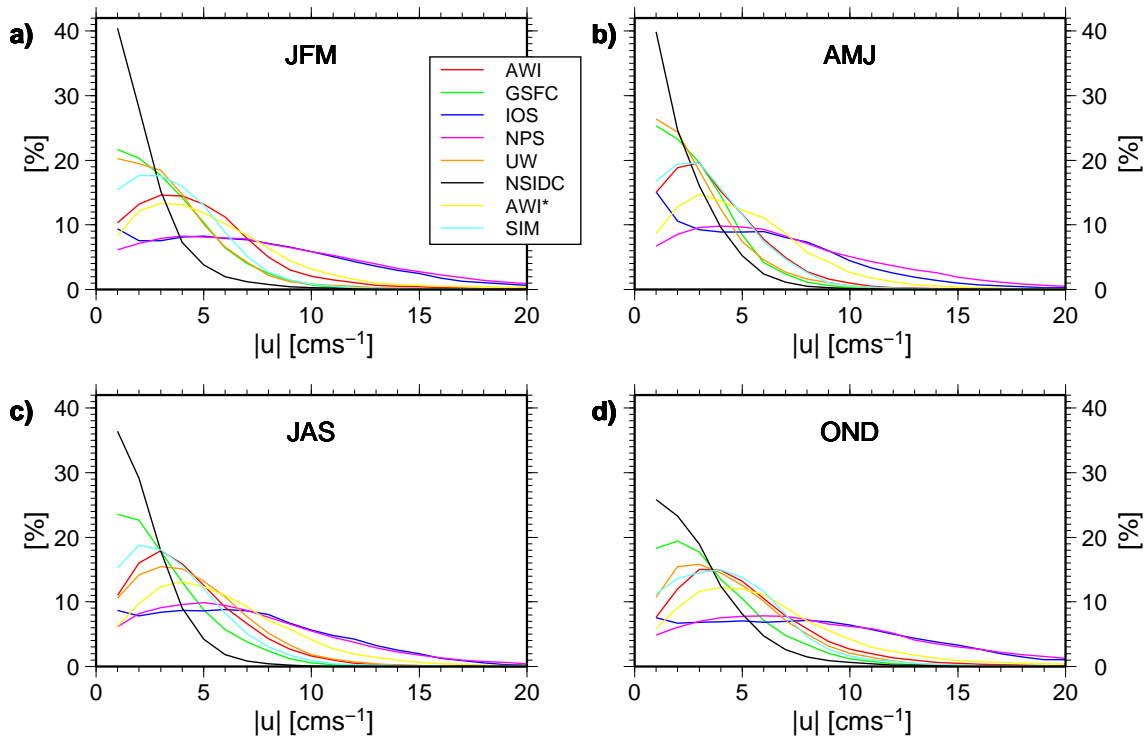
Figure 3.3: Seasonal histograms of periods (**a**) January–March, (**b**) April–June, (**c**) July–September and (**d**) October–December of sea ice drift speed of the interior Arctic for the period 1979–2001 for the AOMIP models as well as the AWI 10m-wind (AWI*) and SIM experiments. Corresponding distributions for the observations from NSIDC have been included. Bin width is 1 cm s^{-1} beginning at 0.5 cm s^{-1} and the legend in panel (a) applies also for panels (b)–(d).

of the modeling groups). Especially the Canadian archipelago is characterised by thick ice and very small drift speeds even in models with high resolution. Thus, we decided to simplify the comparison by compiling the histograms only for speeds above 0.5 cm s^{-1}. Additionally, the drift speed estimates contributing to the histograms are selected from an area (sectors 70–90 $^{\circ}$ N, 50–270 $^{\circ}$ E and 80–90 $^{\circ}$ N, 90 $^{\circ}$ W–50 $^{\circ}$ E) excluding the marginal ice zone in the Greenland and Barents Sea as well as the entire sea ice cover of the Baffin Bay and Labrador Sea. This selected area represents the "interior Arctic", which is of major interest to the regional climate model community. The marginal ice zone to the Nordic seas is excluded, because uncertainties of observational data and the variations in ice concentration and velocity between models is largest here. Ice extent in the models depend largely on the inflow of warm Atlantic water, simulated by the underlying ocean model, which is not subject of this study.

Three AOMIP models (AWI, GSFC, and UW) and the SIM experiment exhibit a mode at speeds below or equal to 3 cm s^{-1} and a relatively rapid decay towards high speeds (see Figure 3.3). In these models, sea ice speeds above 10 cm s^{-1} occur almost exclusively in summer and early fall. Two models (IOS and NPS)
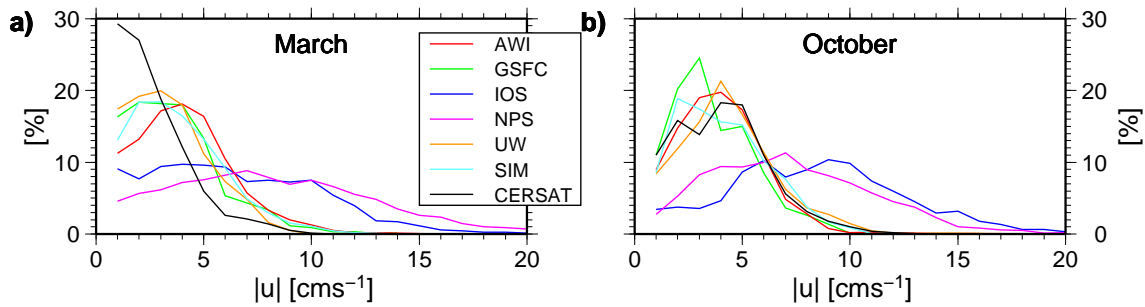
Figure 3.4: Histograms of sea ice drift speed of the interior Arctic for the AOMIP models and CERSAT observations for (**a**) March and (**b**) October of the period 1992–2001. Bin width is 1 cm s^{-1} beginning at 0.5 cm s^{-1} and the legend applies for both panels.

have a much lower frequency of occurrences of low speeds (below 5 cm s^{-1}) and a rather flat distribution with relatively large values at speeds between 10 and 20 cm s^{-1}. The AWI 10m-wind experiment results in a speed distribution that shows a stage between both groups of AOMIP models. The histogram shows additionally the distribution of the NSIDC observations, which are best matched by the first group of models. The mode at or below 1 cm s^{-1} is only reproduced by the GSFC model and partly by the UW model (only during winter and spring). The most pronounced seasonal cycle is present in the UW and SIM results.

Similar results are obtained for the period 1992–2001 for which drift statistics based on the CERSAT observations are derivable. Since summer values are not available, these results are presented as monthly histograms for March and October as typical for seasonal extremes in Figure 3.4. Even in these months, the satellite data do not cover the whole domain. Model statistics have been derived for those grid nodes for which corresponding observations exist. From Figure 3.1 it is already evident for the NSIDC data that the results in general are not significantly changed by this restriction, though small speeds are underrepresented in October. Especially, the differences between the two groups of models discussed above are a robust feature.

In both months, the observations show virtually no sea ice speeds above 10 cm s^{-1}. In March, speeds between 1 and 2 cm s^{-1} have the highest observed frequency of occurrence. Model distributions are generally broader at low drift speeds and show more grid points with speeds at the fast end of the distribution. None of the models reproduces the large number of low speed points indicated by the observations. The IOS and NPS models have a considerable number of occurrences at speeds above 10 cm s^{-1}.

For October, a shift of the observed maximum to higher speeds is visible (see Figure 3.4b). There is also a rapid drop in the frequency of occurrence at 6 cm s^{-1}. The AWI, GSFC, and UW models capture this behavior. The SIM results still belong clearly to this first group of models, though the drop in the
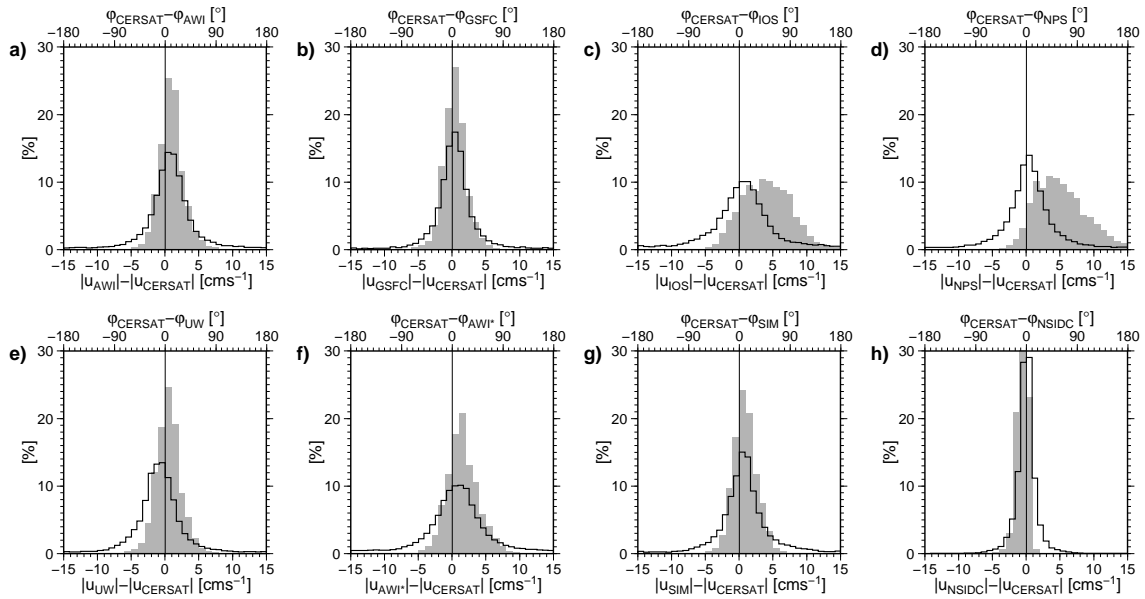
Figure 3.5: Histograms of the differences between model and satellite derived (CER-SAT) sea ice drift speeds (grey shade) and direction (black outline). These histograms refer to the period 1992–2001. Only the months January–April and October–December are considered because of lack of satellite data for the summer months. The models are (**a**) AWI, (**b**) GSFC, (**c**) IOS, (**d**) NPS and (**e**) UW. Panels (**f**) and (**g**) show the same differences for the AWI 10m-wind (here: AWI*) and SIM experiments respectively. In panel (**h**) the two satellite data sets are compared. Differences in direction are presented as angle of deviation between the corresponding drift vectors: positive (negative) value means deviation of the model data to the right (left) of the satellite derived vector.

distribution is less pronounsed. Compared to these observations the IOS and NPS models again have too many occurrences of very high speeds and too little grid points with speeds in the range below 5 cm s^{-1}.

Velocity error histograms (Figure 3.5) corroborate the above results and exhibit the clearest impression on the splitting into two groups of model results. The AWI, GSFC, and UW models have symmetric distributions around zero error speed. On the other hand, the IOS and NPS models are biased towards high speeds. The differences in drift direction between models and CERSAT data are presented in Figure 3.5, too. Obviously the differences in speed do not bias the direction of the drift as the difference angle distributions do not separate into the two speed groups. Though all distributions have a clear mode at zero deviation, difference angles of up to 90 ° occur. Again, the AWI 10m-wind results show larger differences from the observations than the AWI AOMIP run. Errors in this experiment are, however, still smaller than those in the IOS and NPS models. Especially the mode of the speed differences is still close to 0.0 cm s^{-1} (Figure 3.5f). In contrast to the AWI 10m-wind results the SIM distributions (Figure 3.5g) are both very close to those of AWI AOMIP run. The difference angles towards the

observed CERSAT data are even slightly smaller. Differences in speed and direction between the two satellite data sets (Figure 3.5h) are markedly smaller than between model results and either product. Still, differences between the satellite products amount up to 60° in drift direction in a few cases. However, larger differences in drift direction are restricted to smaller drift speeds.

3.5   Two case studies of different drift patterns

Sea ice drift maps are shown for the cyclonic and anticyclonic circulation regimes of *Proshutinsky et al.* [2002] as well as for the winter 1994/95 that was characterised by very strong positive North Atlantic Oscillation (NAO) forcing and an extremely high sea ice export through Fram Strait [*Vinje et al.*, 1998]. These two case studies represent well the typical experimental application and scaling of the AOMIP models. Because the sea ice volume budget of the Arctic is sensitive to the circulation regimes [*Martin and Martin*, 2006], the vorticity of the Beaufort Gyre is examined over the entire period of investigation as a measure of these regimes.

3.5.1   Wind-driven drift regimes

Maps of sea ice drift for different circulation regimes and the differences in drift between them are shown in Figure 3.6 for the AWI and NPS models. These models are taken as representatives of the two groups of AOMIP models identified above. The maps are composites for the anticyclonic and cyclonic circulation regimes (ACCR and CCR respectively) of *Proshutinsky et al.* [2002] during the winters between 1979 and 2001. These composites of the months November to April separate into the ACCR years 1979, 1984–1988 and 1998–2001 and the CCR years 1980–1983 and 1989–1997. Despite basic similarities between the regimes—a persistent anticyclonic direction of rotation in the Beaufort Gyre and a southward flow in the Fram Strait and Greenland Sea—both models show pronounced differences between the circulation regimes. The NPS model shows a weaker Beaufort Gyre with its center shifted towards Alaska during the CCR. With this shift comes an eastward displacement of the transpolar drift. However, the Beaufort Gyre is still a well-pronounced, closed feature in this model result. The export pattern of sea ice from the Laptev Sea changes between regimes and is turned from a southeasterly to a southerly drift direction. In the ACCR, sea ice is directly blown to the Fram Strait. Drift speeds in the Barents, Kara and Laptev Seas increase during the CCR.

The AWI model shows similar differences between circulation regimes as compared to the NPS model. As seen above, sea ice speeds are generally smaller

Figure 3.6: Composite maps of winter sea ice drift for the anticyclonic circulation regime (ACCR) and the cyclonic circulation regime (CCR) of *Proshutinsky et al.* [2002] from (**a**)–(**c**) the AWI model and (**d**)–(**f**) the NPS model. Panels (**c**) and (**f**) show the differences in drift velocity between the regime composites of the respective model results. For clarity reasons the horizontal resolution is individually reduced and changing spatial coverage is due to particular ice extent.
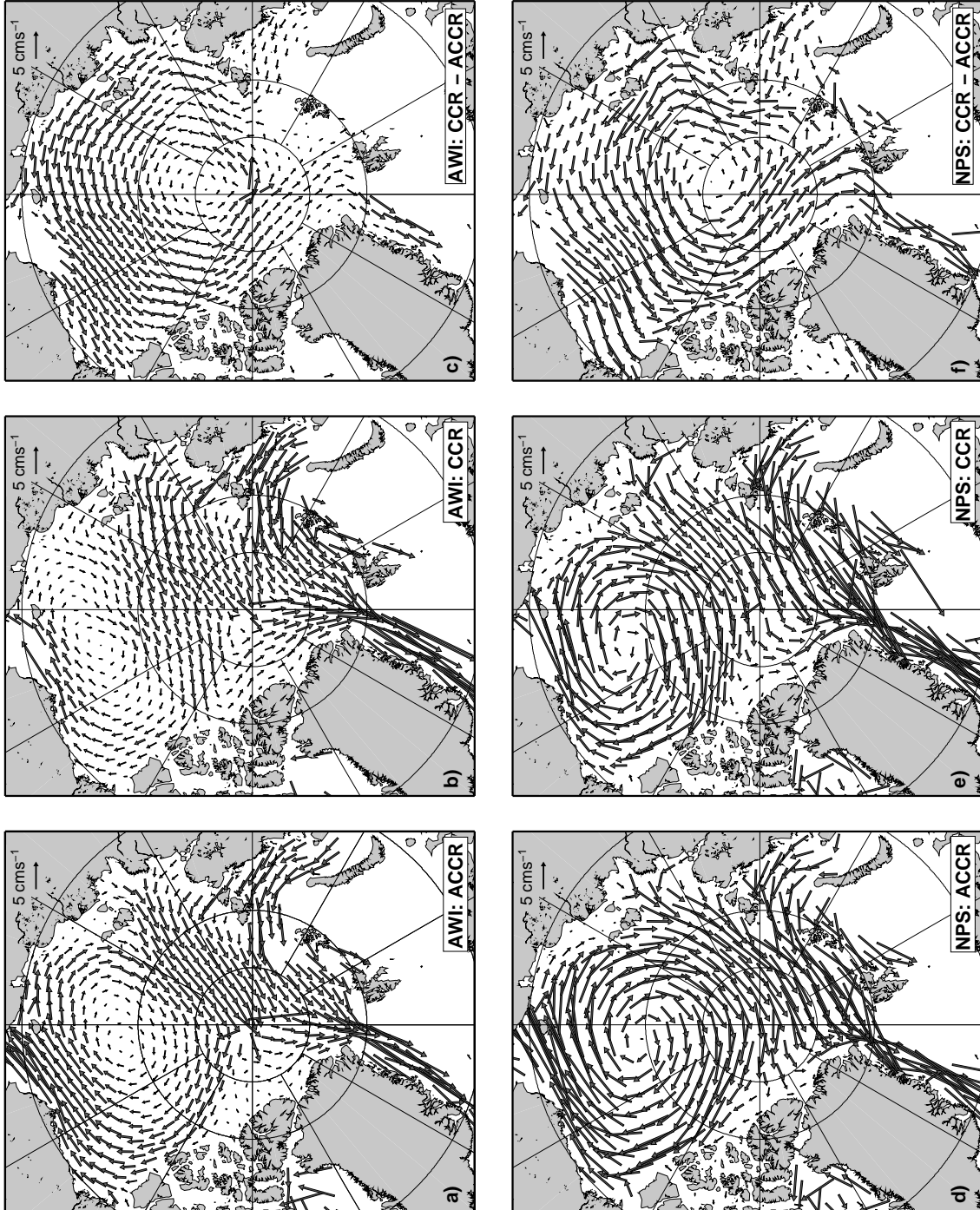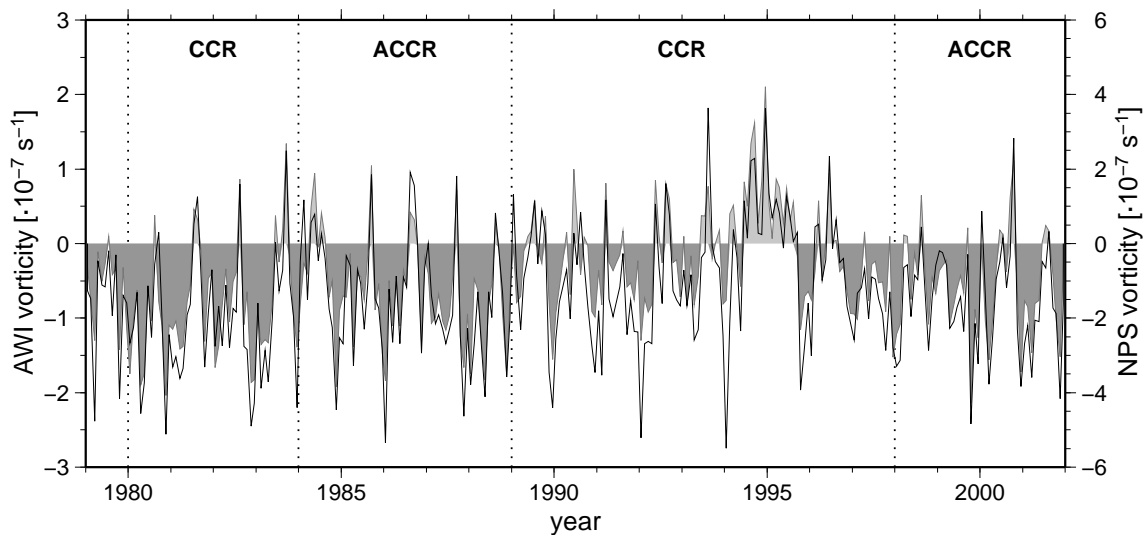
Figure 3.7: Time series of the vorticity of the Beaufort Gyre. Results from the AWI model are shown in grey shade (left axis scaling) and those of the NPS model as black outline (right axis scaling). The regime phases of the wind-driven circulation after *Proshutinsky et al.* [2002] are separated by dotted lines and labeled at the top. Year annotations indicate January 1.

in the AWI model for both circulation regimes. This model exhibits almost a breakdown of the Beaufort Gyre during the CCR with a reversal of the sea ice motion in the western East Siberian Sea. The transpolar drift reaches farther into the Makarov and Canadian Basin than in the NPS model result during the CCR. The ice export direction out of Laptev Sea changes in the AWI model in the same direction as in the NPS results, but from northward to a northeast direction. Associated with the pronounced shift of the transpolar drift is a change in the sea ice drift direction and speed between Greenland and the North Pole. In the CCR phase more thick multi-year ice from north of Greenland and Ellesmere Island—formed during the ACCR phase—is transported towards Fram Strait, indicating a strong sensitivity of the Fram Strait ice export to the atmospheric forcing over the Arctic Ocean. Furthermore, there is a pronounced southwestward ice export out of the Barents Sea during the CCR detectable in the AWI results.

The differences in absolute drift speed between the two regimes are twice as large in the NPS results (-4 to +4 cm s^{-1}) than in the AWI data (-2.5 to +2 cm s^{-1}), which starts from smaller absolute speeds. Normalising these differences by the modal speed averaged over both regimes—2.5 cm s^{-1} for AWI and 6.0 cm s^{-1} for NPS—results in drift speed difference ratios of the range -0.8 to +0.8 equal in pattern for both models. The models' sea ice drift speed differs not only in the long term mean but also in the sensitivity to anomalous forcing. The response in the direction of the drift is very similar, on the other hand.

The vorticity of the sea ice motion in the Beaufort Gyre is calculated in or-

der to show the variability of this dominant feature of the Arctic sea ice drift in the different data sets. Because the model data are given on different grids four fixed positions are chosen to derive one value of vorticity for each month: for the u-component (74 °N, 170 °W) and (84 °N, 170 °W) and for the v-component: (78 °N, 160 °E) and (78 °N, 140 °W). The calculations result in a time series that is presented for the AWI and the NPS model, representing the two model groups, in Figure 3.7. Both models feature strong seasonal and interannual variability. The average of the so defined vorticity is negative because the anticyclonic Beaufort Gyre dominates the region. However, there are short phases, when cyclonic drift prevails, especially in the years 1994 and 1995. In order to integrate all model data sets and also the observations from NSIDC in the vorticity comparison, the mean values of each of the four regime phases falling into the period of our investigation are calculated for each data set (see Table 3.3). However, none of the models show a clear shift in mean vorticity between the two regimes but all feature the extreme cyclonicity of the 1989–1997 phase. The average vorticities derived from the observations do not reflect the regimes as clearly as the model results.

3.5.2 The winter 1994/95

The second case chosen for validation of the model results is the winter of 1994/95, defined as the period of November 1994 to April 1995, which stands out for its large Fram Strait ice export. The composite maps of observed sea ice drift for this winter are presented in Figure 3.1. All AOMIP models fail to reproduce the observed drift pattern of the winter 1994/95. Especially the results of AWI, GSFC and IOS differ considerably from the observed drift pattern

data set	CCR (1980–83) $[10^{-7}\,\mathrm{s}^{-1}]$	ACCR (1984–88) $[10^{-7}\,\mathrm{s}^{-1}]$	CCR (1989–97) $[10^{-7}\,\mathrm{s}^{-1}]$	ACCR (1998–2001) $[10^{-7}\,\mathrm{s}^{-1}]$	correlation coefficient to NSIDC
AWI	-0.80	-0.62	-0.14	-0.54	0.64
GSFC	-0.44	-0.39	-0.15	-0.53	0.68
IOS	-1.55	-0.86	-0.88	-1.29	0.53
NPS	-2.06	-1.48	-0.90	-1.55	0.68
UW	-0.84	-0.64	-0.49	-0.63	0.65
NSIDC	-0.44	-0.29	-0.31	-0.34	(1.0)

Table 3.3: Mean vorticity values of the different data sets separated for the four periods of different circulation regimes covered by this study and overall correlation of the time series to the observations of the NSIDC.

Figure 3.8: Sea ice drift velocity averaged over the winter (November through April) of 1994/95 from AOMIP models (**a**) AWI, (**b**) NPS and (**c**) UW and (**d**) the corresponding NCEP/NCAR reanalysis sea level pressure field. Panels (**e**) and (**f**) show the sea ice drift of this winter from the AWI 10m-wind and SIM experiments respectively. Panels (a), (b), (c), (e) and (f) include IABP buoy drift vectors in red. For clarity reasons the horizontal resolution of modelled data is individually reduced and changing spatial coverage is due to particular ice extent.

61
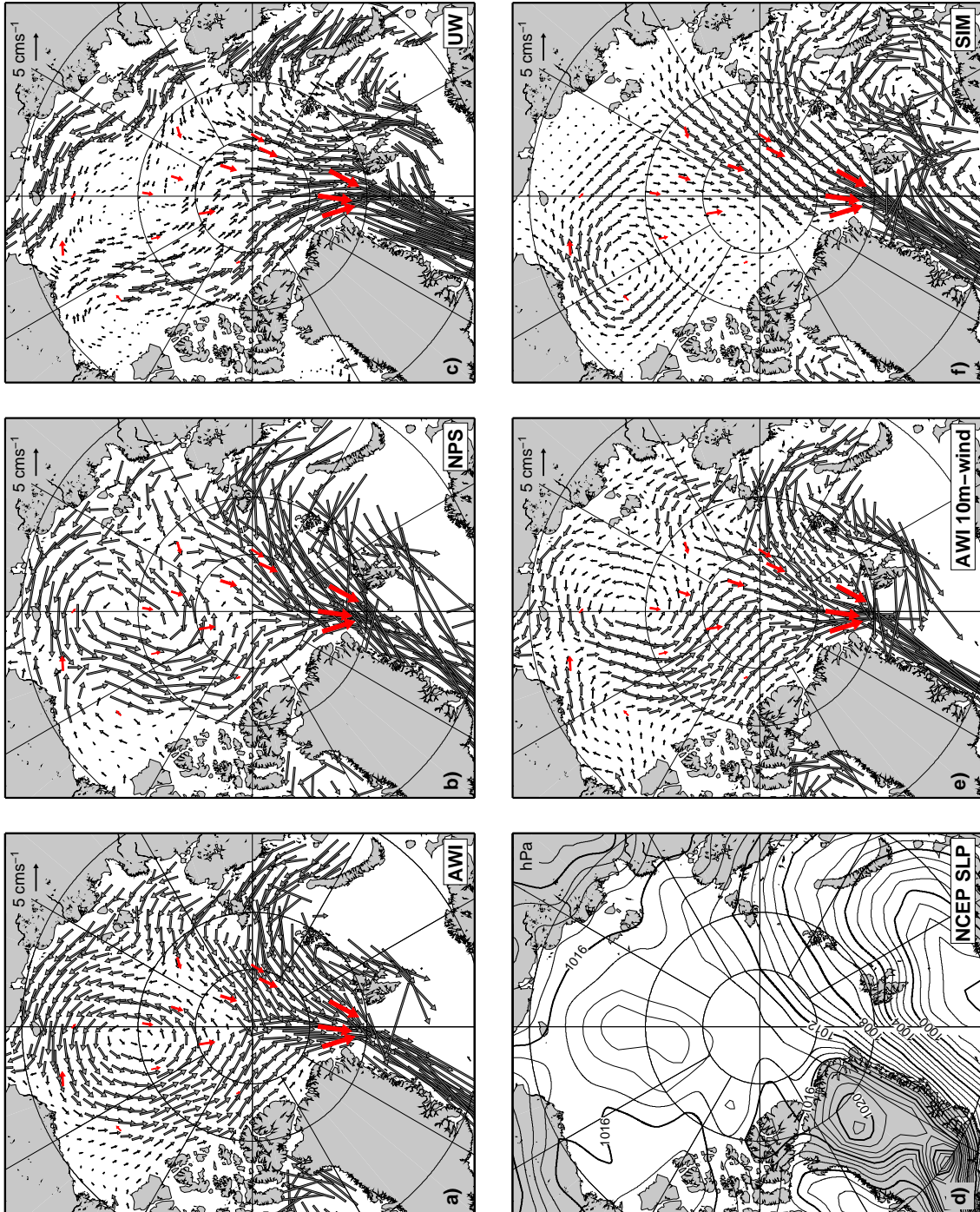
in the sector 150–330 °E (see AWI results in Figure 3.8a as a representative result). These models show a close correlation between sea ice drift and the SLP field (see Figure 3.8d). Though belonging to different groups concerning the absolute drift speeds NPS and UW models feature a pattern that is closer to the observational data (see Figures 3.8b and 3.8c). This is evident, for example, in the Beaufort Sea. Here, the impact of the low in the central Arctic is weaker and the dominant cyclonic gyre is weakened to an extent that an extremely retreated anticyclonic Beaufort Gyre is visible in the Beaufort Sea. The ice drift along the Alaskan coast is directed opposite to the other AOMIP results. This compares well to the observations. Nevertheless, modelled drift speed and direction deviate from the observations in the East Siberian Sea and central Arctic.

The result of the AWI 10m-wind run (Figure 3.8e) differs considerably from the one forced accordingly to AOMIP protocol and is generally closer to the observed drift, resembling the NPS result. Besides the changed pattern in the Beaufort Sea the AWO 10m-wind experiment features also smaller drift speeds in the East Siberian and Laptev seas compared to the AWI AOMIP run. However, the changed wind forcing does not dispose of the central cyclonic gyre. Here, the embedded buoy drift vectors indicate, that the frontier between the remnants of the Beaufort Gyre and the dominant cyclonic gyre in the modelled drift fields is located too far to the east.

In the SIM model the Beaufort Gyre keeps its dominance in the Arctic Ocean though it is realistically retreated in this winter mean. The simulation results of this experiment do not feature the stong central cyclonic gyre and are closest to the buoy (red vectors in Figure 3.8f) and satellite observations (compare Figure 3.1). Only this non-AOMIP simulation shows the observed, extraordinary strong contribution of the Beaufort Gyre to the Transpolar Drift Stream, which finally feeds the Fram Strait ice export, in winter 1994/95. This indicates that the oceanic forcing importantly affects the drift pattern and that the climatological forcing of the SIM results in a more realistic sea ice drift than simulated by the sea ice-ocean coupled models. This finding may not hold for other winters with different weather conditions. The ice exiting through Fram Strait is collected all over the Arctic and does not substantially stem from near-shore regions as seen in the AOMIP simulation results. The contribution of ice from north of Greenland is, however, too weak in the SIM results, indicated by one buoy drift vector.

3.6   Possible reasons of deviations

The analysis of sea ice drift speed statistics revealed two groups of model results, one that is relatively close to observations and one where sea ice speeds are overestimated. The two observational data sets correspond to each other

much more than the models do. Differences between models from different groups are also clearly larger than the differences between the model results of the first group and observations. The fact that modelled drift speeds exceed observed ones has also been shown by *Martin and Martin* [2006], who found a difference of 1.0 cm s^{-1} between modelled and satellite derived modal drift speeds on a monthly scale. Their uncoupled sea ice model is comparable to that used here for the SIM experiment. Also Thomas (1999) supports a bias of 1.0 cm s^{-1} between standard model configurations—matching the AOMIP model specifications best—and daily buoy data. What is the cause of these striking differences between model results? The main contributions to the sea ice momentum balance are the wind forcing, the ocean-ice drag, the internal stresses, and the Coriolis force [*Harder et al.*, 1998]. In the region of the Beaufort Gyre the sea surface pressure gradient force may reach the same magnitude as the Coriolis force and can therefore not be neglected. However, this local momentum balance can not explain the overall differences in the drift speed distributions. Different settings of other parameters, like the ice strength parameter P^* and the lead closing parameter h_0 do not separate clearly into the two groups (see Table 3.1). However, the ice strength parameter P^* enters the equation for the ice strength P

$$P = P^* h \exp\left(C^*(1 - A)\right) \tag{3.4}$$

where C^* is a constant and A and h the ice concentration and mean thickness [*Hibler*, 1979]. Thus, the ice strength parameter is scaled by an exponential function of the ice concentration. This makes the ice strength sensitive to small variations of A for values above 90% ice concentration. However, the mean ice thickness that effects the ice strength linearly may even have a stronger impact. For the interior Arctic (as defined in Section 3.4) the AWI, NPS and UW model exhibit mean ice concentrations of around 95%, less than 98% and 99% respectively. Only in the AWI model the ice strength shows considerable response to the variations of the ice concentration, whereas the ice strength is dominated by the ice thickness in NPS and UW models. Hence, the NPS model, producing thicker ice, features larger ice strengths than the UW model, though both apply the same P^* (see Table 3.1).

Normally large sea ice drift speeds occur preferentially for thin ice and low ice concentrations. Under these conditions, the internal stresses are negligible. One would expect that a thinner ice cover would lead to faster ice drift. Models of group one, which agree well with the observations all exhibit moderate mean ice thicknesses of 1.2 to 1.5 m. On the other hand, both the IOS and the NPS model of the second group of models feature thicker ice. Thus the conclusion obtrudes that the opposite feedback prevails and larger drift speeds result in thicker ice due to enhanced deformation.

Differences in sea ice thickness, concentration and rheology are apparently not responsible for the main model differences in drift speed. In contrast, higher drift speeds due to the chosen forcing are able to increase the mean ice thickness.

3.6.1 Wind forcing

Regarding the possible causes of the differences in sea ice drift between the two model groups the atmospheric forcing variables can not be excluded completely though they are prescribed identically according to AOMIP specifications. Some exchange parameters are fixed by the AOMIP protocol, namely the atmospheric and oceanic drag coefficients. However, there are important details of the implementation of atmospheric and oceanic forcing that differ between models, among them the actual prescription of the wind stress, differences in ocean currents, and the implementation of the ocean-ice drag term. From Figure 3.8 it has become clear that wind stresses derived from SLP and the corresponding reanalysis product lead to different sea ice drift results. In general the wind stress calculated after AOMIP prescriptions is found to have the smallest magnitude of all three wind stress fields. The 10m-wind derived stress field, which also shows differences in direction to the AOMIP stresses, features stronger, partly twice as large wind stresses. Yielding the same pattern as the 10m-wind forcing the momentum flux from NCEP/NCAR reanalysis has a still larger magnitude. The winter 1994/95 sea ice drift pattern turned out to be more realistic in the AWI model when 10m-wind derived stresses were used instead of AOMIP wind stresses. However, the AWI model using AOMIP-derived stresses has a more realistic sea ice speed distribution than when driven with 10m-wind derived stresses. In a tentative conclusion the differences in constructing wind stress forcing are found only partly responsible for the different sea ice drift statistics as the AWI 10m-wind run tends towards higher drift speeds but is still closer to the results of the first than those of the second group of models. And the results of the SIM experiment, driven with the 10m-winds, too, but including only a climatological ocean, point at an important influence of the underlying ocean as this data set exhibits an improved pattern and slightly smaller drift speeds during winter than the AWI model.

Despite the regionally important influence of the oceanic circulation on sea ice drift, the large scale sea ice drift in the winter 1994/95 is governed by the prescribed wind stress. Differently generated wind stress fields (SLP derived, 10m-wind derived or the wind stress taken directly from reanalysis; see Figure 3.9) all include a strong cyclonic forcing over the central Arctic Ocean that is reflected in a pronounced cyclonic sea ice drift. Furthermore, both AWI model
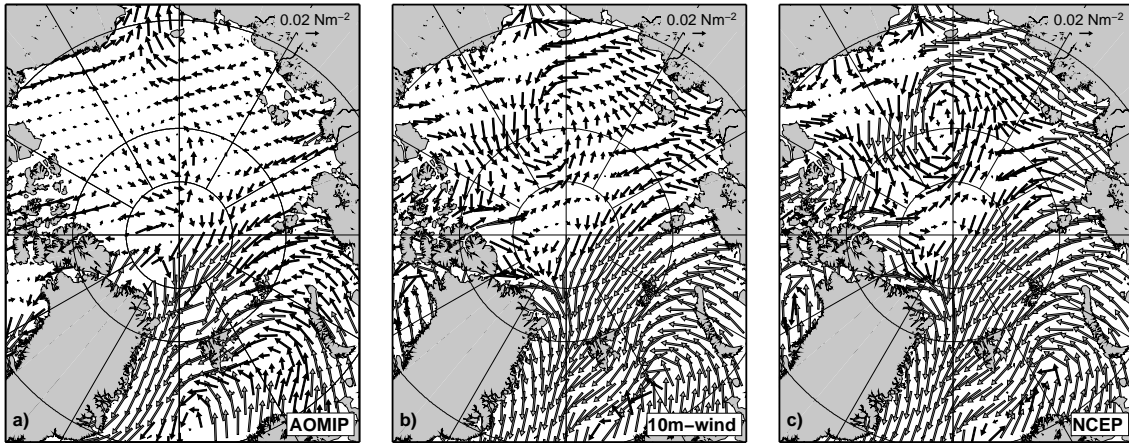
Figure 3.9: Wind stress fields as composites of winter 1994/95 (**a**) calculated according to the AOMIP protocol, (**b**) derived from NCEP/NCAR winds in 10 m height and (**c**) as provided directly from NCEP/NCAR reanalysis. Stresses larger than 0.04 N m^{-2} are represented by grey shaded vectors of constant length, which equals 0.04 N m^{-2}, for clearity.

experiments, the AOMIP-forced and the 10m-wind-forced versions show similar biases in drift speed and direction in the East Siberian Sea and north of it in the central Arctic. These biases are also observed for the other AOMIP models. Actually, the AWI 10m-wind experiment features slightly larger drift speeds (compare Figure 3.3) and thus the absolute values of AOMIP wind stress seem to be more realistic than those of wind stress alternatives. This holds not for the drift pattern as stated before. However, the reanalysis data used to derive the atmospheric forcing include uncertainties. These errors can never be excluded completely, because direct measurements are sparse in the central Arctic.

3.6.2 Ice-ocean stress

The coupled sea ice-ocean models differ in the detail of the dynamic coupling to the ocean. Some, including AWI, apply the technique of *Hibler and Bryan* [1987] where the uppermost grid cell of the ocean is thought of as a mixture of sea ice and water and where the momentum forcing of the mixture contains the wind stress and the internal sea ice stresses. Other ocean models are driven with the sea ice-ocean drag when ice covered. These differences have only an indirect effect on the sea ice drift through changes in ocean circulation. Models further differ in the ocean velocity that enters the ocean drag in the sea ice model. It is the choice of the modeling group to use first ocean level velocities, directly or subject to a turning angle, or some approximation to the geostrophic velocity. The latter is usually the velocity of the second ocean model level, which is already below the Ekman layer, combined with an assumption about the veer-
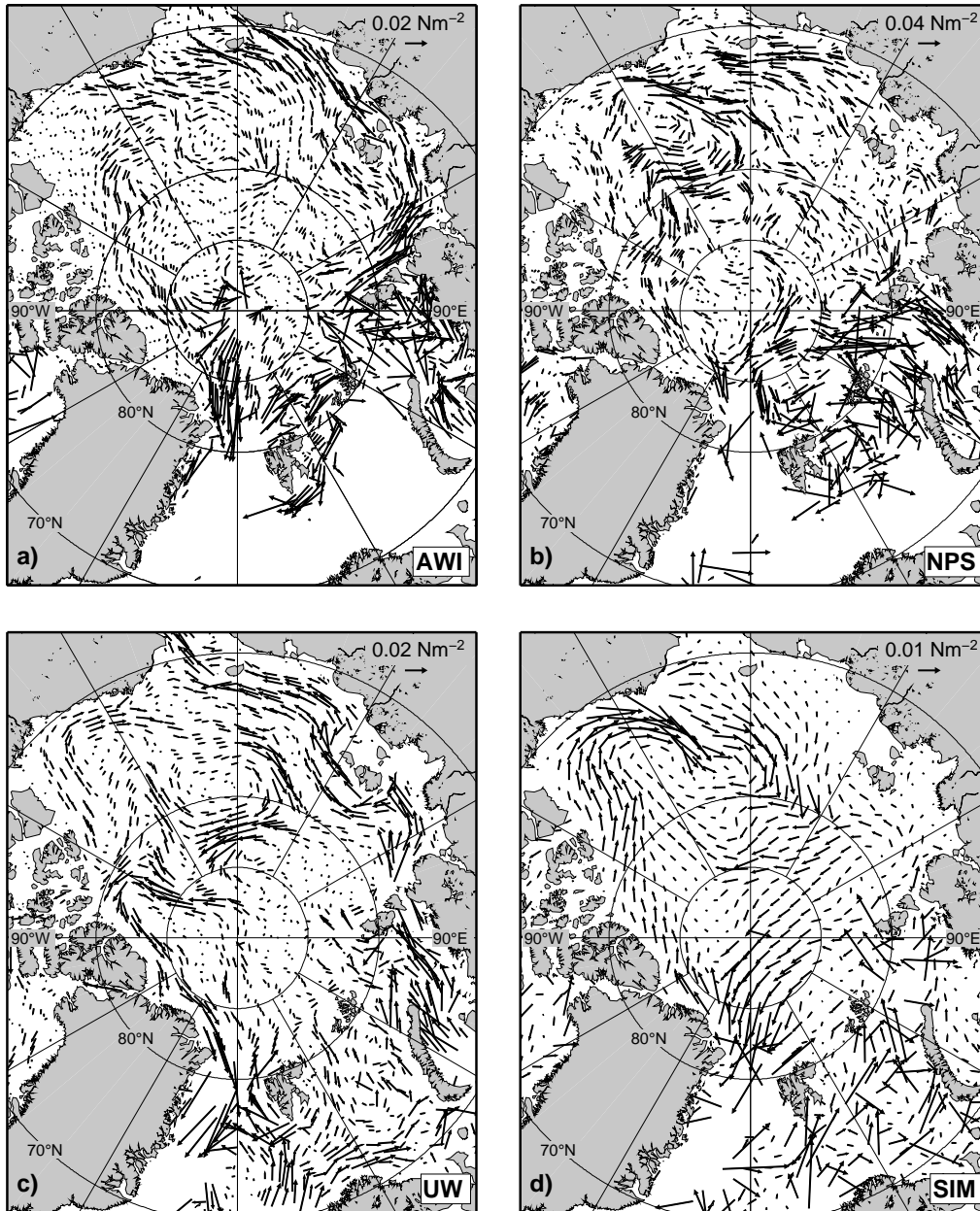
Figure 3.10: Ocean-sea ice stress difference $\tau_{w_0} - \tau_w$ (see details in the main text) for (**a**) AWI, (**b**) NPS, (**c**) UW and (**d**) SIM models averaged over winter 1994/95 corresponding to sea ice drift means in Figure 3.8. For clarity reasons the horizontal resolution is individually reduced and only stresses smaller than 0.05 N m^{-2} (AWI and UW), 0.1 N m^{-2} (NPS) and 0.03 N m^{-2} (SIM) are shown. Watch modified scaling in (b) and (d).

ing of the currents that are relevant for the sea ice drift. For instance, the AWI model employs the ocean velocity of the second layer centered at 15 m depth with a turning angle of 25 °. NPS and UW models use the one of the second and fourth layer, respectively, both centered at 35 m, without a turning angle. For reasons of the stability of the sea ice model, the AWI model employs an average over a few days of the oceanic currents that enter the drag term. It is found that the applied ocean velocities do not vary in speed to an extent that explains

the large ice drift speed of the NPS model. The absolute values of ocean speeds are similar between AWI and NPS models. That means that the ocean-ice stress of the NPS model is dominated by the large ice drift speed. Correspondingly, the NPS ice-ocean stress is approximately twice as large as in the AWI and UW models. To illustrate the oceanic influence on the sea ice momentum balance not only the real ocean stress, affected by ocean and ice velocity τ_w, but also an ocean stress τ_{w_0} with an inactive ocean ($u_w = 0.0$ m s^{-1}) is compiled. The difference $\tau_{w_0} - \tau_w$ presented in Figure 3.10 for the winter 1994/95 for AWI, NPS and UW models as well as the SIM experiment then shows the pure influence of the ocean velocity on the ocean-ice stress.

There are three points of particular interest for this winter mean. The first finding is the opposite direction of $\tau_{w_0} - \tau_w$ comparing AWI result to NPS and UW along the Alaskan coast. The oceanic part of the ocean-ice stress in the AWI model is found to be directed opposite to the AOMIP wind stress direction and thus hinders the ice to drift westward along the coastline. This leads to the weak ice drift found in the AWI model in this region (Figure 3.8a). In the NPS and UW models the ocean velocity is clearly dominant compared to the low ice velocity and drives the ice westward along the coastline to follow the remnants of the Beaufort Gyre (Figure 3.8c), supporting the wind stress in this case. Concerning this aspect of the Beaufort Gyre the SIM model follows the results of the UW model. In the Beaufort Sea the SIM forcing features even stronger currents and thus $\tau_{w_0} - \tau_w$ stresses as the UW model.

The second observation is that an eastward sea ice drift in the East Siberian Sea is strongly supported by the oceanic momentum flux in AWI, NPS, and UW models. A strong eastward ocean movement in the East Siberian Sea results in ice drift in the same direction because of the weak AOMIP wind forcing in this region. Other wind stress forcings, 10m-wind derived and NCEP/NCAR momentum flux, would support this eastward ice drift, which is present in the observational data only to a minor degree (compare Figure 3.1). These strong stresses along the Siberian coast are obviously a result of the sea ice-ocean coupled models as these are missing in the SIM results.

A third finding explains the difference in ice drift between AWI, NPS, UW and SIM models concerning the strong cyclonic gyre in winter 1994/95. Only the UW and SIM result do not show a closed gyre in the region around $80°$ N and $180°$ E. Here the strong impact of the ocean velocity and its matching direction are again the reason why the UW model features the largest deviation to the wind forcing of all considered AOMIP models, which improves the drift pattern in this case. Figure 3.10c shows that the ocean hinders the ice to follow the cyclonic pattern west of $180°$ E and north of $80°$ N. While the NPS model does not feature a coordinated current in this particular region that would hin-

der the cyclonic ice drift, this ice drift is even supported by the ocean velocity in the AWI result (Figure 3.10a). However, it should not be forgotten that the wind forcing causes the dominant cyclonic gyre in sea ice drift. This gyre is not present in the observed sea ice drift fields (see Figure 3.1). It is a strong feature in the NCEP/NCAR reanalysis data that is already present in the SLP field (Figure 3.8d).

Two additional comments on the SIM results are necessary. The extremely weak ice drift north of Greenland found in these data (Figure 3.8f) are caused by a combination of relevant processes. To begin with the oceanic stress $\tau_{w_0} - \tau_w$ is relatively strong in this region, about one-third of the wind stress, and directed opposite to the latter (see Figure 3.10d). In concurrence with the thick multi-year ice (5–6 m) present north of Greenland in the SIM results the ice drift is retarded nearly to a complete halt despite an existing wind stress of about 0.07 N m^{-2}. This diminishes the Fram Strait ice export compared to the AWI and AWI 10m-wind results. The second point is that the SIM model is forced with climatological ocean currents, which are found to be of good quality to simulate the special ice drift situation of the winter 1994/95. However, the composite presented in Figure 3.10d holds for all winter seasons and may lead in combination with the varying wind forcing to an ice drift pattern that corresponds less to the observations than during this special winter.

3.6.3   Different responses in the models

The main findings concerning the comparison of the impact of wind and ocean stress on the ice drift is also supported by the second example we focused on, the cyclonic and anticyclonic drift regimes: The sea ice drift of the AWI model follows closely the applied wind forcing. Compared to NPS and UW models this connection is strongest and has an important impact on the upper ocean velocity field in the AWI model. For example, the southward shift of the Beaufort Gyre centre, a region of small ice drift speeds, during CCR years (compare Figures 3.6a and 3.6b) is a direct implication of the wind forcing. Only in the AWI model the velocity of the upper ocean currents exhibit a close connection to this shift in the wind field and ocean currents speed up where the gyre centre has been before during the ACCR and slows down in the area where the centre has been moved to. A reason for this difference between models may be the different depth where the ocean velocities applied for the ocean-ice stress are centered (AWI 15 m and NPS, UW 35 m).

For the NPS model holds that the ice drift dominates the ocean-ice stress. While ocean speeds are of the same magnitude as in AWI and UW results the NPS ice-ocean stress is twice as large. Thus the cause for the large ice

drift speeds of the NPS model are most probably found in the sea ice model implementation—e.g. a doubled atmospheric drag coefficient [*W. Maslowski*, pers. comm.].

Investigations of the UW results on the other hand show that the ocean velocity is the dominant part of the ocean-ice stress in certain regions, namely along the coastlines of East Siberian, Beaufort and Lincoln seas as well as in parts of the cyclonic gyre in the central Arctic described above. Here, the UW model ocean stress outbalances the comparatively weak wind forcing.

Differences in ocean-ice stress can have a number of reasons. The strategies followed by different groups in coupling ocean and sea ice components differ. The different stresses that enter the ocean component could also play an important role in the differences in the oceanic velocity itself. As the variations of the Coriolis parameter are small at high latitudes, the Sverdrup relationship implies large changes in the horizontal velocity components in response to changes in Ekman pumping velocity. In those models following the approach of *Hibler and Bryan* [1987] the Ekman pumping velocity is determined by the wind stress, while in other models the ocean-ice drag determines the Ekman pumping.

3.6.4   Significance of drift regimes in model comparison

In Section 3.5.1 it was shown that a vorticity index based upon the ice drift is not capable to distinguish the CCR and ACCR phases (Figure 3.7) although the sea ice drift of the AOMIP models has significantly different composite drift patterns for CCR and ACCR (Figure 3.6). This essential outcome holds also for the mean vorticities calculated from the observed sea ice drift of the NSIDC as well as for the AWI 10m-wind or SIM experiments. The correlations between observed and simulated sea ice drift vorticity is between 0.5 and 0.7 (see Table 3.3). A likely reason for the relatively weak correlation is the basic difference between modelled and observed drift patterns as described above. The chosen positions for calculating the vorticity of the Beaufort Gyre does not necessarily match the observed drift conditions though it is well suited to compare the model results.

For all models it holds that the summer mean (May to October) is in nearly all cases less anticyclonic/more cyclonic than the adjoining winter means (November to April). This agrees with the description of *Proshutinsky et al.* [2002]. However, the time series (Figure 3.7) and mean values (Table 3.3) of vorticity of all models agree only partly with the circulation regime phases of *Proshutinsky et al.* [2002]. The number of cyclonic events or their intensity does not change explicitly between the regimes, though the long cyclonic phase of 1989–1997 exhibits more events than before or after this period, at least in the AWI and GSFC data and within the years spanned by our investigation. The most prominent

cyclonic event in 1994/95 coincides with the observed maximum in sea ice export through Fram Strait. A possible reason for the mismatch between ice drift and regime phases in Figure 3.7 is the derivation of the regimes by *Proshutinsky and Johnson* [1997]. They distinguished the regime phases from the interannual variability of the sea surface height gradient. The latter was derived using a two-dimensional, wind-driven, barotropic ocean model coupled with a dynamic sea ice model. This model and its forcing deviate considerably from those examined here and it is conceivable that surface heights in the AOMIP models will be different. The sea surface height determines the sea surface tilt force that enters the momentum balance of sea ice drift. As stated above this force plays a negligible role except for the Beaufort Gyre. But exactly the strength of this feature is important for the difference between the two drift regimes. However, the surface wind transition coefficients and turning angles are the same as used in the AOMIP models that are described in Section 3.3.1.

Concluding, the two wind-driven drift regimes generally have a verified effect on sea ice quantaties, like drift and total ice volume (see also *Martin and Martin* [2006]). The signal in the ice drift pattern is, however, limited in complex sea-ice ocean models, because the oceanic forcing becomes more important on monthly and longer time scales and signals of wind-driven effects weaken.

3.7 Implications for Fram Strait sea ice export

The sea ice flux through Fram Strait, which is directed towards the North Atlantic, has been intensively studied in the past decades and the Fram Strait has been identified as the main exit gate of Arctic sea ice. Average values of the observed ice volume outflow through Fram Strait range between 2200 and 2900 km^3yr^{-1} [*Vinje et al.*, 1998; *Kwok and Rothrock*, 1999; *Vinje*, 2001; *Kwok et al.*, 2004]. This means that each year roughly $^1/_{10}$ of the total Arctic sea ice mass leaves the Arctic Ocean through this passage. Another link to the North Atlantic exists via the Barents Sea, in which itself sea ice is formed and melted during an annual cycle. Observations show that the import from the Arctic Ocean is about 40 km^3yr^{-1} on average though varying strongly with ±300 km^3yr^{-1} [*Vinje*, 1988; *Kwok et al.*, 2004]. The mean Kara Sea net export of sea ice into the Barents Sea amounts to 560 km^3yr^{-1} [*Vinje*, 1988]. Model studies showed that only 20–40% of the sea ice imported into the Barents Sea leave for the North Atlantic [*Kwok et al.*, 2004; *Martin and Martin*, 2006].

West of Greenland sea ice can leave the Arctic Ocean through the Canadian Archipelago. Assuming a mean ice thickness of 2 m and an average outflow speed of 5 cm s^{-1} *Aagaard and Carmack* [1989] estimated that 155 km^3yr^{-1} flow through the narrow passages. The authors expect these passages to be open

for only three months per year. More recently, *Kwok* [2005] estimated the annual outflow through Nares Strait to be already of magnitude 130±65 km³yr⁻¹ assuming an ice thickness of 4 m on average. Further south, the Baffin Bay itself is a region of net sea ice production and therefore, the sea ice transport through Davis Strait towards the North Atlantic has a larger volume than the ice flux through the passages further north. *Cuny et al.* [2005] specified a Davis Strait ice export of 528±50 km³yr⁻¹ based on satellite derived areal fluxes and an assumed ice thickness of 0.5–1 m.

The only link between the Arctic and Pacific oceans is the Bering Strait. *Woodgate and Aagaard* [2005] measured a sea ice inflow to the Arctic of 130±90 km³yr⁻¹ with a moored ADCP. Concluding, the importance of the Fram Strait sea ice flux and the availability of several observations of good quality of this flux, make it an ideal example to study the impact of the drift differences between the various models as well as these models and observations on derived quantities.

3.7.1   Comparison of observed and modelled transports

The differences between the models in drift speed discussed above affect the sea ice transport through Fram Strait. In Figure 3.11a the areal flux of the AOMIP models are presented together with satellite-based observations from *Kwok and Rothrock* [1999] and those of *Vinje et al.* [1998] which are based upon weather and ice charts. While the modelled estimates are relatively close during summer, because the ice concentration is low, the winter areal fluxes split up into the two groups of models that were identified by their drift speed frequency distributions. The second group (IOS and NPS) clearly overestimates the flux. Of the first group the GSFC results match the observations of *Kwok and Rothrock* [1999] best while AWI and UW models tend to have stronger areal exports during winter time. These larger transports are in line with the observations of *Vinje et al.* [1998] which exceed the estimates of *Kwok and Rothrock* [1999] during the winter seasons between October 1993 and April 1996. Furthermore, all models overestimate the seasonal variability of the areal ice export compared to the observational data. This is particularly obvious in the few cases when simulated ice exports become negative, whereas observed export rates are always positive.

The classification of the simulated transports changes partly when the sea ice volume flux (Figure 3.11b) is studied. Both observational data sets of ice volume transport result from the multiplication of the above areal transports with the monthly mean ice thickness recorded by moored upward-looking sonars (ULS) by *Vinje et al.* [1998]. The second group of models biased by its large drift

71

Figure 3.11: Monthly means of Fram Strait sea ice export from 1979 to 2001 (positive for fluxes towards the North Atlantic). (**a**) Areal fluxes $\mathcal{F}_A$ of the AOMIP models and (**b**) volume transports $\mathcal{F}_h$ from AOMIP and SIM results. Export rates derived from satellite observations by *Kwok and Rothrock* [1999] are included as well as the ULS based measurements of *Vinje et al.* [1998]. Year labels are positioned on the 1st of January and the legend relates to both panels.
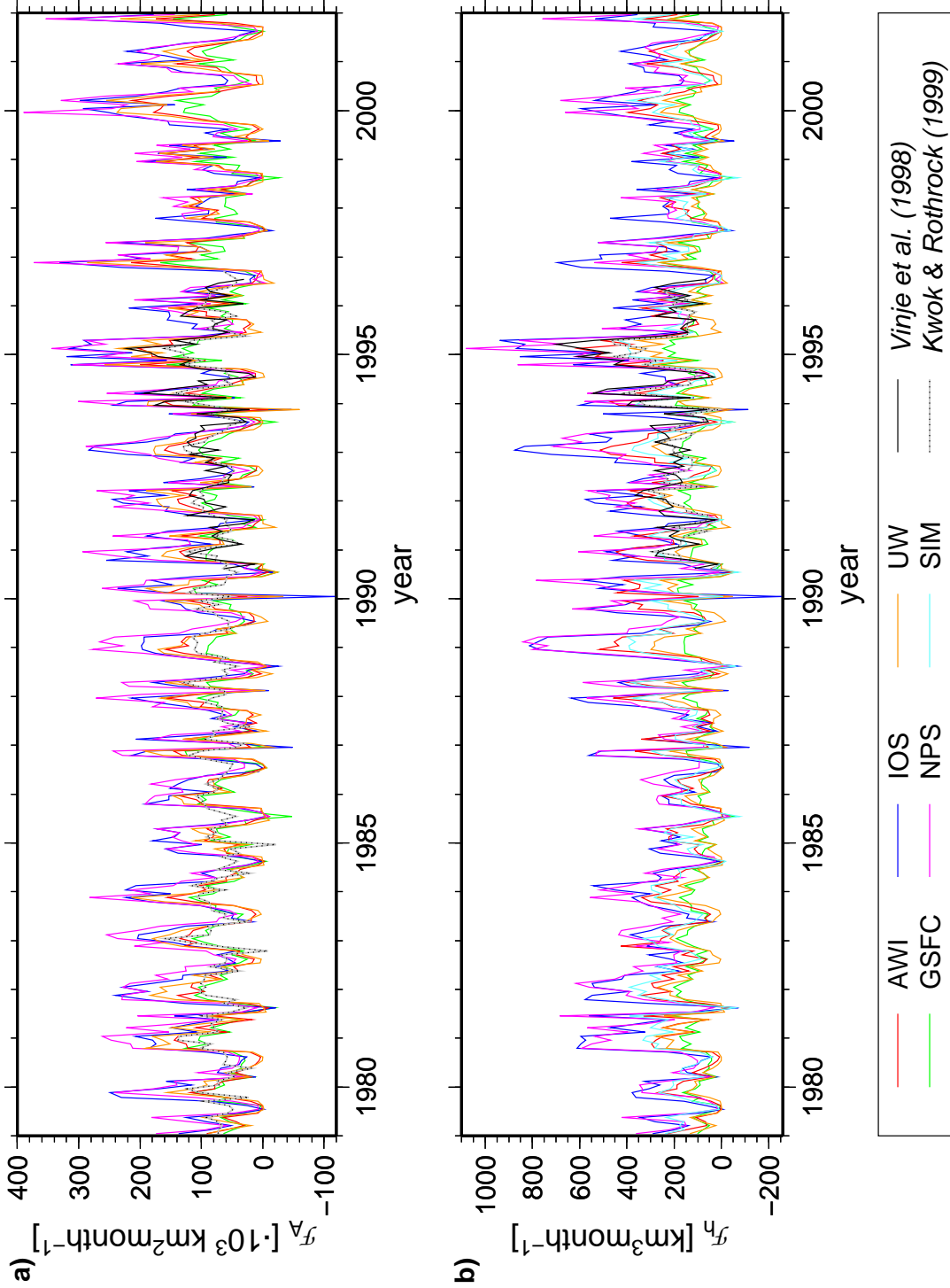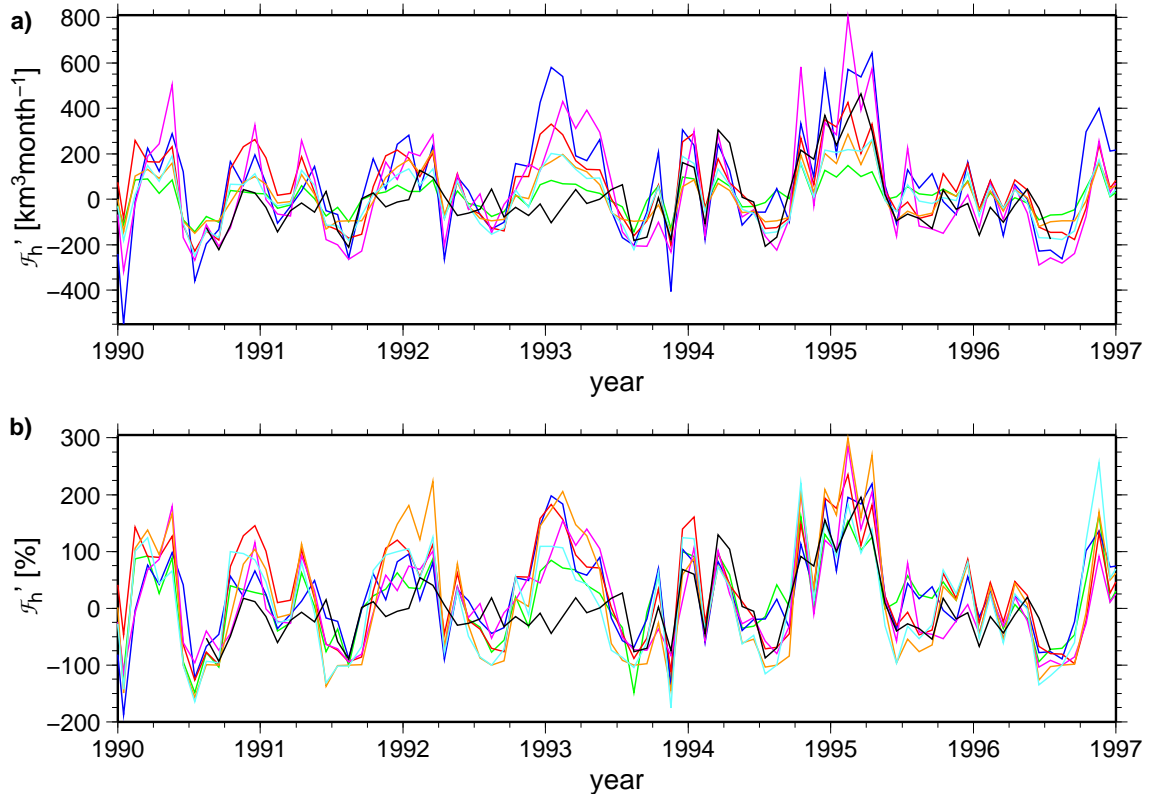
Figure 3.12: Anomalies of monthly averaged sea ice volume exports $\mathcal{F}'_h$ through the Fram Strait of the period 1990–1996 (positive for fluxes towards the North Atlantic). (**a**) Absolute values and (**b**) percentage with respect to the particular model mean of AOMIP and SIM results (for colour coding please refer to legend in Figure 3.11). Observations of *Vinje et al.* [1998] are added as black lines.

speeds has a mean flux of $\sim$3450 km^{3}yr^{-1} for the period 1979–2001 and thus overestimates the volume flux. The first group diverges more than it has with

data set	mean volume export [km^{3}month^{-1}]	std. deviation [km^{3}month^{-1}]	correlation coeff. to *Vinje et al.* [1998]
AWI	239	157	0.72
GSFC	110	64	0.72
IOS	339	221	0.62
NPS	322	228	0.66
UW	113	105	0.67
SIM	190	119	0.73
Vinje	237	142	(1.0)

Table 3.4: Sea ice volume transports through the Fram Strait averaged over the period August 1990 to July 1996 are listed and compared to monthly means of observational data from *Vinje et al.* [1998].

the areal fluxes. The GSFC results provide again the smallest flux rate, which leads to an underestimation of the observed volume export. The volume flux of the UW model also tends towards a smaller flux than observed. The average export rates of both these models are about 1160 km^{3}yr^{-1} for the entire period of interest. The AWI model shows an overestimation during winter, which is not as strong as that of the IOS and NPS models, and a reduced flux compared to measurements in the summer months. The curve of the SIM transports, which are added in Figure 3.11b, range between the AWI and UW models. However, both, AWI and SIM, have mean transports close to 2150 km^{3}yr^{-1}. For the period of the measurements, from August 1990 to July 1996, the AWI model features an average ice volume transport of 239 km^{3}month^{-1} that matches the observed 237 km^{3}month^{-1} best[b] (see Table 3.4). The second best result of 190 km^{3}month^{-1} is achieved with the SIM experiment. This smaller value is possibly caused by the difference in ice ocean stress pattern off the north-eastern coast of Greenland that is pointed out in Section 3.6.2.

The differences between the modelled volume fluxes decrease when transport anomalies are derived. These are presented in Figure 3.12 together with the anomalies of the observations from *Vinje et al.* [1998]. For the winter season still holds that the absolute anomalies of the second group of models are larger than those of the first group and the ranking of the modelled fluxes with smallest values found for the GSFC model and largest for IOS/NPS is unchanged compared to the total ice transport. As indicated by the standard deviations of the average fluxes listed in Table 3.4, the second group of models features more than twice as strong variations in the time series of absolute flux anomalies (Figure 3.12a) than the GSFC and UW models. Only the AWI model is again close to the observed flux variability. This does not hold for winters in the early 1990s, where all models overestimate the observed flux anomalies.

An extraordinary mismatch between simulation results and observations occurs in the winter 1992/93 where the *Vinje et al.* [1998] data feature nearly no deviation from the mean whereas most models have the second largest export anomaly of the shown period 1990–1996. It is very likely that the reason is found in the thickness estimates of *Vinje et al.* [1998], which are used for both observational data sets presented here. *Kwok et al.* [2004] state that the ice thickness measurements and the unknown shape of the cross-strait thickness profile cause the largest uncertainties in the derivation of the Fram Strait ice volume flux. However, in the next section is shown that the simulated positive ice export anomaly of the winter 1992/93 is caused by anomalous thick ice rather than

---

[b] The specification of the sea ice transport changes here from km^{3}yr^{-1} to km^{3}month^{-1} because the observations of *Vinje et al.* [1998] and *Kwok and Rothrock* [1999], which form the basis of the evaluation of the modelled transports, are given in km^{3}month^{-1}.

drift speed variations. Hence, the deviations between modelled and observed export anomaly in this particular winter may be due to a mismatch between the assumed cross-strait ice thickness profile of *Vinje et al.* [1998] and the true thickness distribution.

On the contrary, observed and modelled estimates of the extreme positive export anomaly of the winter 1994/95 agree quite well despite the deviations in upstream drift pattern between models and observations. This is even more obvious when flux anomalies are derived as a fraction of the respective mean flux of each data set (Figure 3.12b). Despite its comparatively small mean ice volume export the UW model features the strongest anomalies followed by the AWI and NPS results. In this representation the export anomaly of 1994/95 confirms its outstanding character being the only event for which almost all data sets feature a departure of more than 200% (up to 300%, UW) from the individual mean export. This representation of the anomaly data emphasises on the one hand that the absolute values of the anomalies are partly due to differences in the main variables of the model, like drift speed and ice thickness, and on the other hand that the models react differently on changes in the atmospheric forcing, which basically drives these anomalies.

3.7.2   Causes of export variability

Decomposition of export anomalies

In order to access the relevant causes of the variability of the Fram Strait sea ice volume export *Arfeuille et al.* [2000] suggested to apply *O. Reynolds*' method of temporal averaging for velocity fields. This means that the ice transport, which is represented by the product of mean ice thickness h and drift speed u in the following, is decomposed into a mean flux component and anomalies

$$hu = \overline{hu} + (hu)' . \tag{3.5}$$

Furthermore, the method allows to express the flux anomalies $(hu)'$ in terms of means and anomalies of its components ($h = \bar{h} + h'$ and $u = \bar{u} + u'$):

$$(hu)' = hu - \overline{hu} = \underbrace{h'\bar{u}}_{I} + \underbrace{\bar{h}u'}_{II} + \underbrace{h'u'}_{III} - \underbrace{\overline{h'u'}}_{IV} . \tag{3.6}$$

The four numbered terms in Equation (3.6) are listed in descending order of their contribution to the overall anomalies. While the first two terms are most and equally important the third term ($h'u'$) has a comparatively small magnitude though it is not negligible. *Arfeuille et al.* [2000] stated that term IV in contrast is negligible small amounting to only 1% of the overall mean of the transport ($\overline{hu}$). In the case of the AOMIP experiments, this limit holds only for the
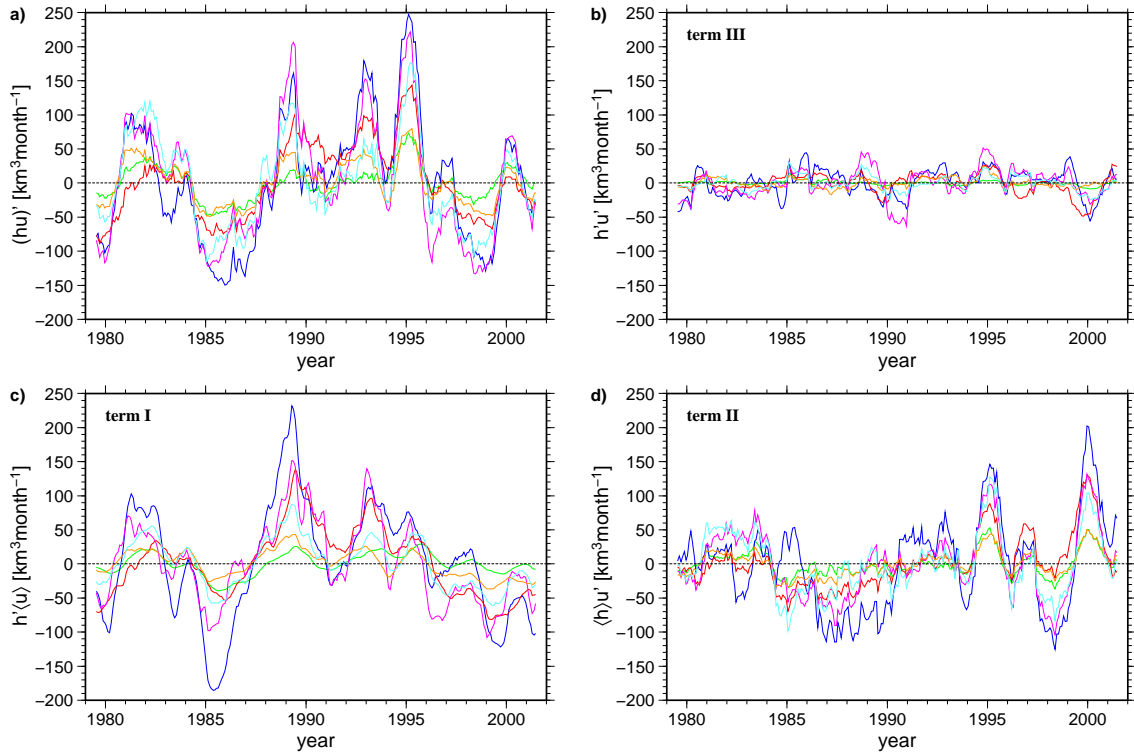
Figure 3.13: Decomposition of (**a**) Fram Strait sea ice volume export anomalies $(hu)'$ into (**b**)–(**d**) contributions from mean thickness $h = \bar{h} + h'$ and drift speed $u = \bar{u} + u'$ according to Equation (3.6). For colour coding please refer to legend in Figure 3.11; remark on annotations: $\langle h \rangle = \bar{h}$ and $\langle u \rangle = \bar{u}$.

GSFC (0.3%) and NPS (1.2%) models. Larger values are found for the AWI (3.4%), SIM (3.6%), IOS (6.1%) and UW (14.2%) results. Term IV directly relates to the correlation of the thickness (h') and drift speed anomalies (u'). These correlation coefficients ($r(h', u')$) are weak as expected and range between -0.22 (IOS) and 0.36 (UW). The defined relationship between $r(h', u')$ and term IV increases its quality from a correlation of 0.966 to 0.995 when IOS and NPS are excluded, which are the only models that have a negative correlation, i.e. $r(h', u') < 0$. This supports the grouping of the models which is made based upon the differences in the drift speed frequency distributions of Section 3.4.

The overall anomalies of the Fram Strait ice export ($(hu)'$) and the terms I, II and III of Equation (3.6) are presented in Figure 3.13 for the AOMIP models and the SIM experiment. The individual mean annual cycle, which is obvious in Figure 3.11b, is subtracted from each data set for clarity. Additionally, a running mean with an averaging interval of 13 data points is applied without reducing the monthly resolution of the data. The interval is twice as large as the integral time scale of the data sets which is derived from the integrated autocorrelation function [see *Emery and Thomson*, 2001]. The procedure allows to decorrelate each time series and to identify distinct and outstanding export anomalies of

the investigated period 1979–2001 (see Figure 3.13). However, the various products of ice thickness and drift speed relating to Equation (3.6) are computed prior to the filtering procedure.

First of all the simulation results presented agree on the chronology and number of occurrence of extreme positive or negative export anomalies (Figure 3.13a). Obviously, this is not affected by the deviations in drift velocity discussed above. Large export rates are found for the winter seasons 1988/89, 1992/93 and 1994/95, where the latter marks the overall maximum of the investigated period in all studied data sets. Negative anomalies are less distinct and the most prominent are found during the periods 1985–87 and 1997–99.

Figure 3.13b suggests that the magnitude of the product of the ice thickness and drift speed anomalies ($h'u'$) is comparatively small, and thus this term is not further discussed here. The part of the export anomalies which is due to variations in the ice thickness ($h'\bar{u}$) is most dominant in the 1980's and culminates in the export maximum of the winter 1988/89 (see Figure 3.13c). After this event and throughout the 1990s the Fram Strait ice export includes a signal originating from the overall negative trend of sea ice thickness in the Arctic Ocean. While the ice thickness decreases the influence of the drift speed anomalies on the Fram Strait ice flux strengthens in the 1990s. Prior to this period the contribution of term II varies largely between models and its value is comparatively small depending on the model (see Figure 3.13d). In the second half of the 1990s the drift anomalies of all models together change into a much more distinct pattern of undulation. Moreover, term II has an increasing amplitude with each cycle in IOS, NPS and SIM models.

Beside the natural variability within each time series the values of the decomposed terms deviate according to the observed differences between the particular models. Model differences are present not only in drift speed but also in mean ice thickness. The respective average values in the Fram Strait

model	$\bar{h}$ [m]	$\bar{u}$ [cm s^{-1}]
AWI	1.67	6.6
GSFC	1.50	3.9
IOS	1.74	10.3
NPS	1.38	12.3
UW	1.09	5.3
SIM	1.72	6.2

Table 3.5: Average values of the mean ice thickness ($\bar{h}$) and drift speed ($\bar{u}$) in the Fram Strait for the period 1979–2001.

region of the period 1979–2001 are listed in Table 3.5 for all models included in Figure 3.13. The differences reflect mainly those already known from Table 3.1, where Arctic-wide mean ice thicknesses are shown, and Figure 3.3, which suggests the differentiation between two groups of drift speed distribution. Regarding the mean ice thickness it should be stated that AWI and GSFC feature larger thicknesses in Fram Strait compared to the overall means of Table 3.1 while all other AOMIP models have thinner ice in this region. The strongest variations in ice thickness (h') in the Fram Strait during the investigated period are found for the AWI results and also the variability of the GSFC ice thickness is stronger than estimated from term I. Both are damped by the smaller average drift speed ($\bar{u}$) while the ice thickness of the IOS model, which is already strongly undulating, is further amplified by the large mean drift speed. The mean drift speeds in the Fram Strait exceed the modal velocities found for the internal Arctic by 2–4 cm s^{-1}. The ice drift in the Fram Strait is mainly driven by the wind [*Schröder*, 2005], which in turn is due to a dominant pressure gradient between Greenland and Svalbard. This is by AOMIP definitions the same for all models. The sea ice flux is also guided by topography and the relatively close coastlines make the internal forces the second largest term in the momentum balance [*Schröder*, 2005]. Furthermore, the ocean currents are an important contributor to the sea ice momentum balance in this region [*Schröder*, 2005], an aspect which is underrepresented in many studies. The differences in ice-ocean stress between the models (see Section 3.6.2) are interpreted as an additional cause of ice volume export differences. However, the export results split into the same two groups as with the Arctic-wide drift speed. Interestingly, the results of the ice-ocean coupled AWI model tend towards larger drift speeds in the second half of the 1990s whereas the drift speed anomalies of the SIM experiment stay within the range typical for the first group of models.

Regression analysis

The dominant cause of the individual ice export event changed from thicker ice to larger drift speeds during the 1990s. While the export event of 1988/89 was clearly caused by an ice thickness anomaly the positive export anomaly of the winters 1992/93 and 1994/95 were due to a combination of both, increased ice thickness and strong southerly drift. The contribution of ice drift was more dominant in the peak of 1993/94. The ice export of the winter 1999/2000 could have been a new maximum if the effect of the great drift speed anomaly would not have been dampened by a negative ice thickness anomaly during this period.

A correlation analysis is performed based upon a linear regression model for the time series of the ice volume flux, ice thickness and drift speed in Fram Strait
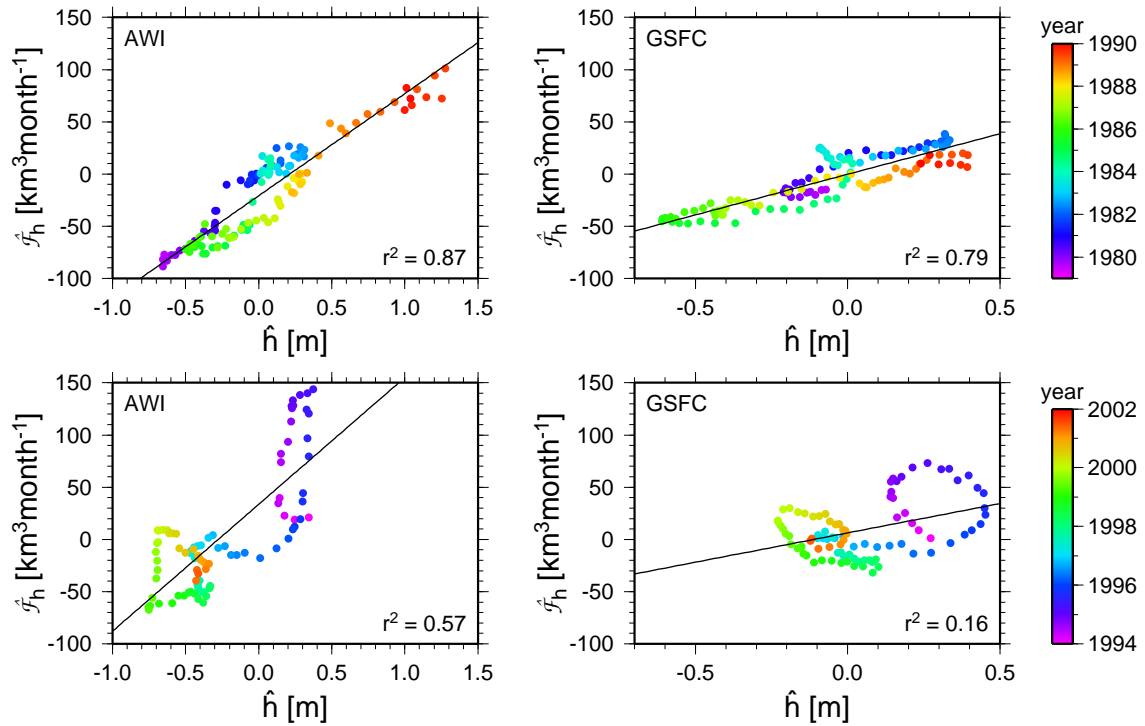
Figure 3.14: Scatter plots of filtered ice thickness ($\hat{h}$) and ice volume flux ($\hat{\mathcal{F}}_h$) through Fram Strait for (**upper row**) the time period 1979–1989 and (**lower row**) 1994–2001 for (**left**) the AWI model and (**right**) the GSFC model. The colour scale at the very right indicates the corresponding date of each data point and relates to both panels of the respective row. Black lines represent linear regressions for which squared correlation coefficients (r^2) are given. Regard that abscissa scaling changes between models.

for all five AOMIP models and the SIM experiment in order to statistically substantiate the above observations. Therefore, the individual annual cycle is subtracted from the time series and a 13 point running mean is applied by analogy

| time | $r^2(\hat{h}, \hat{\mathcal{F}}_h)$ | | $\mathrm{P}(r^2(\hat{h}, \hat{\mathcal{F}}_h))$ | | $r^2(\hat{u}, \hat{\mathcal{F}}_h)$ | | $\mathrm{P}(r^2(\hat{u}, \hat{\mathcal{F}}_h))$ | |
period	mean	std	$(r_l)^2$	$(r_u)^2$	mean	std	$(r_l)^2$	$(r_u)^2$
1979–1989	0.80	0.04	0.73	0.86	0.45	0.32	0.37	0.54
1990–1993	0.52	0.18	0.32	0.69	0.37	0.28	0.21	0.55
1994–2001	0.48	0.19	0.34	0.61	0.62	0.24	0.50	0.72

Table 3.6: Squared correlation coefficients r^2 of linear regression analysis for Fram Strait ice volume exports ($\hat{\mathcal{F}}_h$) are listed. The influence of the ice thickness ($\hat{h}$) and drift speed ($\hat{u}$) is investigated and means composed of results from all AOMIP models and the SIM experiment are displayed together with the respective standard deviation (std). Additionally, the confidence interval $\mathrm{P}(r_l < r_{true} < r_u) = 0.95$ is indicated by listing lower (r_l) and upper bound (r_u) squared correlation coefficients corresponding to the r^2 values.
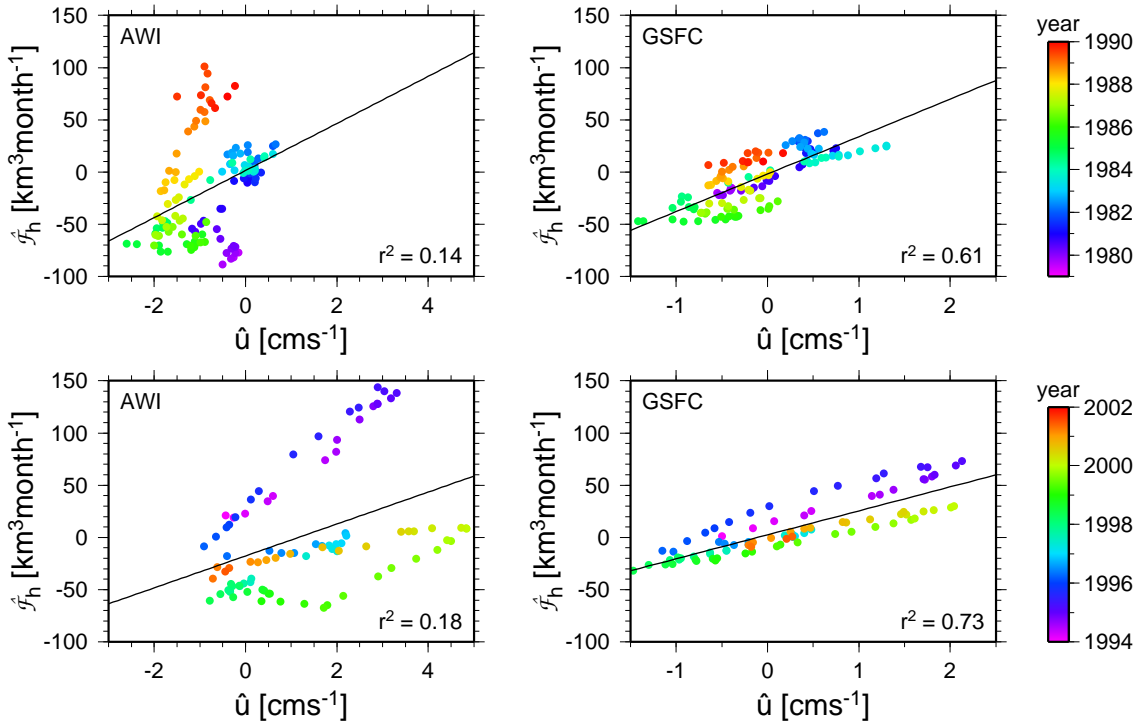
Figure 3.15: Scatter plots of filtered ice drift speed ($\hat{u}$) and ice volume flux ($\hat{\mathcal{F}}_h$) corresponding to Figure 3.14 are shown.

with the treatment of the flux anomalies in Figure 3.13. In order to distinguish between the original and processed data sets variables of the latter are marked with a ˆ (e.g. $\hat{h}$) in the following. Furthermore, the time series are split into three periods 1979–1989, 1990–1993 and 1994–2001. It is expected that the ice thickness explains most of the variance of the ice transport during the first period and the ice drift most during the last one. No clear dominance should be found for the short period of 1990-1993. Correlation coefficients r are computed separately for relationships between ice thickness $\hat{h}$ and drift speed $\hat{u}$, respectively, and ice export through the Fram Strait $\hat{\mathcal{F}}$ for all six data sets and three time periods. In Table 3.6 the squared correlation coefficients r^2 and explained variances ($r^2 \cdot 100\%$), respectively, are presented as averages of all six models for the respective time period. The standard deviation of each mean value is given to indicate the variability of the correlation coefficients among the different model data sets. A good estimator of the quality of the correlation coefficients r is the confidence interval $P(r_l < r_{true} < r_u) = 1 - \alpha$ which is derived for a defined level of significance α [*Emery and Thomson*, 2001]. Here, the calculations of r_l and r_u follow [*Storch and Zwiers*, 2001, Equ. 8.4–8.6] and include a z-transformation after *R. A. Fisher* to ensure normal distribution of the data. A significance level of $Si = 95\%$, i.e. $\alpha = 0.05$, is chosen.

The values presented in Table 3.6 support the expected relationships. The correlation between the ice thickness and the ice volume flux is most signifi-

cant during the period 1979–1989 and decreases strongly for both of the subsequent periods. The behaviour of the standard deviations remarkably coincides to that of the average correlation coefficient, i.e. the differences in correlation of ice thickness and flux between the models increases with decreasing mean correlation of $\hat{h}$ and $\hat{\mathcal{F}}_h$. The mean and standard deviation of the correlation of drift speed and ice flux evolve oppositely within the entire investigated period. Though the correlation of drift speed and ice transport ($r^2(\hat{u}, \hat{\mathcal{F}}_h)$) is larger than that of ice thickness and flux during the last period 1994–2001 it does not become as strong as that of ice thickness and flux ($r^2(\hat{h}, \hat{\mathcal{F}}_h)$) during the first period 1979–1989. The standard deviations of $r^2(\hat{u}, \hat{\mathcal{F}}_h)$ are larger than those of $r^2(\hat{h}, \hat{\mathcal{F}}_h)$ throughout all time periods. The middle period 1990–1993 is characterised by the largest range of the confidence interval. This reflects the small sample size of this short time period in which the dominant factor of the ice volume flux changes from ice thickness to drift.

The above correlation analysis is based upon the assumption that linear relationships between ice thickness and drift speed, respectively, and ice export exist. Figures 3.14 and 3.15 show scatter plots of the related variables together with the corresponding linear regression and illustrate the effect non-linear relationships have to the regression. The graphs help to explain the varying intensity of the particular correlations $r^2(\hat{u}, \hat{\mathcal{F}}_h)$ and $r^2(\hat{h}, \hat{\mathcal{F}}_h)$. For the following comparison the AWI and GSFC models are chosen because AWI is the only data set among the AOMIP results in which $r^2(\hat{h}, \hat{\mathcal{F}}_h) > r^2(\hat{u}, \hat{\mathcal{F}}_h)$ for all three time periods. The GSFC data meet the expectations best as this model exhibits the strongest change in correlation from a dominance of ice thickness anomalies to drift speed anomalies between the first and third time period. As can be seen from the two top panels of Figure 3.14 ice thickness and volume flux form clear linear data distributions for both models in the first period, 1989–1989, with large explained variances of 87% and 79%. Both models show a less linear relationship between ice thickness and flux for the third period. More explicitly, two cycles of increase and subsequent decrease in ice flux are present in Figure 3.14 (bottom row) that have rather a circular shape than following linearity in the space spanned by $\hat{h}$ and $\hat{\mathcal{F}}_h$. These diverging branches of the hystereses lead to an increase in variance and thus a decrease in correlation. The divergence of the branches is due to the increased influence of the drift speed, which has larger anomalies during the third period than during the first one (see Figure 3.13d).

As stated above the AWI model has the strongest variability in ice thickness. This has an important effect on the distribution of the data in the $\hat{h}$-$\hat{\mathcal{F}}_h$-space shown in Figure 3.15. While the GSFC model has a comparatively clear alignment of the drift speed variations along the regression line the AWI model features three and two single linear branches/hystereses for the periods 1979–1989

and 1994–2001 respectively. These branches differ in slope angle but are treated together in a composed data set for the derivation of the values presented in Table 3.6. Thus, the different slopes cause a larger departure from the linear model as when treated independently. Therefore, the linear regression analysis results in a poor correlation of drift speed and ice flux particularly of the AWI data in all investigated time periods. The temporal integration of the monthly data leads to trajectories in the $\hat{h}$-$\hat{\mathcal{F}}_h$-space and $\hat{u}$-$\hat{\mathcal{F}}_h$-space which puts the simple linear statistical relationship on which the regression is based into question.

Interpretation of export variability

The observed regime change from an ice thickness to a drift speed dominated ice volume export between the 1980s and '90s coincides with an increase in ice export magnitude. This finding is consistent with the model study of *Zhang et al.* [2000], who found a Fram Strait ice volume export amplification of 23% between the periods 1979–1988 and 1989–1996. For comparison, the AOMIP models range between 19% (GSFC, NPS) and 48% (AWI, which almost lacks the positive anomaly of 1980–1982). A reason for the aligned pattern of the various term II estimates in the 1990s is given by a strengthening of the link between the air pressure field and the ice flux in Fram Strait. In general about 60% of the effective flux is explained by the pressure gradient between Greenland, which is characterised by strong and constant high pressure, and Svalbard, which is located at the edge of the low pressure field formed by cyclones entering the Arctic from the North Atlantic [*Vinje*, 2001]. *Walsh et al.* [1996] reported a decrease of the Arctic-wide sea level pressure between the 1980s and '90s . The cyclone intensity reaches its maximum of the period 1950–2000 in 1989/90 and cyclones from the North Atlantic advance farther into the Arctic via Norwegian and Barents seas during the 1990s than in the previous decade [*Zhang et al.*, 2004]. This causes an intensified pressure gradient between Svalbard and Greenland and provides a strong and direct forcing of the Fram Strait ice export that is included in the atmospheric forcing of all models investigated here. *Brümmer et al.* [2001] stated that cyclones can cause an increase in Fram Strait ice export by up to 50% of the average transport.

These changes in the atmospheric pattern are one part that leads to a more prominent influence of the ice drift on the ice flux through Fram Strait. Another important reason is the decrease in ice thickness observable in the time series of term I from 1989 onwards accompanying the atmospheric changes. The thinner ice may cause a more frequent occurrence of free drift conditions in the Fram Strait. This is an essential prerequisite for the strong influence of the wind on the ice drift.

However, the differences in Arctic-wide sea ice drift pattern described in Sec-

tion 3.5 imply that incorrect regions of the Arctic Ocean could feed the Fram Strait ice export in the models. This has an effect not only on the export rate of ice volume itself but also on the age distribution of the Arctic sea ice and palaeodata studies. The latter apply backward trajectory calculations of sediment transport with the ice and wrong drift patterns may lead to a false interpretation of the sediment's source region. During the investigated period 1979–2001 the amount of multi-year ice has decreased dramatically in the Arctic. The results of the model study of *Lindsay and Zhang* [2005] imply a fundamental regime change of Arctic sea ice thickness evolution since the end of the 1980s, which is caused by different factors: surface air temperature increase, shift in atmospheric pressure patterns and a change in the oceanic heat balance. Observations show that the occurrence of ice older than 10 years, which has been common in the western Arctic prior to the 1990s, is diminished mainly in the Beaufort Gyre and central Arctic Ocean while it is persistent north of Greenland and the Canadian Archipelago [*Rigor and Wallace*, 2004; *Belchansky et al.*, 2005]. *Belchansky et al.* [2005] further state that the ice motion plays a major role in the distribution and long-term survival of the ice. Mismatches in drift pattern may thus lead to a different age topology of the ice in the models as compared to observations. For example the coupled sea ice-ocean models feature strong ice drift north of Greenland and the Canadian Archipelago in winter 1994/95 (Figure 3.8)—stronger than observed (compare Figure 3.1). This difference may result in an increased retreat of the multi-year ice in these models. An acceleration of the spatial redistribution of this old and thick ice affects not only the composition of the ice in various Arctic sub-regions but also the Fram Strait sea ice export.

3.8 Summary

The comparison of five plus two data sets of Arctic sea ice drift derived from mainly sea ice-ocean coupled models yields significant differences. Two additional independent observational data sets of comparable horizontal resolution and data density helped to evaluate the reliability of the simulated drift fields. Despite very similar experimental settings and coupled sea ice-ocean models that represent the state-of-the-art, two categories of sea ice drift speeds among the results are found: one with a well pronounced, lower modal speed, matching the observations best, and a second with a more even speed distribution featuring also higher drift speeds. Additional investigations of the Arctic-wide drift pattern in two different cases revealed the complexity of the differences between models themselves and the various causes of these differences. Though all models show equal patterns of drift difference between two wind-driven drift

regimes the sensitivity of the models to anomalous atmospheric forcing differs. Large deviations between the models themselves and compared to the observations occurred in the anomalous winter of 1994/95. These differences can not be assigned to the different speed classes and have various reasons.

The Fram Strait sea ice export is studied as an example for the implications of the observed differences between models. It can be concluded that the deviations in drift speed result not only in different sea ice thicknesses but also directly affect the ice export though the ice flux through Fram Strait is strictly connected to the sea level pressure gradient. However, the different export rates do not hinder the models to represent the observed export anomalies well and all models are bound to the same mechanisms causing the flux variations. Moreover, a regime change in the dominance of the Fram Strait ice volume export from ice thickness towards drift speed is found for the early 1990.

Taking individual model parameters into account, no clear consistency or explanation for the differences between the model results is found. Still, owing to the model physics, the most plausible reason lies in the different effective wind stress forcing and in the coupling with the ocean. Besides the coupling mechanism itself, which controls the intensity of the effect that the ocean has on the ice, the different ocean velocities of the models are found to cause some of the observed differences in ice drift pattern. A strong ocean influence on the ice drift coincides most often, though not always, with a weak wind stress forcing. The calculation of the transfer of momentum from the atmosphere to the ice is critical to the sea ice drift. Furthermore, the numerical implementation of the model physics often differs and the resulting sea ice drift, concentration and thickness are definitely sensitive to the implementation.

Finally, the uncoupled sea ice model, which will be applied later for the validation of ridging modules in the present study, is found to perform very well compared to the coupled models and observations. It is found to be a tool of good quality to investigate new numerical approaches on physical processes related to sea ice dynamics like ridging.

Part II

Observations of Pressure Ridges
or: Both sides of the story

Chapter 4

Airborne Laser and Electromagnetic Measurements

4.1 Introduction

Obtaining numerous observations that reflect the typical characteristics of a medium under investigation, e.g. sea ice in this case, is valuable not only for a detailed analysis but is also a prerequisite for numerical modelling. Such data include the helicopter-borne laser altimeter and EM bird measurements performed by the Sea Ice Physics Group at the Alfred Wegener Institute in the Arctic since 1995 ([*C. Haas*, pers. comm.]). The data presented here were collected

Expedition	Region	Dates	Reference
ARK-XI/1	Laptev & Kara Seas	07–09/1995	**M**S, MS**R**
ARK-XII	Laptev & Kara Seas, TDS	07–09/1996	**M**S, MS**R**, **T**DS
SHEBA	Beaufort Sea	08–09/1998	**M**S, MS**R**
ARK-XVII/2	TDS	08–09/2001	**T**DS
ARK-XIX/1a*	Barents Sea	03/2003	**M**S, MS**R**
ARK-XIX/1b*	Fram Strait	04/2003	**F**S
GreenICE-04*	Lincoln Sea	05/2004	**L**S
ARK-XX/2*	Fram Strait, (TDS)	07–08/2004	**F**S
GreenICE-05*	Lincoln Sea	05/2005	**L**S

Table 4.1: Overview of the regions and dates of the expeditions during which laser altimeter measurements for ridge sail observations were carried out. The expeditions are grouped for the study (see Figure 4.1) and the corresponding abbreviations used in the text are listed in the right-hand column. Bold letters are used as symbols in figures. TDS denotes the Transpolar Drift Stream. Expeditions marked with an asterisk (*) are included in the ridge keel investigations.
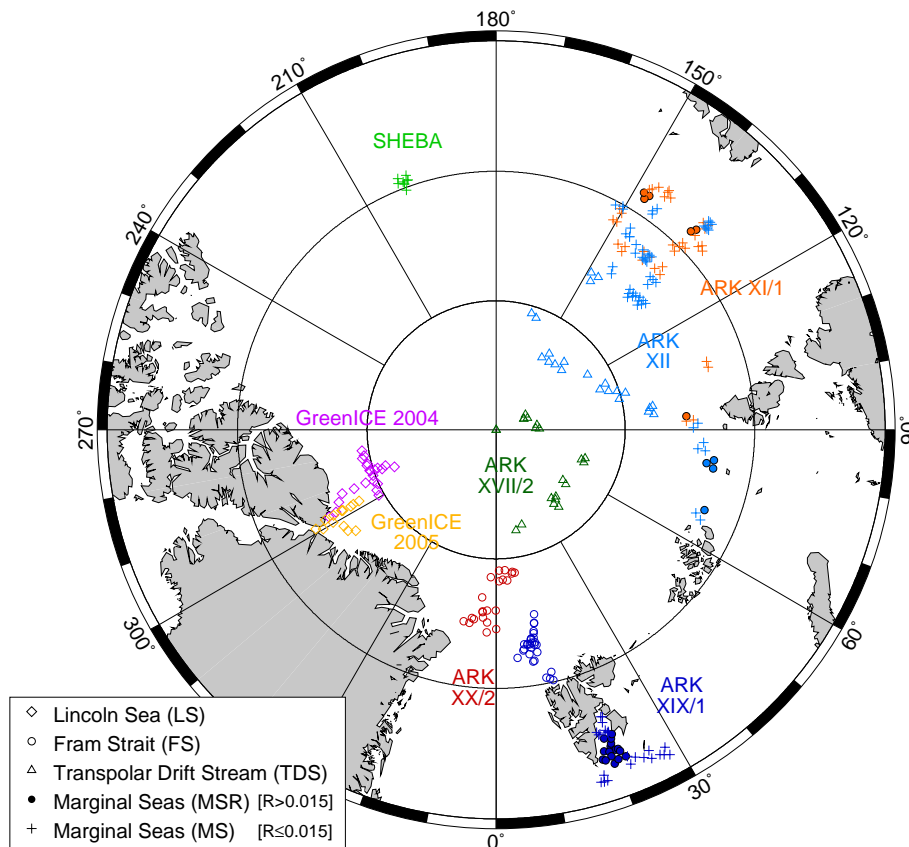
Figure 4.1: Overview of all profile locations included in this study. Expeditions are named and colour coded. Symbols refer to regions separated for the investigation. Abbreviations of region names are given in the legend. The ridge intensity R, a separation criterion, is defined in Equation (4.2).

during several expeditions, mainly using *RV Polarstern* as a research platform (these expeditions are named ARK[a]). A list of all expeditions, including those of the *Surface Heat Budget of the Arctic Ocean* experiment (SHEBA) and the *Greenlandic Arctic Shelf Ice and Climate Experiment* (GreenICE)[b], can be found in Table 4.1. Measurements have been taken over a large part of the Arctic Ocean within the last ten years (see Figure 4.1 for an overview). While most of the expeditions were undertaken during or directly after the melting season, the measurements of ARK-XIX/1 and GreenICE represent winter ice conditions, during which most of the deformation takes place. The Fram Strait region has been visited twice in summer and winter and thus will be used to investigate seasonal

---

[a] ARK stands for "Arktis", the German word for Arctic. For more information on particular ARK expeditions refer to the Reports on Polar and Marine Research of the Alfred Wegener Institute, Bremerhaven, Germany.

[b] All details about SHEBA are presented at http://sheba.apl.washington.edu. More information on GreenICE are given at http://www.greenice.org. An overview of the expeditions performed by the AWI Sea Ice Physics group can be found at http://www.awi.de/en/research/research_divisions/climate_science/sea_ice_physics.

differences.

Three campaigns have been carried out with the same instrument in the Baltic Sea in February and March of the years 2003, 2004 and 2005. These were part of the IRIS project mentioned in the introduction (Chapter 1). While most observations were made in the Bay of Bothnia, some flights in 2003 cover parts of the Finnish part of the Bothnian Sea and the Gulf of Finland. These data are used for comparison and will not be discussed in detail as the Arctic observations are.

The data were collected with two different laser altimeters. Both instruments will be introduced in Section 4.2 including a description of the pre-processing of the raw laser data. That section will provide an insight into the electromagnetic (EM) technique used to derive sea ice draft profiles and keel parameters as well as the measurements of total ice thickness. The latter in turn are used to derive level ice thicknesses, which give the baseline for calculating sail heights. The chapter continues with the statistical analysis of derived ridge parameters. Section 4.3 concentrates on the average values of ridge height and density. The spatial and frequency distributions of ridges in the Arctic are presented and regional differences outlined. Functional relationships between sails and keels are discussed in Section 4.4. Finally, the relation between sail height and level ice thickness, which is of particular interest to the modelling community, is investigated in Section 4.5. However, this chapter is not only meant to emphasise the main characteristics of the ridge measurements but also to present general relationships between ridge parameters that are useful for ridge modelling.

4.2   Instrumentation and data processing

The measurement campaigns prior to 2001 were carried out with a downward-looking laser altimeter *IBEO PS100E* mounted underneath a helicopter. The laser had a wavelength of 905 nm, a frequency of 2 kHz and measured the altitude with an accuracy of ± 3.0 cm. The helicopter speed was typically between 60 and 80 kn. The measurement point spacing of about 1.5–2 cm was later resampled to 15–20 cm for the freeboard calculations. The flight altitude of laser and helicopter ranged between 30 and 40 m. Typical flight patterns have a triangular shape with equal side lengths of 20–30 km. This allows the best compromise between the range of the helicopter and maximum area coverage of the measurements.

In 2001 during the expedition ARK-XVII/2 the so-called EM bird was introduced. The instrument, which is well known in geophysics, was redesigned to measure the sea ice thickness [*Haas*, 2004a]. The EM bird is a torpedo-like tube, and measures 3.4 m in length and 120 kg in weight. The bird is towed 20 m be-

neath a helicopter attached to a cord and flown at 10–15 m height. EM coils at the front and rear end of the bird are utilised to determine the distance between the instrument and the sea ice-ocean interface. Additionally, the bird contains a laser altimeter to measure the altitude of the instrument above the sea ice surface. This *Riegl LD90-3100HS* laser has a wavelength of 905 nm at a lower frequency of 100 Hz and a higher accuracy of ± 1.5 cm. Typical flight speeds and patterns were the same as for the older laser altimeter. The point spacing of only 30–40 cm resulting from the lower frequency is sufficient to derive ridge heights and spacing. Expedition ARK-XVII/2 marked the change of instruments from a single laser, which was used for 1/3 of the flights during this expedition, to the EM bird instrument.

The EM technique enables measurements of the distance between instrument and ice underside, because the saline seawater (mean salinity 34) is a good electrical conductor (2.5 S m^{-1}) compared to only $\sim$0.01 S m^{-1} for the rather fresh sea ice (salinity about 5). One coil in the EM bird produces an electromagnetic field which induces an electrical current in the sea water under the ice. This in turn leads to a weaker electromagnetic field received by a second coil in the bird. The strength of the received signal is found to depend mainly on the height of the instrument above the seawater. The laser altimeter raw-data are subtracted from the EM-derived height and the difference yields the in situ thickness of the ice and snow layer avoiding the need for laborious extraction of the helicopter's flight curve. The EM system works with a sampling frequency of 10 Hz and a sample spacing of 3–4 m is achieved. The coils with EM fields of frequencies 3.6 and 112 kHz, are mounted at the bow (transmitter) and tail (receiver) inside the tube, 2.77 and 2.05 m apart, respectively. The footprint of 10–20 m depends on the instruments altitude, which is determined by safety considerations. This footprint is rather large compared to the laser measurements. According to *Haas* [2004a] this footprint together with the porosity of ridges, which enables saline sea water infiltrate into the keel, result in an underestimation of the maximum draft of deformed floes of about 50%.

4.2.1 Freeboard derivation

The profiles recorded by the laser altimeters include not only the surface roughness of the sea ice but also the altitude variations of the helicopter. The latter varies at a much lower frequency than the surface roughness. Additionally the laser data contain noise and outliers that are caused by backscatter variations, false return signals from sun glint and open water, or both. In order to remove the helicopter movement and noise from the laser data the three-step filtering method of *Hibler* [1972] is applied.
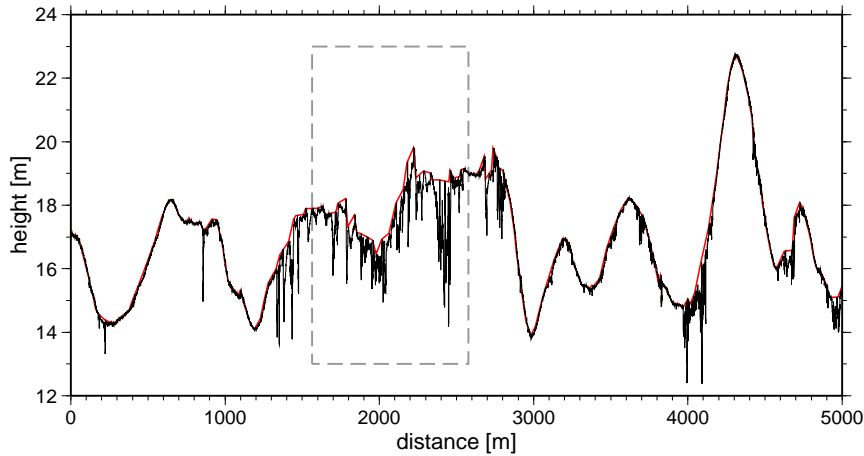
Figure 4.2: Height above ground as recorded by the laser altimeter (black) and helicopter movement (red) derived from the filtering procedure. The difference is the final sea ice surface elevation. The box outlined with a grey-dashed line marks the profile segment that is shown in Figure 4.3b.

In the first step the low frequency undulations of the flight altitude of the helicopter are eliminated by applying a non-recursive high-pass filter. The second step focuses on the detection of local minima in the high-pass filtered profile. These minima are allowed to have a distance of 10–50 m (in the Lincoln Sea 10–80 m) to each other. Their x-coordinates—the defined positions along the profile—are then stored together with the corresponding heights of the unfiltered data. At this point the filtering procedure is interrupted by the operator for assessment and manual correction of the automatically derived tie-points. This in-between step is necessary because sometimes changes in flight altitude apparently occur more abruptly than the filter routine is able to accommodate. Moreover, ridges are "stretched" in the laser profile as they are crossed at oblique angles during the flight. This leads to an overestimation of sail widths and to an undulation of lower frequency in the profile. Another difficulty is that the generated flight altitude profile under-cuts the original curve at turning points, which causes smooth artificial "bumps" in the final surface profile product and may also result in negative freeboard estimates.

In the third and last step the gaps between the stored tie-points are closed by linear interpolation and the resulting curve is low-pass filtered. This smoothed profile, viewed as the actual flight movement of the helicopter, is removed from the raw laser data in order to derive the surface roughness. The latter represents rather the elevation above the level ice surface of the thinnest ice along the profile than the actual freeboard. Figure 4.2 presents a 5 km long excerpt of a raw laser profile and the corresponding helicopter movement as derived by the filtering routine. The example shows the different undulations of the helicopter movement and sea ice surface roughness. It also shows the difficulties to de-
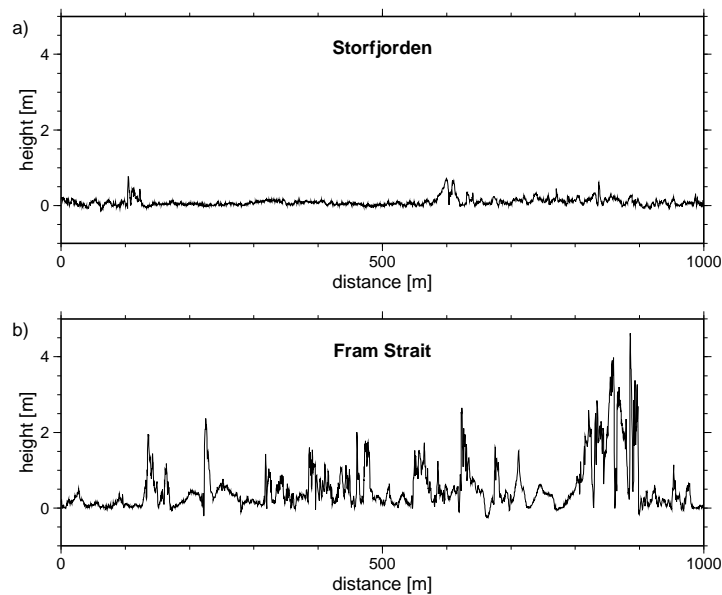
Figure 4.3: Typical surface profiles from March and April 2003: (**a**) in Storfjorden, where new, thin ice formed in polynya areas, and (**b**) in Fram Strait, where much thicker, partly multi-year ice has undergone heavy ridging.

tect the real helicopter curve in areas of heavily deformed sea ice. In these cases the final position of the flight curve depends on the judgement of the operator performing manual corrections.

The early altimeter data were recorded by allocating the height values to fiducial values, i.e. each sample is assigned to a sequential number. This makes it necessary to calculate true positions afterwards. Geographical positions were taken at the beginning and end of each flight leg. The positions were then calculated assuming a constant average flight speed along the straight legs. In 2001 the method changed with the introduction of the EM bird, which has a *Global Positioning System* (GPS) antenna on board, and the positions at each fiducial number is recorded.

Examples of the final freeboard product are presented in Figure 4.3. These two segments show distinct differences between various regions of the Arctic and different sea ice regimes. The profiles were recorded within the same season. The ice in Storfjorden is dominated by the production of new and thin ice covering refrozen polynyas. The profile presented clearly shows the small ridges at the edges of a refrozen lead (see Figure 4.3a, position 100–500 m). The lead ice is much smoother than the floes on both sides next to it, though these are also first-year ice. The mixture of first, second and multi-year ice in Fram Strait features more intense deformation and sails of up to 4 m height. In the following the automated detection of such ridges in the freeboard profile is described.

4.2.2 Ridge detection

The derived freeboard data are processed further to gain sail spacing, height and width. The spacing is the distance between two sail peaks. The actual width of the sail can not be derived reliably from the laser profiles, because the crossing angle is not recorded during the measurements. The ridge density is the number of ridges per km and is also referred to as ridge frequency in some studies. Along a defined profile it is given by the inverse mean spacing of that profile.

For the derivation of the sail quantities a routine selects local maximum values from the freeboard data. These maximum values are expected to be at least 10 m apart and must exceed a threshold, the cut-off height, to be stored. The cut-off height ensures that surface roughness features other than ridges, e.g. sastrugis (snowbanks), and noise do not effect the ridge calculations. Derived sail spacing and heights, however, depend on this threshold. *Hibler* [1975] and *Wadhams* [1980] discuss uncertainties in sail height frequency for sails below about 1.2 m resulting from different choices of cut-off height and applied statistical models, and found threshold values of 0.9–1.0 m to be most useful. *Dierking* [1995] investigated variations in mean sail height and average spacing for cut-off heights of 0.6–1.2 m. The mean sail height varied by up to 0.5 m and the average spacing by between 40 and 400 m. This large range depends on the spacing itself: in an area of high ridge frequency the spacing is very small and does not change as much with the cut-off height, because in clustered areas ridges often have almost the same height. *Dierking* [1995] chose a threshold of 0.8 m, which is also used here.

To ensure that a given maximum is a real sail peak and not part of a multiple peak ridge the stored maximum values are evaluated with the Rayleigh criterion [*Hibler*, 1975; *Williams et al.*, 1975; *Wadhams*, 1980; *Wadhams and Davy*, 1986]: The current maximum is compared to the neighbouring freeboard minimum values within a search radius of 20 m to either side of the maximum. If the maximum is twice as high as the deepest point of the neighbouring troughs its value and the corresponding position along the profile are stored as a sail peak. The positions of the minima are stored as left and right sail widths.

An additional comment has to be made on the recognition of leads in the profiles. The recent EM bird laser data do not allow differentiation between open water and thin, undeformed ice whereas the early single laser data gave the opportunity to calculate the open water fraction of a profile. For consistency the open water fraction is not considered in the laser data presented here, which has a particular effect on the sail spacing. Patches of open water are treated the same way as spacing between sails on a floe in the ridge detection algorithm. Thus, profiles that contain open water between floes have a lower ridge density than they would have with an ice concentration of 100% assuming the surface

roughness of the surrounding floes. One possible solution to the lack of open water classification due to the newer EM bird laser would be to use the older data of the single laser to generate an empirical algorithm for interpreting the newer data set. However, as the fraction of open water varies strongly in space and time, the early laser data can not be used to make assumptions about the fractions of open water in the recent EM bird laser data.

4.2.3   Differences of sail and keel detection

Ridges need not necessarily to consist of a sail and a keel (see Section 1.3). Ridges may occur without sails above the cut-off height or several sails may belong to one keel (and v.v.), particularly when keels are weathered. This complicates the modelling of ridges and especially the comparison of the model results with sail (laser) or keel (ULS, EM) measurements. The resulting ridge density will be affected most strongly. In order to illustrate the differences the 5 km long profile introduced in Figure 4.2 is shown with its total ice thickness—freeboard plus draft—in Figure 4.4.

Since the EM bird is used, sea ice surface and underside profiles are recorded at the same time. The parallel use of laser altimeter and EM coils allows both, measurement of the ice thickness as the difference between the two detected surfaces and differentiation between freeboard and draft of the ice floes. The calculation of the draft includes an averaging of the freeboard because the laser sampling rate is ten times higher than that of the EM technique. This down-sampled freeboard is presented as a black line of positive values in Figure 4.4. The figure includes the full freeboard, shown as a light grey line in the background in order to demonstrate the reduction in surface height. The sails, which are detected by applying the Rayleigh criterion over the full record, and their heights are marked with red triangles.

The draft is calculated by subtracting the down-sampled freeboard data from the EM thickness. This draft is plotted as a black line of negative values in Figure 4.4. In turn, the draft is used to detect keels in the profile and to derive their maximum depth using the sail detection algorithm (marked with red inverted triangles in Figure 4.4). Extensive coincident sampling of various sea ice thickness profiles using standard drill hole measurements showed that the EM measurements represent the level ice thickness well but underestimate the maximum draft of keels by 50–60% [*C. Haas*, pers. comm.]. Due to the integrating effect of the large footprint of the EM technique only level ice thickness is correctly represented. Thus, it is necessary to modify the Rayleigh criterion. The criterion implies that two ridges are independent of each other if the trough between them has half the freeboard (draft) of the larger peak [*Hibler*, 1975].
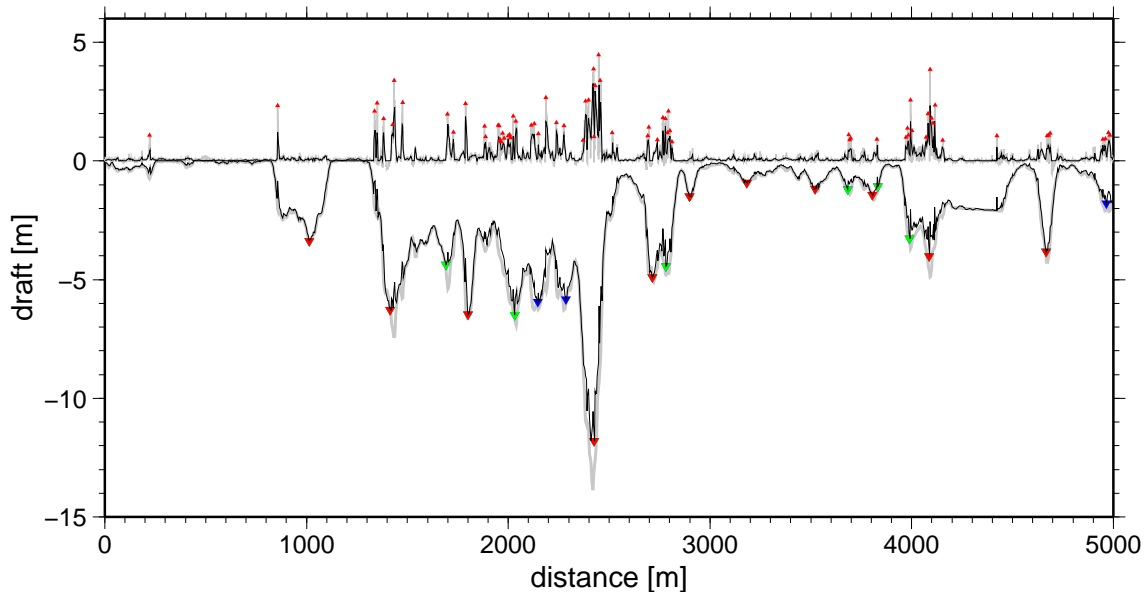
Figure 4.4: Sea ice thickness profile of the segment presented in Figure 4.2 combining coincident laser and EM observations. The total thickness (light grey line with negative values) is separated into freeboard (positive black) and draft (negative black). Sails (triangles) and keels (inverted triangles) are detected using the Rayleigh criterion. The colour coding of the keel markings reflects the different coefficients applied to the Rayleigh criterion (see main text).

Experiments were performed using a trough to peak draft ratio of 1/2, 1/3 and 1/4. The more the threshold is reduced the more keels are detected. These additional keels are marked in green (1/3) and blue (1/4), i.e. a threshold of 1/4 detects all keels marked in red, green and blue in Figure 4.4. As expected, the number of keels is still smaller than the number of sails along the same profile.

Williams et al. [1975] and more recently *Davis and Wadhams* [1995] suggested a cut-off depth of 5 m for keel detection, though *Davis and Wadhams* [1995] mentioned the use of 9 m in other studies. However, for the EM data the latter choice ignores too many keels as can be seen by considering the 5 km leg in Figure 4.4. In the present study, keel quantities are derived from ice underside profiles measured with the EM bird for the first time and tests are made with a cut-off depth of 3.2 and 5 m for these data. The first value is chosen according to the cut-off height for sails of 0.8 m assuming a sail height to keel depth ratio of 4 [*Timco and Burden,* 1997]. The ridge detection algorithm accounts for the underestimation of the maximum draft by a factor of 2 due to effects of the EM technique (see above): The original draft data were processed using half the cut-off depths mentioned above as threshold values. After all processing steps were finished the final keel depths were multiplied by a factor of 2. All keel depths presented in the next sections include this factor for two reasons: (1) easier comparison with other draft data sets and (2) direct applicability of the

results to the model approaches presented later in Chapters 6 and 8. For further investigations the results calculated using a Rayleigh ratio of 1/3 and a cut-off depth of 3.2 m are used. EM bird data from the last four expeditions listed in Table 4.1 are included in the keel-related investigations in this chapter. Hence, the data sets of the marginal sea regions MS and MSR are reduced to data only from the ARK-XIX/1a expedition to the Barents Sea in keel- and ice thickness-related results.

The processed data allow an extensive investigation of many interesting ridge parameters, although sail and keel widths, and thus any slope angle calculations, are excluded, because of the unknown crossing angle. Mean values and functional dependencies of sails, keels and level ice thickness are presented in the remaining part of this chapter.

4.2.4 Derivation of level ice thickness

Two possible ways of using the total ice thickness measured with the EM bird to derive the mean level ice thickness along a defined profile are investigated. Firstly, the modal thickness of a profile is interpreted as level ice thickness. This method, however, did not yield suitable results, i.e. a relationship between level
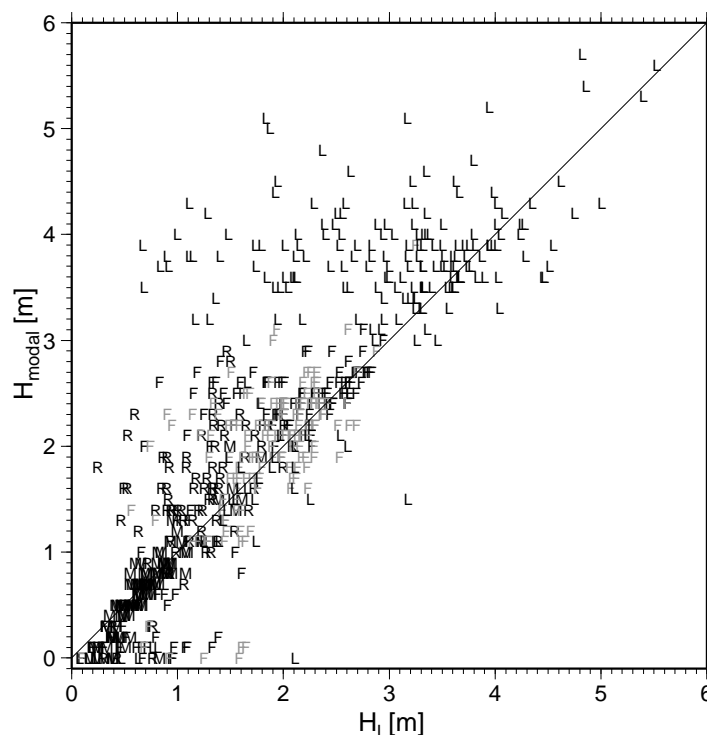
Figure 4.5: Modal ice thickness as a function of the mean level ice thickness $\bar{H}_l$ of 5 km long profile segments. Bins of 0.1 m are used to derive the modal thickness. Symbols indicate the affiliation of the profiles (refer to Table 4.1; Fram Strait profiles from ARK-XX/2 have grey symbols).

ice thickness and sail height was not detectable from the data, though, for example, the work of *Tucker et al.* [1984] and *Lensu* [2003a] show that such a relationship is very likely. Therefore, another approach for deriving the level ice thickness was applied. This approach is explained in more detail in the following and resulting regressions of sail height as a function of level ice thickness are presented in Section 4.5.

The second approach is to follow the definition of level ice proposed by *A. S. Thorndike* in *Wadhams and Horne* [1980]. A thickness measurement H at position x along the profile is regarded as level ice, if $H(x)$ meets the requirement

$$|H(x \pm d) - H(x)| \leq 0.1, \quad d \simeq 13m. \tag{4.1}$$

This means that each $H(x')$ within the range $x' = [x - d, x + d]$ has to fulfil this requirement. The algorithm had to be adapted to the different characteristics of the EM thickness data. Instead of a threshold of 0.25 m as proposed by *Wadhams and Horne* [1980] a value of 0.1 m is used. Although this is rather close to the resolution limit of the EM technique, a larger threshold would lead to a strong increase in derived level ice thickness. Deformation occurs where the ice is thinnest and weakest, respectively, and hence only thin level ice can be considered to be parent ice of ridges. Thermodynamic ice growth is limited to approximately 2.5–3 m in the Arctic by heat exchange coefficients (Section 1.2.2). Although some level ice thickness values exceed this nominal maximum—especially in the Lincoln Sea region (see Figure 4.5)—the overall average is only 1.87 m. The choice of d, which is set to 10 m in *Wadhams and Horne* [1980], depends on the actual spacing of the EM measurements which is usually 3–4 m. Here, a search radius of 4 measurement points x' to either side of x is applied to the algorithm of Equation (4.1) where each point of the profile is tested for level ice. If there are data gaps within these 4+4 points $H_l(x)$ is excluded from the calculation of the mean level ice thickness $\bar{H}_l$. The mean level ice thickness is derived for 5 km long sub-profiles.

A comparison of modal and level ice thickness derived from the same profile segments shows that the modal thickness tends to be larger than the mean level thickness $\bar{H}_l$ (see Figure 4.5). *Wadhams and Horne* [1980] state that the second method defined in Equation (4.1) may not detect all the level ice along a profile, but that all ice detected is level ice. The choice of a comparatively small threshold of 0.1 m in particular contributes to a level ice thickness which is biased towards smaller values. However, the second method turns out to be most useful for finding the possible parent ice thickness of the ridges which is expected to equal the thickness of the thin level ice found along a profile. The results are discussed in Section 4.5, where H_l refers to the mean value $\bar{H}_l$ for consistency with later model experiments.

4.3 Average ridge distributions

4.3.1 Regional characteristics

The different characteristics of deformed sea ice in several Arctic regions are expressed as ridge parameters averaged over 5–40 km, which was the typical flight leg length. Figure 4.3 shows the essential differences in ridge density and height between certain regions; in this case Storfjorden and Fram Strait. The large variability of the surface roughness on a scale of 100–1000 m is partly suppressed by defining the cut-off height. Additionally, the typical length of the helicopter flight legs represents the usual horizontal resolution of state-of-the-art Arctic-wide sea ice models (10–50 km). Thus, the mean ridge values are derived from entire flight legs, if not otherwise stated. The calculation of average sail heights and spacing not only gives access to the ridge density but also enables the calculation of a ridge intensity R. The latter is calculated as proposed by *Lewis et al.* [1993]

$$R = \frac{\langle H_s \rangle^2}{\langle \tilde{d}_s \rangle} \tag{4.2}$$

where $\langle H_s \rangle$ is the average sail height and $\langle \tilde{d}_s \rangle$ the mean spacing of the sails, which also defines the sail density $D_s = 1/\langle \tilde{d}_s \rangle$. In contrast to *Arya* [1973], who proposed the use of $\langle H_s \rangle$ rather than $\langle H_s \rangle^2$ in the above definition of R, Equation (4.2) emphasises the mean sail height. This chosen ridge intensity definition relates R to the thickness of ridged ice whereas *Arya* [1973] applies his definition of R directly to the calculation of the atmospheric form drag of ridges. The relation between R and the deformed ice thickness will be discussed in more detail together with the ridge model approaches in Chapter 6.

Figure 4.6 represents an overview of the spatial distribution of mean ridge density, height and intensity. The majority of the average sail densities are comparatively small with values of less than 10 sails per km. Ridges are generally more frequent in coastal zones or at the fast ice edge. This can not be concluded directly from the data presented in Figure 4.6a. However, the ridges found in the measurements were not necessarily formed where they were detected. The ridge density in the Lincoln Sea where a large area is covered with 20 and more sails per km is particularly high. A larger number of sails per km was found in 2003 at the outlet of Storfjorden. Inside Storfjorden and Nares Strait newly formed smooth sea ice was found covering refrozen polynyas. While the ridge density emphasises local effects, the sail height features a gradient from the marginal seas where sails are smaller than 1.2 m on average, through the central Arctic Ocean (1.2 to 1.5 m) to the Lincoln Sea with mean sail heights reaching 1.7 m (see Figure 4.6b). The TDS data itself show that this gradient is
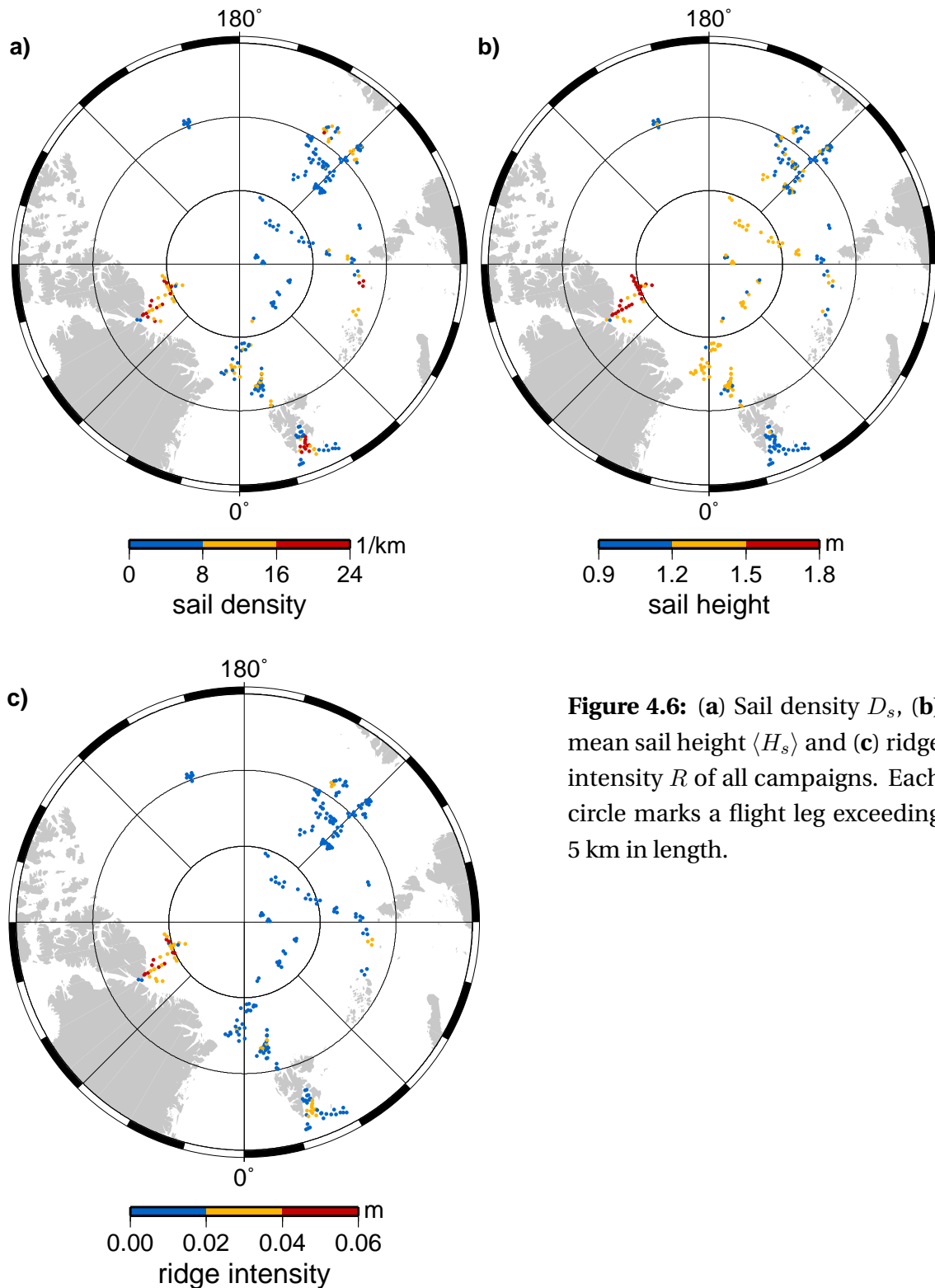
Figure 4.6: (**a**) Sail density D_s, (**b**) mean sail height $\langle H_s \rangle$ and (**c**) ridge intensity R of all campaigns. Each circle marks a flight leg exceeding 5 km in length.

persistent even within the grouped data sets [see *Schuster and Haas*, 2002, Fig. 30]. Besides location the threshold of 1.2 m in sail height is used to separate TDS and MS data sets (compare Figure 4.1).

Though the ridge intensity has a stronger dependence on sail height than on sail density by definition its spatial distribution shown in Figure 4.6c has more in common with the sail density distribution because the order of magnitude
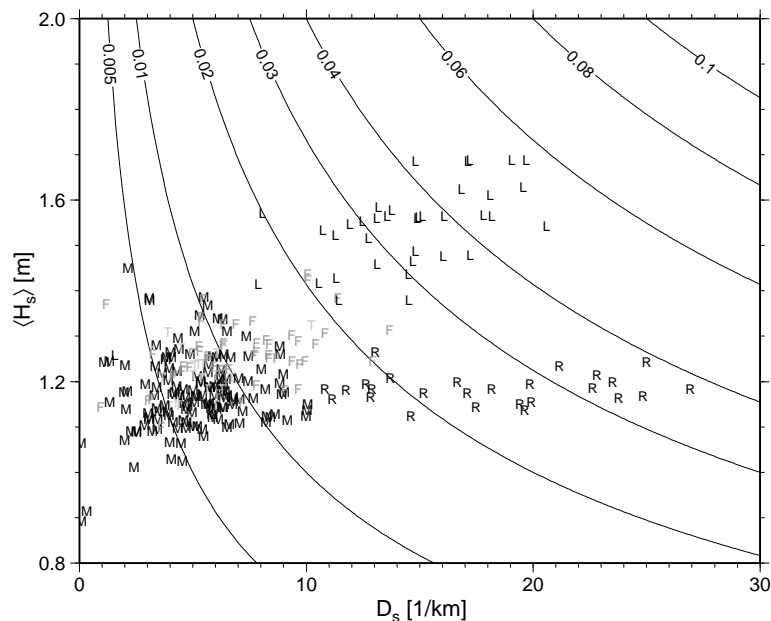
Figure 4.7: Mean sail height $\langle H_s \rangle$ as a function of sail density D_s. The contour lines give intervals of ridge intensity R in metres. Flight legs longer than 5 km are considered and each is marked according to Table 4.1. Grey shading of symbols is only used for clarity.

of the variations of sail density (10 km^{-1}) is greater than that of sail height variations (0.1 m). The ridge intensity emphasises the most interesting areas, for example a tongue of heavily ridged second-year ice at the edge of the Storfjord and the Lincoln Sea region where the most deformed ice of all the data presented here is found. Because ridge intensity marks areas of strong deformation a threshold of $R = 0.015$ m is used to separate data from the marginal seas into less deformed (MS) and heavily ridged sea ice (MSR) (compare Figure 4.1).

Another impression of the distribution of these mean values is seen in Figure 4.7, where sail heights are shown as a function of sail density. Most obvious is the two-branch structure of the graph. A cloud is formed by scattered values with sail densities between 3 and 10 per km and mean heights between 1.05–1.35 m. From this centre one branch extends with an almost constant mean sail height of 1.1–1.2 m towards densities of up to 27 per km. This branch consists exclusively of the MSR profiles from the Barents, Laptev and Kara seas and exhibits a ridge intensity larger than 0.015 m (see Figure 4.1). The second branch is formed exclusively by values from the Lincoln Sea. In this region, north of Greenland and the Canadian archipelago, one expects the most intense ridging because the sea ice is forced towards this coastline with the prevalent Arctic sea ice drift field (Figure 1.6). A special focus is placed on these two branches and their corresponding geographical regions in the comparison of modelling results with the laser measurements in Section 8.3.

Isolines of ridge intensity have been added to the graph. Another possible

100

way of grouping Arctic sea ice roughness data utilises three different categories of ridge intensity: $R \leq 0.02$ m, $0.02m < R \leq 0.04$ m and $R > 0.04$ m. It is shown in Figure 4.6c that most flight legs are characterised by the lowest ridge intensity category. Though these are mainly found in the central Arctic they are also present in the marginal seas. The middle category is not only found in the Lincoln Sea but also at distinct places where heavy ridging is restricted to local effects as in the outlet of Storfjorden. Only flight legs from the Lincoln Sea have values greater than 0.04 m and hence form the third category.

4.3.2 Sail and keel frequency distributions

The frequency distributions of sail and keel density and of height and depth show strong regional differences and are therefore presented in groups reflecting differences in location, sail height and ridge intensity (see above).

Sails The frequency distributions of sail density in the marginal seas (MS) and TDS areas are similar (Figure 4.8a). Both regions exhibit a strong mode at 3–5 sails per km. The sail density distribution in the Fram Strait (FS) matches these characteristics, though the curve is shifted towards higher densities. The distributions of the rough areas in the marginal seas (MSR) and Lincoln Sea (LS) are different. Their structure is nonuniform and multi-modal. Both have modes in the range of 11–15 sails per km and in the MSR additionally at 21 and 30 per km. Thus, the heavily deformed ice in the MSR exceeds the LS densities, which were expected to have the highest number of ridges per km. It is remarkable that the MSR and LS do not have ridge densities smaller than 7 per km. The overlap of these two regions with the MS, TDS and FS distributions is very small. It should be noticed that the MSR data feature up to ten times more ridges per km than the MS data, which are deduced from the same geographical region but originate from different locations with diverse local characteristics (e.g. open sea and coastlines).

The sail height distributions are consistent between the MS and MSR data sets (Figure 4.8b) and hence are independent of the ridge density, which differs markedly between MS and MSR data. TDS and FS sail height distributions are also similar, which is possibly due to the fact that the latter region is mainly supplied by the TDS, and furthermore, ridges found in the FS have formed within the TDS. The distribution of sail heights in the Lincoln Sea is different as large sails exceeding 2 or 3 m are found three times more often here than in any other study area. This is also evident in the overall mean and even more so in the mean of the largest 10% of all sails of each of the five separate regions (see Table 4.2). While four of the Arctic regions are close in their overall mean values of 1.16–1.28 m, the Lincoln Sea features larger sails with an average of 1.55 m,
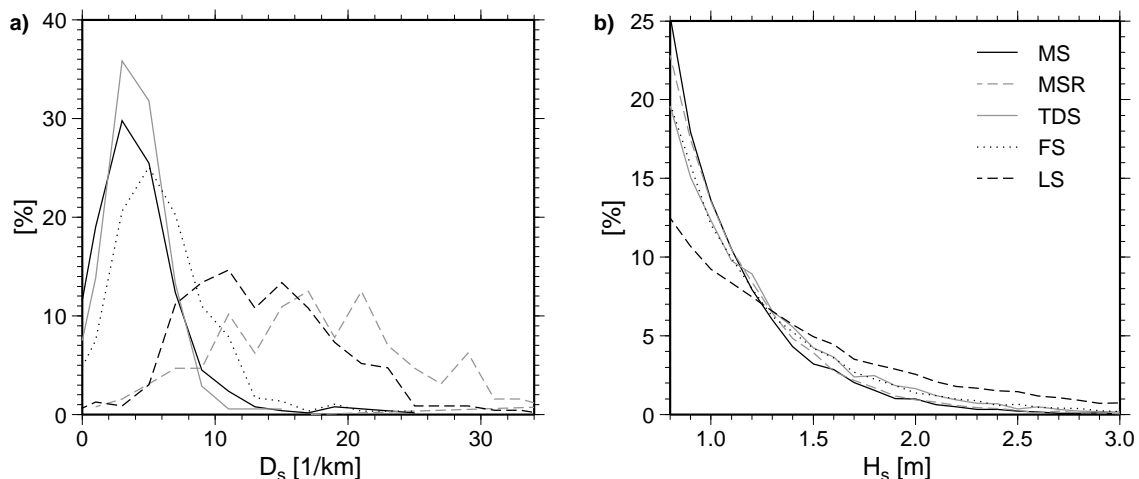
Figure 4.8: (**a**) Histograms of sail density D_s calculated from approximately 5 km long segments of all flight legs. (**b**) Distributions of sail height H_s of all available ridges. Each line represents one of the separate regions (see legend and Table 4.1). Legend in (b) holds for both figures. Percentage values of the ordinate correspond to histogram bins along the abscissa with a bin width of (a) 1 km^{-1} and (b) 0.1 m beginning at 0 km^{-1} and 0.8 m respectively. Lines of linear interpolation between bin values are shown instead of stairs-step diagrams for clarity.

compared to only 1.06 m in the Baltic[c]. Only first-year ice in the Barents Sea is found to be close to this Baltic value. However, focussing on the largest sails found in these regions, the differences increase and a range of 1.7 to 3.3 m is

---

[c] Baltic Sea results are derived from EM bird measurements performed during the IRIS campaigns.

region	overall mean [m]	mean of largest 10% [m]	exponential fit a	b [m^{-1}]	RMSE [$\cdot 10^{-3}$]
MS	1.16	2.01	2.16	2.76	2.49
MSR	1.18	2.04	2.02	2.67	2.47
TDS	1.26	2.31	1.12	2.17	2.40
FS	1.28	2.41	0.93	2.04	3.18
LS	1.55	3.27	0.35	1.31	0.85
Baltic Sea	1.06	1.68	4.24	3.52	17.63

Table 4.2: Overall mean and mean of largest 10% of sail heights from different Arctic and sub-arctic regions. The exponential fit (Equation (4.3)) to the distributions of Figure 4.8b is valid for sail heights between 0.8 and 3.0 m and the correlation coefficient is larger than 0.99 in all cases. The root mean squared error (RMSE) is given as a quality estimator of the regression over the entire range of sail heights.

found. Four of the Arctic regions are close in their overall means and show only a difference of 10 cm between MS/MSR and TDS/FS. This increases to 30 cm if the largest-10%-averages are taken into consideration.

Sail height clearly follows an exponential distribution[d], whereas the ridge density data resemble a log-normal distribution[d] (Figure 4.8). This is in agreement with results of past ridge studies performed with different instruments [*Wadhams*, 2000]. The log-normal distribution of ridge density and spacing respectively is more pronounced in the frequency distribution of non-averaged spacing values (not shown here).

The sail height distribution will later be used to develop a ridging algorithm for a numerical sea ice model (see Section 6.3). Therefore exponential regressions of the form

$$\mathsf{f}(H_s) = a \, \exp\left(-b \, H_s\right) \tag{4.3}$$

are additionally calculated; $\mathsf{f}(H_s)$ is the probability density function (PDF, see Appendix B.3) of sail heights. The parameters a and b of the regressions, listed in Table 4.2 for each of the graphs of Figure 4.8b, emphasise the agreement of the pairs MS and MSR, and TDS and FS. However, it can not necessarily be assumed that the regression coefficients support the same grouping as the average values do because the maximum sail height has a strong influence on the two different means but these large sails represent only a small part of the flight legs. Thus, the regression coefficients represent larger parts of the profiles, i.e. the typical sail heights of the different regions. The Fram Strait area is mainly fed by the TDS with an intermixing of a stream of heavily deformed ice derived north of Greenland varying in strength, whereas a much smaller amount of ice from the central Arctic reaches the Barents Sea and covers only a small area there.

The parameters a and b of Equation (4.3) can be approximated from the mean sail height $\langle H_s \rangle$ and the cut-off height H_0 by the relationships

$$b = \left(\langle H_s \rangle - H_0\right)^{-1} \qquad \text{and} \qquad a = c \, b \exp\left(b \, H_0\right) \tag{4.4}$$

following the approach of *Wadhams and Davy* [1986]. In contrast to their study the factor c does not resemble the average number of sails per unit distance here but is found to have a constant value of 0.09 for all Arctic values in Table 4.2 and equals 0.07 for the results from the Baltic Sea.

Keels   The same study is performed for the keel data gained from the EM bird draft profiles. One has to keep in mind that the original EM-derived ice draft underestimates the true keel depths and that the EM data investigated in the following include therefore a correction factor of 2. The density distributions of the keels have less in common with those of the sails. The Barents Sea

---

[d]More general information on the log-normal and exponential distributions is given in Appendix B.1 and B.2 respectively.
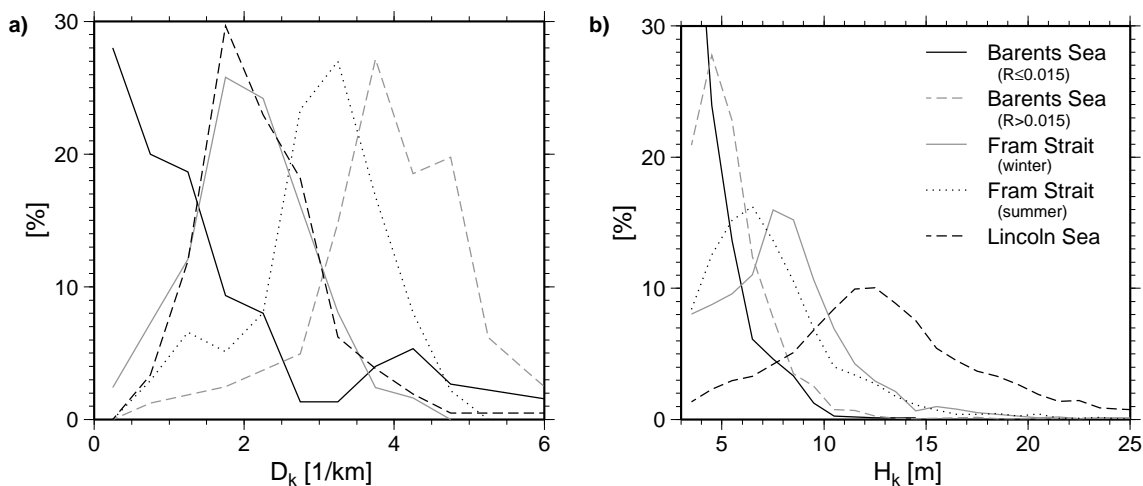
Figure 4.9: (**a**) Histograms of keel density D_k, which is calculated from profile segments of 5 km length. (**b**) Distribution of keel depth H_k, where only keels of profiles with at least 5 km length are included. Legend in (b) holds for both figures. Flights from the Barents Sea are separated according to MS and MSR of sail distributions. Fram Strait flights are split into winter and summer data. Histogram bin width in (a) is 0.5 km^{-1} and in (b) 1 m beginning at 0 km^{-1} and 3.2 m respectively; interpolated lines are shown for clarity (refer to caption of Figure 4.8). The modal value of the Barents Sea data with $R \leq 0.015$ is at $(3.7, 46.5)$ and is omitted for improved scaling of the ordinate.

profiles of $R \leq 0.015$ (hereafter still referred to as MS) show a mode at zero to half a keel per km (Figure 4.9a). Profiles with only one or two keels are found inside Storfjorden. Rougher ice in the Barents Sea ($R > 0.015$, MSR) has the most keels (4 per km) of all investigated regions, as was already shown for sail density. The second mode of MS keel data is smaller with 4 keels per km and reflects that the separation criteria chosen according to sail characteristics do not necessarily hold for the ice underside. In contrast to the sail density distribution in the Lincoln Sea, the keel density is less or equal to that in the Fram Strait. The reason may be the enormous clustering of keels in the Lincoln Sea. If ridges are pushed into each other they will form one wider keel rather than two that are distinguishable by the Rayleigh criterion. The spacing between sails, which span a smaller area, is still large enough to be detected as a single feature in the profiles.

Ice underside profiles from the Fram Strait are separated in order to study differences between summer and winter keel characteristics due to different ice conditions. Because a decrease in ice concentration leads to larger spacings between floes and thus also between ridges a smaller keel density in the summer data was expected. In addition keels are weathered in summer and may fall below the cut-off depth. However, Figure 4.9a shows the opposite: the modal keel density of summer 2004 is found to be larger than that of winter 2003. Rea-
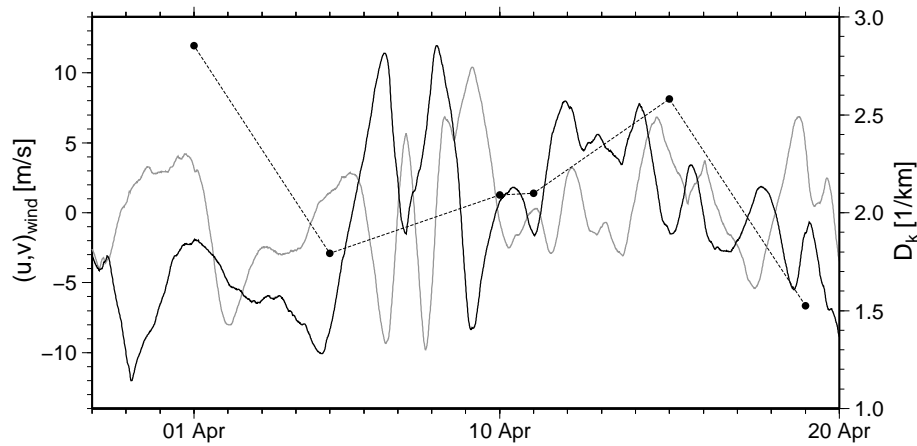
Figure 4.10: Dependence of observed keel density D_k and local wind events. North-south (v, black curve) and east-west (u, grey curve) components of wind measurements from automated recording on board *RV Polarstern* during campaign ARK-XIX/1b in April 2003 is displayed (left axis). Black dots mark mean keel densities of entire flights during this expedition (right axis).

sons for the larger keel density in the summer profiles compared to those of winter include the ice and weather conditions which vary with time and region. The wind regimes in the Fram Strait varied strongly between April 2003 and August 2004. In contrast to March and April 2003, when northerly winds prevailed, the wind direction changed to southerlies in August 2004 (compare NCEP/NCAR reanalysis data, *Kalnay et al.* [1996]). Northerly winds accelerate ice export through the Fram Strait and stretch the ice cover, which results in leads oriented across the main drift direction [*Schauer and Kattner*, 2004, Fig. 3.1.5 and 3.1.8]. The divergent drift field of winter 2003 resulted in an open water and thin ice (<10 cm thick) fraction twice as large as was deduced from the summer 2004 EM bird profiles. Actually, the mean ridge density is directly related to the wind characteristics preceding the measurements. As shown in Figure 4.10 northerly winds (negative v-component) cause the ice cover in the Fram Strait to diverge and the mean keel density is smaller than that found directly after southerly wind events. However, the differences in ridge density between the daily flights are smaller than the density variations within each flight track. The mean standard deviation of the six presented daily averages composed of 5 km long profile segments is 0.76 per km^2 and exceeds the standard deviation of the daily means by 55%. The large keel density observed on 1 April 2003 is caused by north-westerly winds and has to be explained separately. On this day the flight was undertaken in the vicinity of the north-west corner of Svalbard. The north-westerly wind was in turn causing convergent ice motion towards the coast and strong deformation. The ice close to the coast was heavily deformed and separated from the large multi-year ice floes of the Fram Strait by a strip of rubble

region	overall mean [m]	mean of largest 10% [m]	log-normal fit					
			μ	μ_-	μ_+	σ	σ_-	σ_+
MS	4.67	8.26	1.50	1.48	1.52	0.28	0.27	0.30
MSR	5.45	9.61	1.65	1.63	1.66	0.29	0.28	0.30
FS (w)	8.11	15.13	2.01	1.99	2.03	0.38	0.36	0.39
FS (s)	7.56	15.27	1.93	1.91	1.94	0.38	0.37	0.39
LS	13.19	24.11	2.43	2.42	2.44	0.37	0.36	0.38

Table 4.3: Overall mean and mean of the largest 10% of keel depths from different Arctic regions. The frequency distributions (Figure 4.9b) resemble a log-normal statistical distribution with parameters μ and σ (see Appendix B.1). Additionally, ranges of μ and σ are given at a significance level of 95%.

and very small floes, possibly crushed by shear motion between the ice stream leaving through the Fram Strait and the coastline of Svalbard [*Schauer and Kattner*, 2004]. However, the number of keels per km found in Fram Strait during summer 2004 is twice as large as in winter 2003 and represents a completely different ice regime rather than seasonal variations.

In Figure 4.9b the frequency distributions of keel depth are shown separately for five regions. In contrast to the sail height distributions (Figure 4.8b) the keel depths are distributed log-normally. This is contradictory to other ridge keel studies, for example *Wadhams and Davy* [1986] found exponentially distributed keel depths for data from submarine-borne ULS measurements. Therefore, the log-normal PDF evident in the EM bird data are tested with the Kolmogorov-Smirnov-Test [*Press et al.*, 1992]. For all keel data, despite those from the MS, the log-normal fit matches the frequency distribution of keel depth with a 5% risk of error (see Table 4.3). The sample size N, i.e. the number of single keels per region included in the present study, ranges between approximately 700 and 3000 and is 4 to 5 times smaller than that for sails (see next section). Only the data from the Barents Sea can also be expressed by an exponential PDF (see

region	exponential fit			RMSE
	a	b [m^{-1}]	r	
MS	3.31	-0.58	0.98	0.417
MSR	1.94	-0.48	0.96	0.638

Table 4.4: Coefficients of the exponential fit of the Barents Sea keel depth data (Figure 4.9b) according to Equation (4.3) with H_k instead of H_s. Additionally, the correlation coefficient r and the root mean squared error (RMSE) are given.

Table 4.4). The modal values of keel depth ranging between 3.7 and 12.7 (Figure 4.9b) show also that the log-normal distribution can not be detected if a too large cut-off depth, for example 9 m [e.g. *Wadhams*, 1981], is used.

As with sail height basic differences in keel depth can be observed between the regions. As for the sail height distributions (Figure 4.8b) the PDF of keel depth form three groups: Barents Sea, Fram Strait and Lincoln Sea; this is even more evident in the cumulative distribution functions of keel depth (not shown). The smallest keels were found in the Barents Sea and the largest in the Lincoln Sea (up to ∼40 m). In Table 4.3 average keel depths of the various regions are listed. The tripartition is particularly noticeable in the maximum values of keel depth represented by the largest 10% of all keels, with maximum keel depths of 9 m in the Barents Sea, 15 m in the Fram Strait and 24 m in the Lincoln Sea. Considering the mean as well as modal values of the two data sets obtained in the Fram Strait region the keels of summer (2004) are smaller than those found in winter (2003) by about 1 m. Besides the possibility of two different ice regimes, this difference in keel depths might have been caused by melting and might represent the difference between summer and winter. Keel depths derivations are not affected by a change in ice concentration like ridge density and hence are not coupled as tightly to wind direction as was shown for ridge density. Considering different regimes one would expect the modal keel depth during the summer campaign of 2004 to be larger because this expedition covered the western Fram Strait (west of the prime meridian) with ridges formed of thicker ice from north of Greenland than the ridges observed during the winter expedition (east of the prime meridian). Data from the latter campaign reflects the thinner ice of the marginal seas. Thus, melting is a probable explanation for the smaller value found in the summer data.

4.4 Relations of sails and keels

Coincident measurements of sea ice surface and underside—or freeboard and draft—with the EM bird results in a unique data set that enables a study of the relationships of sail height and keel depth as well its densities. To date the possibility of such an investigation was rather rare. A first comparison of independent sail and keel profiles near the North Pole from 1971 is described by *Hibler* [1975]. A second improved study was performed by *Wadhams* [1980, 1981] by using observations of parallel profiles that were obtained by submarine ULS surveys and airborne laser measurements in 1976. The author, however, states that the temporal difference between ice underside and surface profiling ranged between 0 hours and 5 days. Additionally, the best possible simultaneous coverage was 2 km apart. These problems do not occur with the EM bird as both
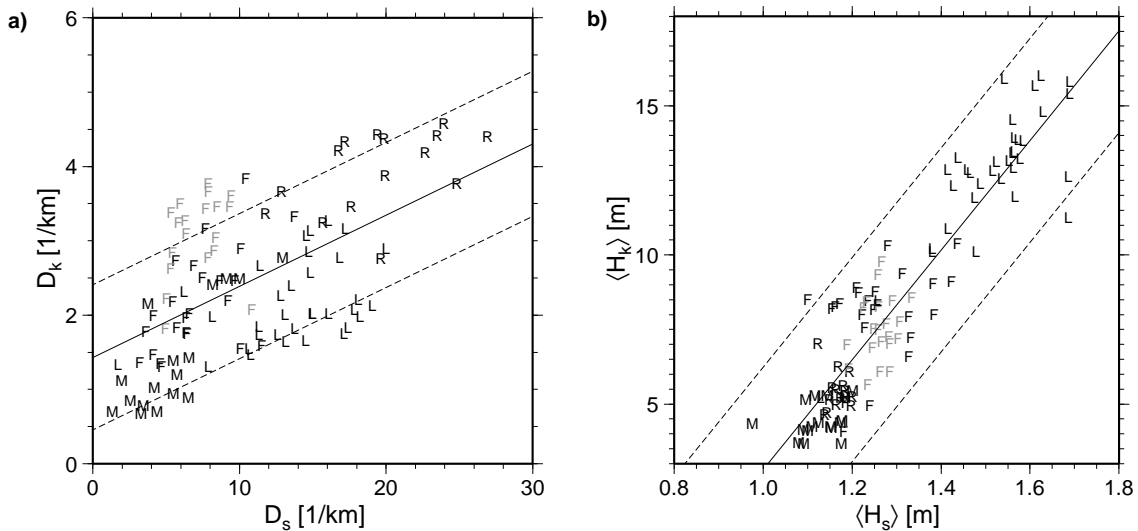
Figure 4.11: (**a**) Keel density D_k as a function of sail density D_s and (**b**) mean keel depth $\langle H_k \rangle$ versus mean sail height $\langle H_s \rangle$ for all flight legs exceeding a length of 5 km. Linear regressions are represented by a solid line and $\pm 1\sigma$ standard deviation by dashed lines (see Table 4.5 for regression coefficients). Symbols refer to regions according to Table 4.1: Barents Sea (M [$R \leq 0.015$], R [$R > 0.015$]), Fram Strait (F, black: winter 2003, grey: summer 2004) and Lincoln Sea (L).

profiles are obtained with the same instrument and hence exactly coincident measurements are guaranteed. The study of *Wadhams* [1981] examines a region (Fram Strait, off Greenland's northern coast to the North Pole) which is also

Data		cut-off [m]		linear regression			σ [m]
		height	depth	$a_{D,H}$	$b_{D,H}$ [m]	r	
AWI	D	0.8	3.2	0.10	1.43	0.57	0.97
	H			18.38	-15.57	0.92	3.42
AWI	D	1.0	9.0	0.14	0.14	0.83	0.65
	H			8.31	-0.39	0.76	1.65
W81	D	1.0	9.0	0.24	1.69	0.76	–
	H			9.51	-1.83	0.85	–

Table 4.5: Regression parameters for ridge density $D_{s,k}$ and sail-height keel-depth relation $H_{s,k}$ in reference to Equation (4.5) and the corresponding correlation coefficients r. The *AWI* parameters are derived from average heights and densities of 120 flight legs which all have a length of at least 5 km. The *AWI* keel depths H_k include a correction factor of 2. Standard deviations σ are given for the dependent variable, the keel values. *W81* denotes results of the study of *Wadhams* [1981] and *AWI* denotes the EM bird data of the present study.

covered by the EM bird measurements and thus can be used for comparison. In the following the data sets are referred to as *W81* and *AWI*.

Figure 4.11 shows average values of sail and keel density, and height and depth for each of the flight legs longer than 5 km. Both graphs suggest a linear relationship between sail and keel values accounting for all three regions Barents Sea, Fram Strait and Lincoln Sea:

$$D_k = a_D D_s + b_D \quad and \quad \langle H_k \rangle = a_H \langle H_s \rangle + b_H . \tag{4.5}$$

This is in agreement with the findings of *Wadhams* [1981, Equ. 18 and 19], although both the cut-off height and depth differ. For a better comparison the regression of the *AWI* data is recalculated for the same cut-off values applied by *Wadhams* [1981]. All three resulting pairs of regression parameters are listed for density (D) as well as height and depth (H), in Table 4.5. The cut-off values affect the regression parameters, mainly those of the height-depth relation. Equal cut-off values lead to a close agreement between *AWI* and *W81* data of the values of slope a of Equation (4.5) and of the correlation coefficients of sail and keel quantities, which range between 0.76–0.85. It should be noted that the correlation between sail and keel densities decreases with smaller cut-off values (0.57), whereas the correlation between height and depth increases to 0.92. The correlations based on the *AWI* data are all statistically significant (Student's t-test [*Press et al.*, 1992]) with a 0% ($<10^{-10}$%) risk of wrongly rejecting the null-hypothesis that the data are not linearly related because of the large sample size ($N = 120$). The confidence interval of the correlation coefficients is determined to be $0.44 \leq r_{true} \leq 0.68$ and $0.89 \leq r_{true} \leq 0.94$ for densities and height-depth relationships, respectively, applying the Fisher's z-transformation [*Storch and Zwiers*, 2001]. These results are significant at the 5% level.

In order to simulate the correct ridged ice volume in a numerical sea ice model it is important to find a simple and realistic relationship between ridge sails and keels. The above findings do not support the assumption of a direct proportionality between sail and keel quantities, i.e. $a_{D,H} \neq 0$ and $b_{D,H} = 0$ in Equation (4.5). A simple ratio would enable easy access to sail and keel relations in ridge modelling. *Timco and Burden* [1997] found a ratio of 1:3.95 and 1:3.17 for first year and multi year ice respectively (their Figures 3 and 12) based on a collection of 176 single ridge measurements: However, their linear regression clearly passes through the origin and it is not stated whether this is forced. Calculating the equivalent ratio from the *AWI* data results in an average ratio of 1:6.27. This value includes also the correction, i.e. the doubling of the original EM ice draft. The ratio resembles the slope (1:6.66) of the linear regression line in the case it is forced to pass through the origin. Though twice as large as the results of *Timco and Burden* [1997] the values are supported by the laser altimeter profile study of *Hibler* [1975], who found a ratio of 1:6.58 for sail height to

keel depth with an offset b_H of 1.12, which the author explained by the difference between zero-height of the processed altimeter data and real water level. Here, a possible explanation for the absence of direct proportionality in the *AWI* data might be found in the use of averaged values, which depend on the cut-off height and depth respectively, and not of single ridge measurements as in the study of *Timco and Burden* [1997].

For numerical modelling of ridges the relationship between sails and keels discussed in this section is important for correct representation of the volume of ice stored in a ridge.

4.5   The dependence of sail height on the parent ice thickness

Besides the functional dependency of sail height and keel depth the relationship between sail height and the parent (level) ice thickness is of interest because the ice thickness is a prognostic variable in a typical large scale sea ice model (see Chapter 2). In the following the EM bird data are investigated with respect to such a relationship. The derivation of the level ice thickness from the EM data is described in Section 4.2.4. Mean level ice thickness estimates will be related to average and maximum sail heights where all quantities are derived from the same 5 km long profile segments. It will be shown that there is a linear link between mean sail height and level ice thickness and a non-linear relationship between maximum sail height and the level ice thickness in the EM bird profiles.

Beginning with the dependence of the mean sail height $\langle H_s \rangle$ on the average thickness of the undeformed ice, Figure 4.12 shows that despite the rather large scatter a linear relationship of

$$\langle H_s \rangle = 0.11\, H_l + 1.11 \tag{4.6}$$

can be used to describe the distribution. Though the correlation of 0.57 is rather weak it is statistically significant with a 0% risk of error because of the large number of samples ($N = 669$). The range of $0.52 \leq r_{true} \leq 0.62$ is significant at the 5% level. 79.5% of all values are within the interval of ± 1 standard deviation $\sigma = 0.2$ m, which is marked with two dashed lines in Figure 4.12, and 97.7% lie within $\pm 2\sigma$. The root mean squared error (RMSE) is 0.17 m. One possible reason for the scatter is the time lag between ridge formation and observation. The average level ice thickness of a flight leg does not necessarily represent the parent ice thickness of the sails along the profile at the time of ridge formation. The level ice thickness changes due to lead opening and refreezing and subsequent thermodynamical growth. Ridge sails may weather and be covered by snow.

Studying single ridges *Tucker et al.* [1984] found a relationship between the maximum sail height of a certain ridge and the thickness H_b of the blocks from which the ridge is formed of:

$$H_s = 3.71\sqrt{H_b}\,. \tag{4.7}$$

The block thickness H_b refers clearly to the thickness of the level ice H_l from which the blocks stem, which is the parent ice thickness of the ridge. This allows H_b to be replaced with H_l in Equation (4.7). However, fitting functions that follow a power law to the data of Figure 4.12 results in $H_s = 1.05\,H_l^{0.5}$ and $H_s = 1.24\,H_l^{0.1}$ respectively both with weaker correlations of 0.52 and 0.49 than found for the linear fit of Equation (4.6). For the square-root fit the RMSE increases to 0.37 but for the power law with free exponent the RMSE stays at 0.17 compared to the linear fit. Thus, the linear relationship is considered as the best fit to the data though a power law is more suitable for modelling approaches because sail height tends to zero for decreasing level ice thickness.

The above relationship changes when the maximum sail height along each profile segment is considered instead of the segment mean. In the following, the maximum sail height denotes the average height of the largest 10% of all sails of each segment. This maximum sail height $H_{s_{max}}$ is presented as a function of the mean level ice thickness H_l in Figure 4.13. Using these data to parameterise the
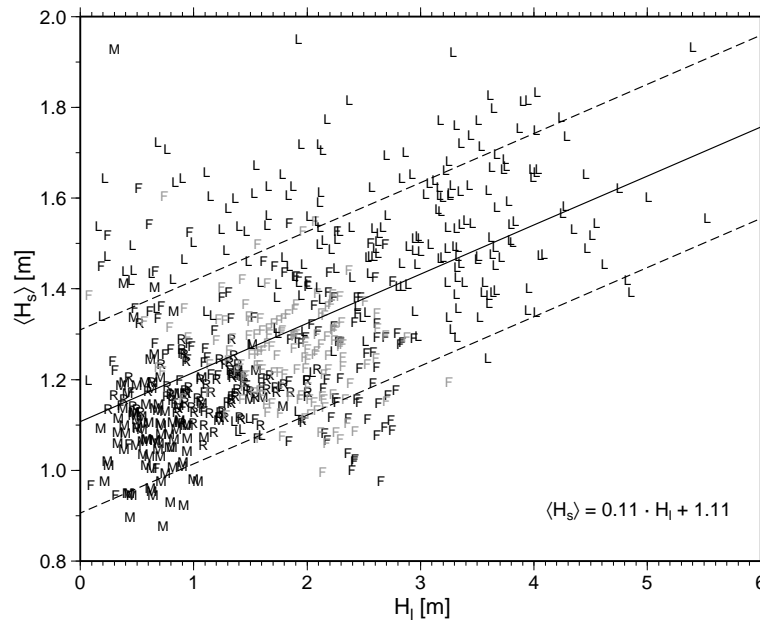

Figure 4.12: Mean sail height $\langle H_s \rangle$ as a function of the mean level ice thickness H_l of 5 km long profile segments separated into different geographical regions (for symbol declaration see caption of Figure 4.11). Additionally, the linear regression of Equation (4.6) is shown as a straight black line and the corresponding $\pm 1\sigma$ interval is marked with dashed lines.
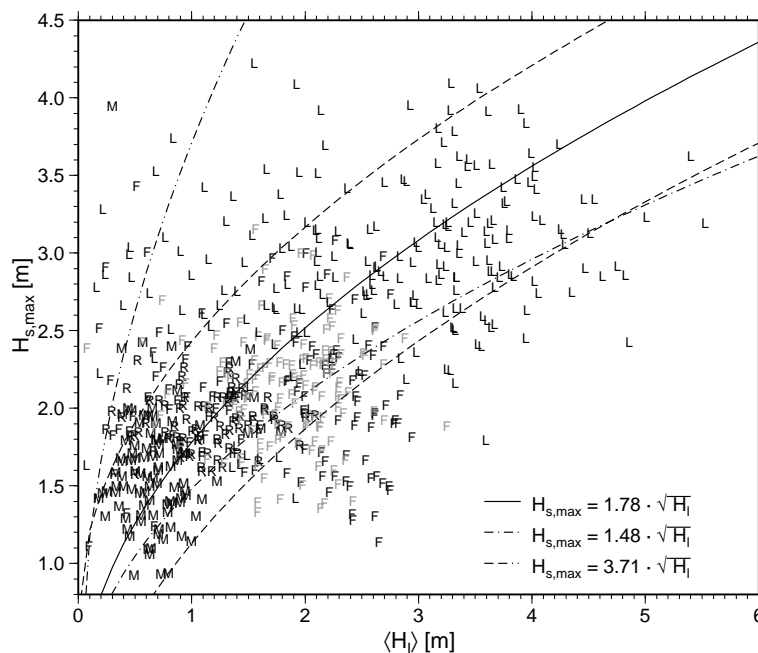
Figure 4.13: Maximum sail height $H_{s_{max}}$ in dependence of the average level ice thickness H_l of 5 km long profile segments. Symbols mark different geographical regions (see caption of Figure 4.11). The black solid line shows the regression of Equation (4.8) and the dashed black lines the $\pm 1\sigma$ interval. The solid dash-dotted line shows a related function for level ice thickness and maximum sail height of *Lensu* [2003a] and the double-dash-dotted line follows that of *Tucker et al.* [1984].

relationship between H_l and $H_{s_{max}}$ results in

$$H_{s_{max}} = 1.78\sqrt{H_l} \tag{4.8}$$

The correlation of 0.55 is similar to the above and has a significant confidence interval of $0.49 \leq r_{true} \leq 0.60$ at the 5% level. The RMSE of 0.66 m is larger than that of the level ice thickness to mean sail height relation. Although a linear regression $H_s = 0.34\sqrt{H_l} + 1.64$ with about the same correlation and RMSE can also be derived from the EM bird data, the relationship of Equation (4.8) is preferred in agreement with the studies of *Tucker et al.* [1984] and *Lensu* [2003a]. The regressions following these two studies are included in Equation (4.8). The differences found here may be explained by the different measurement techniques. *Tucker et al.* [1984] collected their data by measuring about 80 single ridges, avoiding rubbled, clustered or grounded features. The authors stated that they always selected the highest point within a radius of about 0.5 km. The maximum sail height $H_{s_{max}}$ used in the present study would be smaller by definition compared to that measured by *Tucker et al.* [1984] and includes all types of ridges. Moreover, the sail height derived from the laser altimeter data does not necessarily represent the maximum height of a defined ridge; the laser might even have missed the crest of the sail. Still, the laser altimeter data are of

good statistical quality considering the great inhomogeneity of ridges and the large number of samples.

Lensu [2003a] suggested a parameterisation

$$H_s = 0.4 \cdot 3.71 \sqrt{H_b} = 1.48 \sqrt{H_b} \tag{4.9}$$

which includes a factor of 1/2.5 and thus, corrects sail height measurements of the type *Tucker et al.* [1984] performed. *Lensu* [2003a] showed that measured sail crests are typically 2.5 times higher than the sail height that would satisfy the common ridge link model—assuming a triangular cross-sectional shape for the sail. The function Equation (4.9) yields a curve that is much closer to the regression found here (Equation (4.8)) as can be seen in Figure 4.13. The smaller slope at larger ice thickness values may be caused by the fact that *Lensu* [2003a] used mainly Baltic Sea observations as well as some from the Barents and Kara seas.

Tucker et al. [1984] also determined a value of 5.24 for Equation (4.7) describing the upper envelope of the sail heights. Such an upper bound can not be defined with the required accuracy from the data presented here.

However, the findings presented in this section are most valuable to enable the derivation of ridge parameters, i.e. estimates of mean and maximum sail height in a certain region, with a numerical sea ice model. The relationships given in Equation (4.6) and Equation (4.8) will be used in the ridging algorithms presented in Chapter 6.

4.6 Summary

The most important results of Chapter 4 are listed here and some will be applied directly to the ridge modelling (see Chapters 6).

- Keel depth can be expressed as a function of sail height following

$$H_k = 18.38 H_s - 15.57$$

  (see Table 4.5). Although this relation has a high correlation of 0.92 and 0% risk of error because it is determined from a large set of EM bird data, the result depends strongly on the cut-off height and depth of 0.8 m and 3.2 m respectively. The function is not applicable for sail or keel values smaller than these thresholds. An average ratio of 1:6.27 is determined for sail height to keel depth from the measurements.

- The keel density is smaller than the sail density and can be parameterised by

$$D_k = 0.10 D_s + 1.43$$

(see Table 4.5) considering sail and keel cut-off values of 0.8 m and 3.2 m. The mean ratio of the observed sail and keel numbers is 4.8.

- The mean sail height can be parameterised as a function of the parent ice thickness (see Figure 4.12):

$$\langle H_s \rangle = 0.11\, H_l + 0.11$$

However, for application to numerical models the power law

$$\langle H_s \rangle = 1.24\, H_l^{0.1}$$

is more suitable because the regression function passes through the origin. Again the cut-off value for sail height of 0.8 m must be considered.

- An estimate of the maximum sail height can be derived from

$$H_{s_{max}} = 1.78\sqrt{H_l}$$

(see Figure 4.13). Besides the mentioned cut-off height it should be considered that $H_{s_{max}}$ does not necessarily represent the upper bound of sail height but rather an average of the largest sails observable in a region with a level ice thickness of H_l.

- The ridge density and height are positively correlated though the significance of the correlation depends on region and season. No clear functional dependence is found for the presented data.

Part III

Numerical Modelling of Pressure Ridges
or: From the small scale to the large scale

Chapter 5

Principles of deformation schemes in numerical sea ice models

This chapter reviews the studies of *Schulkes* [1995] and *Gray and Killworth* [1996] because their work is considered to be the key to understanding and distinguishing between different approaches in ridge modelling. Additionally a new approach to the so-called β-function is presented. The β-function is included in common deformation schemes and relates the impact of the various schemes to the compactness of the ice cover. In context with Chapter 6 this chapter explains the difference between those ridge models that approximate the ridging process in order to change ice concentration and thickness due to deformation and those that compute realistic estimates of particular ridge parameters such as ridge density and height. In order to introduce different states of sea ice drift and to explain the connections between these and deformation processes the chapter begins with an overview and classification of motion in general.

5.1 States of motion

The analysis of a velocity field like the drift of the Arctic ice cover demands a detailed view of its components—the pure states of motion. These states describe the deformation of the ice cover and are the basis for its parameterisation as will be discussed in more detail in the following section. It is possible to derive the velocity field at a given position, which is here chosen as the origin of the coordinate system (index o), from a Taylor series expansion:

$$\vec{u}(\vec{r}) = \vec{u}_o + \vec{r} \cdot (\nabla \vec{u})_o + \mathcal{O} \,. \tag{5.1}$$

For clarity the expansion is only considered in two dimensions. Accordingly $\vec{u} = (u, v)$ denotes the drift vector on a plane, $\vec{r} = (x, y)$ denotes the position

vector, and $\nabla = (\partial/\partial x, \partial/\partial y)$ is the Nabla-operator. Higher-order terms of the series expansion are expressed in $\mathcal{O}$ and may be neglected if only the velocity field in the close neighbourhood of the origin is considered. Splitting the drift vector into its components, the Taylor expansion looks like

$$u = u_o + \left.\frac{\partial u}{\partial x}\right|_o x + \left.\frac{\partial u}{\partial y}\right|_o y \tag{5.2a}$$

$$v = v_o + \left.\frac{\partial v}{\partial v}\right|_o x + \left.\frac{\partial v}{\partial y}\right|_o y \tag{5.2b}$$

After transformation by splitting terms T into $1/2T + 1/2T$ or adding terms such as $1/2T - 1/2T$ one derives

$$u = u_o + \frac{1}{2}D_o x - \frac{1}{2}\zeta_o y + \frac{1}{2}E_o x + \frac{1}{2}F_o y \tag{5.3a}$$

$$v = v_o + \frac{1}{2}D_o y + \frac{1}{2}\zeta_o x - \frac{1}{2}E_o y + \frac{1}{2}F_o x \tag{5.3b}$$

The abbrevations D_o, ζ_o, E_o and F_o describe divergence, vorticity, strain deformation and shear deformation, respectively, and are defined as follows:

$$D_o = \left.\frac{\partial u}{\partial x}\right|_o + \left.\frac{\partial v}{\partial y}\right|_o \tag{5.4a}$$

$$\zeta_o = \left.\frac{\partial v}{\partial x}\right|_o - \left.\frac{\partial u}{\partial y}\right|_o \tag{5.4b}$$

$$E_o = \left.\frac{\partial u}{\partial x}\right|_o - \left.\frac{\partial v}{\partial y}\right|_o \tag{5.4c}$$

$$F_o = \left.\frac{\partial v}{\partial x}\right|_o + \left.\frac{\partial u}{\partial y}\right|_o \tag{5.4d}$$

If D_o is negative this term is also called convergence. It can be shown that D_o and ζ_o are invariant under a rotation of the coordinate system. This also holds for the combined term $\sqrt{E_o^2 + F_o^2}$ but not for the single terms E_o and F_o. If the orientation of the coordinate system is chosen such that $\partial v/\partial x = -\partial u/\partial y$ the term F_o will be zero and coordinate axes are called principle axes with respect to a velocity field characterised by $E_o > 0$. The four pure states of motion discussed below are illustrated in Figure 5.1. The expressions used refer to a planar element centred in the origin of these velocity fields.

- pure translation ($D_o = \zeta_o = E_o = 0$): The shape and size of the element are not changed in such a velocity field.

- pure extension ($u_o = v_o = \zeta_o = E_o = 0$): This velocity field is shape-invariant but the size of the element is increased ($D_o > 0$) or decreased ($D_o < 0$, pure compression).

- pure rotation ($u_o = v_o = D_o = E_o = 0$): Though being shape- and size-invariant this velocity field results in a change of the orientation of the element; the direction of rotation is either cyclonic or anticyclonic[a].

---

[a]The actual direction of a rotation in atmosphere or ocean depends on the Coriolis force

a) $\vec{u} = \vec{u}_o$ b) $D_o > 0$ c) $\zeta_o > 0$

d) $E_o > 0$ e) $F_o > 0$
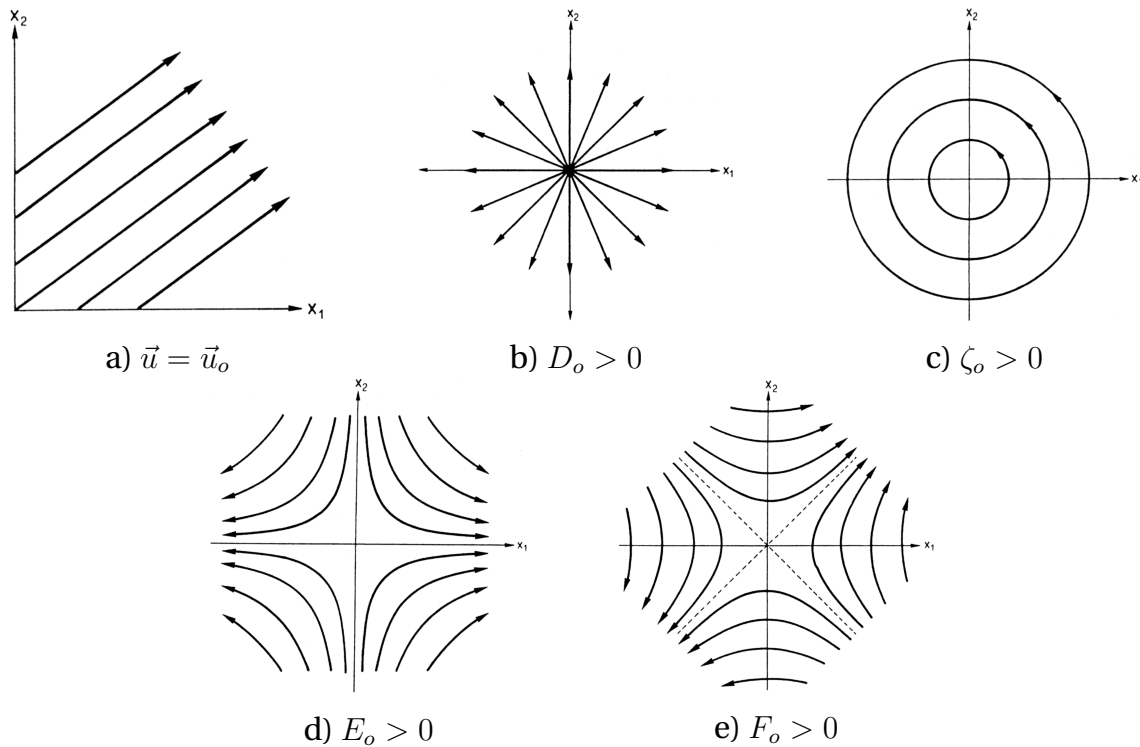
Figure 5.1: The four states of pure motion: (**a**) translation, (**b**) extension, (**c**) rotation and deformation due to (**d**) strain and (**e**) shear. [from *Pichler*, 1997, Figs. 2-14 to 2-18]

- pure deformation ($u_o = v_o = D_o = \zeta_o = 0$): Deformation separates into strain deformation where $E_o \neq 0$ and shear deformation with $F_o \neq 0$; here, the shape of the element is changed; for sea ice holds that these velocity fields are size-invariant only in the three-dimensional case but not in two-dimensional space, because sea ice is only approximatively a fluid and has plastic characteristics; in contrast to a divergent field the strain along the x-axis (y-axis) is compensated by a contraction along the y-axis (x-axis) in the case $E_o > 0$ ($E_o < 0$); for most arbitrarily oriented coordinate systems, $F_o \neq 0$.

Commonly only the three invariant states of motion are considered: divergence D_o, vorticity ζ_o and shear $\sqrt{E_o^2 + F_o^2}$. A comparison with the invariants of the strain rate tensor $\dot{\varepsilon}$ of Equation (2.16) shows that $\dot{\varepsilon}_I = D_o$ and $\dot{\varepsilon}_{II} = \sqrt{E_o^2 + F_o^2}$ (see also Appendix C.1).

The various states of motion have different effects on the sea ice cover. While ice floes drift apart during divergent motion and tensile stress occurs, floes collide in convergent situations and compressive stress acts on the ice. Both compression and shear motion cause formation of sea ice ridges. Though

---

and therefore on the hemisphere in which it is observed: in the northern hemisphere cyclonic means counter-clockwise ($\zeta_o > 0$) and anticyclonic clockwise ($\zeta_o < 0$). In the southern hemisphere cyclonic and anticyclonic denote the exact opposite.

ridges formed by compression (pressure ridges) can be distinguished from those caused by shear motion (shear ridges) by their shape [e.g. *Tucker et al.*, 1984, Fig. 1], this separation is usually not considered in large-scale ridge modelling.

5.2   Deficits of a two-dimensional sea ice cover

Common Arctic-wide sea ice models, such as the one described in Chapter 2, are based on the assumption that the sea ice cover is a two-dimensional medium. This assumption is valid—within certain restrictions—because the horizontal length scales (10^3–10^5 m) are several orders of magnitude larger than the vertical (10^0 m). Hence, the vertical motion of the ice is neglected. Vertical ice motion occurs (1) as external forcing due to tidal change of the sea surface height and (2) during deformation, e.g. ridging.

A closer look at the evolution equation for sea ice in the three-dimensional space of $\vec{r}_3 = (x, y, z)$ with ice drift velocity $\vec{u}_3(\vec{r}_3, t) = (u, v, w)$, shows what the neglected term looks like. The sea ice cover is characterised by the ice concentration A and its actual thickness H and is situated in the (x, y)-plane.

$$H\frac{\partial A}{\partial t} + H\,\nabla \cdot (A\,\vec{u}) + A\,(w_s - w_b) = 0 \tag{5.5}$$

This equation equals Equation (2.3) which has been deduced from the conservation of ice mass (see Section 2.1). Here, the important term is the difference of the vertical velocities $w_s - w_b$. The assumption of a two-dimensional ice cover equals the state $w_s = w_b$. This assumption has also been used to derive the evolution equations of the sea ice model applied in the present study and described in Chapter 2. The term $\nabla \cdot (A\vec{u})$ of Equation (5.5) can be split into $A\nabla \cdot \vec{u} + \vec{u} \cdot \nabla A$. The advection term $\vec{u} \cdot \nabla A$ simply transports ice concentration from one grid cell to the next and therefore cannot change the total ice area. In contrast, the term $A\nabla \cdot \vec{u}$ changes the total ice area due to deformation. This process consumes ice area while mass is conserved. Deformation prevents the ice concentration from exceeding unity (100% coverage). Thus also the variable A in a numerical sea ice model is supposed to remain less than or equal to unity. Therefore the term $A\nabla \cdot \vec{u}$ needs to be balanced in the case of the two-dimensional approximation.

In the case that $A = 1$, Equation (5.5) allows explicit determination of the vertical velocity difference:

$$w_s - w_b = -H\,\nabla \cdot \vec{u} \tag{5.6}$$

where $\dot{\varepsilon}_I = \nabla \cdot \vec{u}$ is a measure of divergence of the drift field that is defined in Equation (2.16a). The assumption that sea ice motion is essentially two-dimensional is an important simplification for Arctic-wide sea ice models and

120

results in the feasibility of numerical calculations with less computational cost, especially as the horizontal resolution of model grids increases steadily. In order to keep the realisation of sea ice models simple an approximation of the vertical velocity component for cases of $A < 1$ needs to be simple and effective itself.

5.3 An approximation for sea ice deformation

In the absence of a proper approximation of vertical motion in continuum ice models the ice concentration is able to exceed unity in a grid cell. *Hibler* [1979] solved this by including an artificial sink term, in the evolution equation of the ice concentration, which simply resets ice concentrations $A > 1$ to unity. This function has also been used in the sea ice model on which this study is based [*Harder*, 1996, and subsequent studies, see Chapter 2]. Regarded as the ice area consumption due to ridging, this consequently increases the actual ice thickness $H = h/A$ because the ice volume or mean thickness h remains unchanged. Although this approach is pragmatic because the ice volume is conserved, the constraint depends on the time step of the model and does not account for ridging until $A = 1$. This simple approach is suitable only for models with one ice thickness category because there is no direct way to correctly redistribute this surplus of ice area.

Another possibility is to apply the full evolution equation (5.5) but with a parameterisation of the w-components based on Equation (5.6):

$$w_s - w_b = -\psi' H \nabla \cdot \vec{u} \tag{5.7}$$

Here, the so-called "ridging function" ψ' is introduced. There are several possible definitions of ψ', some of which will be listed in the following. In general this function is bound by the limits $0 \leq \psi' \leq 1$ and requires $\psi' \to 0$ for $A \to 0$, because no deformation can take place if there is no ice, and $\psi' \to 1$ when $A \to 1$ for consistency with Equation (5.6). There are no further constraints and ψ' may also depend on A, H or principle invariants of the strain rate. ψ' can include a simple step function or a function $\beta(A)$ that represents a smooth transition into the ridging case while monotonically increasing with A. The ridging function needs to prevent A from exceeding unity and considers ridging already when $A < 1$. Defining the relation

$$\psi = \psi' A \nabla \cdot \vec{u} \tag{5.8}$$

enables a connection between the studies of *Schulkes* [1995] and *Gray and Killworth* [1996] and allows a rather simple definition of the deformation schemes ψ as functions of the invariants of the strain rate tensor independently of the coordinate system (see Appendix C.2). So far, only the cartesian coordinate sys-

tem has been considered, for which $\dot{\varepsilon}_I = \nabla \cdot \vec{u} = \dot{\varepsilon}_{11} + \dot{\varepsilon}_{22}$ (see Equation (2.16a)) and $\Delta_{\dot{\varepsilon}} = (\dot{\varepsilon}_I^2 + (\dot{\varepsilon}_{11} - \dot{\varepsilon}_{22})^2/2 + 2\dot{\varepsilon}_{12}^2)^{1/2}$ of Equation (2.23).

- The simple approach of *Hibler* [1979] can be described as

$$\psi_{H1} = A\,\beta(A)\,\dot{\varepsilon}_I\,. \tag{5.9}$$

  In *Hibler* [1979] the β-function equals $\mathcal{H}(A-1)^{\text{b}}$. In general and in the way the β-function is applied in the following equations it is a monotonically increasing function of A with the restraint that β should only deviate from zero if A approaches unity. This β-function will be discussed in more detail in the next section.

- *Gray and Morland* [1994] suggested

$$\psi_{GM} = A\,\beta(A)\,\dot{\varepsilon}_I\,\mathcal{H}(-\dot{\varepsilon}_I) \tag{5.10}$$

  The main differences between this approach and the previous one are that ψ_{GM} allows deformation to take place already when $A < 1$. However, the deformation intensity depends on $\beta(A)$. Thus, it is necessary to exclude situations of divergent motion from contributing to deformation, which is expressed by $\mathcal{H}(-\dot{\varepsilon}_I)$.

- *Hibler* [1984] already introduced briefly an approach of ψ, which accounts of ridging during shear motion, although he actually used it first to describe the creation of open water (compare to Equation (2.36) in Chapter 2).

$$\psi_{H2} = A\,\beta(A)\,\frac{1}{2}\,(|\dot{\varepsilon}_I| - \Delta_{\dot{\varepsilon}}) \tag{5.11}$$

- Finally *Shinohara* [1990] presented a combined version of ψ_{GM} and ψ_{H2} in order to achieve a description for ridging in all states of sea ice motion.

$$\psi_S = A\,\beta(A)\,\frac{1}{2}\,(\dot{\varepsilon}_I - \Delta_{\dot{\varepsilon}}) \tag{5.12}$$

  Actually $\psi_S = \psi_{GM} + \psi_{H2}$ exactly.

After *Gray and Killworth* [1996] these functions can be expressed in a cylindrical coordinate system (see Appendix C.2), which is spanned by the total rate of deformation $|\dot{\varepsilon}|$ and the deformation angle θ of Equation (2.17) and (2.18) respectively. The terms $\dot{\varepsilon}_I$ and $\Delta_{\dot{\varepsilon}}$ can be substituted simply by their respective

---

[b] $\mathcal{H}$ denotes the Heaviside step function, which here is defined as $\mathcal{H}(a) = 0$, if $a \leq 0$ and $\mathcal{H}(a) = 1$, if $a > 0$, where $a \in \mathbb{R}$.
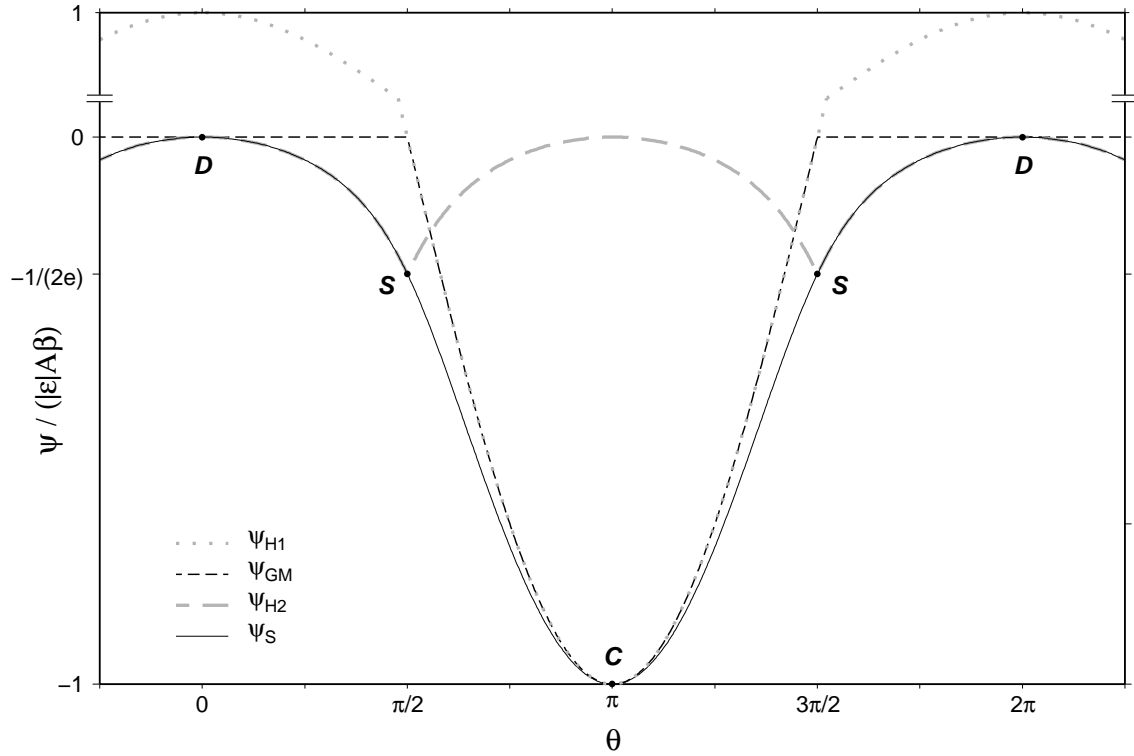
Figure 5.2: Illustration of the deformation schemes ψ of Equations (5.9)–(5.12) as function of the deformation angle θ [after *Gray and Killworth*, 1996]. Note the change in scale of the ordinate.

expressions, which can be found in Table C.1.

$$\psi_{H1} = |\dot{\varepsilon}|A\,\beta(A) \qquad \cos\theta$$

$$\psi_{GM} = |\dot{\varepsilon}|A\,\beta(A) \qquad \cos\theta \ \times \ \mathcal{H}\left(-\cos\theta\right)$$

$$\psi_{H2} = |\dot{\varepsilon}|A\,\beta(A)\,\tfrac{1}{2}\left\{|\cos\theta| - \left[\tfrac{1}{2}(1+e^{-2}) + \tfrac{1}{2}(1-e^{-2})\cos(2\theta)\right]^{1/2}\right\}$$

$$\psi_{S} = |\dot{\varepsilon}|A\,\beta(A)\,\tfrac{1}{2}\left\{\cos\theta \ - \left[\tfrac{1}{2}(1+e^{-2}) + \tfrac{1}{2}(1-e^{-2})\cos(2\theta)\right]^{1/2}\right\}$$

The eccentricity e of the yield curve is considered to equal 2 in all equations as described in Section 2.2. The behaviour of the different deformation schemes can be illustrated for all measures of divergence and shear using the deformation angle θ. In Figure 5.2, $\psi/(|\dot{\varepsilon}|A\beta(A))$ is presented as a function of θ. In this graph four special points are marked explicitly which correspond to cases where θ equals a multiple of $\frac{1}{2}\pi$. The points of pure divergence ($\theta = 0$) and pure convergence ($\theta = \pi$) are labelled with 'D' and 'C' respectively. The functions ψ_{GM} and ψ_{S} are equal in these two points, which is reasonable in both cases because no deformation should occur in the case of pure divergence, and in the state of pure convergence just enough ridging happens to restrict A to unity. Points $\frac{1}{2}\pi$ and $\frac{3}{2}\pi$ correspond to pure shear motion and are marked 'S'. These are situated at the turning points between divergent and convergent motion. This means that divergence occurs in the range $-\frac{1}{2}\pi < \theta < \frac{1}{2}\pi$ and convergence for

$\frac{1}{2}\pi < \theta < \frac{3}{2}\pi$. The graph also shows that the amount of deformation during any shear motion is always smaller than the deformation rate in pure compression 'C'. The ice drift state markings 'C', 'S' and 'D' as well as the angle θ are directly comparable to those given with the yield curve in Figure 2.3 (where 'O' corresponds to 'D').

Assuming that ridging is isotropic[c] the ψ-functions have reflective symmetry in the lines $\theta = n\pi$, where $n \in \mathbb{Z}$. This symmetry is extended for ψ_{H2} to $\theta = \frac{1}{2}n\pi$ because it does not distinguish between divergence and convergence. The deformation function ψ_{H2} reaches its maximum value in pure shear and thus cannot restrict A to a value of less than or equal to unity. However, as mentioned above, this function was intended to simulate the formation of leads under shear motion (see Section 2.4) and not intended to govern deformation of the ice.

Because of its simplicity, ψ_{H1} is a special case. This function does not account for the ice drift state directly as all other presented deformation schemes do. *Hibler* [1979] intended to restrict A and not to model the deformation process in detail. Indirectly, the drift state is considered with ψ_{H1} because the ice concentration exceeds unity in the model only in the case of convergent or shear motion. In order to show its deficit formulation in comparison to the other deformation schemes it is added to Figure 5.2. Assuming that $\beta(A)$ equals zero or unity ψ_{H1} equals ψ_{GM} in a situation of convergent drift. However, from this graph ψ_{H1} seems also to be active during divergent motion. This is actually not the case because A will not exceed unity in such ice drift conditions and thus the expression $\mathcal{H}(A-1)$ remains zero. Although ψ_{GM} has the advantage of enabling deformation also when $A < 1$, it does only account for deformation during compression.

Gray and Morland [1994] constructed ψ_{GM} as a mechanical redistributor to bound A to $[0, 1]$. Thus ψ_{GM} describes the minimum amount of deformation necessary to match this requirement. Any function $\psi(\theta) > \psi_{GM}(\theta)$ can not prevent A from exceeding unity for this θ, for example ψ_{H2} for the largest part of the interval of convergent motion. As $\psi_S \leq \psi_{GM}$ for all θ the function of *Shinohara* [1990] is a suitable approach to limit A. Moreover it accounts for additional deformation during shear motion. Summarising, ψ_S represents the best approach presented here.

Finally, the deformation function is applied to the evolution equations of ice concentration and ice thickness Equations (2.4) and (2.7) respectively. Fol-

---

[c] An isotropic medium shows the same characteristics in all directions. Assuming isotropy of ridging means that for example the number of ridges counted along profiles of constant length is the same in all cases no matter which orientation the profile lines have on the sea ice cover. The assumption is only true for areas of considerable size, e.g. a model grid cell of $\sim 28 \times 28$ km^2.

lowing the studies of *Schulkes* [1995] and *Gray and Killworth* [1996] the vertical velocity components are substituted according to Equations (5.7) and (5.8) and thermodynamic effects are neglected for simplicity:

$$\frac{\partial A}{\partial t} + \vec{u} \cdot \nabla A + A \nabla \cdot \vec{u} - \psi = 0 \tag{5.13}$$

$$\frac{\partial H}{\partial t} + \vec{u} \cdot \nabla H + \frac{H}{A} \psi = 0 \,. \tag{5.14}$$

Multiplying Equation (5.13) with H and Equation (5.14) with A, and adding the two new equations yields the evolution equation of mean ice thickness, which is already known from Equation (2.8):

$$\frac{\partial h}{\partial t} + \vec{u} \cdot \nabla h + h \nabla \cdot \vec{u} = 0 \,. \tag{5.15}$$

Obviously, an implication for the mean ice thickness does not evolve by introducing the deformation function ψ because the terms including the deformation function are eliminated when adding the modified Equations (5.13) and (5.14). This is the required result: keeping conservation of ice volume while limiting ice concentration ($A \leq 1$).

5.4 The β-function

After examining the dependence of the deformation schemes on the state of motion a closer look at their dependence on ice concentration is necessary.

The deformation scheme ψ_{H1} of *Hibler* [1979] satisfies the numeric requirements but describes ridging only in the case of a completely closed ice cover. However, deformation occurs even when the overall ice compactness of a defined unit area, i.e. a model grid cell, is still below 100%. Concentrations above 80% may already imply the collision of single floes and hence result in ridging within the unit area.

Moreover, ψ_{H1} includes an unsteadiness given by the application of the step function $\mathcal{H}(A - 1)$ when the ice concentration reaches unity. This may cause high frequency oscillations while the system adjusts to the new state [*Schulkes*, 1995]. In order to avoid these artificial oscillations and to account for ridging before ice concentration reaches unity a smooth transition function is required that is differentiable in all cases of A. Different approaches of the function $\beta(A)$ after *Gray and Morland* [1994] and *Hibler* [1979] are presented in Figure 5.3 and are listed below:

$$\beta_1 = \begin{cases} 0 & , \text{ if } 0 \leq A \leq A_{crit} \\ \dfrac{A - A_{crit}}{1 - A_{crit}} & , \text{ if } 0 < A_{crit} < A \leq 1 \end{cases} , \quad A_{crit} = 0.9 \tag{5.16a}$$

$$\beta_2 = A^m , \quad m = 20 \tag{5.16b}$$

$$\beta_3 = \exp\left(-C^*[1 - A]\right) , \quad C^* = 20 \tag{5.16c}$$
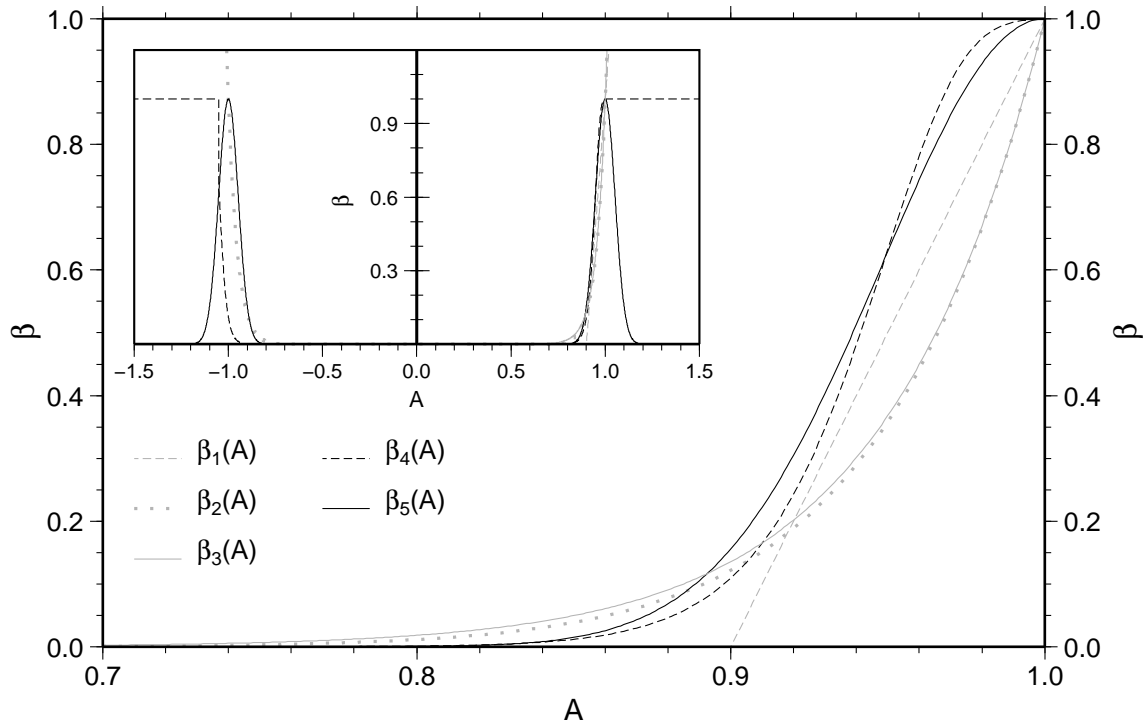
Figure 5.3: Different approaches of the β-function. Complete function formulations are given in Equation (5.16).

The functions β_1 and β_2 were suggested by *Gray and Morland* [1994] together with the Introduction of the deformation scheme ψ_{GM}. The definition of β_1 is the simplest approach apart from applying a Heaviside step function $\mathcal{H}(A-1)$. Unfortunately *Gray and Morland* [1994] did not give a defined value af A_{crit}. Here, 0.9 is chosen in Equation (5.16a) because with $A_{crit} = 0.9$ the curve of β_1 is positioned between the results of various other β-function approaches, as shown in Figure 5.3. For the same reason $m = 20$ is chosen for Equation (5.16b).

The function β_3 was introduced by *Hibler* [1979] for application in the formulation of the ice strength P (see Equation (2.22) and Figure 2.2). In the case of $m = C^*$, functions β_2 and β_3 converge with increasing m and C^* respectively. The advantage of β_2 is that its function value equals zero exactly when A equals zero whereas β_3 will allow a finite though small amount of ridging to take place, even if there is no ice. Thus β_3 might lead to negative ice concentrations during ongoing pure shear motion although this is very unlikely to happen in sea ice simulations [*Gray and Morland*, 1994].

The application of a deformation scheme ψ to a model is intended to restrict the ice concentration to $0 \leq A \leq 1$. However, numerical inaccuracies, due to the discretisation of the evolution equations, may still cause $A > 1$ within a time step[d]. The ice concentration may exceed unity after calculation of the

---

[d]The calculation of the advection term consists of two steps in each time step Δt: (1) using

advection term $\nabla \cdot (A\,\vec{u})$ and before the calcualtion of the deformation scheme ψ balances the possible surplus. Hence, the β-function included in ψ should not exceed unity in the case of $A > 1$. However, this is not the case for functions β_1, β_2 and β_3, which all feature a strong slope for $A > 1$.

Prescribing a constant value of 1.0 for ice concentrations above unity causes an undifferentiable point at $A = 1$ for functions β_1, β_2 and β_3 and leads to the same problems known from β_1 at A_{crit}. In order to match the requirements $\beta(A \leq 0) = 0$ and $\beta(A \geq 1) = 1$ with differentiability for all A two new realisations of the β-function are introduced and discussed in the following. The first new β-function

$$\beta_4 = 1 - \exp\left(-[1.05\,A]^{42}\right) \tag{5.17}$$

does not fulfil these requirements entirely because it holds $\beta_4(A = 1) = 1$ only within an error of magnitude 10^{-4}. The function values of β_4 approach unity asymptotically for $A \to \infty$.

A second new β-function

$$\beta_5 = \left| \cos\left(\frac{\pi}{2}[1 - A]\right) \right|^k , \quad k = 200 \tag{5.18}$$

equals exactly zero and unity at the limits $A = 0$ and $A = 1$ respectively. The parameter k determines the positive slope of the function within the interval $A = [0, 1]$ and thus the minimum ice concentration for which deformation is allowed. k is chosen to equal 200 here in order to have a similar minimum ice concentration for β_5 as for β_2 and β_3. As can be seen in the inset panel in Figure 5.3 the values of β_5 decrease exponentially for $A > 1$. The requirement $\beta_5(A > 1) = 1$ can be met by replacing β_5 by the constant value of 1 when $A > 1$. This does not affect the differentiability because the first derivative $(\partial\beta_5/\partial A)_{A=1}$ equals 1.0 at this point. The reflective symmetry in the point $A = 0$ of both new functions β_4 and β_5 can be handled the same way, since $(\partial\beta_{4,5}/\partial A)|_{A=0} = 0$ holds in each case. This means that the functional values can be replaced by a constant of 0. Summarising, the β-function finally applied to the sea ice model equations described in the next chapter is

$$\beta(A) = \begin{cases} 0 & , \text{ if } A < 0 \\ \beta_5(A) & , \text{ if } 0 \leq A \leq 1 \\ 1 & , \text{ if } A > 1 \end{cases} \tag{5.19}$$

The shape of the new β-function differs from those of the previous approaches of Equations (5.16a)–(5.16c) (Figure 5.3) and more deformation is allowed for ice concentrations above 0.9. With the new β-function the amount

---

the old scalar quantities and a time step $^1\!/_2\Delta t$ to estimate their distribution at the time when the new velocities are defined, and (2) using these temporary scalar quantities and a time step Δt to calculate the new distribution (M. Harder, 1994, comment in model code).

of deformation at ice concentrations in the range of $[0.98, 1.0)$ does not change significantly. However, as there are no constraints on the shape of β within the range $0 \leq A \leq 1$—besides the fact that deformation is rather unlikely for low ice concentrations—any shape is possible. In the new β-function a change in shape can be achieved by varying the exponent k in Equation (5.18). For smaller (larger) values of k deformation is enabled for lower (higher) ice concentration.

5.5 Rafting: an intermediate state of deformation

Two different kinds of deformation are most common in sea ice: rafting and ridging. Thin ice is elastic enough not to break into blocks, and floe sheets shift on top of each other. With increasing floe thickness the elasticity vanishes and the pressure is released in a crushing of the ice floe edges at the frontal zone rather than in a clear fracture. The critical thickness above which ridging is more likely than rafting depends on material properties, such as temperature of the ice as well as porosity and brine volume. *Parmeter* [1975] found this critical ice thickness H_{crit} to be predictable using

$$H_{crit} = 14.2 \frac{1 - \nu^2}{\rho_w \, g} \frac{\tilde{\sigma}_t^2}{\mathcal{E}} \tag{5.20}$$

where $\nu = 0.3$ denotes the Poisson ratio. The water density is $\rho_w = 1028.5 \, \mathrm{kg^1 m^{-3}}$ and gravity $g = 9.81 \, \mathrm{m^1 s^{-2}}$. The critical ice thickness H_{crit} of rafting depends mainly on the tensile strength $\tilde{\sigma}_t$ and the elastic modulus or Young's modulus $\mathcal{E}$. Young's modulus is defined as the ratio of tensile stress and strain. Average values of first-year ice for the tensile strength and Young's modulus are $\tilde{\sigma}_t = 0.8$ MPa and $\mathcal{E} = 5.5$ GPa respectively [*Richter-Menge and Jones*, 1993]. These values yield a critical ice thickness of 15 cm.

The ranges of both tensile strength and Young's modulus have been found to be larger than originally stated by *Parmeter* [1975]. *Richter-Menge and Jones* [1993] specified $0.1 \leq \tilde{\sigma}_t \leq 1.1$ MPa and $3 \leq \mathcal{E} \leq 8$ GPa depending on the actual strain rate acting on the ice. The authors derived these values from an investigation of 103 ice cores from real floes—instead of the usual ice laboratory experiments. Applying Equation (5.20) the observations of *Richter-Menge and Jones* [1993] yield critical ice thicknesses in the range of 5 to 25 cm. The early calculations of the critical ice thickness of *Parmeter* [1975] lie within this range. The mean value of 15 cm of this range matches the impression of *Weeks and Kovacs* [1970] that there is a state of transition between rafting, finger rafting and ridging at about 15 cm ice thickness, especially when both floes have the same thickness.

In numerical models for which rafting is a subscale process this deformation process is reflected by a simple doubling of the actual level ice thickness

(e.g. *Haapala* [2000]). The ridging algorithms presented in the next chapter neglect rafting entirely or account for this process only as an intermediate state of deformation, which is not parameterised separately. Though rafting is not considered, the critical ice thickness $H_{crit} = 15$ cm is applied in order to disable ridging in case of very thin ice.

Chapter 6

Three approaches to ridge modelling

In this chapter the sea ice model presented in Chapter 2 is extended to include the computation of ridge quantities such as sail density and height. For this purpose a new ice category which represents ridged ice is introduced to the model, allowing level and ridged ice to be distinguished and treated in separate evolution equations. The additional ice category is used in two of the three ridging algorithms presented in the following sections. Furthermore, the simplified deformation scheme—the cut-off of surplus ice concentrations—is replaced by a physically more suitable approach which was presented in the previous chapter as deformation function ψ_S.

In a large-scale sea ice model ridging is a sub-scale process and thus a parameterisation of related physical processes is required. Coarse models can only compute average values which are valid for a defined area: the model grid cell. In order to obtain the most realistic distribution of modelled ridge quantities and to evaluate the characteristics and quality of different ridge models three approaches are investigated and adapted in the present study. The first ridge algorithm (RA1) is based upon a deformation energy which is determined by the work of internal forces and works with only one ice category. The second approach (RA2) includes a stochastic model for the derivation of ridge density and height. In the third algorithm (RA3) the ridge quantities are introduced as prognostic variables. The two latter ridge models distinguish between level and ridged ice categories. Each of the ridge algorithms are presented in the following. The implications for the underlying sea ice model (SIM) of Chapter 2, which forms the basis of the study, vary between the different approaches.

6.1   Deformation energy based ridging (RA1)

This ridging algorithm was first presented by *Steiner et al.* [1999] and is based upon the deformation energy E_{def} introduced by *Harder* [1997]. The deforma-

tion energy is determined by the evolution equation

$$\frac{\partial E_{def}}{\partial t} + \nabla \cdot (\vec{u}\, E_{def}) = E_{int} + m_{E_{def}}\, E_{def}\, \tilde{M}_h \,. \tag{6.1}$$

This equation is applied to the SIM without affecting previously implemented physical processes. The approach was designed for only one ice category.

The deformation energy is interpreted as sea ice surface roughness. Newly formed ice is considered to be level and to have no stored deformation energy, i.e. the rate of internal work E_{int} performed by the ice during deformation is its only source. This rate of work is expressed by the product of the stress and strain rate tensors [*Rothrock*, 1975]

$$E_{int} = \boldsymbol{\sigma} \cdot \dot{\boldsymbol{\varepsilon}} = \sigma_I \dot{\varepsilon}_I + \sigma_{II} \dot{\varepsilon}_{II} \,. \tag{6.2}$$

It can be split into the sum of the products of the respective principle components because the principle axes of stress and strain rate for sea ice are aligned. During the ridging process energy is absorbed by fracture, elastic deformation, friction and gravitational potential energy which is stored in the newly formed ridge [*Parmeter and Coon*, 1973]. Hence, the rate of internal work of the deformation is balanced by the sum of the rates of potential energy per unit area and of frictional energy loss per unit area [*Rothrock*, 1975]:

$$\sigma_I \dot{\varepsilon}_I + \sigma_{II} \dot{\varepsilon}_{II} = E_{pot} + E_{fric} \,. \tag{6.3}$$

Here, stress is considered to take the unit of force per unit length.

The mean ice thickness h, one of the model's main conserved quantities, is regarded as a carrier of ice roughness and thus the stored deformation energy is considered to decrease at a rate proportional to $\tilde{M}_h = M_h/h$ which relates to the melt rate M_h of the mean ice thickness (see Section 2.3) [*Harder*, 1997]. This yields the sink term on the right hand side of Equation (6.1). The proportionality factor $m_{E_{def}}$, which controls the magnitude of the sink term, is chosen equal to unity [*Steiner et al.*, 1999], i.e. the amount of stored deformation energy decreases at the same rate as the ice volume.

Based on the deformation energy which represents only a general surface roughness, *Steiner et al.* [1999] developed a method to derive ridge quantities such as keel density and depth. As implied by Equation (6.3) only a certain portion (about 5–20% [*Hopkins et al.*, 1991; *Hopkins and Hibler*, 1991; *Hopkins*, 1994]) of the deformation energy is converted into potential energy to be stored in ridges

$$E_{pot} = c_E\, E_{def} \,. \tag{6.4}$$

Following the study of *Steiner et al.* [1999] a proportionality coefficient $c_E = 0.075$ is chosen, i.e. 92.5% of the deformation energy is lost due to friction. The

potential energy of Equation (6.4) is considered to be an accumulated quantity of all individual potential energy amounts stored in the various ridges of the model grid cell area

$$E_{pot} = \int_{H_0}^{\infty} E'_{pot}(H'_k)\, D_k\, \mathsf{f}_k(H'_k)\, dH'_k\,.$$ (6.5)

Here, E'_{pot} is the potential energy of a single ridge with keel depth H'_k. *Steiner et al.* [1999] linked the keel density D_k directly to the deformation energy itself in the expression

$$D_k = \frac{1}{c_D}\sqrt{\frac{E_{def}}{h}}$$ (6.6)

where h is the mean ice thickness. The proportionality constant c_D has an empirically derived value of $14 \cdot 10^3\ \mathrm{J}^{1/2}\mathrm{m}^{-1/2}$.

In order to describe the probability of occurence of certain keel depths the study of *Steiner et al.* [1999] relied on the probability density function (PDF)

$$\mathsf{f}_k(H'_k) = \frac{1}{\langle H_k \rangle - H_0}\exp\left(\frac{H_0 - H'_k}{\langle H_k \rangle - H_0}\right)$$ (6.7)

which follows the approach of *Wadhams and Davy* [1986]. The PDF depends on the cut-off depth (height) H_0 considered in keel (sail) derivations from observational data.

Steiner et al. [1999] derived the mean keel depth based on the assumptions of a Gaussian cross-sectional shape of the ridge keel and sail (see Figure 1.11d) as well as a sail height to keel depth ratio of 4.5 [empirical, after *Tucker et al.*, 1984] and a porosity of 20% [*Melling and Riedel*, 1995]. The one real solution of the integral of the potential energy (Equation (6.5)) yields a cubic equation for the mean keel depth.

In the present study the above algorithm of *Steiner et al.* [1999] is used for comparison and is adapted for deriving sail quantities instead of keel values because both the observational data that will be used for algorithm evaluation and the two alternative ridge algorithms presented in the following all are based upon sail quantities.

Finally, it should be stated that the deformation energy E_{def} enables the derivation of a roughness dependent drag coefficient [*Steiner*, 2001]. A spatially varying drag coefficient may affect the model results on different levels and is not considered in the following in order to keep the subsequent model experiments on ridge formation simple.

6.2   Redistribution of deformed ice

In contrast to the previous ridging algorithm the second and third ridge algorithms require two ice categories: level and ridged ice. The implementation of

these ice categories to the SIM follows the work of *Harder and Lemke* [1994] for a similar sea ice model applied to the Weddell Sea and is based upon the ideas of *Flato and Hibler* [1991]. The conserved quantities ice concentration (A) and mean ice thickness (h) are now the sums of contributions of level (index l) and ridged ice (index r):

$$h = h_l + h_r \tag{6.8}$$

$$A = A_l + A_r \,. \tag{6.9}$$

Ice strength and ice drift velocity are computed from the total values on the left hand side of the above equations. Further, the actual ice thicknesses of the level and ridged categories are defined as $H_l = h_l/A_l$ and $H_r = h_r/A_r$, consistent with Equation (2.1).

The introduction of a new ice category has implications for the evolution equations of ice concentration and mean thickness. First, separate evolution equations are required for each ice category and second, a redistribution function is added which accounts for the transformation of ice from one thickness category to the other driven by mechanical deformation. The evolution equations of ice concentrations are

$$\frac{\partial A_l}{\partial t} + \nabla \cdot (\vec{u} \, A_l) = R_A \, T_A - Q_A + \text{growth rates} \tag{6.10a}$$

$$\frac{\partial A_r}{\partial t} + \nabla \cdot (\vec{u} \, A_r) = -R_A \, T_A + \text{growth rates} \tag{6.10b}$$

and for the mean ice thicknesses

$$\frac{\partial h_l}{\partial t} + \nabla \cdot (\vec{u} \, h_l) = T_A \frac{h_l}{A_l} + \text{growth rates} \tag{6.11a}$$

$$\frac{\partial h_r}{\partial t} + \nabla \cdot (\vec{u} \, h_r) = -T_A \frac{h_l}{A_l} + \text{growth rates} \,. \tag{6.11b}$$

The rate of dynamic change is given by the transformation term T_A which is defined as

$$T_A = \frac{1}{2} \left[(\dot{\varepsilon}_{11} + \dot{\varepsilon}_{22}) - \Delta_\varepsilon \right] \beta(A) \tag{6.12}$$

and is interpreted as level ice area transformed to ridged ice according to *Harder and Lemke* [1994]. Hence, the product $T_A \, H_l$ gives the transformed ice volume in Equation (6.11). The term T_A yields negative values and accounts for deformation and subsequent redistribution under both shear and convergent ice drift. The Δ_ε-term is defined in Equation (2.23) and equals $\sqrt{\dot{\varepsilon}_I^2 + e^{-1} \dot{\varepsilon}_{II}^2}$. According to Chapter 5 the term T_A equals ψ_S of Equation (5.12) divided by ice concentration, which is that of level ice (A_l) in this case. The β-function was originally chosen by *Harder and Lemke* [1994] to equal β_3 of Equation (5.16c) but is replaced in

the present study by $\beta(A)$ of Equation (5.19) due to the reasons discussed in Section 5.4.

The ridging factor R_A of Equation (6.10) is a dimensionless positive number smaller than one and is chosen to be 0.5 [*Harder and Lemke*, 1994]. It represents the ratio of the area covered by the newly deformed ice to the former parent ice area and reflects the fact that the new ridged ice thickness is larger than the thickness of the level ice: $H_r > H_l$.

In the above evolution equations the thermodynamic growth rates are the thermodynamic source and sink terms of the original SIM Equations (2.35) and (2.34). However, newly formed ice is considered to be initially undeformed, so that growth rates for open water are only applied to the level ice category. The same holds for the rate of lead opening (Q_A) under shear motion which is introduced in Equation (2.36). Here, Q_A is required in order to make the deformation process energetically consistent with the elliptical yield curve because the shear strength which results from the energy sink of ridge formation is assumed to be finite [*Rothrock*, 1975; *Flato and Hibler*, 1991].

The model thermodynamics include seven artificial level ice thickness classes which are equally distributed between 0 and $2H_l$ (see Section 2.3) and seven ridged classes which are equally distributed between H_l and $2H_r$. *Harder and Lemke* [1994] chose a distribution between 0 and $2H_r$ for ridged ice but here it is found to be more suitable to assume the deformed ice to be at least as thick as the level ice on average.

The evolution equations of level and ridged ice concentrations as presented in Equation (6.10) are applied to the second ridge algorithm (RA2) but are changed for the third ridge algorithm (RA3): In RA3 the ridged ice area fraction A_r is calculated as a function of the modelled sail density (D_s) and sail height (H_s) deviating from the underlying study of *Lensu* [2003a] (see Section 6.4). A relationship between sail density and height and the corresponding ridged ice thickness H_r is found

$$H_r = 0.3 \, H_s \exp\left(0.5 \, \sqrt{D_s}\right) \tag{6.13}$$

based upon studies with a one-dimensional ridge profile model, which was introduced by *Lensu* [2003c] but improved in the present study (see Appendix A). The absolute ridged ice thickness H_r represents the thickness of the deformed ice if all ridge rubble were equally distributed over the entire ice-covered area. The area fraction covered by ridged ice is determined by $A_r = h_r/H_r$. As sail height and density in Equation (6.13) refer to old, advected and newly formed ridges, A_r is a diagnostic variable and does not require an evolution equation. In RA3 the level ice concentration now follows the evolution equation

$$\frac{\partial A_l}{\partial t} + \nabla \cdot (\vec{u} \, A_l) = \psi_s + \text{growth rates} \tag{6.14}$$

134

where the level ice area is reduced by the magnitude of ψ_s according to Equation (5.13).

6.3 Stochastic model derived ridging (RA2)

Based on the redistribution of level ice to a ridged ice category (Equation (6.11)) the sea ice model is now extended to derive estimates of sail density and height. From the volume of newly deformed ice ($T_A H_l$) one can derive the size and the number of ridges, which are represented by the computed deformed ice volume. For this purpose a Monte Carlo simulation[a]-like method is applied. Here, random samples of ridges are generated where the sample size is limited by the newly deformed ice volume. The probability distributions of sail height and length inferred from observational data are prescribed.

In this ridge algorithm sail density (D_s) and height (H_s) are determined by evolution equations

$$\frac{\partial D_s}{\partial t} + \nabla \cdot (\vec{u}\, D_s) \quad = \quad D'_s \quad + \text{ablation} \tag{6.15}$$

$$\frac{\partial (D_s H_s)}{\partial t} + \nabla \cdot (\vec{u}\, D_s H_s) \;=\; D'_s \langle H'_s \rangle + \text{ablation}\,, \tag{6.16}$$

The sail height H_s represents an average height of the newly formed sails $\langle H'_s \rangle$ and old, advected ridges weighted by the sail density of the new and old sails respectively. The above evolution equations emphasise the source terms of dynamic ridge growth which, in this case, are based upon the stochastic model because the present study focusses on ridge formation. These first terms on the right hand side of the above equations will be explained in detail in the following. Additional sink terms describing the effect of ridge ablation, i.e. a thermodynamic decrease of sail density and height, are discussed separately in Section 6.5.

The volume of a ridge is determined by the height and length of its sail under the following assumptions: sail and keel are of triangular cross-sectional shape (see Figure 1.11b), and ratios of keel depth to sail height k as well as sail width to sail height l_s and keel width to keel depth l_k are constant. The three-dimensional volume of a ridge with sail height H'_s and length L'_s is given by

$$V' = \frac{1}{2}\, c_v\, \left(l_s + l_k\, k^2\right)\, H'^2_s\, L'_s \tag{6.17}$$

---

[a] The Monte Carlo method is used to verify a statistical hypothesis which is based upon a small sample size. The test statistics are improved by enlarging the sample size artificially on a computer. Hence, a Monte Carlo simulation bases on the resampling of observational data consistent with the null hypothesis. The artificial data set has the same statistical characteristics as the original data collection. Most random number algorithms generate pseudo-random numbers which are sufficient for Monte Carlo simulations but as the quality of the generators varies a careful use is essential. [e.g. *Wilks*, 1995; *Storch and Zwiers*, 2001]

where $c_v = 0.7$ is a correction factor which accounts for the porosity of ridges, because 20–35% [*Melling and Riedel*, 1995; *Hoyland*, 2002] of the triangular ridge consists of enclosed air and sea water. Only the ridge volume fraction containing sea ice from the parent level ice floe is considered because the total ridge volume V of all newly formed ridges must balance the redistributed ice volume $T_A H_l$. Ratios $l_{s,k}$ and k are determined from observational data. While the keel depth to sail height ratio k is considered to be 6.3 based on the findings from EM bird data (see Section 4.3) the ratio of sail width to height (l_s) is chosen to be 4.5 and that of keels (l_k) to be 3.5 following average values of first year ridges[b] [*Timco and Burden*, 1997; *Wadhams*, 2000].

Random numbers of a particular statistical distribution can be drawn by applying the inverse function of the respective cumulative distribution function (CDF, see Appendix B.3) [*Wilks*, 1995]. The CDF is used to transform computer generated uniform random numbers to the desired PDF. The CDF for sail height is derived from the PDF given in Equation (4.3)

$$\mathsf{F}_s(H_s) = 1 - \tilde{a} \, \exp\left(-b \, H_s'\right) \tag{6.18}$$

where parameters $b = (\langle H_s \rangle - H_0)^{-1}$ and $\tilde{a} = 0.09 \exp\left(b \, H_0\right)$ are determined from observational data (see Equation (4.4)). A cut-off height $H_0 = 0.8$ m, which is the same applied to laser altimeter data, is introduced to the model in order to allow direct comparison between simualtions and observations. The average sail height $\langle H_s \rangle$ is derived from the level ice thickness according to the power law $\langle H_s \rangle = 1.24 \, H_l^{0.1}$ presented in Section 4.5.

The length of pressure ridges corresponds to the length of fractures in the sea ice cover and hence is directly proportional to the floe size. The CDF of fracture lengths typically follows the power law

$$\mathsf{F}_L(L_s) = 1 - \left(\frac{L_s'}{L_0}\right)^{-\hat{b}} \tag{6.19}$$

where L_s' is measured in km and exponent $\hat{b}$ ranges between 1.3 and 2.2 [*Weiss and Marsan*, 2004, and citations therein]. Here, $\hat{b}$ is chosen to be 1.8 [*Zyryanov and Smirnov*, 2006]. L_0 is a lower bound of ridge lengths considered, which is

---

[b] Assuming ratios of the magnitude $l_s = 4.5 \pm 1$ and $l_k = 3.5 \pm 1$ the mean of the ridge volume factor $\frac{1}{2}\left(l_s + l_k \, k^2\right)$ of Equation (6.17) increases exponentially from about 20 to 90 for values $k \in [3, 7]$. The standard deviation due to the varying l_s- and l_k-values amounts to about 16% of the respective mean value. The fraction of the sail volume compared to total ridge volume decreases exponentially with increasing k from 13% to 3%. Applying the chosen ratios $l_s = 4.5$, $l_k = 3.5$ and $k = 6.3$ the volume factor amounts to 71.7 and is thus at the upper end of the typical range of values, implying that the algorithm tends to generate fewer ridges with these parameter settings.

larger than zero and set to 0.1 km here[c].

The generation of random values of H'_s and L'_s is repeated until the sum of the single ridge volumes $\sum V'$ balances the volume of the newly deformed sea ice $T_A H_l$.

The average sail height $\langle H_s \rangle$ which enters Equation (6.18) is derived from observations and represents the basic population of the distribution. It may differ from the average of all random samples $\langle H'_s \rangle$ drawn within one model time step. The random samples are interpreted as a sub-sample of the population and $\langle H'_s \rangle$ represents the mean sail height of all newly formed ridges and is thus the source of the model variable H_s (see Equation (6.22)).

After *Mock et al.* [1972] the sail density (D'_s), which can be observed along arbitrarily oriented profiles across a certain ice-covered area assuming isotropy of ridging, is determined by the total length of all sails $\sum L'_s$ within this area

$$D'_s = \frac{2}{\pi} \frac{\sum L'_s}{A \, \Delta x \, \Delta y} \frac{1}{\Delta t} \,. \tag{6.20}$$

The area dimensions Δx and Δy equal the grid node spacing of the large-scale sea ice model. D'_s represents the number of newly formed ridges per km within one time step Δt and is thus added to the number of old, advected ridges in the evolution equation of sail density D_s (Equation (6.15)).

After *Lewis et al.* [1993] the above Equation (6.20) also allows the actual thickness of ridged ice H_r to be linked to the ridge intensity $R = H_s^2 D_s$ of Equation (4.2). Assuming the cross-sectional area of a ridge is given by $(1+k) \cot \phi \, H_s^2$ where k is the ratio of keel depth to sail height and ϕ denotes the ridge slope angle, which is assumed to be the same for sail and keel, it is possible to derive the relation $H_r = \frac{1}{2}\pi(1+k) \cot \phi \, R$ [compare *Lewis et al.*, 1993, Equ. 8]. This offers the opportunity to derive the ridge intensity R from sea ice models which consider a ridged ice thickness category prescribing only two parameters: the keel to sail ratio and the slope angle.

In summary, the evolution of pressure ridges in algorithm RA2 is strictly linked to the deformation rate of ice volume as derived by the redistribution function T_A. The values of sail density and height do not have any implication on the amount of deformed ice in this ridge model approach.

---

[c] The sail length L'_s may not exceed the dimensions of the model grid cell and an upper bound of 10 km is chosen. Monte Carlo simulations showed that the maximum values randomly drawn from the inverse function of Equation (6.19) follow a log-normal distribution with a modal value of 0.5 km and less than 0.5% of all L'_s drawn exceed 10 km. If L'_s exceeds the grid cell dimensions the algorithm will reject this sample and repeat the random process.

6.4 Prognostic derivation of ridge quantities (RA3)

The third ridging algorithm also includes evolution equations for sail density and sail height. The underlying theory describes the change of ridge density per unit change of total ice area and considers formation of new ridges as well as changes in sail density due to the advection of old ridges. However, in this ridging algorithm the amount of newly formed ridges relies on a constant level ice area consumption per ridge. The algorithm is based upon the ridge model of *Lensu* [2003a] as described in *Lensu et al.* [2003] and *Axell et al.* [2005]. The evolution equations for sail density D_s and sail height H_s are

$$\frac{\partial D_s}{\partial t} + \nabla \cdot (\vec{u}\, D_s) \quad = \quad \alpha\, \gamma(H_l) \qquad\qquad + \text{ablation} \qquad (6.21)$$

$$\frac{\partial (D_s H_s)}{\partial t} + \nabla \cdot (\vec{u}\, D_s H_s) \quad = \quad \alpha_0\, H_s' + (\alpha - \alpha_0)\, H_s + \text{ablation}\,. \qquad (6.22)$$

The model of *Lensu* [2003a] only describes ridge formation and neglects ridge ablation. This simplification is practicable for the seasonal sea ice cover of the Baltic Sea but is insufficient for multi-year ice of the Arctic Ocean. Therefore, possible parameterisations describing the effects of ridge weathering on sail density and height are presented in Section 6.5.

First, the source term of sail density $\alpha\, \gamma(H_l)$ is reviewed. It depends mainly on the total increase in ridge density per unit length

$$\alpha = \frac{\psi_S}{\varphi}\,, \qquad (6.23)$$

which not only represents the rate of newly formed ridges but also accounts for the increase in sail density due to the differential movement associated with the ridge formation [*Lensu*, 2003b]. The latter reduces the spacing between existing ridges and thus increases the sail density. The deformation function ψ_S stems from Equation (5.12)[d].

The ridging algorithm RA3 essentially controls the relative change in total ice area per unit change of ridge density which is given by

$$\varphi(D_s) = \frac{1}{\tilde{A}} \frac{\partial \tilde{A}}{\partial D_s} \qquad (6.24)$$

where $\tilde{A} = A\, \Delta x\, \Delta y$ denotes the total ice covered area within a defined area with dimensions Δx and Δy. The ridge density is characterised by the sail density

---

[d] The ridge model of *Lensu* [2003a, see Equ. 136] as well as subsequent developments presented in *Lensu et al.* [2003] and *Axell et al.* [2005] only account for ridging under pure convergent motion, i.e. $\alpha = -\nabla \cdot \vec{u}/\varphi$ in the case of $\nabla \cdot \vec{u} < 0$ and $\alpha = 0$ otherwise. Now, in order to consider ridging also under shear motion the complete deformation scheme ψ_S of Equation (5.12) is used in Equation (6.23) instead.

D_s assuming that each ridge consists of exactly one sail and one keel. Furthermore, a geometrical ridge model of triangular shape is applied (see Figure 1.11b) with a cross-sectional volume (V) and a fixed ratio between sail height and keel depth. This choice allows the total ridge height to be expressed simply by the sail height. The total ice volume stored in ridges in a defined area is expressed as

$$V_r = \tilde{A}\, D_s\, V\,. \tag{6.25}$$

The expression volume actually denotes an area—volume per unit ridge length—in this case because a cross-section perpendicular to the longitudinal dimension of the ridge is described. This model approach considers that there are types of deformation different from ridging, such as rafting, although ridging is considered to be the main contribution to the total deformed ice volume per unit area (h_r). Thus, the ridged ice volume per unit ice-covered area $D_s V$ is smaller than or equal to h_r. The relative change of the ridged ice volume is balanced by the level ice area consumed times its thickness

$$-\, H_l\, \partial \tilde{A} = \partial V_r\,. \tag{6.26}$$

Differentiating Equation (6.25) with respect to D_s and applying Equation (6.26) allows Equation (6.24) to be rewritten:

$$\varphi(D_s) = -\frac{1}{D_s\, V + H_l}\frac{\partial(D_s\, V)}{\partial D_s}\,. \tag{6.27}$$

Lensu [2003a] states that the volume V of the geometric ridge model is affected by clustering. If large ridge densities occur, the keels of neighbouring ridges will merge and hence the assumption of triangular keels no longer holds. Therefore, *Lensu* [2003a] introduced a clustering function $\xi(D_s, H_s)$ which accounts for the volume reduction due to clustering depending on sail density and height

$$\xi(D_s, H_s) = \max\left\{1.24\,\exp\left(-0.16\sqrt{D_s\, H_s}\right), 1\right\}\,. \tag{6.28}$$

This function is derived by *Lensu* [2004] with a Monte Carlo-type model, which simulates the distribution of ridges along a one-dimensional profile including estimates of sail height and keel depth based upon geometrical constraints (see Appendix A). The volume of the ridge per unit ridge length is thus $V = \xi(D_s, H_s)\, V_0$, where V_0 denotes the assumed triangular cross-sectional volume in the case of completely developed sail and keel, i.e. in the case of $D_s \to 0$.

The variable V_r represents the volume of all ridges within a defined area. Equation (6.26) describes the total amount of ice area consumed by the ridging process assuming that the level ice in the considered area is of constant thickness. The level ice area per unit ridge length consumed by a single ridge is

$$\varphi_0 = \frac{V_0}{H_l}\,. \tag{6.29}$$

Lensu [2003a] derived a value of $1/3.17$ km for φ_0, which corresponds to a consumed ice area per unit ridge length of 315.5 m, using laser profile data of the Baltic and Kara seas. According to the method of *Lensu* [2003a][e] a value of $1/2.51$ km, which corresponds to 402.5 m, is derived from the results of the EM bird data presented in Chapter 4. *Amundrud et al.* [2004] stated that a consumed ice area per unit ridge length of 560 m would be necessary to reach the maximum ridge height in the Beaufort Sea region. This yields $\varphi_0 = 1/1.79$ km and shows that the value of 2.51 km^{-1} used here is a suitable mean value and a valid assumption for Arctic sea ice.

Applying Equations (6.28) and (6.29) to Equation (6.27) the relative change of ice area per unit change of sail density $\varphi(D_s)$ is finally

$$\varphi(D_s) = \begin{cases} -\dfrac{1}{D_s + \frac{1}{\varphi_0}} & \text{, if } \xi = 1 \\[2em] -\dfrac{\xi(D_s, H_s)}{D_s\,\xi(D_s, H_s) + \frac{1}{\varphi_0}}\left(1 - 0.08\sqrt{D_s\,H_s}\right) & \text{, otherwise}. \end{cases} \tag{6.30}$$

The value of $\varphi(D_s)$ is always smaller than or equal to zero and thus the rate of ridge density increase $\alpha \geq 0$.

Turning back to the evolution equation of sail density, it is further considered in the source term of Equation (6.21) that ridging is not the only deformation process and also rafting may take place when thinner ice prevails. In such a case no or fewer new ridges are formed. Thus, the source of sail density includes the transition function γ, which is, in contrast to *Lensu* [2003b] and *Lensu et al.* [2003], a continuous function in the present study. This function accounts for a smooth initiation of the ridging process because it is more likely that thin ice only rafts (see Section 5.5).

$$\gamma(H_l) = \begin{cases} 0 & \text{, } H_l < H_{low} \\[0.5em] \dfrac{1}{2}\left[1 + \cos\left(\pi\dfrac{H_l - H_{low}}{H_{up} - H_{low}}\right)\right] & \text{, if } H_{low} \leq H_l \leq H_{up} \\[1em] 1 & \text{, } H_l > H_{up} \end{cases} \tag{6.31}$$

The bounds H_{low} and H_{up} mark the ice thickness range in which rafting and ridging change probability. They are chosen to be $H_{low} = 0.15$ m, which corresponds to H_{crit} of Section 5.5, and $H_{up} = 2H_{low}$. Below a level ice thickness of H_{low} no

---

[e] Following the ideas of *Lensu* [2003a, section 7.3] a mean sail height of 1.25 m is chosen to be typical for the Arctic sea ice cover (compare Table 4.2), whereas *Lensu* [2003a] used 0.75 m for Baltic sea ice. Moreover, a cut-off height of 0.8 m is used instead of 0.5 m. In this case the ridge link model of *Lensu* [2003a] yields $H_l = 0.384$ m and $V_0 = 152.9$ m^2. Moreover, a mistake in the Equations (152a, d) of *Lensu* [2003a] was corrected by replacing the term $\left((1 - r)\left(\frac{\pi}{2} - 1\right) + 1\right)$ with $\left((1 - r)^2\left(\frac{\pi}{2} - 1\right) + 1\right)$. The mistake also affected Equations (157a, d) and (158) of *Lensu* [2003a].

ridging is assumed to take place and above H_{up} all deformation is attributed to ridging.

Reviewing the evolution equation of sail height (Equation (6.22)) newly formed ridges and those that occur in the profile due to the differential movement are treated separately. Therefore, the rate of new ridge formation α_0 is introduced

$$\alpha_0 = -\frac{1}{\xi} \frac{\psi_S}{\varphi_0} \qquad (6.32)$$

where ξ denotes the clustering factor of Equation (6.28) and φ_0 is the ice area consumed per ridge (Equation (6.29)). It is important to distinguish between old and newly formed ridges because new ridges may have a different sail height (H_s') than existing ones (H_s). After *Lensu et al.* [2003] the height of sails is considered to be linked to the parent ice thickness (H_l). Deviating from *Lensu et al.* [2003], the relationship $\langle H_s \rangle = 1.24\, H_l^{0.1}$, which is deduced from the results of the EM bird measurements of Chapter 4, is used in the present study in order to emphasise Arctic sea ice characteristics.

However, in the evolution equations for sail density and height of RA3 it is neglected that *Lensu* [2003b] originally weighted sail density and height by ice concentration because the EM bird measurements, which will be used for validation, do not allow the open water fraction of the profiles to be calculated (see Section 4.2).

As presented in Section 6.2, sail density and height affect the areal fraction covered by ridged sea ice in this ridging algorithm RA3. This is in contrast to RA2, where ice concentration and thickness of deformed ice are not influenced by the ridge quantities.

6.5   Descriptions of ridge ablation

The decay or weathering of ridges particular during the summer season is still infrequently investigated and therefore it is difficult to include this thermodynamically driven process in the ridge algorithms presented in this chapter. In general, ridges offer a larger active surface to the ocean heat flux than level ice does because ridges have a blocky structure with large voids. This implies an increased melting rate for deformed ice. On the other hand, ridges are thicker at their peak keel depths than a mean ridged ice thickness and hence the vertical conductive heat flux through the ridge is smaller—assuming a linear vertical temperature gradient inside the ice—than the heat flux computed for the mean thickness. Observations of ridge ablation are rare and the process has been the subject of few model studies. However, such models focus on the description of very detailed processes in a single ridge. The link to large-scale sea ice models is

still missing. For example, observations of *Leppäranta et al.* [1995] showed that the volume of a single ridge decreased by about 25% within one spring month and the model study of *Schramm et al.* [2000] suggests enhanced basal melting of ridges. *Schramm et al.* [2000] already took into account a two-dimensional ridge structure instead of the common one-dimensional treatment of sea ice thermodynamics.

In the present study simple melt terms are introduced and added to the evolution equations of sail density and height in ridge algorithms RA2 and RA3 according to the thermodynamic sink term in the evolution equation of the deformation energy of RA1 (see Equation (6.1)). The melt rate of sail height used in RA2 and RA3 is

$$M_{H_s} = m_{H_s} \, D_s \, H_s \, \tilde{M}_{h_r} \tag{6.33}$$

where $\tilde{M}_{h_r} = M_{h_r}/h$ relates to the melt rate of the mean ridged ice thickness and $M_{h_r} \leq 0$ by definition. The proportionality coefficient m_{H_s} is set to unity for simplicity. This means that the ridge height decreases at the same rate as the mean ridged ice thickness. Based on the above discussion a value deviating from unity is also possible in principle.

Ablation of ridges also means a decrease in sail density, particularly if a cut-off height commonly applied to observational data is considered in the models. A sail does not contribute to the sail density as soon as its height becomes smaller than the cut-off height. Thus, a possible thermodynamic reduction of sail density based upon the CDF of the sail height in ridge algorithm RA2 (Equation (6.18)) is now considered in both evolution equations, that of RA2 and RA3:

$$M_{D_s} = -D_s \left[\mathsf{F}_s(H_s \, \tilde{M}_{h_r}) - \mathsf{F}_s(H_0) \right]. \tag{6.34}$$

The distribution function F_s gives the fraction of sails which drop below the cut-off height H_0 due to the sail height melt rate $H_s \, \tilde{M}_{h_r}$.

Chapter 7

Idealised experiments and sensitivity studies

In this chapter the three ridge algorithms described in the previous one are applied to idealised experiments. These tests show the behaviour of the different algorithms in response to varying initial ice conditions, wind forcing and topography. The simple experimental set-up enables precise control of the model environment and offers the opportunity to investigate the behaviour of the individual algorithms with respect to a few well defined changes in the model configurations. This eases interpretation of the simulation results and ensures a proper applicability of the ridging algorithms for realistic Arctic conditions later on. A few preliminary results of the following experiments are also included in *Martin* [2006].

7.1 Experimental set-up

As ridge formation is an entirely dynamic process any thermodynamic processes are neglected in all experiments of this chapter. The ridging events studied in these idealised tests take place within 30 hours. This period is considered to be short enough to neglect the change in ice thickness due to freezing or melting[a]. Furthermore, the ocean is defined to be inactive, i.e. its speed is zero ($|\vec{u}_w| = 0$), and the oceanic drag acts only as a retarding force.

---

[a] Following the zero-layer model of *Semtner* [1976] the sea ice growth rate is given by $\frac{\partial H}{\partial t} = \frac{\lambda_i}{\rho_i L_i} \frac{\tilde{T}}{H}$. Applying parameter values of thermal conductivity $\lambda_i = 1.0$–2.5 W m^2, sea ice density $\rho_i = 910$ kg m^{-3}, specific latent heat $L_i = 3.34 \cdot 10^5$ J kg^{-1}, temperature difference between ice surface and bottom $\tilde{T} = 0$–30 K and ice thickness $H = 0.3$–1.5 m yields a mean ice growth of 1–2 cm within 30 hours and a maximum of 9 cm.
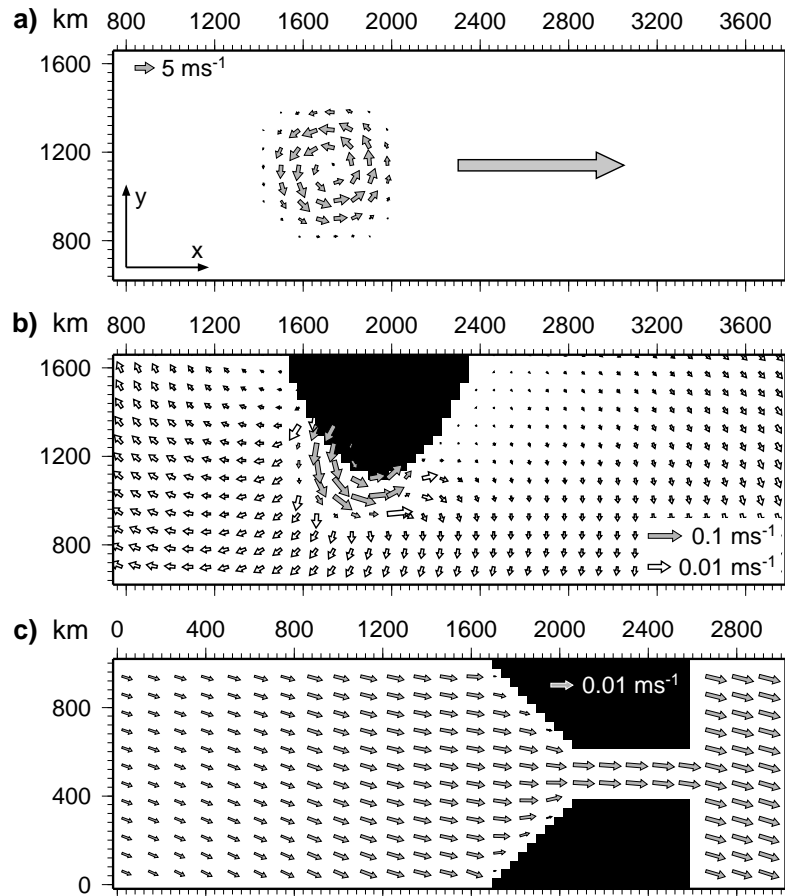
Figure 7.1: In the idealised tests various model grids are applied: (**a**) A basin with no topographic features; the wind field of the cyclone is shown and its direction of travel is indicated with a large, grey arrow to its right. (**b**) A peninsula protruding into the pathway of the cyclone; vectors indicate the ice drift field caused by the cyclone wind forcing—regard the two different speed scales. (**c**) A strait parallel to the wind direction; vectors indicate the ice drift from a steady westerly wind forcing. Black shaded grid cells mark land areas. The x-y indicator in (a) is valid for all three figures and the maps are oriented such that y points to the north. In all cases only every second vector is plotted for enhanced clarity.

7.1.1 Model grid and topography

In all experiments the sea ice model is applied to a simple rectangular domain with a horizontal grid resolution of 40 km. This resolution is chosen in order to obtain results which are directly comparable to the study of *Haapala et al.* [2005]. A time step of 2 hours is chosen in order to make changes in wind forcing small between time steps.

The grid topography is modified for different experiments. First, tests are made with no topography. All boundary grid cells are defined to be outflow cells, i.e. the rectangular domain is not decoupled from its surrounding environment and can be interpreted as a cut-out of a larger ice-covered ocean (see

Figure 7.1a). The grid is centred at $80\,^\circ$ N (y-position 1200 km) as in *Haapala et al.* [2005]. This is particularly important for the coriolis force. The grid dimensions are chosen to be rather large (4000 km $\times$ 2400 km) in order to avoid any interference with the grid boundaries.

In a second step the geometry of the model grid is changed. The ice drift is disturbed by a topographic obstacle, a peninsula of almost triangular shape protruding into the track of the cyclone (see Figure 7.1b and Section 7.1.3).

A third grid set-up contains a strait of width 240 km (Figure 7.1c). In this experiment the grid has smaller dimensions (3200 km $\times$ 1200 km) because the homogeneous wind field does not cause perturbations at the grid boundaries.

7.1.2   Initial ice conditions

The initial ice concentration and thickness are an important factor of the sensitivity studies. By definition all sea ice is regarded to be level ice at the beginning of each experiment. The initial ice conditions are varied in order to identify and understand individual behaviour of the three ridge algorithms. The underlying assumption for the choice of the initial sea ice concentration is that ridging occurs only for concentrations above 80%, as discussed in Chapter 5. Hence, the ridging algorithms are tested for concentrations between 0.8 and 1.0. The magnitude of deformation also depends on the ice thickness, initial ice thicknesses are varied here between 0.3 and 1.5 m. As described in Section 5.5 an ice thickness of 0.3 m is considered to be the minimum ice thickness for which ridging is the only deformation process.

Additionally, the effect of an abrupt change of ice thickness and concentration in the sea ice cover is studied. Two different cases are investigated: (1) an ice regime with an ice concentration of 92% and a thickness of 0.5 m opposes one with 97% and 1.0 m, and (2) the thinner ice regime (0.3 m) has a greater ice concentration (99%) while the thicker ice (1.3 m) is less compact (95%).

For the experiment with the strait topography an initial ice concentration of 0.95 and an ice thickness of 1.0 m were chosen.

7.1.3   Wind forcing

Two different wind fields are applied during the experiments. Most of the tests are made with a cyclone of diameter 640 km centred on y-coordinate 1200 km, moving with a constant travel speed of 480 $km^1 d^{-1}$ in x-direction from west to east. As can be seen from Figure 7.1a the maximum wind speed amounts to about 5 ms^{-1}. The cyclonic wind field was derived from a depression of 970 hPa with a surrounding normal sea level pressure of 1000 hPa. A turning angle of $20\,^\circ$ was used in the final derivation of the surface wind velocity, yielding

cyclonic wind forcing resembling that of *Haapala et al.* [2005] and allowing to set-up an optimal basis for comparison.

The strait experiment is forced with a different wind regime. Here, a field of westerly winds is applied which is constant in the y-direction but variable in strength along the x-axis. The wind speed ranges between 2 and 5 ms^{-1} and reaches a maximum at $x = 2400$ km ($u_a = 2.0 + 3.0\,(1 - |x/2400 - 1|)$), see Figure 7.1c.

7.2 Results of experiments

7.2.1 A moving cyclone

This first test applies the cyclone forcing to a basin covered with a rather thin (0.5 m) though compact (95%) sea ice cover. All main variables, such as level and ridged ice concentration, ridged ice thickness as well as sail density and height, display the same dominant pattern in the wake of the cyclone, which is almost homogeneous along the track (x-direction) but varies considerably across-track
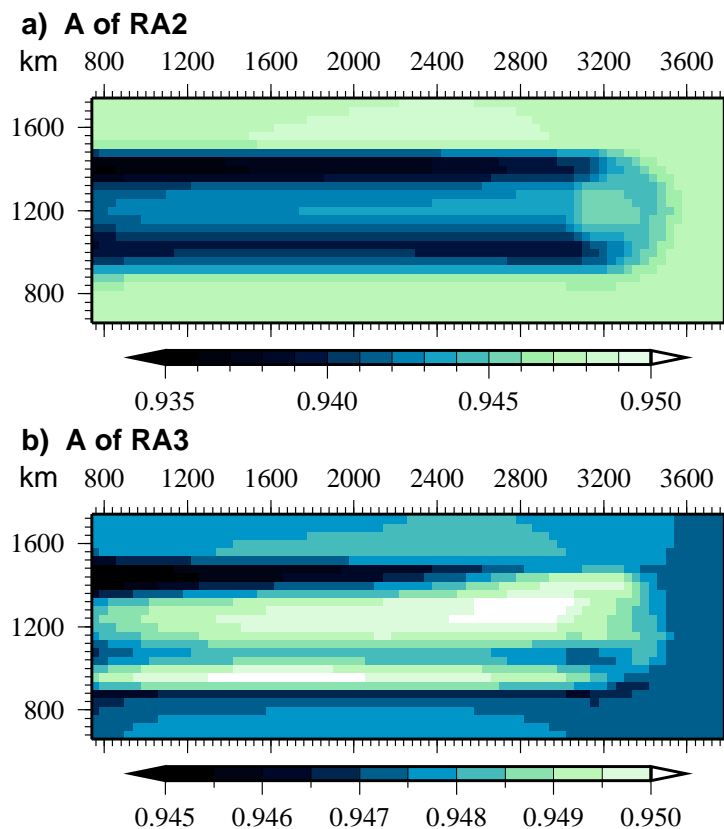
Figure 7.2: Variations in total ice concentration A as caused by the cyclone experiment. For both realisations, with RA2 and RA3, the initial ice concentration was 0.95. Note different colour scales.
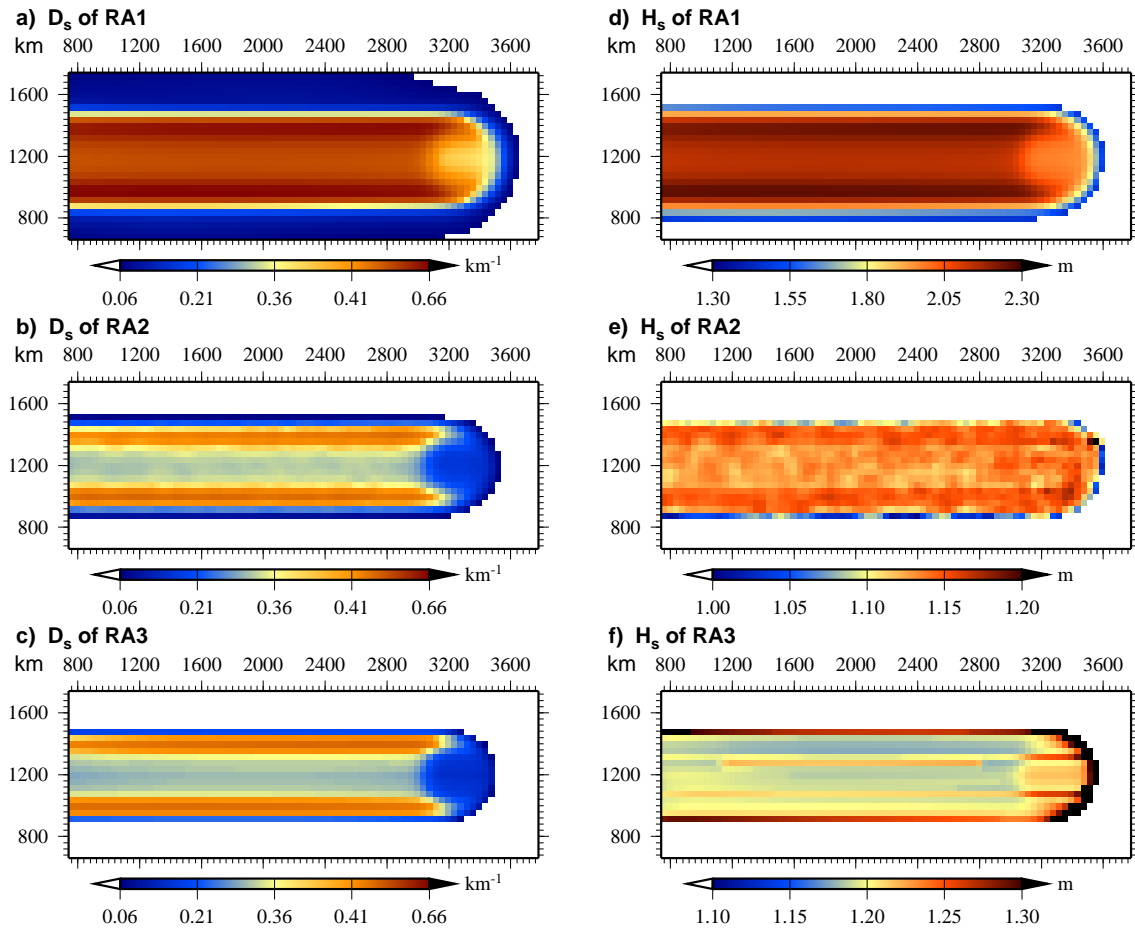
Figure 7.3: (**a–c**) Sail density D_s and (**d–f**) sail height H_s of all three ridge algorithms as caused by the moving cyclone on a grid with no topography. The initial ice concentration was 0.95 and the initial ice thickness 0.5 m.

in the y-direction. The total ice concentration of RA2 is shown as an example of this pattern in Figure 7.2a. The ice concentration is most reduced ($>1\%$) in two bands parallel to the direction of travel of the cyclone. The decrease of ice concentration is smallest in the center of the cyclone track (less than 1%). These values match the results of *Haapala et al.* [2005], who performed a similar study with a sea ice model with multiple ice thickness categories.

Figure 7.3 shows the resulting sail density and height for all three ridge algorithms: deformation energy based ridging (RA1), stochastic model-derived ridging (RA2) and prognostic derivation of ridge quantities (RA3). All show the largest sail density in two bands next to the edges of the cyclone track with a smaller density, reduced by about 0.15 km^{-1}, in the middle of the track (see Figures 7.3a–c). This pattern coincides with that of (level) ice concentration: most ridges occur where the (level) ice concentration is most reduced (compare Figure 7.2a and Figures 7.3a–c). The sail density also has a rather smooth decline towards zero in the y-direction from both maximum bands to the very edge of the track in all three cases. At the current position of the cyclone the sail density

147
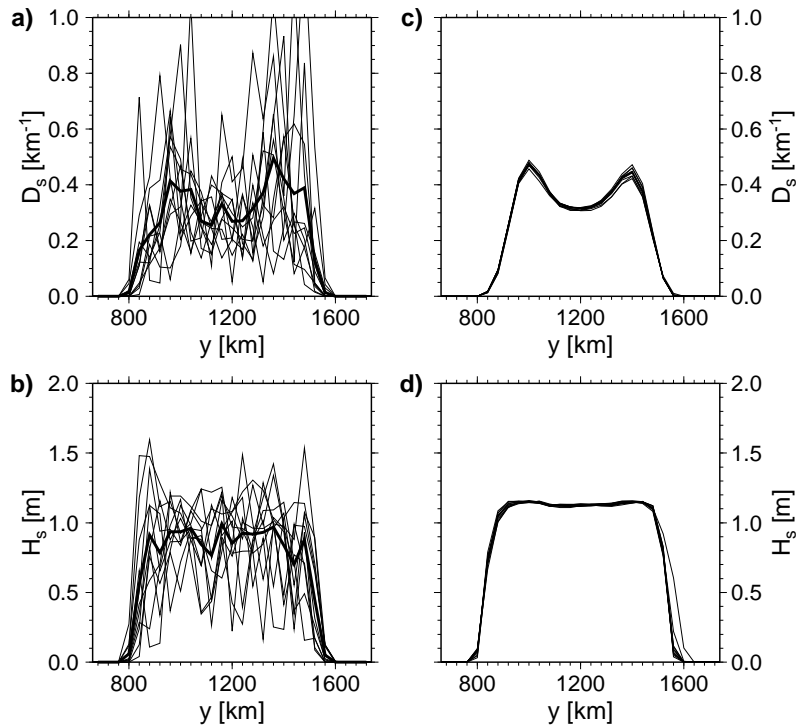
Figure 7.4: The random process included in ridging algorithm RA2 causes artificial noise. Cross-sections along the y-axis at various x-coordinates between 800 and 2800 km (interval is 200 km): (**a**) sail density and (**b**) sail height without averaging, and (**c**) sail density and (**d**) sail height after a 3×3 grid cells smoothing procedure has been applied. Thick black lines in panels (a) and (b) show averages of all cross-sections.

is markedly reduced, particularly in the centre of the cyclone, with a minimum at the front end of the track. The values of sail density range between 0.2 and 0.6 km^{-1}. Ridge algorithm RA1 generally produces a ridge density which exceeds the values of RA2 and RA3 by about 0.15–0.2 km^{-1}. Furthermore, RA1 features a very low, widely spread density whereas the sail densities of RA2 and RA3 decrease much faster towards zero in the vicinity of the cyclone track, with RA3 showing the steepest decrease at the track edges.

The sail heights derived with the three ridging algorithms vary to a greater degree than the sail densities (Figures 7.3d–f). While RA2 and RA3 produce sail heights in the range of 1.0–1.5 m the sails of RA1 are almost twice as large, up to 2.3 m. However, RA1 and RA2 have in common that the sail heights have the same pattern as the sail density: two maximum bands in the region of lowest ice concentration separated by a central band with reduced sail height. In contrast, RA3 has largest sails at the very edge of the cyclone track and at the inner edges of the bands of greatest level ice concentration decrease. With RA3 the sail height in the bands of low ice concentration is the same as in the centre of the cyclone track. However, apart from the pronounced bands of greater sail height, a small positive gradient is also detectable towards the southern rim of

the track.

Sail density and particularly sail height of RA2 feature small-scale variations which are not found in the results of RA1 and RA2. This noise is caused by the Monte Carlo simulation of RA2 and illustrates the non-negligible influence of the random number-based derivation of sail height and density in this ridge algorithm. However, Figures 7.3b and 7.3e show data which are already smoothed during the simulation. The original effect of the random numbers is much stronger as can be seen in Figure 7.4. The original results of the Monte Carlo simulation show considerable noise levels and sail density can vary by up to a factor of 2 and sail height by 50%. Therefore, a smoothing function is applied to derive an average over the 3×3 grid cell-vicinity of each data spot in which the centre value is weighted by a ratio of 3:1 compared to its neighbouring grid cell values. This yields a markedly improved result for the ridge quantities in RA2 (see Figures 7.4c and 7.4d). The magnitude of the smoothed results is about the same as for the average of the noisy data and emphasises clearly the across-track pattern in sail density and height which is also evident in RA1 results and RA3 sail density.

7.2.2   Varied initial ice conditions

In a next step the cyclone experiment is repeated for different ice conditions, i.e. the initial ice concentration and thickness are varied. The initial ice conditions affect not only the evolution of the ridge parameters but also the impact of the cyclone on level and ridged ice concentrations and thicknesses.

Standard sea ice parameters

In this section only results of ridge algorithms RA2 and RA3 are presented because RA1 is typically applied to models with only one ice category and the ridging algorithm has no effect on an eventual redistribution of sea ice. Thus, most of the results presented in the following can not be retrieved from a model to which RA1 would typically be applied.

All experiments are initiated with a homogeneous sea ice cover of pure level ice. Figures 7.5a, 7.5b, 7.5e and 7.5f show the departure of the final level ice concentration from different initial ice conditions for RA2 and RA3. For initial ice concentrations above 0.9 the decrease in concentration exhibits a pattern which was first seen in Figure 7.2a: a general reduction in concentration which is strongest in two parallel bands close to the edges of the cyclone track. Even strong variations of the initial level ice thickness of about 1 m can not change this basic pattern (Figures 7.5e and 7.5f); only the magnitude of the level ice concentration decrease is affected by a change in ice thickness. However, with

149
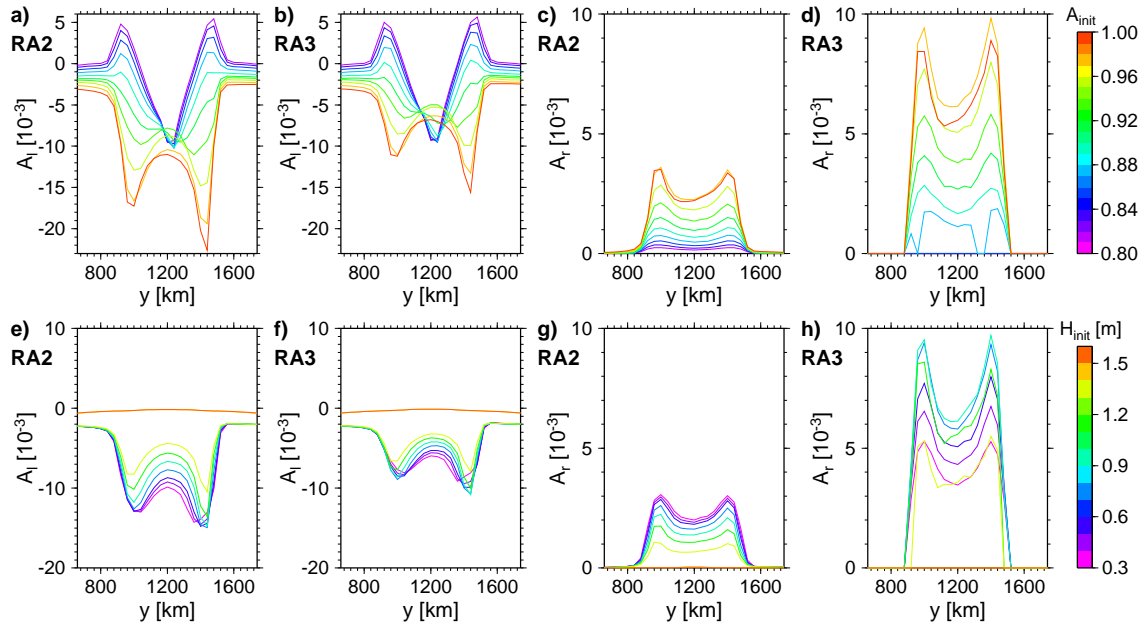
Figure 7.5: Variations in level ice concentration A_l and ridged ice concentration A_r of ridge algorithms RA2 and RA3 across the cyclone track at x-position 2400 km, dependent on the initial ice concentration A_{init} and thickness H_{init}. In the upper row variations of A_{init} are indicated by the colour scale at the very right and $H_{init} = 0.5$ m; in the lower row H_{init} varies as indicated by the colour scale at the very right and $A_{init} = 0.95$ m;

initial level ice concentrations of less than 0.9 the cyclone leaves a different pattern in the ice cover. In these cases an increase in level ice concentration is observed at the edges of the cyclone track where the maximum increase is closer to the track edges than the maximum decrease for initial ice concentrations above 0.9. In contrast to this strong change at the track edges, the reduction of level ice concentration in the centre of the track is almost identical for all initial ice concentrations: -0.01 for RA2 and -0.0075 for RA3 (Figures 7.5a and 7.5b). This causes a steep gradient between the edges and the centre of the track particularly for initial ice concentrations of less than 0.85. These observations are valid for both ridge algorithms RA2 and RA3. However, the decrease in level ice concentration in the cases of an initial value of more than 0.9 is twice as large with RA2 compared to RA3.

The results regarding the ridged ice concentration differ from those of level ice. Level and ridged ice concentration patterns have only in common that both feature a clear symmetry (see Figure 7.5). For initial ice concentrations above 0.9 the ridged ice concentration reflects a negative image of the level ice distribution along the cross-section. The highest fractions of ridged ice area are found in the two bands along the track edges already referred to above as areas of minimum level ice concentration. The track centre shows smaller though non-zero
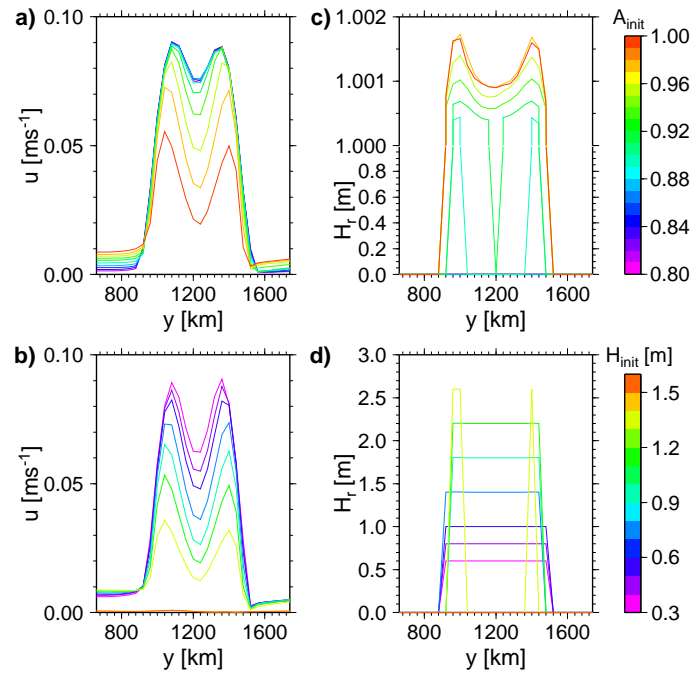
Figure 7.6: (**a**) and (**b**) Variations of the absolute ice drift speed u of a cross-section at $x = 3200$ km; (**c**) and (**d**) variations of the actual ridged ice thickness H_r of a cross-section at $x = 2400$ km. Results of ridge algorithm RA2 are shown for various initial ice conditions which are indicated by different line colours. The colour scale at the right hand side of each row is valid for both panels of the respective row.

values of ridged ice concentration. In contrast to the level ice the ridged ice does not change its concentration distribution along the cross-section for initial ice concentrations below 0.9, i.e. the ridged ice has an almost constant pattern for all initial ice concentrations and only the magnitude decreases with decreasing initial ice concentration or thickness. However, the ridged ice concentration of RA3 is particularly sensitive to changes in initial ice thickness: maximum ridged ice concentrations are found for initial thicknesses of 0.7 m and 0.9 m whereas the same ridged ice area production is found for thicknesses of 0.3 m and 1.3 m (Figure 7.5h). The magnitude of the ridged ice concentration formed with RA3 is about three times larger than that from RA2. The change in ridged ice concentration for RA3 is of about the same magnitude as the corresponding level ice concentration change for cases of an initial concentration of more than 0.9. The ridged ice concentration derived by RA2 is only about one-fifth of the level ice concentration decrease.

The initial ice conditions also affect the ice drift, although this is forced by the same wind speeds in each of the cyclone experiments, because the strength of the internal forces varies. A cross-section of ice drift speed through the centre of the cyclone is presented in Figures 7.6a and 7.6b. The graphs clearly show that the drift speed is greatest for small ice concentrations and thicknesses. Fur-

thermore, the maximum drift speeds of the cross-sections coincide with the two bands of strongest change in ice concentration. In the experiments with initial ice thicknesses above 1.3 m—and a concentration of 0.95—the drift ceases.

The thickness of the deformed ice depends on the initial ice conditions. However, the variations due to a change in ice concentration are very small (0.002 m) for ice concentrations above 0.9 (Figure 7.6c). For smaller initial ice concentrations the actual ridged ice thickness equals zero. In the case of a varied initial ice thickness the difference between the resulting actual ridged ice thicknesses is much larger and values between 0.6 m and 2.6 m can be found for initial level ice thicknesses between 0.3 and 1.3 m respectively. The ridged ice thickness is zero for initial ice thicknesses of 1.4 and 1.5 m (Figure 7.6d) because of the absence of ice drift. The same holds for the ridged ice concentrations in Figures 7.5g and 7.5h. In Figure 7.6c the plateau of the ridged ice thickness profile is particularly highly resolved in order to show the cross-sectional profile of ridged ice thickness which has a very small magnitude (0.001 m and less). Its shape is similar to that of ridged ice concentration. These variations within the cyclone track are three orders of magnitude smaller than the differences caused by a changing ice thickness (Figure 7.6d). The pattern within the cyclone track is also present in all cross-sections of Figure 7.6d, although this is not visible due to the coarse resolution. Only results of the ridge algorithm RA2 are shown because the respective profiles of RA3 are very similar.

Ridge parameters

Beside the main sea ice quantities, the sail density and height are also affected by the initial ice conditions. Here, results of all three ridge algorithms are considered.

As can be seen in Figure 7.7 the sail density is highly sensitive to variations in ice concentration and thickness. All three ridge algorithms show clear increases in sail density with increasing ice concentration (Figure 7.7a). An average maximum sail density of $0.64 \, \mathrm{km}^{-1}$ (RA1) and $0.46 \, \mathrm{km}^{-1}$ (RA2 and RA3), respectively, is found for an ice concentration of 0.97 in all three graphs. The sail density of RA1 is generally higher than that of RA1 and RA2 by an offset of $0.2 \, \mathrm{km}^{-1}$. Ridge algorithms RA2 an RA3 agree very well in sail density for initial ice concentrations of 0.89 and above. RA3 simulates no sails for ice concentrations of 0.85 and below. The relationship between sail density and initial ice thickness varies among ridge algorithms. RA1 and RA3 feature a clear decline of the sail density for increasing ice thickness, whereas the sail densities of RA2 do not follow a one-to-one relationship—the run of the curve resembles an inverted parabola. A maximum sail density of $0.5 \, \mathrm{km}^{-1}$ is found for RA2 at an ice thickness of 0.9 m. The results of RA2 and RA1 agree for 0.9 m and higher ice thicknesses. However,
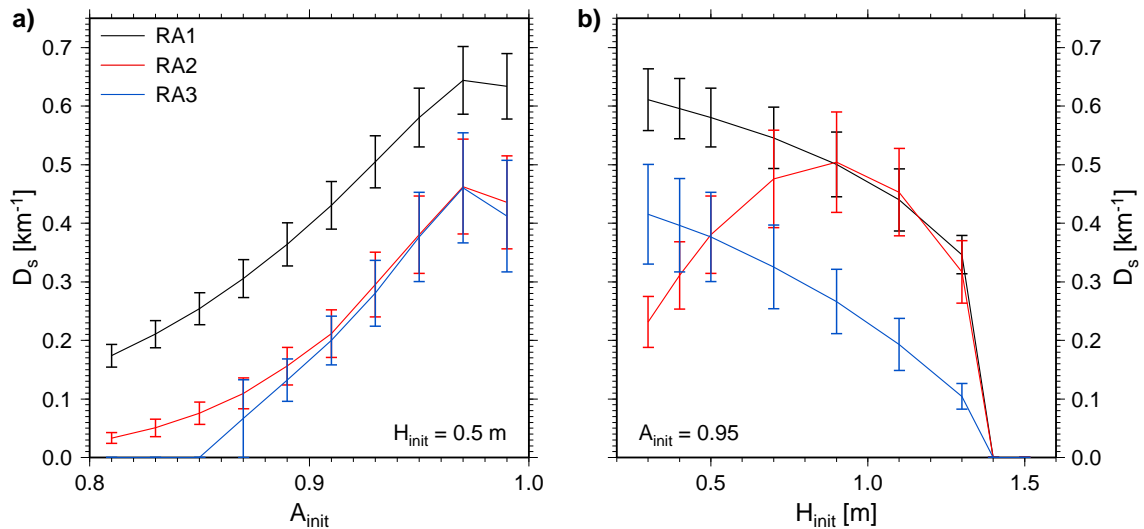
Figure 7.7: Sail density D_s as a function of (**a**) initial ice concentration A_{init} and (**b**) thickness H_{init}. Average values of cross-sections at x-position 2400 km are shown; error bars indicate the minimum and maximum value of the particular cross-section.

RA1 and RA3 have a maximum of 0.61 km^{-1} and 0.41 km^{-1}, respectively, at the thinnest ice thickness tested (0.3 m). The offset between RA1 and RA3 observed in Figure 7.7a is also found for ice thickness variations. At an initial ice thickness of 0.5 m the sail densities of RA2 and RA3 equal. All three ridge algorithms have a sail density of zero for ice thicknesses above 1.3 m because the ice drift comes to rest in these experiments.

Error bars in Figure 7.7 indicate the range in sail density within the respective cross-sectional profile. In general, the magnitude of this range is smaller than the variations caused by the initial ice conditions and increases with increasing sail density for all ridge algorithms. With RA2 and RA3 the departures of the minimum and maximum values from the cross-sectional mean vary more strongly than was found for RA1; in Figure 7.7b error bars for RA1 appear to be of almost constant length whereas those of RA2 and RA3 vary strongly with the mean sail density. A special case is the result of RA3 at an initial ice concentration of 0.87. Here, the range of sail densities along the cross-section is unusually large for the rather small mean density. This needs to be considered in connection with the finding that RA3 produces a sail density of zero for smaller ice concentrations of 0.85 and below.

The mean sail height of the across-track profiles is also found to be sensitive to changes of ice concentration and thickness though the results of the experiments differ from those for sail density. For RA1 and RA2 sail height increases with increasing ice concentration and thickness (Figure 7.8). This effect is expressed much more strongly in the results of RA1 than in those of RA2. The sail height of RA1 grows from 1.5 m to 2.3 m for initial ice concentrations of 0.81–
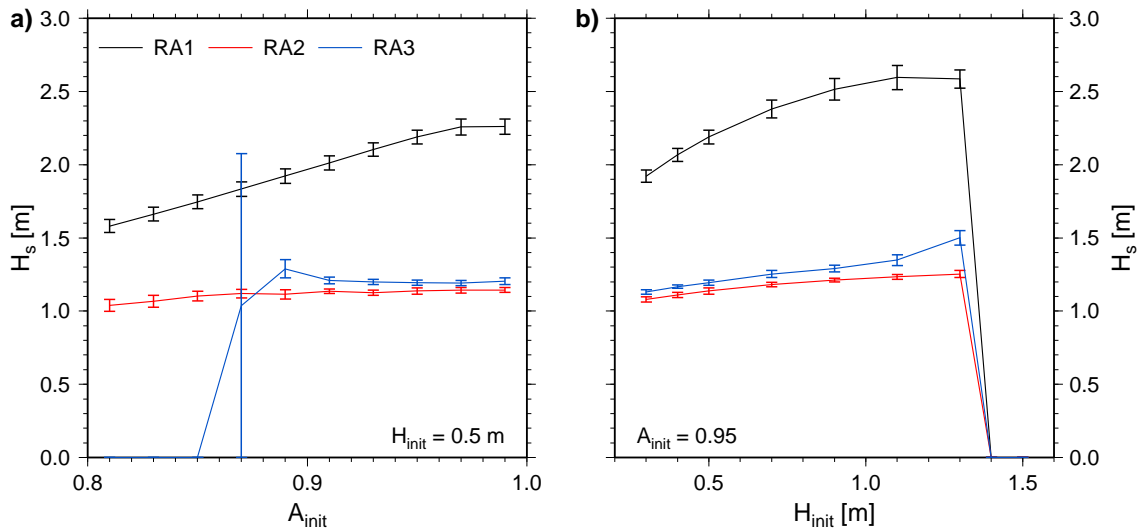
Figure 7.8: Sail height H_s as a function of (**a**) initial ice concentration A_{init} and (**b**) thickness H_{init}. Average values of cross-sections at x-position 2400 km are shown; error bars indicate the minimum and maximum value of the particular cross-section.

0.99 and follows almost exactly the path of the RA1 sail densities in the same experiments. In contrast to sail density, sail height increases with increasing ice thickness. Average sail heights of RA1 range between 1.9 m and 2.6 m. However, RA2 shows a rather uniform mean sail height between 1.0 m and 1.3 m in all experiments. For ice concentrations above 0.9 and ice thicknesses below 1.0 m the sail height from RA3 follows that from RA2 though it is slightly larger by a margin of about 0.1 m. In the experiments with varied ice concentration RA3 exhibited exceptional behaviour between ice concentrations of 0.86 and 0.9. The curve has a maximum at 0.89 and features an extraordinarily high cross-sectional variance at 0.87. For ice concentrations of 0.85 and below RA3 yields a sail height of zero. Furthermore, the sail height of RA3 increases rapidly with ice thicknesses above 1.0 m than below this threshold. Again, all ridge algorithms have no sails for ice thicknesses above 1.3 m.

The range of sail height across-track is indicated by error bars in Figure 7.8. Compared to sail densities the variance in sail height is generally smaller for all ridge algorithms. In the case of the ice concentration experiments, RA1 has an almost constant range of ±0.05 m in all experiments whereas the range in sail height increases slightly from 0.01 m ($A=0.99$) to 0.05 m ($A=0.81$) with decreasing ice concentration in RA2. RA3 results have a cross-sectional variance which is comparable to that of RA1 for ice concentrations above 0.9. As mentioned above, the variability in RA3 sail heights along the cross-section is extremely high at 0.87 where the sail height changes from zero to 1.0 m. All ridge algorithms show a dependency of cross-sectional variance on the ice thickness. The cross-sectional variability in sail height is strongest for RA1, which also exhibits

the most pronounced variation in cross-sectional average sail height.

7.2.3   Transition of ice regimes

The above experiments showed that the three ridge algorithms are differently affected by variations in initial ice conditions. This poses the question of how the ridge algorithms will behave if the cyclone passes over different ice regimes, i.e. ice concentration and thickness vary in the same experiment. The results regarding sail density are presented in Figure 7.9 for two such experiments. In both experiments thicker ice is surrounded by thinner ice, though the difference of the ice thickness amounts to 0.5 m in the first experiment and to 1.0 m in the second. In the first experiment the thicker ice is more compact than the thinner ice and vice versa for the second experiment.

In general the results of these experiments show differences between the
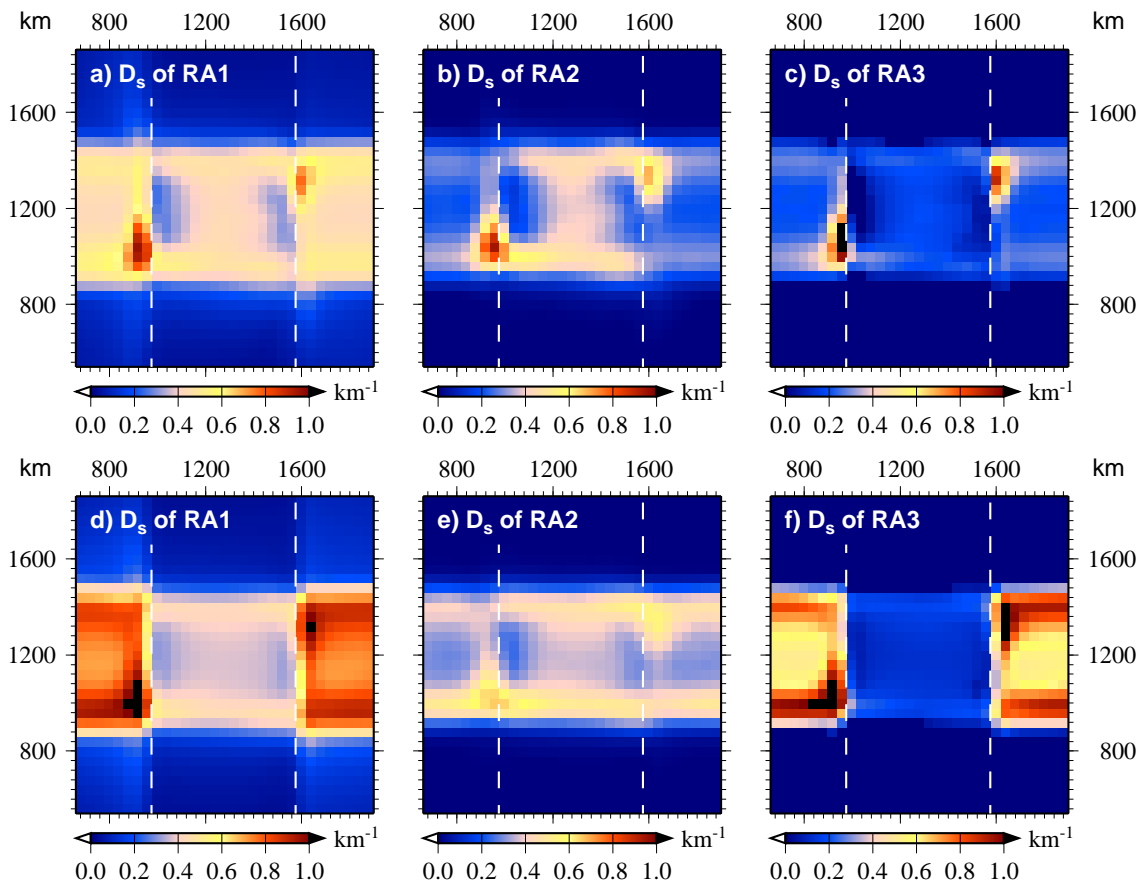
Figure 7.9: The sail density from the three ridge algorithms is presented for two experiments of changing ice regimes: (**a–c**) a central band of sea ice with initial concentration 0.97 and thickness 1.0 m was surrounded by ice of thickness 0.5 m and a concentration of 0.92, and (**d–f**) the central sea ice band had an initial concentration of 0.95 and thickness 1.3 m and was surrounded by ice of thickness 0.3 m and concentration 0.99; dashed white lines mark the margins of the ice regimes.

three ridging approaches which mirror those identified in the above experiments. Moreover, the signature of the cyclone as shown in Figure 7.3 dominates the sail density pattern about 160 km each side of the regime transition zone.

Already the first experiment shows that all three ridge models agree in two zones of pronounced ridging (see Figures 7.9a–c). These zones are located in the thin ice area where the wind forces the thin ice against the rim of the thick ice area. Apart from these zones RA1 has the highest sail densities followed by RA2. It can be seen that the sail densities of RA2 are close to those of RA3 for an ice thickness of 0.5 m but resemble densities of RA1 for a thickness of 1.0 m, which was also seen in Figure 7.7b. The most prominent ridging in the described deformation zones occurs with RA3 which otherwise produces the smallest sail densities. Another feature is observable, which occurs only in connection with the change in ice thickness. Inside the thick ice area in the centre of the cyclone track in the y-direction and at both sides not more than 160 km away from the edge of the thick ice there are zones of decreased sail density, in the case of RA3 the sail density even falls to zero. On the side of the thin ice an increase in sail density is observable which is, however, not as strong as in the most prominent deformation zones. This feature occurs for two reasons: (1) When the front end of the cyclone meets the edge of the thick ice, deformation takes place and ridges are formed of the thin ice but the forces are not strong enough to deform the thicker ice. This is also the reason why the sail density on the western side (left) of the thick ice area is more strongly reduced than on the eastern side (right). (2) When the centre of the cyclone is positioned above the regime interface, prominent ridging zones are formed and the thick ice in the track centre lies in the downwind shadow of these features where the ice drift is weak so that no deformed ice can be advected from the track edges into the centre of the track.

The features described above are principally also detectable in the results of the second experiment (Figures 7.9d–f). The particular ice thickness of the two regimes is chosen so that the problem which follows from the parabola-shaped relationship between sail density and ice thickness of RA2 becomes more obvious. For thicknesses of 0.3 m and 1.3 m RA2 shows almost no difference between the two regimes, although the general features—ridging zones and ridge shadows—are still detectable (Figure 7.9e). However, RA1 and RA2 show very strong differences in magnitude of sail density between the two regimes. With RA1 the two bands of high sail density caused by the cyclone almost cover the deformation zone at the regime interface. The different regions of deformation are most pronounced with RA3 and a strong gradient between the two regimes can be seen.

Furthermore, it is found that the magnitude of the resulting sail density de-

156

pends less on the difference in thickness or concentration between the two ice regimes than on characteristics of the parent ice at the location where the ridges form. The influence of the parent ice thickness dominates over the effects of initial ice concentration. The thicker ice acts as an obstacle for the thinner, faster drifting ice and distinct zones of pronounced ridging result from the concurrence of strong wind forcing and the presence of an obstacle.

7.2.4 Topographic features

Peninsula

In this experiment a topographic obstacle is added to the experimental set-up. A peninsula protrudes from the north into the path of the cyclone and strongly changes the magnitude and pattern found so far for these ice and forcing conditions (compare Figure 7.3). The along-track homogeneity of sail density and height is lost in all three simulations. The spatial distribution of the ridge quantities is perturbed mainly on the windward side but some effects is also seen in the lee of the peninsula (Figure 7.10). The area affected by the peninsula is about the same in the results of all three ridge algorithms: in the x-direction about 500 km to each side of the centre of the obstacle and across the entire cyclone track in the y-direction.

The sail density clearly marks the ridging zones at the tip of the peninsula and at its eastern coast (Figures 7.10a–c), both these areas are regions where the wind blows onshore and strong convergence prevails. At the western side of the peninsula—on its lee side—a polynya opens up (seen in the ice concentration which is not shown here) and almost no ridges can be found along this coastline. It is remarkable that the zone of reduced ridging which used to be in the centre of the cyclone track is only partly reduced in its areal extent and shifted to the south in the vicinity of the peninsula head. Here, it narrows the band of high sail density caused by the cyclone. However, the southern edge of the cyclone track is not shifted and remains as sharp as in the previous experiments. The ridging zones around the obstacle are most pronounced in the RA3 data (up to 1.42 km^{-1}) whereas RA1 produces the weakest (0.99 km^{-1}) though still prominent signal of all algorithms.

Regarding sail height the three ridge algorithms give divergent results. With RA1 the sail height distribution follows that of sail density and has sail heights of up to 2.52 m on the east side of the peninsula. The sail heights of RA2 and RA3 reach only half of this maximum. The results of RA2 are again rather noisy and no clear pattern is detectable. However, there are increased sail heights at the windward side of the peninsula and smaller ones leeward of it. This agrees well with the results of RA1. A completely different result is found for RA3: sail

157
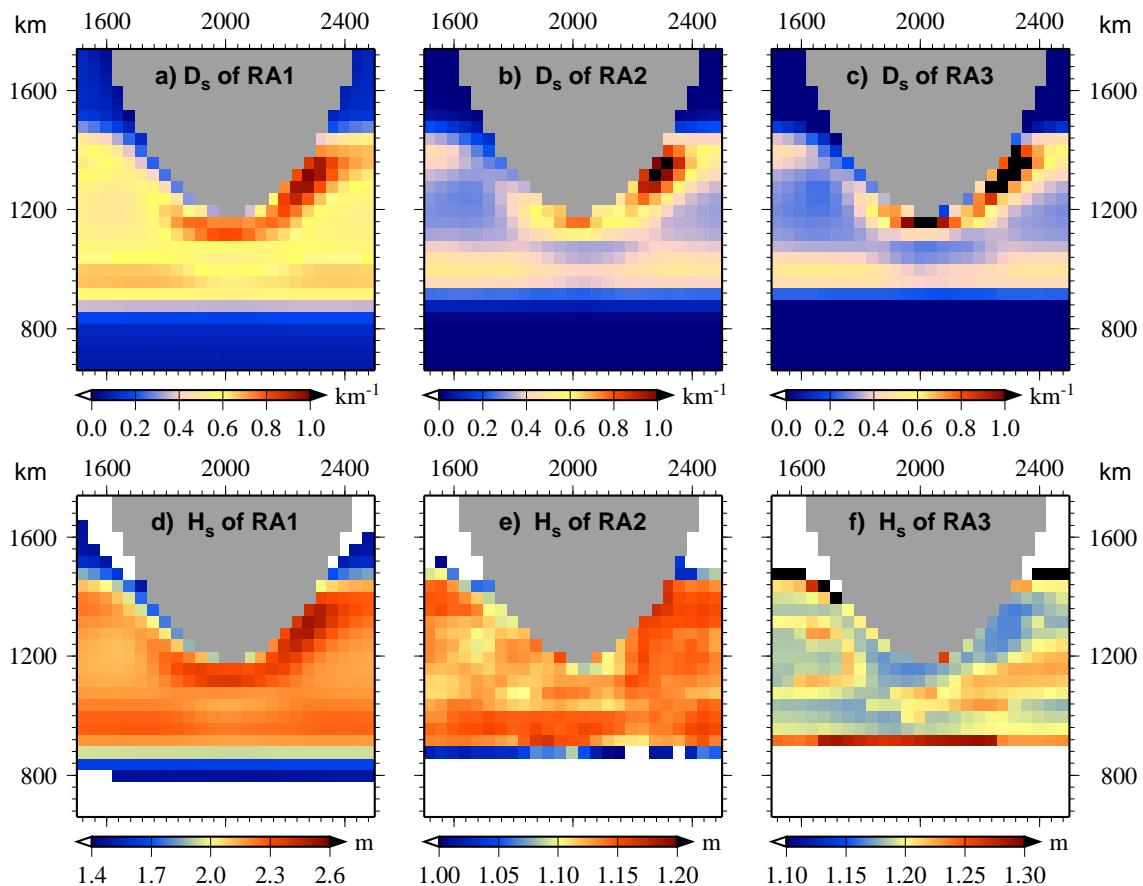
Figure 7.10: (**a–c**) Sail density D_s and (**d–f**) height H_s from an experiment with a peninsula protruding into the cyclone track. The concentration of the initial level ice cover was 0.95 and its thickness was 0.5 m.

height is smallest (about 1.16 m) where all the ridge algorithms show the most dense ridging. However, this region of small sails is characterised by a markedly uniform sail height distribution. In the south-east of this area follows an area of increased sail height in the centre of the cyclone track which is not observable in the cyclone experiments without an obstacle (Figure 7.3f). Further deviations of RA1 and RA2 follow those observed with the simple cyclone experiments.

Strait

This experiment is designed to study the ridging process in the region of influence of a strait, and also demonstrates the different effects of convergent and shear motion. The model grid includes a strait as topographic feature and a different wind forcing is applied: the wind blows constantly eastward, parallel to the strait, with its maximum speed inside the strait (see Section 7.1).

In all three ridge algorithms heaviest ridging takes place along the western coast of both land areas where onshore winds cause ridging due to convergent and shear sea ice motion (Figures 7.11a–c and Figure 7.1c). Pure shear forces
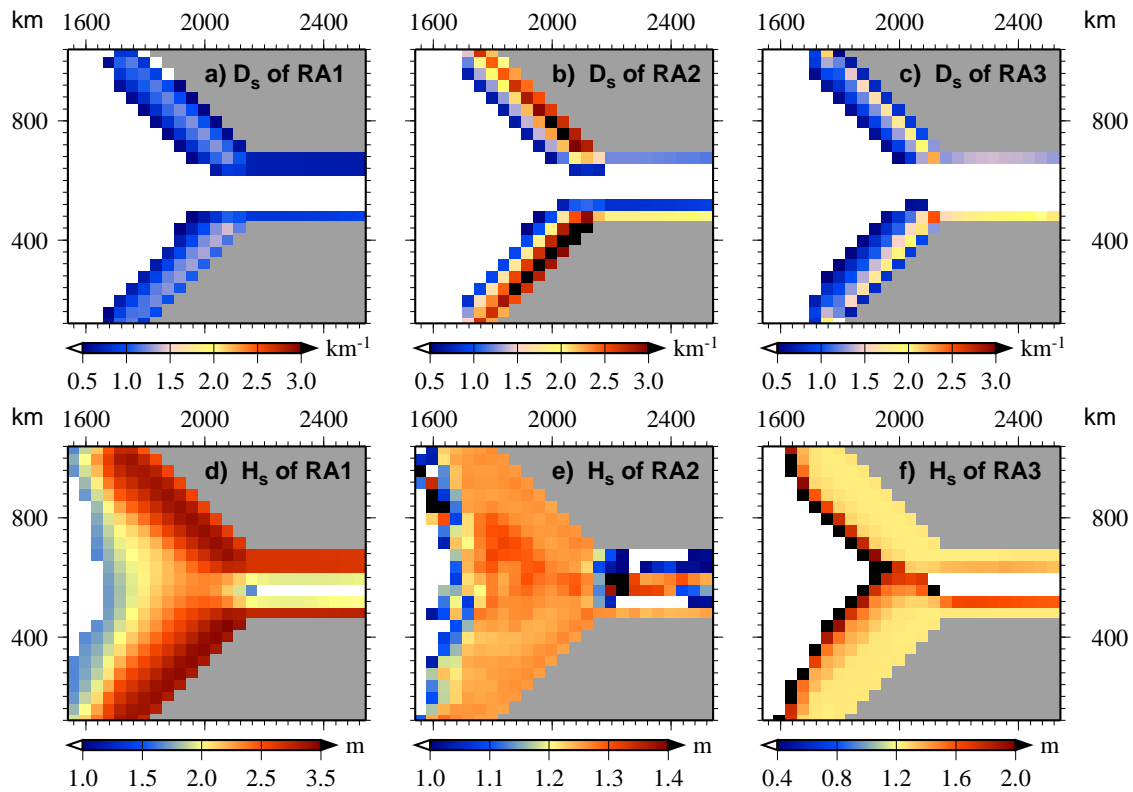
Figure 7.11: (**a–c**) Sail density D_s and (**d–f**) height H_s from an experiment in which a constat wind blows parallel to a strait (see Figure 7.1c). The initial ice concentration was 0.95 and the thickness 0.5 m.

cause fewer ridges along the coastlines inside the strait. However, the sail density is much smaller here. Interestingly, about twice as many ridges are found with RA2 (up to 3.7 km^{-1}) in this case compared to the results of RA1 and RA3, which are similar with sail densities of 1.4 km^{-1} and 2.0 km^{-1} respectively. The sail density distribution is dominated by a gradient perpendicular to the coastline. The maximum sail density is not located directly at the coast but found one grid cell further on.

This experiment exhibits differences in sail height magnitude and distribution between the three models. The RA1 simulation has the largest sails ($\sim$3 m) as can be seen in Figures 7.11d–f. In RA1 regions of largest sail heights agree again with the sail density distribution; a clear gradient perpendicular to the shoreline is found. In contrast, RA2 has sail heights which are only half as large and a maximum is found in the centre of the funnel formed by the opening of the strait. Furthermore, the Monte Carlo simulation causes noisy results at the edge of the ridged region as well as inside the strait. However, the sail height distribution is very uniform within the prominent ridging zones along the western coasts at a sail height of 1.25 m (Figure 7.11e). This resembles the results of RA3 which feature an extremely uniformly distributed sail height of 1.2 m in these ridging zones, although RA3 has its largest sails in a small band at the edge

of the deformation zone. This characteristic has already been observed in the previous experiments. Deviating from the previous experiments, in which the wind forcing did not cover the entire model domain, the area covered by sail heights greater than 0.8 m is larger than the area of sail densities above zero in the results of all three ridge algorithms.

7.3 Discussion

The ridge algorithms differ in their inter-relation between ridge quantities and general sea ice parameters: ice concentration, thickness and drift. As can be seen in Figure 7.2 the cyclone leaves different patterns of reduced total ice concentration for ridge algorithms RA2 and RA3. The result of RA2 shows the typical pattern found for the cyclone experiments which is also present in the level ice concentration of both, RA2 and RA3 (see Figure 7.5). Obviously, the differing derivation of the ridged ice concentration has a strong impact on the total ice concentration. The evolution equation of level ice concentration of RA2 (Equation (6.10a)) includes the term Q_A for additional creation of open water. Hence, the level ice area is more strongly reduced with RA2 than with RA3 (Figure 7.5) where this term is not considered. This also implies that the redistribution function in RA2 can not compensate for all open water formation and the cyclone reduces the total ice concentration more effectively in RA2 (up to 1.5%) than in RA3 (up to 0.5%) (Figure 7.2). Moreover, the magnitude and pattern of the total ice concentrations from RA3 are different to RA2 because the deformed ice covers a larger areal fraction with the newly developed derivation of the ridged ice concentration (Figure 7.5), and ridged ice concentration can compensate the level ice reduction in RA3 in some parts of the cyclone track. The description of the ridged ice area formation in RA3 does not resemble a redistribution of the ice and thus an overcompensation of the level ice decrease is possible which may cause problems such as $A > 1$. For the idealised tests this was not the case but this circumstance can not completely be disregarded.

Nevertheless, the magnitude of the ice concentration decrease in the present experiments has a similar magnitude to that found by *Haapala et al.* [2005] in a comparable model study (up to 1.0–1.4%). The pattern produced by RA2 (Figure 7.2a) compares best to the results of the multi-category model of *Haapala et al.* [2005, Fig. 4c] and those of RA3 (Figure 7.2b) are similar to their two-category model [*Haapala et al.*, 2005, Fig. 4d]. While *Haapala et al.* [2005] placed greater stress on the investigation of different cyclone speeds and ocean-drag turning angles the impact of different initial ice concentrations and thicknesses are investigated in more detail in the present study. However, *Haapala et al.* [2005] also experienced that the ice drift speed drops to (almost) zero for

initial ice thicknesses of 1.5 m and a closed ice cover. These findings show that, regarding open water formation, results of good quality are obtained from the present cyclone experiments and that these tests are a suitable basis for reviewing the effects of the different ridge calculations. Furthermore, the present study shows that changes of 10% in the initial ice concentration already cause drastic variations in the redistribution of ice mass, which are followed by markedly different patterns of ice concentration in the wake of the cyclone.

As a driving force the sea ice drift velocity has a strong impact on the intensity of ridge formation which is most reflected by the sail density in all three ridge algorithms. Moreover, it is found that shear motion has an important impact on the intensity of ridging and hence, needs to be considered in the ridging algorithms, which was not the case with RA3 prior to the present study (see Section 6.4). In the strait experiment shear forces create all deformed ice inside the passage and also along the western coastlines ridging is partly due to shear motion because the ice drifts almost parallel to land directly at the coast (Figure 7.1c). This is also the reason why the greatest sail density is found one grid cell away from the coast in Figures 7.11a–c. Here, the forces of convergent motion are strongest.

However, it is not only the drift velocity but also the ice thickness and particularly the combination of both which has a strong influence on the formation of ridges. For RA2 there is obviously an optimal combination of ice thickness and drift speed because the sail density of RA2 has a clear maximum at a thickness of 0.9 m (Figure 7.7b) although thinner ice allows greater drift speeds. For the same initial ice thickness RA3 shows a maximum in the ridged ice concentration (Figure 7.5h). This behaviour illustrates the opposing design of RA2 and RA3 since, in the latter, the ridged ice area is derived from the prognostic ridge quantities whereas sail density and height are calculated from the redistributed ice mass in RA2.

The magnitude of sail density in these idealised tests (0.0–0.7 km^{-1}) may be regarded as too small compared to the measured sail densities presented in Chapter 4 (2–30 km^{-1}). However, the observations reflect ridge growth of an entire winter season or even multi-year roughness evolution. These ridge densities have been formed by many, repeated events such as the passage of a single cyclone. All three ridging algorithms are adjusted to reproduce the ridge formation in the Arctic for a whole winter season and therefore the sail densities of the idealised experiments are not particularly small.

The three ridge algorithms are based not only upon different mechanisms for ridge derivation but also on different values for the same parameters (e.g. keel depth to sail height ratio k). Therefore, the large sail heights of RA1 could be reduced by about one-third if the keel depth to sail height ratio were 6.3, which

is derived from EM bird measurements, as in RA2 instead of 4.5, which was chosen by *Steiner et al.* [1999]. In this case sail heights of RA1 would be almost within the same range of values as those of RA2 and RA3. The sail density of RA2 can be increased by reducing this keel to sail ratio and sail densities from RA3 increase with decreasing level ice area assumed to be consumed by each single ridging event (see φ_0 of Equation (6.29)).

7.4   Summary and conclusions

The cyclone experiments revealed that generally all three ridge algorithms agree very well in sail density, particularly in its pattern, which is directly linked to the ice drift field. Although the magnitude of sail density of RA1 is larger than that of RA3 throughout the experiments and those of RA2 range between the two, the variations within one simulation are of the same magnitude as the deviations between different ridging algorithms. In contrast, the resulting sail heights vary markedly in pattern as well as in magnitude between the ridge algorithms and the variations within one simulation are almost an order of magnitude smaller than the differences between the algorithms. While the sail height patterns of RA1 and RA2 agree, algorithms RA2 and RA3 are close in their range of values in most cases. The ridge algorithm RA3 exhibits the greatest sensitivity to abrupt changes of ice concentration or thickness of the parent ice cover. Moreover, with RA3 the patterns of sail density and height are much more diverse compared to those of RA1 and RA2, which both have similarities in the spacial distribution of sail density and height.

While proper sail density patterns are obtained from all three ridge algorithms, only the sail height patterns of RA1 and RA3 seem to be equally appropriate for further model experiments. The noise in the RA2 sail height due to the Monte Carlo simulation can not be dampened completely by the smoothing routine and causes unrealistic inhomogeneities or disturbances (e.g. Figure 7.11e). Therefore, the sail height derivation in RA2 falls back upon the direct relationship between level ice thickness and sail height $H_s = 1.24\,H_l^{0.1}$ (see Section 4.5) in the following Arctic experiments. This will also amplify the variability of RA2 sail height with changing ice thickness. Such a relationship is only useful in combination with a thermodynamically changing level ice thickness, which is not the case in the idealised tests of this chapter but is realised for the Arctic experiments in the next chapter.

Although the idealised experiments revealed different characteristics of the three ridging algorithms and made the original derivation of the sail height in RA2 questionable, a decision on the quality and individual suitability for climate studies or forecast systems of the different models can be made only after an

evaluation of simulations with realistic Arctic topography and atmospheric and oceanic forcing. For example, it needs to be studied how the abrupt changes in sail density and particularly height from RA3 have its effects in long-term model runs with Arctic conditions compared to the rather smooth behaviour of RA1 quantities. In general, the above sensitivity studies showed that an increase in level ice thickness reduces the sail density but increases sail height. Considering a sea ice cover of persistent high compactness (>95%) as it is shown by large-scale sea ice models during the Arctic winter, which makes the influence of the ice concentration negligible small, and further, considering the ridge intensity introduced for observational data in Equation (4.2)—the ratio of sail height-squared and sail spacing—a most effective combination of ice thickness and drift velocity, which leads to a maximum ridge intensity, can be identified for all ridge algorithms.

Chapter 8

Ridge modelling with realistic Arctic conditions

The applicability of the three ridge algorithms is finally evaluated by applying these to a fully dynamic-thermodynamic sea ice model on an Arctic-wide grid with realistic atmospheric and oceanic forcing data. As the present study focuses on ridge formation the following comparison is based on observational data from the second half of the winter season (March–May). Most of the sea ice deformation takes place during winter due to the high compactness of the sea cover and the formation of thin and weak young sea ice. Results of the winter seasons 2003 and 2004 are presented in this chapter, since ridge data were measured with the AWI EM bird in three different regions of the Arctic—the Barents Sea, Fram Strait and Lincoln Sea—during these winters. It was shown in Chapter 4 that the three regions exhibit different ice regimes, which are all representative of the Arctic sea ice cover which features a wide range of roughness characteristics. Parts of the following investigation are published in *Martin* [2006].

8.1   Model set-up for the Arctic Ocean

In contrast to the idealised tests, the stand-alone sea ice model (SIM) as applied here includes thermodynamic processes for sea ice and snow growth and melt as well as a fast ice scheme (see Chapter 2). The SIM is applied to a domain covering the entire Arctic Ocean and parts of the northern North Atlantic (Figure 8.1). The model grid is rotated so that the model equator runs along $30°$ W and $150°$ E and the zero meridian along $60°$ E and $120°$ W. The grid resolution is $1/4°$ and because of the rotation the grid cells are of almost equal area (27.78×27.78 km^2). With a time step of six hours (Δt=21600 s) the Courant number (see Equation (2.37)) is $C_{cfl} \leq 0.31$ assuming sea ice drift speeds of

164
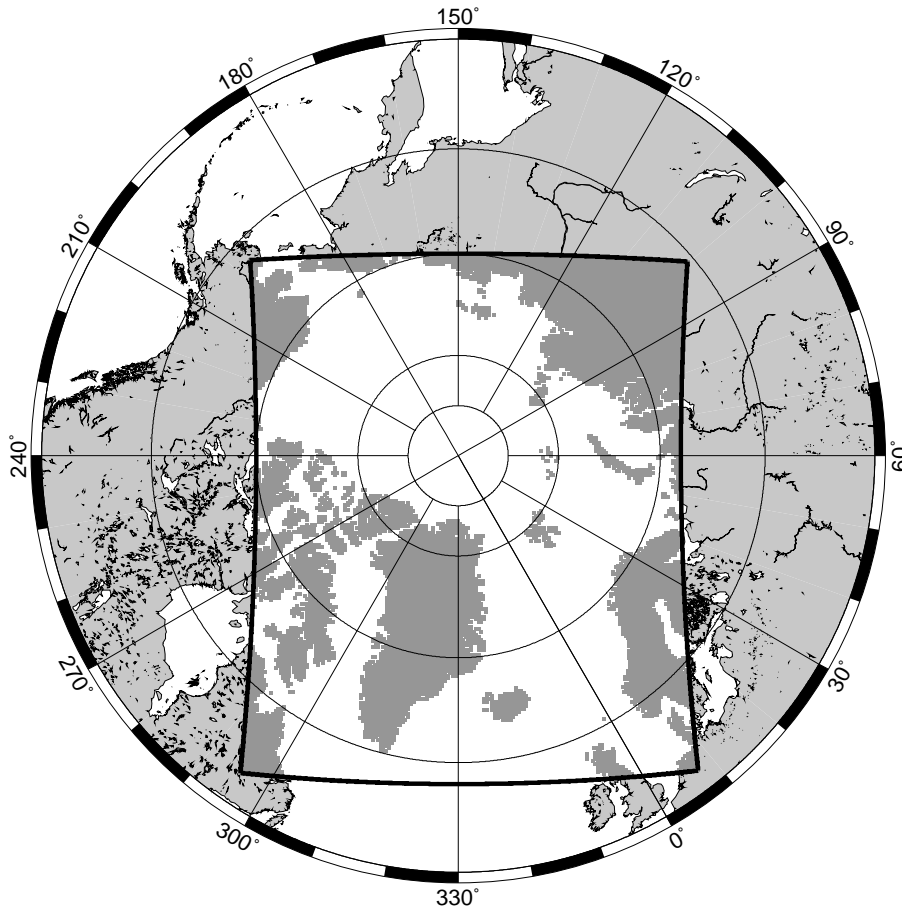
Figure 8.1: The Arctic-wide model domain (box with bold black outline) and the topography as resolved by the grid (dark grey areas inside the box).

$u \leq 0.4 \, \text{ms}^{-1}$ and hence C_{cfl} remains below the critical value of 0.5.

The forcing of these experiments is made more complex than that of the idealised tests in order to achieve realistic Arctic atmospheric and oceanic conditions to drive the evolution of the sea ice cover and also its deformation.

Atmospheric quantities, particularly the surface wind field and the surface air temperature, are obtained from global, high resolution reanalysis models to force the SIM. Reanalysis data provided by the *European Centre for Medium Range Weather Forecast* (ECMWF) are used here. The ECMWF data are preferred because they offer a higher spatial resolution of $1.125\,°$ compared to the NCEP/NCAR reanalysis data ($2.5\,°$). The wind field at 10 m height and the 2 m air temperature are the main forcing fields and are applied with their full temporal resolution of 6 hours. Further forcing quantities are the relative air humidity and dewpoint temperature, which are prescribed as monthly long-term means over the period 1986-1992 and derived from ECMWF data, as well as the cloud coverage and precipitation, which are provided as monthly long-term means constant in space after *Ebert and Curry* [1993] and *Vowinkel and Orvig* [1970] respectively.

The ocean is represented by long-term means of near-surface currents and heat fluxes. These are given as composites over the period 1979–1992, maintaining a seasonal cycle. These data are taken from a sea ice-ocean coupled version of the SIM, the NAOSIM [*Karcher et al.*, 2003] (see also Section 2.5 and Section 3.3.2).

All monthly long-term averaged forcing fields are applied to a linear interpolation in time in order to derive the 6-hourly forcing demanded by the sea ice model.

8.2 Intercomparison of ridge models

The sensitivity studies of Chapter 7 have shown that the three ridge algorithms have partly diverging magnitudes and patterns of sail density and height. However, these results could be biased by the idealised conditions of these model tests. Therefore, the findings of the idealised tests need to be re-evaluated using results of the ridge models from simulations with realistic Arctic conditions before it is useful to go ahead with a comparison of the modelled ridge quantities with observational data.

8.2.1 Results

Examples of Arctic-wide sail density and height are presented in Figure 8.2 showing results from the three ridging algorithms: deformation energy based ridging (RA1), stochastic model derived ridging (RA2) and prognostic derivation of ridge quantities (RA3). Averages for March 2003 are shown because March is considered to be the height of the winter season when most of the ridge formation takes place and thus provides a good example period for the comparison of the ridge algorithms.

All three ridge algorithms produce realistic ridge densities of up to 30 ridges per km and sail heights of up to 3 m, which are within the range of observational values. The sail density distribution closely follows the topography, i.e. the coastlines of the Arctic Ocean, in all simulations because convergent and shear forces are strongest in coastal regions, particularly north of the Canadian Archipelago and Greenland. In general, the simulations with RA1 and RA2 have greater sail densities than the results of RA3. In the central Arctic Ocean, away from coastal regions, the ridge models RA1 and RA2 produce sail densities of more than 10 km^{-1} or 20 km^{-1} whereas the sail density from RA3 stays below 12 km^{-1}. This is also evident in the Arctic-wide medians of sail density in Table 8.1. RA3 has a median of 6.4 km^{-1} which is only half as large as those of RA1 and RA2. The RA2 simulation shows the strongest gradient across the Arc-

Figure 8.2: (**a–c**) Sail density D_s [km^{-1}] and (**d–f**) mean sail height H_s [m] derived with ridge algorithms RA1, RA2 and RA3 for realistic Arctic conditions. Mean values of March 2003 are shown.

167
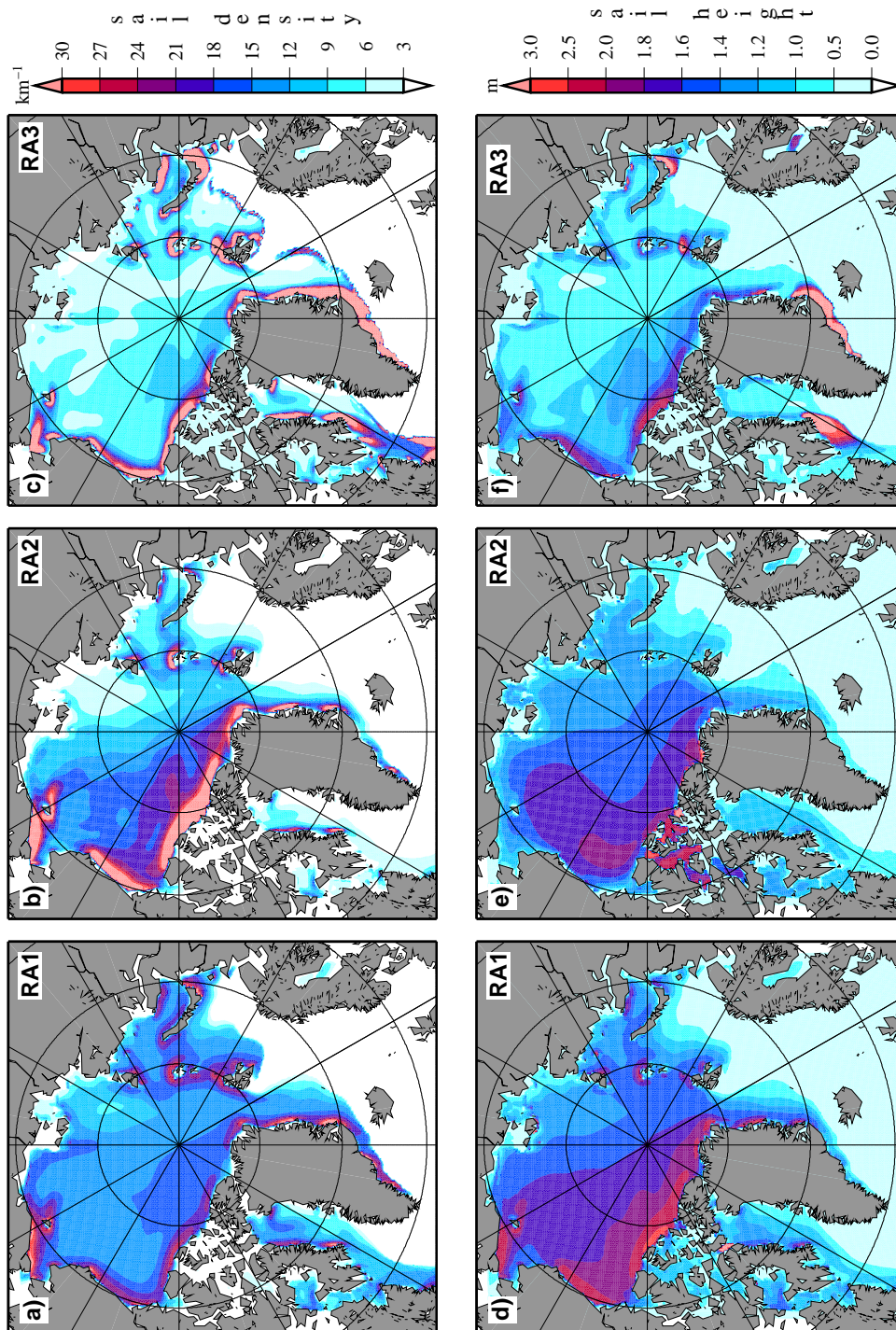
| ridge | sail density D_s | | sail height H_s | |
model	median [km^{-1}]	std [km^{-1}]	median [m]	std [m]
RA1	13.6	6.1	1.44	0.51
RA2	13.2	10.1	1.28	0.54
RA3	6.4	7.3	0.89	0.59

Table 8.1: Median and standard deviation (std) of simulated sail densities D_s and mean sail heights H_s corresponding to the results presented in Figure 8.2.

tic basin from Siberia to Canada and correspondingly has the largest standard deviation of all three ridge algorithms for the entire Arctic Ocean (10.1 km^{-1}, see Table 8.1). The RA2 simulation also has the most pronounced pattern and its sail density field reflects ice drift features such as the Beaufort Gyre showing a greater density in the ring of increased drift speeds than in the centre of the gyre (Figure 8.2b). Independent of the differing median sail densities RA1 and RA3 have similar standard deviations of 6.1 km^{-1} and 7.3 km^{-1}, respectively, which agree well with the similar sail density patterns these two ridge algorithms produced.

Areas with less than 5 ridges per km in the Laptev and East Siberian seas are partly attributed to fast ice, which is implemented in the SIM by assuming grounding of the ice in shallow shelf seas (see Section 2.4). Ridging zones along the fast ice edge are most prominent in sail density from RA1 in Figure 8.2a and sail height from RA3 in Figure 8.2f. North of the Laptev Sea divergent ice motion dominates and ice drift is accelerated into the Transpolar Drift Stream (TDS). The TDS is characterised by a uniform drift velocity and thus the simulated ice cover exhibits a generally low ridge intensity in this region. This behaviour is evident in the results of all three ridge models. The low sail density is best reproduced by RA3 though this model misses the increase in ridge intensity towards the Fram Strait, which in turn is well reproduced by RA2.

In contrast to sail density the distribution of sail height is less related to the topography and ice drift patterns but depends on the local (level) ice thickness. The sail heights from RA1 and RA2 (Figures 8.2d and 8.2e), in particular, resemble typical ice thickness distributions. Small sails of up to 1.2 m and correspondingly thin ice are found in the Siberian marginal seas. Sail height as well as ice thickness increase across the Arctic basin towards the Lincoln and Beaufort seas, where the thickest ice and the largest sails (2–3 m) are observed in the field and also reproduced in these simulations. RA3 generally produces much smaller sails. Furthermore, the areas off the Canadian and Alaskan coasts, in which the mean sail height exceeds 2 m, are much smaller compared to RA1

and RA2, and are only very narrow bands. This is also represented by the comparatively small median of 0.89 m for RA3 (Table 8.1). RA1 and RA2 have larger median sail heights of 1.44 m and 1.28 m. The difference in medians corresponds to wide areas of the central Arctic Ocean where the sail heights from RA3 are smaller than those from RA1 and RA2 by about 0.5 m. In the narrow coastal bands of great deformation RA3 sail height compares well with the results of the two other ridge algorithms. Altogether this yields standard deviations of sail height of all three ridge algorithms which are similar and range between 0.51 m and 0.59 m (Table 8.1). The spatial sail height distribution is generally less diversified than the distribution of sail density. While RA1 and RA2 feature sail height patterns which are directly linked to the mean (level) ice thickness, RA3 shows variations in sail height which partly resemble the sail density pattern. In RA2 the level ice is obviously advected with the Beaufort Gyre which causes amplified sail heights not only in the Beaufort Sea but also in a pronounced tongue extending towards the East Siberian Sea. A similar distribution is found for RA1 sail heights. In contrast to RA1, which works with only one ice thickness category, RA2 produces small sails along the Alaskan coast and in the Chukchi Sea.

In summary, all three ridge algorithms simulate realistic ridge densities and sail heights. However, the models vary strongly in the spatial distributions of the ridge quantities. Nevertheless, agreement was found for prominent ridging zones north of Greenland and the Canadian Archipelago and around the islands of the Eurasian shelf, where topography dominates ridge formation.

8.2.2   Discussion

The close dependency of RA1 and RA2 sail heights on the (level) ice thickness is due to the direct functional relationship between these two quantities in both algorithms. In contrast, the correlation between RA3 sail height and level ice thickness is small because the sail height derivation in RA3 depends little on the local ice thickness but is closely related to the sail density. Both quantities rely on the same source term and the sail height is weighted with sail density. As a direct consequence the patterns of sail density and height from RA3 are rather similar. This gives RA3 the capability to generate distinct sail heights along the coastlines and the fast ice edge. The fast ice edge is very pronounced with a sharp gradient in the sail heights from RA3 and the fast ice itself has a sail height of only 0.5 m being deformed in an early state of thermodynamic growth (see Figure 8.2f, particularly in the vicinity of the New Siberian Islands).

Both RA1 and RA2 produce large sail heights in the Beaufort Sea and beyond. While RA2 simulates small sail heights along the Alaskan coast, RA1 derives particularly large sail heights there. The amplified sail density at the Alaskan coast

present in both model results is considered to be realistic. Although RA3 supports an increased sail height at the Alaskan coast the smaller sails from RA2 are considered to be more realistic because the Beaufort and Chukchi seas are ice free during summer and are thus covered by thinner first-year ice during winter. However, very large sails can occur at the shore or fast ice edge. The sail height which is represented by the models is interpreted as an average value and can thus be comparatively small. Ridge intensity is more likely to be increased by large numbers of ridges than by large sails.

The sail density from RA2 exhibits the most pronounced variability in its pattern of all simulations and shows, for example, the Beaufort Gyre (Figure 8.2b). This detailed pattern results from the redistribution function of level to ridged ice—and is thus strongly related to the sea ice drift—on which RA2 is based and is less attributed to the sail density algorithm itself.

The result from RA3 features large sail densities of more than 30 km^{-1} in the marginal ice zone (MIZ), particularly in the Greenland and Barents seas (Figure 8.2c). These result from the scaling of sail density with ice concentration, a procedure which was proposed by *Lensu* [2003a,b] in order to account for the open water fraction because the theory of sail density derivation in RA3 relies on a closed ice cover. However, the procedure leads to unrealistically large sail densities in presence of a strongly reduced ice concentration, for example, in the MIZ. The sea ice model is not able to resolve highly deformed (multi-year) ice floes, which drift in the East Greenland Current in a region of common storm tracks. In the interior Arctic the sea ice concentration is almost 100% and the scaling of sail density does not affect the RA3 results away from the MIZ.

In the idealised tests of the previous chapter it was found that the sail density and height from the three ridge algorithms depend on the compactness and thickness of the parent sea ice cover. However, variations in ice concentration in the interior Arctic can be neglected because a concentration of almost 100% with variations of less than 3% is typically simulated, and only negligibly small variations in sail density or height are found for such ice concentration changes in the idealised experiments. Hence, all variations in sail quantities in the Arctic experiments are due to the sea ice motion and the parent ice thickness. The decrease in sail density as a function of level ice thickness is not repeated in the Arctic results. Here, sail density distribution is dominated by topography and ice drift. Topography is already found in the idealised tests to be an important factor strongly amplifying sail density, because land mass can cause compressive and shear forces which are considerably stronger than in the open sea.

The Arctic results also reflect the discrepancy in sail height between RA1 and RA3, which ranges between 0.5 m and 1 m in the idealised experiments. However, sail heights from RA2 are the smallest in the idealised tests. Due to the

changed derivation of sail height in RA2—a direct functional dependency between level ice thickness and sail height is used (see Section 7.4)—the magnitude of sail height is now closer to that from RA1.

The patterns of sail density and height were similar using both RA1 and RA2, while those from RA3 diverged in the idealised tests with cyclonic wind forcing (see Figure 7.3). In contrast, the Arctic experiments show an increased similarity of sail density and height patterns from RA3 and differing ones for RA1 and RA2. This characteristic can be regarded as a coincidence considering the individually different results of the idealised strait test. This incident emphasises the complexity of the ridge models and demonstrates that the idealised experiments can not entirely demonstrate the characteristics of the ridge models.

8.3 Comparison of model results with observations

The evaluation of the model results relies on the airborne laser altimeter data and subsequent sail density and height derivation presented in Chapter 4. The following comparison focuses on three subregions of the Arctic Ocean: Barents Sea/Storfjord, Fram Strait and Lincoln Sea. These regions were found to exhibit generally different regimes of ridged sea ice. Sails are smallest in the Barents Sea (1.2 m on average, see Table 4.2) and largest in the Lincoln Sea (1.6 m). The sea ice of the Fram Strait is characterised by a mixture of ridged ice floes from different origins and thus has an intermediate mean sail height of 1.3 m. However, the sail height was not observed to be coupled to sail density, which was found to be related to local effects. Observational data covering these three regions are available for the end of the winter season. The Barents Sea and Fram Strait data were obtained in March and April 2003, respectively, and the Lincoln Sea data were measured during May 2004. These observations provide a unique set of ridge information from the end of the winter season before summer melt begins and are thus chosen for the following investigation. For consistency with the model results the observational data are averaged over 25 km bins.

8.3.1 Results

First, selected examples from RA2 and RA3 are used to demonstrate the individual ice conditions and agreements between modelled and observed quantities. Then all three models are collectively compared to observations of the three example regions.
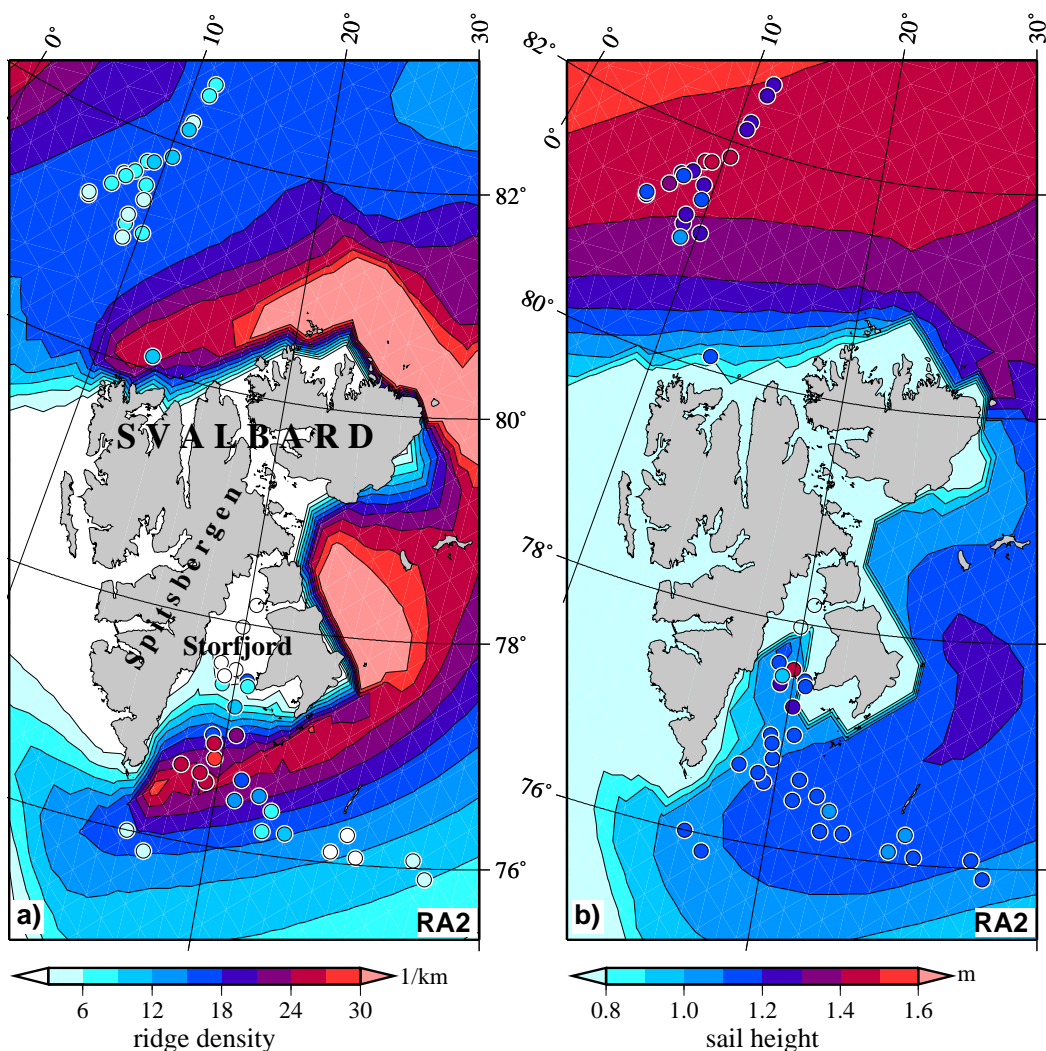
Figure 8.3: (**a**) Sail density D_s [km^{-1}] and (**b**) mean sail height H_s [m] around Svalbard derived from ridging algorithm RA2 and retrieved from laser profiling. Contours show results of RA2 from end of March 2003 and filled circles represent observations averaged in 25 km bins from March (Storfjord, Barents Sea) and April (Fram Strait) 2003.

Barents Sea/Storfjord

The results for the Barents Sea and Storfjord region are presented on the basis of the simulation results of the second ridge algorithm (RA2). The sea ice model reproduces very well the observed tongue of heavily deformed second-year ice protruding from higher latitudes into the Barents Sea and blocking the Storfjord opening (Figure 8.3a). The sail density is very low (<3 km^{-1}) inside Storfjorden and increases along a $\sim$100 km long transect towards the open sea to a maximum value of almost 30 ridges per km in the middle of this transect at the inlet of Storfjorden and decreases again to 10 km^{-1} or less in the Barents Sea. Model and observations are very similar in magnitude and pattern of sail density inside Storfjorden and of the tongue of second-year ice. However, the area

172

of greater sail densities is overestimated by the model and thus a too weak gradient towards the Barents Sea is found in the simulation although the gradient is generally well-reproduced.

The agreement between modelled and observed sail heights is also very good. Both data sets show an uniform spatial distribution and a magnitude of about 1.1 m with only small natural variations and differences of ± 0.1 m. This agrees with observations (Figure 8.6) that the mean sail height of the highly deformed second-year ice is of the same magnitude as sail heights inside Storfjorden and out in the Barent Sea. However, there are a few EM bird profiles inside Storfjorden which have larger sail heights and these are not reflected by the model results.

Fram Strait

The model results are dominated by gradients reaching across the Fram Strait (Figure 8.3). Sail density is greatest towards the coastlines of Svalbard and Greenland (25 km^{-1}) and smallest in the central Fram Strait (15 km^{-1}). The modelled sail height increases steadily from Svalbard (1.0 m) to Greenland (1.6 m). These gradients are not found in the observations, which, however, do not cover the entire strait and are more aligned in a north-south direction, perpendicular to the model gradients. The observed sail densities range from less than 6 km^{-1} to 15 km^{-1} and is hence partly overestimated by the model. More important than this general difference is the finding that the model does not reproduce the variations shown by the laser altimeter data which, in this case, have the same horizontal resolution as the model grid. The simulation results are much more homogeneous than the observations. This is also true for sail height. While both data sets agree on the maximum mean sail height found in the Fram Strait (1.5 m), observations and model results are also seen to deviate by 0.3–0.4 m.

Lincoln Sea

The laser profiling data from the Lincoln Sea during May 2004 are presented in Figure 8.4 together with RA3 model data for the same period. Although observational data—averaged to 25 km bins—and model results are within the same range of values there are again differences in the gradients and the spatial scale of variability. In the simulation, sail density and height have a similar gradient: an increase from 8 ridges per km and 1.3 m in height to 27 km^{-1} and 1.9 m height towards the coast of Ellesmere Island. However, the ridge intensity in the opening of Nares Strait is reduced. This large-scale gradient is also found in the observational data, although it is weaker. The observations are located more
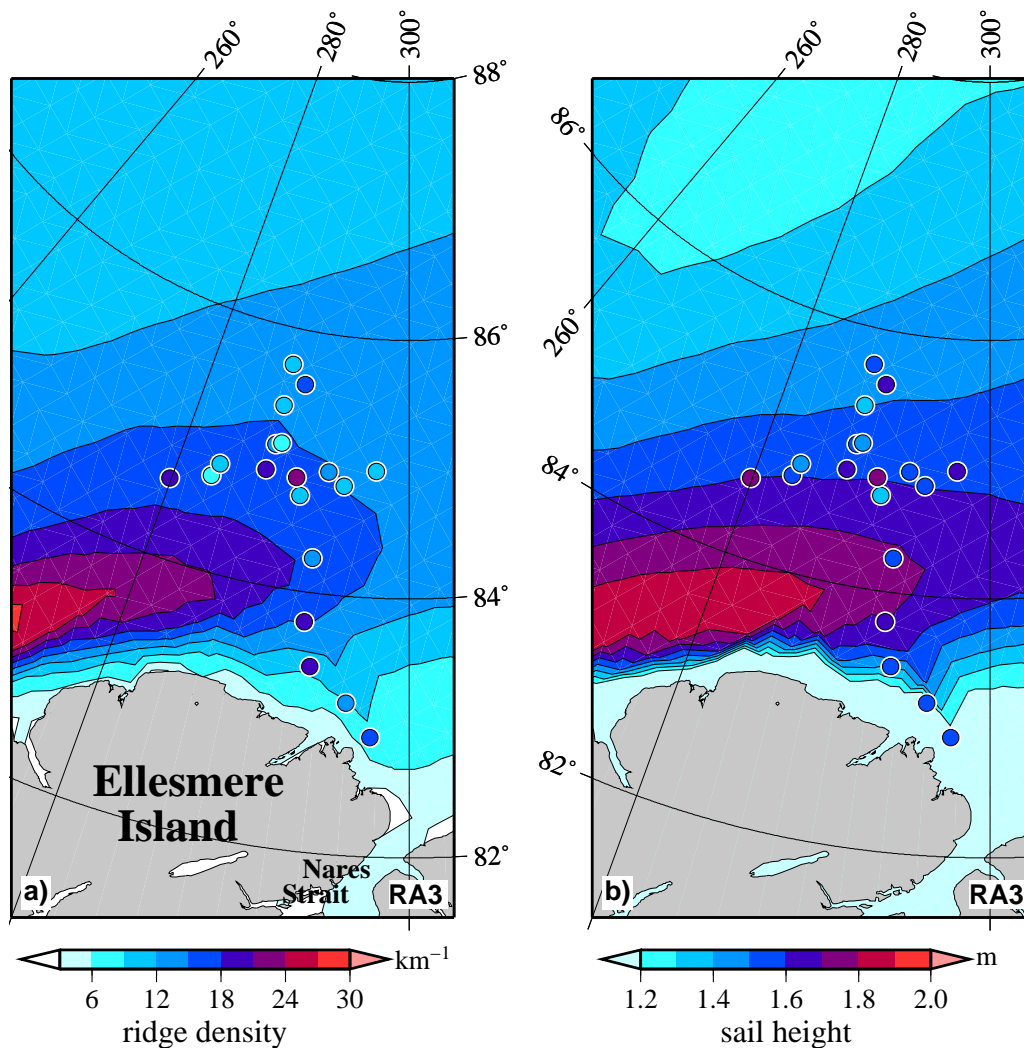
Figure 8.4: (**a**) Sail density D_s [km^{-1}] and (**b**) mean sail height H_s [m] of the Lincoln Sea region derived from ridging algorithm RA3 and retrieved from laser profiling. Contours show results of RA3 and filled circles represent observations averaged over 25 km bins, both from mid of May 2004 .

conveniently in the Lincoln Sea compared to the Fram Strait because they are mainly parallel to the modelled gradient, although they do not cover the area of greatest ridge intensity in the simulation north of Ellesmere Island. The laser data show an increase in sail density (6–20 km^{-1}) and height (1.2–1.7 m) from the open sea towards the coastline decreasing again towards the Nares Strait. However, this gradient is disturbed by variations in sail density and height which have a larger magnitude of up to 24 sails per km with a maximum average height of 1.8 m. This small-scale variability is under-represented in the model results comparable to the findings in the Fram Strait.

Three times three model results vs. observations

At the Arctic-wide scale all ridging models reproduce the observed characteristics of a deformed Arctic sea ice cover. The sail density emphasises local ridging events caused, for example, by topography and the sail height shows a clear increase from the Siberian marginal seas via the TDS towards the northern coasts of Greenland and the Canadian Archipelago.

The above case studies showed that there are differences in magnitude as well as small-scale variability (at the model grid scale of below 100 km) between model results and observations. The above examples are produced with simulations which best represent the averaged laser data. In order to extend this comparison to all ridging algorithms, results from the three ridge models are presented together as a function of the respective observed sail density and sail height from March and April 2003 and May 2004 in Figure 8.5. For this comparison the observational data are averaged over only 10 km long flight segments in order emphasise the variability of the measurement results. A nearest-neighbour algorithm is used to retrieve the corresponding ridge values from the gridded model data.

The results of the comparison differ between the three regions and also the performance of the ridge algorithms varies with respect to the sail quantities derived from laser altimeter data.

In general, the observed variance in sail density is best matched by RA2 whereas RA3 is closest to the observational average. In the Barents Sea region all three simulations exhibit strong variability in sail density which is of the observed magnitude. While RA2 almost matches the observed variance of 81.82 km^{-2}, RA1 underestimates and RA3 overestimates this value by about 50% and 70% respectively (see Table 8.2). All models deviate to almost the same extent from the observations in the Barents Sea and the individual root mean squared errors (RMSE) are close at 7.74–8.94 km^{-1} (Table 8.2). However, for the Fram Strait all models have almost constant sail densities which are mainly larger than observed. Only RA3 is rather close to the laser data with a comparatively very small RMSE of 2.49 km^{-1}. The observed variance is also not reproduced by RA1 and RA3 in the Lincoln Sea. Although RA2 produces a realistically large variability of 24.43 km^{-2} in this region the model markedly overestimates the magnitude of sail density and has a large RMSE of 13.72 km^{-1}. The RMSE of RA1 and RA3 are similar at a half of this value.

Regarding sail height the differences between the simulations are larger and altogether the modelled sail heights span a greater range than those observed. The sail height is generally overestimated by RA1 whereas RA2 matches the upper bound of observed sail heights (Figures 8.5d and 8.5e). The model results of RA3 span about the same range as the observations while underestimating sail

175
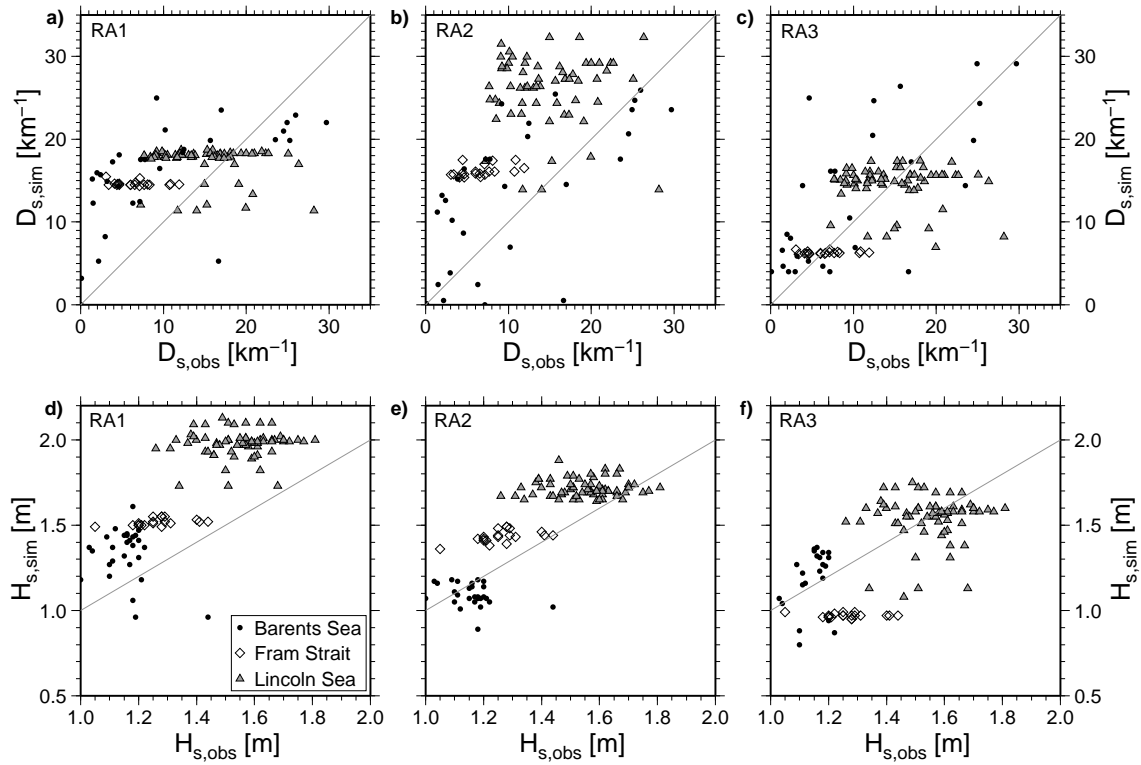
Figure 8.5: Comparison of simulated (*sim*) and observed (*obs*) (**a–c**) sail densities D_s and (**d–f**) mean sail heights H_s from the Barents Sea, Fram Strait and Lincoln Sea regions. The legend in panel (d) is valid for all graphs; grey lines indicate 1/1 lines.

height in the Fram Strait (Figure 8.5f). In general, the variance in sail height is overestimated for the Barents Sea and mostly underestimated in the Fram Strait

data:	obs	RA1	RA2	RA3	RA1	RA2	RA3
region	sail density						
	variance [km^{-2}]			RMSE [km^{-1}]			
Barents Sea	81.82	39.06	78.32	138.54	8.94	7.74	8.83
Fram Strait	6.49	0.08	0.48	0.03	8.39	9.78	2.49
Lincoln Sea	23.19	4.02	24.43	5.92	5.98	13.72	5.56
	sail height						
	variance [m^2]			RMSE [m]			
Barents Sea	0.035	0.086	0.081	0.282	0.27	0.27	0.54
Fram Strait	0.0081	0.0004	0.0013	0.0001	0.27	0.19	0.31
Lincoln Sea	0.014	0.006	0.003	0.019	0.45	0.21	0.18

Table 8.2: Variance of sail density and height of laser altimeter data (obs) and model results (RA1–3) as well as root mean squared error (RMSE) of the differences between modelled and observed quantities. Values relate to the data illustrated in Figure 8.5.

and Lincoln Sea by all model results (Table 8.2). Apart from the Fram Strait RA3 shows the largest variability in sail height of all three ridge algorithms (see variances in Table 8.2). However, in the Barents Sea the variance of RA2 of 0.282 m^2 is one order of magnitude larger than the observed value of 0.035 m^2. RA1 and RA2 produce almost equal, greater than observed, variances of about 0.08 m^2. As with sail density, the models exhibit an almost constant sail height in the Fram Strait and fail to reproduce the observed variability. RA1 and RA3 give variances of less than 0.0005 m^2, which is an order of magnitude smaller than the observed variance (0.008 m^2). The sail height from RA2 fluctuates more strongly and varies by one-sixth of the observed value in the Fram Strait. In contrast, RA3 features most variability of all ridge models in the Lincoln Sea and matches the observed variability of sail height in this region (0.014 m^2) best with a variance of 0.019 m^2. This variance of RA3 is three to six times larger than the corresponding variances of RA1 and RA2 respectively. The results of RA2 match the observed sail heights around Svalbard best with a smallest RMSE of 0.19 m in Fram Strait (see Table 8.2). However, RA2 and particularly RA1 overestimate the sail height in the Lincoln Sea (Figure 8.5e). In this region the best match in sail height is obtained from RA3 with a low RMSE of 0.18 m.

Interpreting the RMSE between modelled and observed data as a skill score for the ridge algorithms, the best results regarding sail density are generally obtained from RA3, while RA2 succeeds in matching the observed sail heights best on average. In most cases the RMSE amounts to about one quarter of the range of values given by the observations.

This conclusion is restricted by the use of a direct functional relationship between sail height and level ice thickness in RA2. It implies that the sail heights from RA2 match the observations best in terms of smallest RMSE. However, this result shows that the relationship $H_s = 1.24\,H_l^{0.1}$ can successfully be applied though it is based on a rather weak correlation (see Section 4.5).

8.3.2   Discussion

This discussion is mainly about the complexity of real Arctic sea ice conditions and the ability of large-scale ridge models to reproduce these.

The different sea ice regimes in the Storfjord and Barents Sea region can clearly be distinguished in the photographs of regular sea ice observations from *RV Polarstern* presented in Figure 8.6. Inside Sorfjorden very smooth, newly formed ice often covered by snow is found in areas of refrozen coastal polynyas, which form frequently here. The ice closing Storfjorden off from the Barents Sea was identified as second-year ice from the central Arctic [*Schauer and Kattner*, 2004] and is characterised by a very large number of ridges. However, as the

Figure 8.6: Visual sea ice observations from *RV Polarstern* during expedition ARK-XIX/1a: (**top left**) inside Storfjorden on March 16, 2003, (**top right**) in the opening of Storfjorden on March 19, and (**left**) in the open Barents Sea on March 24. [*Lieser*, 2005]

laser altimeter data and also the photograph show, the sail height in this field of second-year ice is homogeneous and small compared to typical Arctic sea ice of, for example, the Fram Strait region. In the open Barents Sea single sea ice floes can easily be distinguished because they have a mainly level surface in the interior and feature deformed rims due to collisions with other floes (Figure 8.6, left).

While the above ice regime changes are also found in the simulations, because their spatial extent is large enough to be resolved on the model grid, the models miss the observed heterogeneity of sea ice roughness in the Fram Strait. The ridge algorithms may fail to reproduce this sea ice variety for three reasons: (1) the horizontal spacing of the model grid is not sufficient to resolve small-scale variations in ice concentration and ice drift, (2) the simulated ice drift is less variable than the real ice motion, as it also depends on the quality and resolution of the wind fields used to force the sea ice model and (3) the ridges observed in the Fram Strait originate from the entire Arctic Ocean and floes may have undergone several deformation processes depending on their age. These multi-year ice features are not represented sufficiently in the ridging algorithms.

The sea ice observation photos regularly taken during EM bird flights show the great variety in the sea ice roughness in the Fram Strait. On the one hand, large multi-year ice floes exhibit level surfaces as well as weathered ridges (Figure 8.7, top left) and on the other hand zones of intense deformation are found
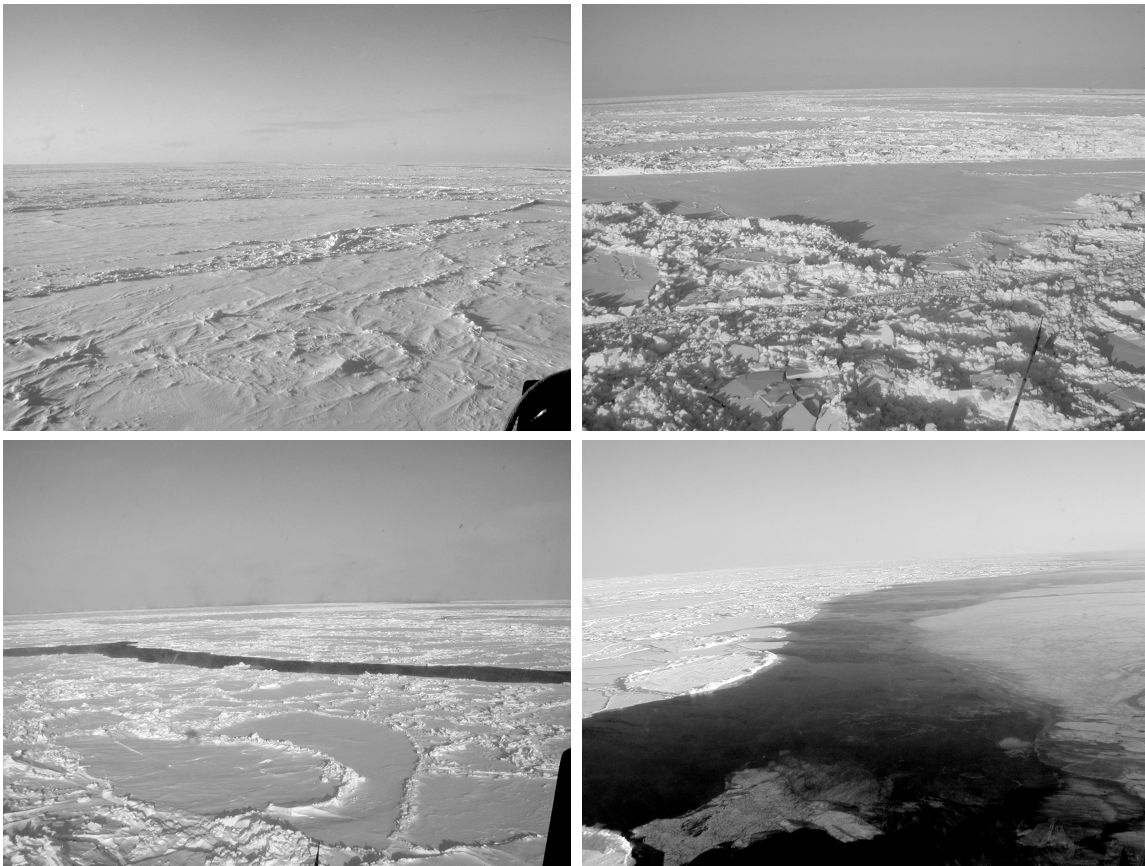
Figure 8.7: Visual sea ice observations in the Fram Strait from a helicopter during EM bird flights of expedition ARK-XIX/1b (flight altitude ~30 m): (**top left**) large floes on April 19, 2003, (**top right**) very intense ridging on April 5, (**bottom left**) smaller floes and ridges but dense ridging, and (**bottom right**) coastal polynya near Svalbard on April 1. [photos by AWI Sea Ice Physics group]

showing large pressure ridges formed of first-year ice and smaller shear ridges (Figure 8.7, top right).

A special case is the EM bird flight right at the north-western tip of Spitsbergen on April 1, 2003 (see Figure 8.3). The mean observed sail height of 1.1 m is almost reproduced by the simulation (0.9 m). However, the sail density varied strongly off the coast due to large open water areas, which began to refreeze. The ice floes were generally strongly deformed but a coastal polynya and frequent leads reduced the sail density in the measurement profiles (see Figure 8.7, bottom panels). Although the magnitude of the deformation is well represented by the model the reduction in sail density due to lead opening and polynya formation is not reproduced, which explains the deviation between model result (24.3 km^{-1}) and measurements (9.2 km^{-1}). The large number of smaller ridges as well as the leads and the coastal polynya are shown in the photographs of Figure 8.7 (bottom row).

The sea ice model can not reproduce abrupt changes in ice conditions be-
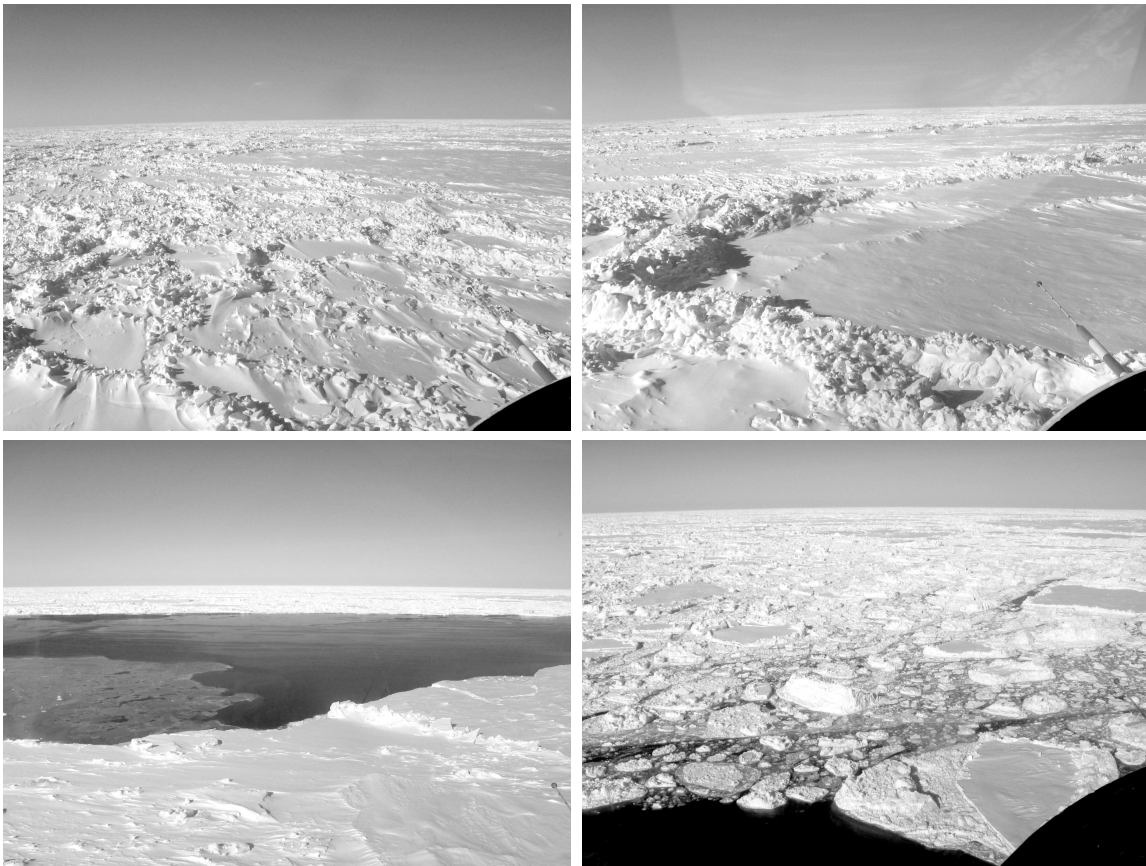
Figure 8.8: Visual sea ice observations in the Lincoln Sea from a helicopter during the EM bird flight on May 12, 2004 of the GreenICE campaign (flight altitude ~30 m). This was the most extensive flight during this campaign beginning at Alert on Ellesmere Island and extending farthest north (see Figure 8.4). The region is dominated by (**top row**) large ridges but also shows (**bottom row**) leads and loose, heavily deformed ice floes. [photos by AWI Sea Ice Physics group]

tween grid cells and tends to smooth gradients. This is observed in the Fram Strait not only but also in the Lincoln Sea. A large-scale gradient evolves in the simulations reaching across the Arctic Ocean and dominating the height and partly also the density distribution of ridge sails. However, the comparison with observations revealed that this gradient is less dominant in the laser data which show more local differences in sail density and height. The photographs of the helicopter-borne ice observation support both the strong local variations and the large-scale differences. As can be seen in the Lincoln Sea photographs (Figure 8.8, top row) very large ridges are found in this region and weathered sails on floes are larger compared to those in the Fram Strait (Figure 8.7, top left). However, during the EM bird flights there were several leads of varying magnitude of orders 10^1–10^2 m (Figure 8.8, bottom left) which are not resolved by the sea ice model, which tends to produce ice concentrations of 100% during winter in this area independent of the ridging algorithm applied. Therefore, features

such as small, broken floes which underwent intense deformation (Figure 8.8, bottom right) are also not resolved by the model. This explains the missing high frequency variability in the simulations. However, such floes and leads—all small-scale features—contribute significantly to the observed ridge data. As can be seen in Figure 4.11 or Figure 4.12 of the investigation on EM bird data the parameterisations applied to the large-scale sea ice model can not be derived for individual sub-regions (e.g. the Fram Strait) due to the large heterogeneity within each region. The parameterisations rely on the large spatial coverage of the observations, because great differences are found between several Arctic regions. This is another important reason why the ridge models fail to reproduce the observed small-scale variability of ridge quantities and large-scale patterns are more pronounced in the simulations than in the observations.

In general, conclusions drawn from the comparison of the different model results with observations have to be discussed carefully, because the selected observational data cover only a small part of the Arctic at the end of one winter season.

8.4 Summary of ridge modelling

A dynamic-thermodynamic continuum sea ice model of a type common for regional or global climate studies was used for the Arctic experiments. The model introduced in Chapter 2 was extended by adding each of the three ridging algorithms presented in Chapter 6 in turn. Comparison of results from the different algorithms using realistic Arctic forcing data revealed that all three approaches produce ridging quantities within the same range of values. Nevertheless, there are pronounced differences in the spatial extent and distribution of the deformed ice areas. It was found that the sail density depends strongly on the topography and the state of ice motion whereas the sail height depends more on the mean (level) ice thickness and less on topography. Sail heights from ridge algorithms RA1 and RA2 resemble particularly closely the typical ice thickness distribution of the Arctic Ocean known from observations and common large-scale sea ice simulations: an increase from the Siberian marginal seas towards the northern coasts of Greenland and the Canadian Archipelago. In contrast, the sail height distribution of RA3 is strongly related to the corresponding sail density. In comparison with laser profiling data ridge algorithm RA3 gives the best sail density distribution in terms of smallest RMSE values whereas the mean sail height distribution is represented best in the results of RA2.

The above results allow ridge algorithms to be recommended for different applications. For climate studies, RA2 is most appropriate as it best (re-)produces inner Arctic patterns, including large-scale gradients already known from pre-

vious studies. In addition, this model includes a redistribution scheme for the transition of sea ice between level and ridged ice categories which is proven to be stable in multi-decadal model runs. The disadvantage of this algorithm is the slight increase in computational time depending on the model grid resolution due to the Monte Carlo simulation. For sea ice forecasting and decision-making in shipping operations RA3 is preferable because near shore features and fast ice-related characteristics are resolved best. These are of special interest along, for example, the Northern Sea Route. However, this algorithm has deficiencies in stability related to the redistribution method but these are negligible in the recommended applications, because the temporal scale of forecasts is typically limited to one or two weeks and forecast models are often restricted by assimilation of observational data, for example, satellite-derived sea ice concentration and drift. The above recommendations are limited due to the following reasons: (1) the set of observational data used for evaluation of the models is limited, (2) an uncoupled sea ice model is used, i.e. the ocean dynamics are limited to the climatological monthly mean circulation, and (3) the ridges evolving in the model have no feedback to the remaining model system, for example, via the atmospheric or oceanic form drag.

Ridging is a very complex process. Thus, it is very difficult to identify a simple parametrisation of this process to be implemented in numerical sea ice models. The ability to simulate detailed ridges is strongly related to the horizontal resolution of the model grid. Nevertheless, the model results resemble the distribution of ridge height and density observed in laser profiles. Numerical forecasting of sea ice conditions in the Baltic Sea were successfully extended with the parameters ridge density and height during the IRIS project.

Chapter 9

Overall conclusions and outlook

New measurement techniques and the steady increase in knowledge about ridging processes has allowed observational data and model approaches for large-scale sea ice models to be presented in a broader context in this study. The investigation of sea ice pressure ridges based on observations as well as modelling approaches is not new and important theories for numerical modelling of ridges have been developed since the 1970s. However, the derivation of ridge quantities was not provided in large-scale sea ice models so far. The combination of electromagnetic instrumentation and a laser altimeter in the new helicopter-borne EM bird allows measurements of the roughness of the sea ice surface and underside to be made simultaneously with a comparatively large areal coverage, giving a unique set of data for studying sail and keel relationships as well as deriving model parameterisations. Regarding ridge modelling, this study presents a comparison of three different approaches to ridge modelling applicable to large-scale sea ice models for the first time. Two of the three ridge models were newly developed or improved during the study. Finally, a subsample of the EM bird data was used to evaluate the model results from the different ridging algorithms. The evaluation resulted in a rating of the ridging algorithms according to given applications.

The study began with an intercomparison of five sea ice-ocean coupled models and the uncoupled model used later on for ridge modelling and the evaluation of the modelled sea ice drift velocity with satellite-derived data. The comparison showed that almost all models exhibit greater drift speeds than derived from satellite products, though a group of four models (including the uncoupled model) compared rather well with the observations particularly for loose ice conditions at the end of the summer season. However, deviations in drift direction between all models and observations were generally of acceptable range ($\sim$90% within $\pm$5 degrees). An investigation of sea ice drift patterns related to great sea ice export events through the Fram Strait revealed that the models differ strongly from observed drift patterns in some areas. Causes of

the diverging behaviour of the modelled sea ice drift were found in the wind forcing as well as the differing simulated ocean currents. However, the modelled ice export rates were found to be much more strongly influenced by the fundamental differences in drift speed rather than by the diverging drift pattern in the interior Arctic.

Laser altimeter and EM bird data, collected by the AWI for more than a decade now, are available for large tracts of the Arctic Ocean, mainly the Eurasian sector but also the Lincoln Sea. These data were used to derive sail and keel density as well as height and depth, respectively. The spatial distribution of mean sail height featured a clear increase from the Eurasian marginal seas via the Transpolar Drift Stream (and Fram Strait) to the Lincoln Sea. These regional differences were also present in the statistical distribution of the data and, for example, in the Lincoln Sea more sails were found with heights above 2 m or even 3 m. The sail density was found to emphasise limited areas of great roughness, which form at coastlines though may be advected away from their origin with the general ice drift. This also shows that ridges form a kind of memory to the sea ice cover. The coincident measurements of ice surface and underside were used to calculate linear regressions for sail and keel density as well as sail height and keel depth. The linear functions did not suggest a simple proportionality which is often proposed. This is possibly due to the applied cut-off heights. The derived ratio of 10 sails per keel and a ridge height to depth ratio of 1:6.3 m are at the upper limit of observed mean values. The derivation of a relationship between sail height and parent level ice thickness is important for ridge modelling. A linear relationship for the mean sail height and a square root function for maximum sail height were derived from the EM bird data with, however, small correlation coefficients compared to those of the sail to keel relationships.

The basis for the investigation of different ridging algorithms was an uncoupled dynamic-thermodynamic continuum sea ice model. Many such numerical models applied to climate studies use a very simplified deformation scheme only to limit the ice concentration to unity. For more detailed information on ridging, particularly with respect to the needs of ship routing, this simple scheme is insufficient and needs to be replaced by more complex algorithms. Formerly studies using such models focused on comparatively simple quantities, for example the volume of deformed sea ice per unit grid cell area. The present study focused on the derivation of ridge quantities. It was found— as an agreement of the IRIS project partners (see Section 1.4)—that sail density and height are most suitable for a study of ridging including the comparison between models and observations and for application to sea ice forecast for ship routing. These two parameters can be modelled, derived from measurements

184

and remote sensing products (under development) and are important factors in ship transit time calculations. However, ridges are sub-scale features in large-scale sea ice models. Sub-scale processes, such as ridge formation and ablation, need to be parameterised and are only partly linked dynamically to the model itself. The calculation of the ridge quantities is based on statistical analysis of observational data.

Three different ridging algorithms were compared and evaluated with observational data of sail density and height. It was found that sail density is most closely related to topography and sea ice drift whereas the parent ice thickness plays an important role for sail height. Modelled values were within the observed range of sail density (0–30 km^{-1}) and average sail height (1–2 m). The simulations also matched general patterns, for example an increase in sail height from the Siberian marginal seas towards the Canadian Archipelago. Within the Transpolar Drift Stream this gradient was also present in simulations and observations, although it was found to be weaker. However, patterns and magnitudes of sail height and density diverged between models. In terms of a difference in magnitude as compared to the laser altimeter data, the third ridging algorithm—the prognostic derivation of ridge quantities—was found to represent the sail density distribution best whereas the second algorithm—the stochastic derivation of ridges—produces the most realistic sail heights. The second ridge algorithm is recommended for climate studies because of the numerical stability of the redistribution function used. The third algorithm was found to be most appropriate for numerical forecasts of sea ice and ridge quantities.

Parameterisations of the sub-scale ridging process for use in large-scale sea ice models include values prescribed to the model which bind the simulation to ranges of observed quantities. The model performance depends strongly on the accuracy and validity of the various parameters and regression functions derived from measurements. The observations used here and also those previously reported show high variability in the various ridge quantities which complicates the derivation of useful and generally valid parameterisations for ridge formation in large-scale sea ice models. In order to describe ridges a comparatively large set of parameters is necessary—sail height to width ratio, keel depth to width ratio, sail height to keel depth ratio, porosity, number of sails per keel, etc. In contrast to functional relationships (e.g. physical laws) constant parameters restrict simulations from developing freely. The larger the number of parameters the greater the risk to prescribe the model result depending on the individual effect of the parameterisation. Model parameterisations are based on similarities between various natural features or processes. However, only few such similarities were found for the complex structure of ridges. Ridge forma-

tion is very diversified and depends on many small-scale conditions of ice thickness, strength and fracturing. Only the driving force, the ice drift, is linked to the large-scale wind field. However, the wind forcing data may not include local characteristics, particularly in the vicinity of land masses. This is one explanation for differences between simulations and observations since coastlines are a centre of ridge formation. These restrictions make ridging algorithms embedded in large-scale sea ice models comparatively weak tools for representing the diversity of nature. Nevertheless, the present study showed that realistic ridge quantities can be simulated.

The results of the ridge model experiments need to be interpreted from different points of view depending on the application of the sea ice model. On the one hand, model studies which aim at investigating regional climate mean states and variations may well be performed without any ridging algorithms additional to those introduced in Chapter 6. However, as has been shown previously it is very necessary to consider a differentiation between level and deformed ice, which is achievable with redistribution functions as discussed in Chapter 5 and applied to the second ridge algorithm. Another possibility is to use sea ice models based on a distribution function of ice thickness representing several ice thickness categories, but these have a different underlying model concept. The information which is most important for climate studies is contained in the sea ice thickness and concentration. Nevertheless, a deformed ice category provides a memory for the modelled sea ice because the effect of large deformation events is stored in this ice thickness and as the melt rate of thick ice is lower than with thin ice, the intensity and frequency of deformation events affect subsequent ice conditions. To include this memory in a sea ice model ridge quantities are not particularly necessary. In the case that additional ridge information is desired the second ridge algorithm can easily be implemented without affecting the other model physics.

On the other hand, the fast and safe passage of a ship through sea ice depends not on long-term average sea ice conditions but on rapid changes and small-scale variations in the ice cover. Besides mean ice and snow thickness ridges are the main obstacles to ships in ice covered sea. Thus, it is an improvement and an advantage to offer a model to sea ice forecasting which includes the simulation of mean and maximum ridge quantities. However, decision-making in shipping operations also relies on the small-scale sea ice pressure, information which is also important for the correct simulation of pressure ridge formation. In the case of short-term forecasting the third ridge algorithm is most appropriate because it emphasises ridge formation under compressive forces and is sensitive to topographic obstacles and edges in ice concentration. Detailed ridge information gains importance with the ongoing increase in hor-

186

izontal model grid resolution.

Though the present study showed that the implementation of certain ridge quantities in large-scale sea ice (forecast) models is possible its applicability and usefulness still requires trials during ship passages. On board *RV Polarstern* experience has been gained with the use of satellite remote sensing products for navigation through ice covered seas. It has been shown that experience in interpreting such products with respect to ice coverage and roughness is most valuable for a safe and fast passage. Often the existence of small leads, which is difficult to determine from large-scale products, makes the ship passage much easier, independent of the actual ice thickness or state of deformation of the surrounding floes. Thus, the usefulness of forecasting average ridge densities and heights as well as maximum ridge heights can only be determined by intensive application tests.

In the present study the modelled ridge quantities did not affect other model variables and thus represented only additional information. However, a variable drag coefficient coupled to ridge height and density would, for example, result in feedback which influences the sea ice drift velocity and thus subsequent deformation events. This is an improvement which is of interest independent of the application of the sea ice model. The study of different sea ice drift velocity estimates showed that the atmospheric and oceanic drag coefficients are an important quantity because they control the magnitude of the ice drift speed and thus also the magnitude of deformation. In the present study the atmospheric and oceanic drag coefficients were prescribed as constant values. However, it is known that the stress on the ice caused by wind and ocean currents varies with, for example, ice concentration, floe size, shape of floe edges and height and density of ridges.

As described in Chapter 1 the Arctic sea ice cover experiences intense, ongoing changes: ice concentration and thickness are decreasing. Therefore, coefficients and parameterisations of dynamic as well as thermodynamic processes need to be reconsidered, because many are still based on findings from the 1970s, for example from the AIDJEX. The changes in ice conditions cause the interior Arctic ice pack to approach the conditions found so far mainly in the marginal ice zone during summer: larger open water fractions, smaller floes which will, however, be heavily deformed after the winter season because the ice becomes generally thinner and counteracting internal forces are smaller. A reconsideration of parameters might include a simple change of the value as well as the introduction of a dynamic relationship with other model quantities. In the latter case variables such as ice concentration and mean ice thickness, which are prominent model quantities, are preferable because these rely more on the model dynamics itself than on inflexible parameterisations and are thus

subject to fewer restrictions. However, detailed sea ice models with high resolution grids can be improved by including the suggested ridging algorithms. Moreover, parameterisations based on the mean ice thickness or concentration for usage in (global) climate models can be developed and evaluated with a computer time saving regional sea ice model which includes detailed ridging algorithms.

Appendix A

A 1-D stochastic ridge distribution model

Lensu [2003c] introduced a one-dimensional (1-D), horizontally oriented Monte Carlo-type ridge model. In the following a brief overview is given of the principles of the model and possible applications. Furthermore, improvements of the model of *Lensu* [2003c] are discussed and simulation results are shown in which this model is applied to the large-scale sea ice model in association with the ridging algorithm RA3 (Section 6.2).

Model description

The 1-D model can be used to generate random ridge profiles or cross-sections for sails and keels (see Figure A.1). The Monte Carlo simulation places ridge sails on a strait line starting from a complete level profile. The probability that a spacing of length $\tilde{d}_s$ is chosen for the placement of the next sail is proportional to

$$\mathsf{f}(\tilde{d}_s) \propto 1 - a\,\tilde{d}_s\,. \tag{A.1}$$

With $a \in [0.5, 2.0]$ the model reproduces the observed ridge spacing distributions well. Here, $a = 1.1$ is adopted from the study of *Lensu* [2004]. Physically this value corresponds to a strong tendency for ridges to form clusters. For the position X of the ridge within a given length $\tilde{d}_s$, it can be stated:

$$X(r) = c_r\,r^b\,(1 - r)^b \tag{A.2}$$

where c_r is a normalisation constant, so that $\int_0^1 X(r')\,dr' = 1$. The exponent b is a shorthand for $\beta/\tilde{d}_s$ with $\beta \simeq 1000$ m.

The sail height H_s is assumed to follow the modified exponential density function

$$\mathsf{f}(H) = \frac{2}{\pi\,(\langle H_s \rangle - H_{min})}\,\exp\left(-\frac{1}{\pi}\left[\frac{H_s - H_{min}}{\langle H_s \rangle - H_{min}}\right]^2\right) \tag{A.3}$$
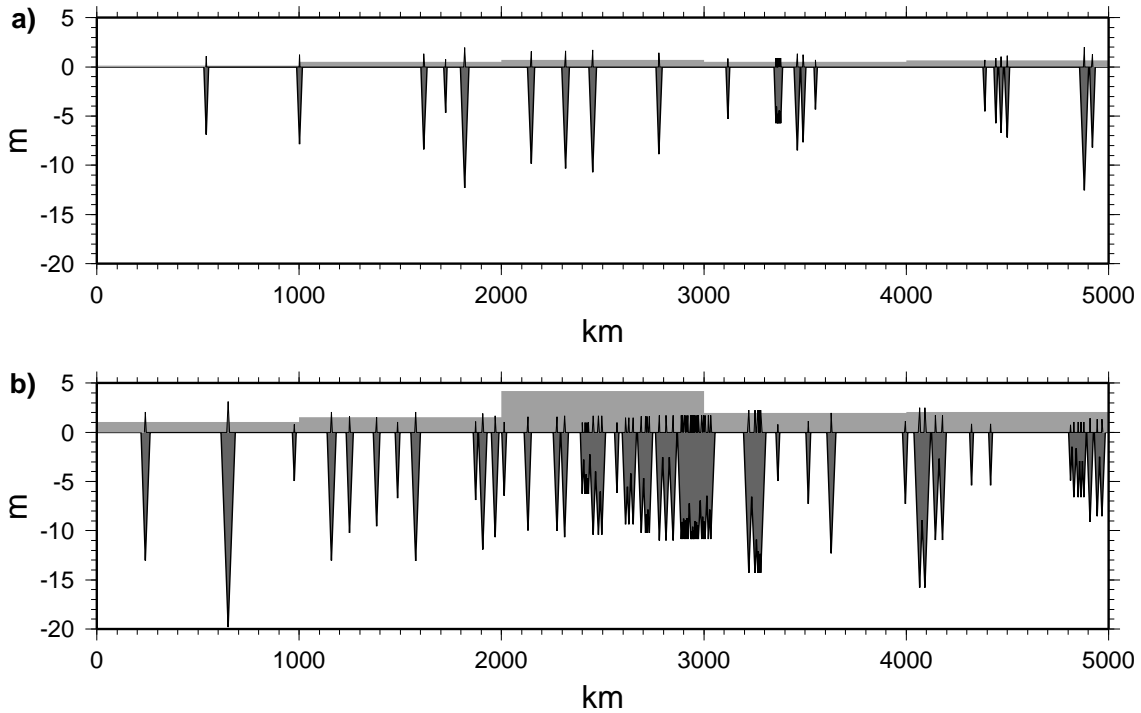
Figure A.1: (**a**) Profile related to the Fram Strait region with a sail density of 5 km^{-1} and a mean sail height of 1.28 m. (**b**) Cross-section related to the Lincoln Sea where 15 ridges per km with an average sail height of 1.55 m are found. Triangular sails and keels are dark grey shaded and light grey shaded stair steps in the background indicate the equivalent ice thickness of ridge volume within 1 km long segments.

where $\langle H_s \rangle$ is the mean sail height, which is a user-defined input parameter. It is used to define a lower bound sail height of $H_{min} = \frac{1}{2} \langle H_s \rangle$ and an upper bound $H_{max} = 5 \langle H_s \rangle$. The model is based upon the assumption of a triangular cross-sectional shape of sail and keel respectively (see Figures 1.11b and A.2a) and that each sail is related to exactly one keel. Further input parameters are therefore ratios of keel depth to sail height k as well as sail width to sail height l_s and keel width to keel depth l_k. In the present study these are chosen based on EM bird observations and literature [*Timco and Burden*, 1997; *Wadhams*, 2000] (see Section 6.3). These ratios are constant during a model run. In the original model of *Lensu* [2003c] the sail to keel ratio was constant at $k = 10$ and $l_s = l_k$. In the present study the model is improved such that the value of k can vary for different simulations and l_s and l_k can differ.

Further, the model takes into account ridge clustering. This process reduces the cross-sectional ridge volume when the spacing between ridges becomes small. Two different types of ridge clusters and the associated decrease in cross-sectional ridge volume are distinguished in the model of *Lensu* [2003c]: type I is created by lateral ridge growth, i.e.

$$\tilde{d}_s < k \left(H_{s_1} + H_{s_2} \right) \tag{A.4}$$

190
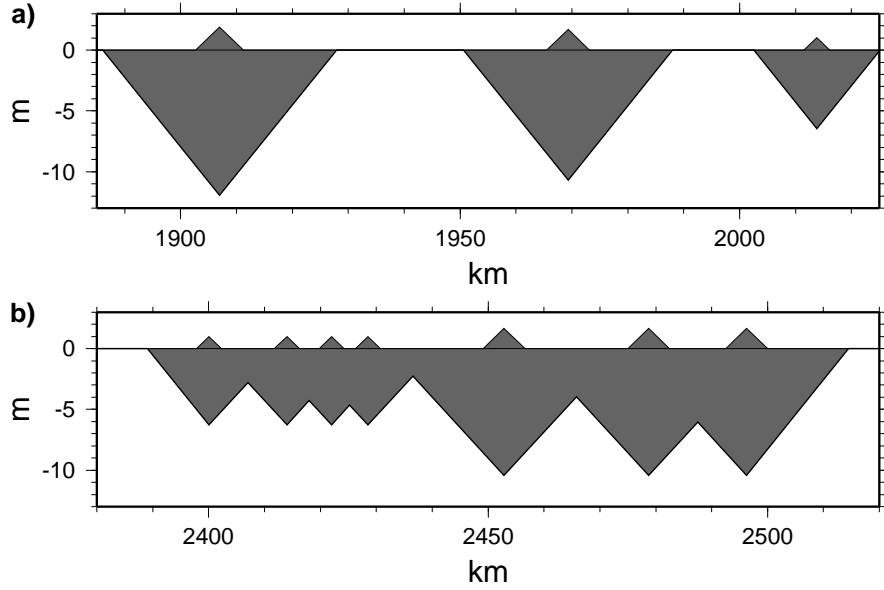
Figure A.2: Magnified segments of the profile in Figure A.1b. (**a**) Separated ridges of completely developed triangular shape. (**b**) Clustered ridges of reduced cross-sectional area.

and assumes constant sail height and keel depth of all ridges which belong to the same cluster. Type II is created by random keel contact

$$k\left(H_{s_1} + H_{s_2}\right) \leq \tilde{d}_s < \tfrac{1}{2}\, l_k\, k\left(H_{s_1} + H_{s_2}\right). \tag{A.5}$$

Different ridges of type-II-clusters can have different sail heights and keel depths. The above equations were adapted to the new variability of l and k for different model runs. However, the model of *Lensu* [2003c] only accounts for the volume reduction of keels in clustering events. Now, the clustering of sails is also enabled.

Example profiles and results

Two example profiles are generated according to the EM bird measurements in the Fram Strait and Lincoln Sea regions presented in Chapter 4. First, a profile length of 5 km is chosen. From Table 4.2 an average sail height of 1.28 m is chosen to represent sea ice in the Fram Strait and 1.55 m that of the Lincoln Sea. Representative ridge densities are found to be 5 and 15 sails per km respectively (see Figure 4.8a). The keel depth to sail height ratio k is chosen to be 6.3 based on the findings from EM bird data (see Section 4.3) and the ratio of sail width to height (l_s) is set to 4.5 and that of keels (l_k) to 3.5 following average values of first year ridges. Two sample realisations of several Monte Carlo simualtions based upon these parameters are presented in Figures A.1a and A.1b for the Fram Strait and Lincoln Sea respectively.
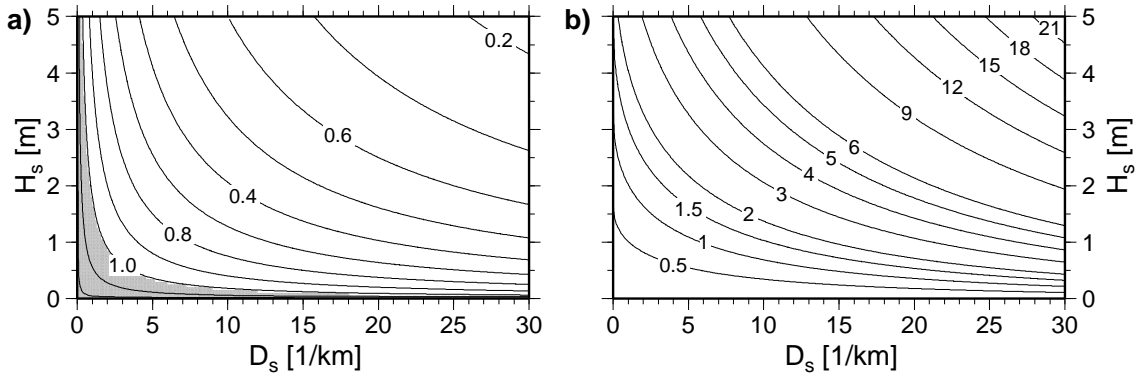
Figure A.3: (**a**) Clustering parameter ξ of Equation (6.28) as a function of sail density D_s and sail height H_s. The grey shaded area marks the interval in which ξ is limited to 1.0. Contour interval is 0.1. (**b**) Actual ridged ice thickness or equivalent ice thickness H_r of Equation (6.13) as a function of sail density D_s and sail height H_s. Regard variations in contour intervals.

With the 1-D model one can calculate the equivalent ice thickness, which is the mean thickness or volume per unit profile length and ridge length of the ice stored in all sails and keels within a certain length segment. Hence, the equivalent ice thickness corresponds to the actual ridged ice thickness in a two-thickness-categories large-scale sea ice model because an ice concentration of 1.0 is assumed for the 1-D simulations.

Figure A.2 shows magnifications of the profile which relates to the Lincoln Sea. While Figure A.2a shows ridges with fully developed cross-sectional area, Figure A.2b shows the effect of clustering. The latter segment includes two type-I-clusters, one on the left with four ridges of the same ridge height, and three on the right with a larger constant height. All seven ridges together form a type-II-cluster.

The 1-D model is useful for deriving ridge parameterisations for application to large-scale sea ice models. The model was used by *Lensu* [2004] to estimate a factor which accounts for the reduction of the cross-sectional ridge volume caused by clustering as a function of sail height and density (see Equation (6.28))

$$\xi(D_s, H_s) = \max\left\{1.24\,\exp\left(-0.16\sqrt{D_s\,H_s}\right), 1\right\}\,.$$

The results of this relationship are presented in Figure A.3a in which the grey-shaded area marks the part of $D_s H_s$-space where ξ is reset to unity by the maximum inquiry in the above equation. The contour lines indicate that ξ would increase up to 1.2 otherwise.

In the present study the 1-D model is used to derive a relationship between sail height and density and the stored equivalent ice volume (Equation (6.13))

$$H_r = 0.3\,H_s\exp\left(0.5\,\sqrt{D_s}\right)\,.$$

The ridged ice thickness resulting from different combinations of average sail height and density are displayed in Figure A.3b. Both functions, that of the clustering factor and that of the equivalent thickness, are applied to the large-scale sea ice model in ridge algorithm RA3 (see Chapter 6).

The relationships between the clustering factor and the equivalent ice thickness and sail density and height are rather similar. Considering that only one quantity, sail density or height, is varied, both functions develop their effect for sail heights larger than 1 m and densities above 5 km^{-1}. It is mainly a simultaneous change in both sail density and height, which causes larger effects. However, it is important to note that the sail density has a very weak impact on the equivalent ice thickness for sail heights smaller than 1 m whereas the sail height strongly affects the equivalent ice thickness for all sail densities (Figure A.3b)

In RA3 an impact of the sail height on the ridge growth, which is determined by the function φ, is introduced by applying the clustering function ξ for $\xi < 1$ (see Equation (6.30)). Otherwise φ is only determined by the sail density. For small sails with heights less than 1 m ξ reduces the impact of a changing sail density on the ridge growth rate whereas for sail heights above 1 m the influence of the sail density on the ridge growth is strengthened compared to the case of $\xi = 1$. In general the impact of sail density and height on the ridge growth in RA3 is similar to that on the clustering function illustrated in Figure A.3a. This also means that for an increasing sail density the sail height gains influence on the clustering factor as well as the ridge growth. Furthermore, the impact of clustering on sail volume is found to be negligibly small compared to the effect on keel volume because the sail cross-sectional volume is small compared to that of keels and sails overlap only in the rare case of very strong clustering.

Appendix B

On statistical distributions

B.1   The log-normal distribution

Initially ridge spacing was thought to fit a negative exponential distribution [*Mock et al.*, 1972] which is a good assumption for ridge sail heights or keel drafts. But *Wadhams and Davy* [1986] found that the distribution of ridge spacings satisfies a log-normal distribution[a] even better. This is supported by investigations of e.g. *Key and McLaren* [1989] and the present study.

An easy way to find out whether a continuous random variable x shows a log-normal distribution or not is to investigate the ability of the transformed random variable $y = ln(x)$ to satisfy a normal distribution $\mathcal{N}(\mu(y), \sigma(y))$. The mean μ is defined as

$$\mu(y) = \frac{1}{n} \sum_{i=n}^{n} y_i \qquad (B.1)$$

and equals the mode and the median in the case of a normal distribution. The integer n denotes the number of samples contained in the data set. The variance σ^2, and standard deviation σ are given by

$$\sigma^2(y) = \frac{1}{n-1} \sum_{i=n}^{n} (y_i - \mu(y))^2. \qquad (B.2)$$

The median $\hat{\mu}$ of the log-normally distributed variable x equals $e^{\mu(y)}$ of the mean of the normally distributed variable y (Equation (B.1)). In geosciences, the log-normally distribution is often applied to cases where the object of interest yields only positive values ($x > 0$).

---

[a]For a first reference on log-normal distributions see *Aitchison and Brown* [1957] or refer to the modern compendium of *Crow and Shimizu* [1988]. The definitions in Appendix B.1 and B.2 are mainly based on *Storch and Zwiers* [2001].
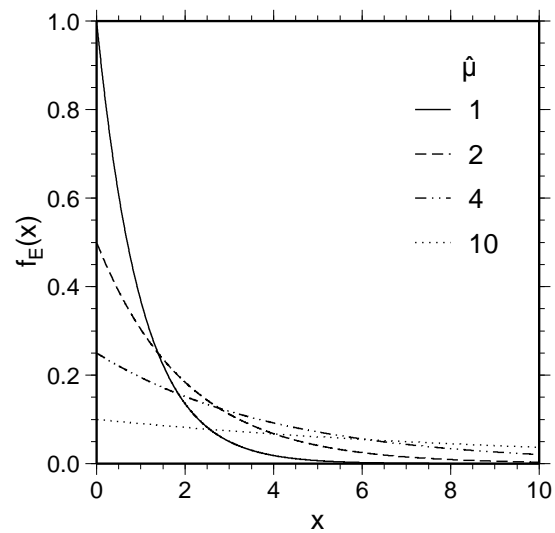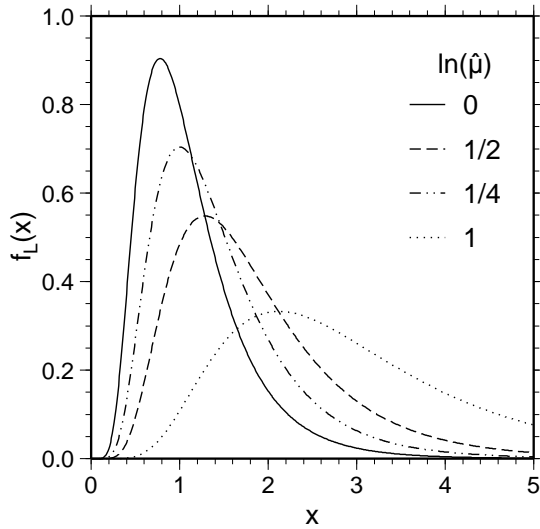
Figure B.1: Examples of the log-normal distribution with $\sigma^2 = \frac{1}{2}$ and $\ln\hat{\mu} = 0$, $\frac{1}{2}$, $\frac{1}{4}$ and 1.

Figure B.2: Example of the exponential distribution with $\hat{\mu} = 1$, 2, 4 and 10.

The probability density function (PDF) of the log-normal distribution is

$$
f_L(x) = \begin{cases} \dfrac{1}{\sqrt{2\,\pi\,\sigma^2(y)}}\,\dfrac{1}{x}\,\exp\left(-\dfrac{(\ln(x)-\hat{\mu}(x))^2}{2\,\sigma^2(y)}\right) & ,\ \text{if } x > 0 \\ 0 & ,\ \text{otherwise}\,. \end{cases} \tag{B.3}
$$

The geometric mean μ_G is closely related to log-normal distributed values, such as x,

$$
\mu_G = \sqrt[n]{\prod_{i=1}^{n} x_i} \tag{B.4}
$$

because the logarithm of the geometric mean $\ln\mu_G(x)$ equals the median $\hat{\mu}(x)$. The mean μ_L and the variance σ_L^2 of the log-normal distribution are

$$
\mu_L = \hat{\mu}\,e^{\frac{1}{2}\sigma^2} \tag{B.5}
$$
$$
\sigma_L^2 = \hat{\mu}^2\,e^{\sigma^2}\left(e^{\sigma^2}-1\right)\,. \tag{B.6}
$$

The graph of the log-normal distribution is limited to zero on its left and resembles a negative exponential decline on its right (see Figure B.1). The position of the mode and the shape of the curve are determined by σ and μ.

B.2   The exponential distribution

The exponential distribution is typically used to describe the temporal duration of certain processes, though it may also be applied to model situations where certain events occur with a constant probability per unit distance. In the

present study, the latter relationship is considered and the exponential distribution is used to describe the distribution of different sail heights along a profile of ridged sea ice, where smaller sails are more frequent than larger sails. The striking difference to the log-normal distribution is that the modal value of a set of samples of an exponentially distributed variable x always equals the smallest sample x, considering that $x > 0$. Compared to the log-normal distribution the exponential distribution shows only the exponential decline from the maximum $f_L(x)$ towards larger x (see Figure B.2).

The PDF of the exponential distribution is

$$
f_E(x) = \begin{cases} \dfrac{1}{\hat{\mu}(x)} \, \exp\left(-\dfrac{x}{\hat{\mu}(x)}\right) & \text{, if } x > 0 \\ 0 & \text{, otherwise} \end{cases} \tag{B.7}
$$

where $\hat{\mu}$ denotes the median of x. The mean and variance of the exponential distribution are given by

$$
\mu_E = \hat{\mu} \tag{B.8}
$$
$$
\sigma_E^2 = \hat{\mu}^2 \,. \tag{B.9}
$$

B.3 Density and distribution functions

After *Storch and Zwiers* [2001] the probability density function (PDF) or density function is a continuous function $f(x)$ defined in $\mathbb{R}$ with the following properties

$$
f(x) \geq 0 \quad \text{for all } x
$$
$$
\int_{-\infty}^{\infty} f(x') \, dx' = 1
$$
$$
P(a < x < b) = \int_a^b f(x') \, dx'
$$

where P is the probability that $x \in (a, b)$. The PDF is defined as the derivative of the cumulative distribution function (CDF) or distribution function $F(x)$

$$
\frac{d}{dx} F(x) = f(x)
$$

and hence,

$$
F(x) = \int_{-\infty}^{x} f(x') \, dx' \,.
$$

The CDF is a non-decreasing differentiable function defined in $\mathbb{R}$ with the constrains

$$
\lim_{x \to -\infty} F(x) = 0
$$
$$
\lim_{x \to \infty} F(x) = 1 \,.
$$

The CDF is often used to calculate probabilities because

$$\mathsf{P}(a < x < b) = \mathsf{F}(b) - \mathsf{F}(a)$$

and is thus suitable to convert samples of an equal-distribution random-number generator into random numbers of a prescribed density function.

Appendix C

On invariants of the strain rate tensor

C.1 Derivation and meaning of the invariants

A tensor is a fundamental mathematical expression. For its determination two values are important: the dimension of the space x in which it is defined and its rank y. These two values determine the number of components a tensor has: x^y. For example a scalar is a tensor of rank 0. Following this definition a vector is a tensor of rank 1. Assuming a two dimensional space, in which the sea ice cover is typically defined, the number of components of a tensor of rank 2, such as the strain rate $\dot{\varepsilon}$, is $2^2 = 4$.

The components of a tensor change with the choice of the coordinate system. This characteristic is used to rotate the reference coordinate system in a way that the new off-diagonal tensor components equal zero and the normal components reach extreme values [*Mellor*, 1986]. The new normal components are called principle components and the new coordinate axes are the principle axes. The principle components are derived from the characteristic or eigenvalue equation:

$$\det(\dot{\varepsilon} - \dot{\varepsilon}_k \, \delta_{ij}) = 0 \tag{C.1}$$

where $\dot{\varepsilon}_k$ denotes the eigenvalues and δ_{ij} is the Kronecker delta. The calculation of the determinant yields

$$\det(\dot{\varepsilon} - \dot{\varepsilon}_k \, \delta_{ij}) = \begin{vmatrix} \dot{\varepsilon}_{11} - \dot{\varepsilon}_k & \dot{\varepsilon}_{21} \\ \dot{\varepsilon}_{12} & \dot{\varepsilon}_{22} - \dot{\varepsilon}_k \end{vmatrix} = (\dot{\varepsilon}_{11} - \dot{\varepsilon}_k)(\dot{\varepsilon}_{22} - \dot{\varepsilon}_k) - \dot{\varepsilon}_{21}\dot{\varepsilon}_{12} \, .$$

This result is inserted in Equation (C.1) and solved for $\dot{\varepsilon}_k$ using the fact that the

trace of a tensor is $\mathrm{tr}(\dot{\boldsymbol{\varepsilon}}) = \dot{\varepsilon}_{11} + \dot{\varepsilon}_{22}$ and its determinant $\det(\dot{\boldsymbol{\varepsilon}}) = \dot{\varepsilon}_{11}\dot{\varepsilon}_{22} - \dot{\varepsilon}_{12}^2$.

$$\dot{\varepsilon}_k^2 - \dot{\varepsilon}_k \mathrm{tr}(\dot{\varepsilon}) + \det(\dot{\varepsilon}) = 0 \tag{C.2a}$$

$$\implies \quad \dot{\varepsilon}_k^2 - \dot{\varepsilon}_k \mathrm{tr}(\dot{\varepsilon}) + \left(\tfrac{1}{2}\mathrm{tr}(\dot{\varepsilon})\right)^2 - \left(\tfrac{1}{2}\mathrm{tr}(\dot{\varepsilon})\right)^2 + \det(\dot{\varepsilon}) = 0 \tag{C.2b}$$

$$\implies \quad \dot{\varepsilon}_k = \frac{1}{2}\mathrm{tr}(\dot{\varepsilon}) \pm \sqrt{\frac{1}{4}\mathrm{tr}^2(\dot{\varepsilon}) - \det(\dot{\varepsilon})}, \quad k = 1, 2. \tag{C.2c}$$

Relating these results to the strain rate, $\dot{\varepsilon}_1$ and $\dot{\varepsilon}_2$ are the principle strain rates and the shear strain rates are zero in principle coordinates.

Associated with the rotation of the coordinate system are quantities that do not change their value: the invariants. The number of invariants of a tensor equals its dimension x. All invariants are scalars that are intimately related to the tensor. A first invariant is always the trace of the tensor and the last its determinant. The coefficients of Equation (C.2a) are such invariants, i.e. $\mathrm{tr}(\dot{\boldsymbol{\varepsilon}}) = \mathrm{tr}(\dot{\boldsymbol{\varepsilon}}')$ and $\det(\dot{\boldsymbol{\varepsilon}}) = \det(\dot{\boldsymbol{\varepsilon}}')$ where $\dot{\boldsymbol{\varepsilon}}'$ is the strain rate tensor in principle coordinates. As $\mathrm{tr}(\dot{\boldsymbol{\varepsilon}}')$ already shows, linear combinations of the principle components, such as their sum or difference, are also invariants. The international agreement (AID-JEX convention) provides the following pair of invariants [*Thorndike et al.*, 1975; *Rothrock*, 1975; *Coon*, 1980; *Leppäranta*, 1998]:

$$\dot{\varepsilon}_I = \dot{\varepsilon}_1 + \dot{\varepsilon}_2 = \mathrm{tr}(\dot{\varepsilon}) = \dot{\varepsilon}_{11} + \dot{\varepsilon}_{22} \tag{C.3a}$$

$$\dot{\varepsilon}_{II} = \dot{\varepsilon}_1 - \dot{\varepsilon}_2 = \sqrt{\mathrm{tr}^2(\dot{\varepsilon}) - 4\det(\dot{\varepsilon})} = \sqrt{(\dot{\varepsilon}_{11} - \dot{\varepsilon}_{22})^2 + 4\dot{\varepsilon}_{12}^2}. \tag{C.3b}$$

Comparing these invariants with those described in Section 5.1 for a general velocity field (see especially Equation (5.4)), it is obvious that $\dot{\varepsilon}_I$ equals the rate of divergence D_o (see Section 5.1). The second invariant $\dot{\varepsilon}_{II}$ reflects twice the maximum of the rate of shear $\sqrt{E_o^2 + F_o^2}$. The shear rate depends on the orientation of a planar element in the drift field. For example a square will experience no shear, if it is aligned with the principle axes, whereas the shear rate reaches its maximum of $\frac{1}{2}\dot{\varepsilon}_{II}$ in the case that the square is rotated by $45\,^\circ$ to the principle axes.

C.2   Representation in different coordinates

The strain rate tensor and its invariants can be expressed in different coordinates: cartesian, principle axes and cylindrical. The expression in cartesian coordinates as shown in Equation (2.15) has normal strain rates, $\dot{\varepsilon}_{11}$ and $\dot{\varepsilon}_{22}$, and shear strain rates $\dot{\varepsilon}_{21} = \dot{\varepsilon}_{12}$ which differ from zero. In principle axes the coordinate system is rotated such that the shear strain rates are identically zero. What remains are the new components along the leading diagonal of the rotated tensor, the principle strain rates $\dot{\varepsilon}_1$ and $\dot{\varepsilon}_2$ from Equation (C.2c). These are linked to

the strain rate tensor in cartesian coordinates by

$$\dot{\varepsilon}_k = \frac{1}{2}\dot{\varepsilon}_I \pm \frac{1}{2}\dot{\varepsilon}_{II} \tag{C.4}$$

The advantage of a principle axes coordinate system is that each strain rate state can be expressed by just two components, the vector $(\dot{\varepsilon}_1, \dot{\varepsilon}_2)$. The various states of deformation can also be expressed in cylindrical coordinates. The cylindrical coordinates $(|\dot{\boldsymbol{\varepsilon}}|, \theta)$ are given by the absolute deformation rate and the deformation angle

$$|\dot{\boldsymbol{\varepsilon}}| = \sqrt{\dot{\varepsilon}_I^2 + \dot{\varepsilon}_{II}^2} \quad \text{and} \quad \theta = \tan^{-1}\left(\frac{\dot{\varepsilon}_{II}}{\dot{\varepsilon}_I}\right) \tag{C.5}$$

(compare Equations (2.17) and (2.18)). These relationships further imply that $\dot{\varepsilon}_I = |\dot{\boldsymbol{\varepsilon}}|\cos\theta$ and $\dot{\varepsilon}_{II} = |\dot{\boldsymbol{\varepsilon}}|\sin\theta$. For an illustration of the absolute rate of deformation and the deformation angle see Figure 2.3.

The change between reference coordinate systems from $(\dot{\varepsilon}_I, \dot{\varepsilon}_{II})$ to $(\dot{\varepsilon}_1, \dot{\varepsilon}_2)$ means an anti-clockwise rotation of $45°$. Expressions of the reference system $(\dot{\varepsilon}_1, \dot{\varepsilon}_2)$ are apostrophied ($'$) in the following. The absolute rate of deformation as well as the deformation angle can be expressed in the $(\dot{\varepsilon}_1, \dot{\varepsilon}_2)$-coordinate system:

$$|\dot{\boldsymbol{\varepsilon}}'| = \sqrt{\dot{\varepsilon}_1^2 + \dot{\varepsilon}_2^2} = \frac{1}{\sqrt{2}}|\dot{\boldsymbol{\varepsilon}}| \quad \text{and} \quad \tan\theta' = \frac{\dot{\varepsilon}_2}{\dot{\varepsilon}_1} = \tan\left(\theta + \frac{\pi}{4}\right) \tag{C.6}$$

The deformation angle is the angle between the x-axis of the reference system and the normal vector $\dot{\varepsilon}$ [*Rothrock*, 1975].

Now that three different coordinate systems, cartesian, principle axes and cylindrical, and different sets of invariant expressions have been mentioned an overview is given here for clarity. This overview is especially of use in Chapter 5,

coordinates	$\dot{\varepsilon}_I$	$\dot{\varepsilon}_{II}$
cartesian	$\dot{\varepsilon}_{11} + \dot{\varepsilon}_{22}$	$\left[(\dot{\varepsilon}_{11} - \dot{\varepsilon}_{22})^2 + 4\dot{\varepsilon}_{12}^2\right]^{1/2}$
principle axes	$\dot{\varepsilon}_1 + \dot{\varepsilon}_2$	$(\dot{\varepsilon}_1 - \dot{\varepsilon}_2)$
cylindrical	$|\dot{\boldsymbol{\varepsilon}}|\cos\theta$	$-|\dot{\boldsymbol{\varepsilon}}|\sin\theta$
	$|\dot{\boldsymbol{\varepsilon}}'|(\sin\theta' + \cos\theta')$	$|\dot{\boldsymbol{\varepsilon}}'|(\cos\theta' - \sin\theta')$
	$\Delta_{\dot{\varepsilon}}^2$	
cartesian	$(\dot{\varepsilon}_{11} + \dot{\varepsilon}_{22})^2 + e^{-2}\left[(\dot{\varepsilon}_{11} - \dot{\varepsilon}_{22})^2 + 4\dot{\varepsilon}_{12}^2\right]$	
principle axes	$(\dot{\varepsilon}_1 + \dot{\varepsilon}_2)^2 + e^{-2}(\dot{\varepsilon}_1 - \dot{\varepsilon}_2)^2$	
cylindrical	$\frac{1}{2}|\dot{\boldsymbol{\varepsilon}}|^2\left[(1 + e^{-2}) + (1 - e^{-2})\cos(2\theta)\right]$	
	$|\dot{\boldsymbol{\varepsilon}}'|^2\left[(1 + e^{-2}) + (1 - e^{-2})\sin(2\theta')\right]$	

Table C.1: Strain rate invariants $\dot{\varepsilon}_I$ and $\dot{\varepsilon}_{II}^2$ and the $\Delta_{\dot{\varepsilon}}$-function expressed in three different coordinate systems [after *Gray and Killworth*, 1996].

where deformation schemes are transformed towards the cylindrical representation in order to demonstrate their behaviour in various states of ice motion.

The two invariants of the two-dimensional strain rate tensor can be expressed independently from the reference coordinate system by

$$\dot{\varepsilon}_I = \text{tr}\left(\dot{\boldsymbol{\varepsilon}}\right) \quad \text{and} \quad \dot{\varepsilon}_{II}^2 = -4 \det\left(\hat{\dot{\boldsymbol{\varepsilon}}}\right) \tag{C.7}$$

following the study of *Rothrock* [1975] and correcting *Gray and Killworth* [1996]. Here, $\dot{\boldsymbol{\varepsilon}}$ is the strain rate tensor in terms of the respective coordinate system, and δ_{ij} denotes the Kronecker delta. The terms

$$\bar{\dot{\varepsilon}} = \frac{1}{2}\text{tr}\left(\dot{\boldsymbol{\varepsilon}}\right) \quad \text{and} \quad \hat{\dot{\boldsymbol{\varepsilon}}} = \dot{\boldsymbol{\varepsilon}} - \bar{\dot{\varepsilon}}\,\delta_{ij} \tag{C.8}$$

denote the bulk and deviatoric strain rate respectively [*Mellor*, 1986].

The function $\Delta_{\dot{\varepsilon}}$ of Equation (2.23) can also be generalised to

$$\Delta_{\dot{\varepsilon}} = \sqrt{\dot{\varepsilon}_I^2 + \frac{1}{e^2}\dot{\varepsilon}_{II}^2} \tag{C.9}$$

where e denotes the eccentricity of the elliptical yield curve, which is 2 in the present study.

An overview of the invariant expressions that need to be substituted in Equations (C.7) and (C.9) to gain the correct relationship expression for the particular coordinate system is given in Table C.1. The list includes expressions for both cylindrical reference systems, $(\dot{\varepsilon}_I, \dot{\varepsilon}_{II})$ and $(\dot{\varepsilon}_1, \dot{\varepsilon}_2)$, following the deformation scheme formulation of *Shinohara* [1990] and match the study of *Gray and Killworth* [1996] (see Section 5.3).

202

List of Acronyms

ADCP	Acoustic Doppler current profiler
AIDJEX	Arctic Ice Dynamics Joint Experiment (1970–1976)
AO	Arctic Oscillation
ARK	Label for Arctic expeditions of *RV Polarstern*
AUV	Autonomous underwater vehicle
AVHRR	Advanced very high resolution radiometer (satellite sensor)
AWI	Alfred Wegener Institute for Polar and Marine Research, Bremerhaven, Germany
BS	Barents Sea
CDF	Cumulative distribution function
CERSAT	Centre ERS d'Archivage et de Traitement (French ERS Processing and Archiving Facility), Plouzane, France
ECMWF	European Centre for Medium Range Weather Forecast, Reading, United Kingdom
EM	Electromagnetic
ERS	European Remote Sensing of the European Space Agency
FS	Fram Strait
GreenICE	Greenland Arctic Shelf Ice and Climate Experiment
GSA	Great salinity anomaly
GSFC	Goddard Space Flight Center, Greenbelt, MD, USA
IFREMER	Institut français de recherche pour l'exploitation de la mer (French Research Institute for Exploitation of the Sea), Issy-les-Moulineaux Cedex, France
IOS	Institute of Ocean Science, Sidney, BC, Canada
IRIS	Ice Ridging Information for Decision Making in Shipping Operations (EU project)
IABP	International Arctic Buoy Program, hosted by the University of Washington, Seattle, WA, USA
LASER	Light amplification by stimulated emission of radiation
LS	Lincoln Sea
MIZ	Marginal ice zone
MOM	Modular Ocean Model

MS	Marginal seas
MSR	Marginal seas (with strongly ridged ice)
NAO	North Atlantic Oscillation
NAOSIM	North Atlantic and Arctic Ocean Sea Ice Model
NCAR	National Center of Atmospheric Research, Boulder, CO, USA
NCEP	National Centers for Environmental prediction, Camp Springs, MD, USA
NPS	Naval Postgraduate School, Monterey, CA, USA
NSIDC	National Snow and Ice Data Center, Boulder, CO, USA
PDF	Probability density function
POM	Princeton Ocean Model
POP	Parallel Ocean Program model
QuikSCAT	Quick Scatterometer (satellite sensor)
RA	Ridging algorithm
RMSE	Root mean squared error
SAT	Surface air temperature
SHEBA	Surface Heat Budget of the Arctic Ocean (international project)
SIM	The AWI dynamic-thermodynamic sea ice model
SLP	Sea level pressure
SMMR	Scanning multichannel microwave radiometer
SONAR	Sound navigation and ranging
SSM/I	Special sensor microwave/imager (satellite sensor)
TDS	Transpolar Drift Stream
ULS	Upward-looking sonar
UW	University of Washington, Polar Science Center, Seattle, WA, USA

List of Variables

All variables and parameters in this study are given in unscaled SI units, e.g. [m], if not mentioned otherwise. The two expressions $\bar{x}$ and $\langle x \rangle$ refer both to the arithmetic mean and the expression ice always means sea ice. In the following table the main variables used in this study are listed with the respective symbol. Variables only used once are declared on the spot. An eventual diverging usage of symbols is explained on the spot as well in each case.

symbol	variable name	symbol	variable name
A	total ice concentration	H_l	actual level ice thickness [m]
A_l	level ice concentration		
A_r	ridged ice concentration	H_r	actual ridged ice thickness [m]
C_{cfl}	Courant number		
D_k	keel density [km^{-1}]	H_s	sail height [m]
D_s	sail density [km^{-1}]	$H_{s_{max}}$	maximum sail height [m]
$\tilde{d}_s$	sail spacing [m]	h	total ice volume (per unit area) [m]
E_{def}	deformation energy (per unit area) [J m^{-2}]		
		h_l	level ice volume [m]
E_{pot}	potenial energy (per unit area) [J m^{-2}]	h_r	ridged ice volume [m]
		h_s	snow volume [m]
F_h	freezing rate of ice volume [m]	$\vec{k}$	vertical unit vector
		L_A	consumed level ice area (per unit ridge length) [m]
$\vec{F}_{int}$	internal ice force (per unit area) [N m^{-2}]		
		L_i	specific latent heat of sea ice [J kg^{-1}]
f	Coriolis parameter [s^{-1}]		
H	actual ice thickness [m]	L_s	length of sail/ridge [m]
H_0	cut-off height/depth [m]	M_h	melt rate of ice volume [m]
H_b	ice block thickness in a ridge [m]	$\tilde{M}_h$	melt rate of ice volume per ice volume
H_{eq}	equilibrium ice thickness [m]	P	ice strength [N m^{-1}]
		P^*	ice strength parameter [N m^{-2}]
H_k	keel depth [m]		
$H_{k_{max}}$	maximum keel depth [m]	p_a	sea level pressure [hPa]

symbol	variable name
Q_A	open water formation due to shear motion
Q_a	atmospheric heat flux [$\mathrm{W\,m^{-2}}$]
Q_c	conductive heat flux through the ice [$\mathrm{W\,m^{-2}}$]
Q_w	ice-ocean heat flux [$\mathrm{W\,m^{-2}}$]
R	ridging intensity [m]
R_A	ridging factor in ice redistribution
S_A	thermodynamic change of ice concentration
S_h	thermodynamic change of ice volume [m]
S_{h_s}	thermodynamic change of snow volume [m]
T_A	ice redistribution function
T_a	surface air temp. [$^\circ$C]
T_b	bottom ice temp. [$^\circ$C]
T_s	surface ice temp. [$^\circ$C]
$t, \Delta t$	time, time increment [s]
$\vec{u}$	ice drift velocity [$\mathrm{m\,s^{-1}}$]
$\vec{u}_a$	surface wind velocity [$\mathrm{m\,s^{-1}}$]
$\vec{u}_g$	geodtrophic wind velocity [$\mathrm{m\,s^{-1}}$]
$\vec{u}_w$	ocean current velocity [$\mathrm{m\,s^{-1}}$]
V	ridge volume [$\mathrm{m^3}$] (per unit ridge length: [$\mathrm{m^2}$])
$w_{b,s}$	vertical ice velocity [$\mathrm{m\,s^{-1}}$] (at ice cover bottom and surface respectively)
x, y	horizontal dimensions
$\Delta x, \Delta y$	horizontal distances [m]
z	vertical dimension

symbol	variable name
$\mathcal{F}_A$	ice area flux [$\mathrm{km^2\,month^{-1}}$]
$\mathcal{F}_h$	ice volume flux [$\mathrm{km^3\,month^{-1}}$]
$\mathcal{H}$	Heaviside step function
α	sea ice surface albedo
α	change in ridge density [$\mathrm{km^{-1}}$] ($\rightarrow$ RA3)
α_0	new ridge formation [$\mathrm{km^{-1}}$] ($\rightarrow$ RA3)
β	function relating a quantity to ice concentration
$\dot{\varepsilon}$	strain rate of ice [s^{-1}]
λ_i	thermal conductivity of sea ice [$\mathrm{W\,m^{-1}K^{-1}}$]
φ, φ_0	change in ice area (per unit ridge length) [km] ($\rightarrow$ RA3)
ψ	deformation scheme
ρ_a	density of air [$\mathrm{kg\,m^{-3}}$]
ρ_i	density of sea ice [$\mathrm{kg\,m^{-3}}$]
$\boldsymbol{\sigma}$	ice stress [$\mathrm{N\,m^{-2}}$]
σ	standard deviation
$\vec{\tau}_a$	atmospheric stress (per unit area) [$\mathrm{N\,m^{-2}}$]
$\vec{\tau}_w$	oceanic stress (per unit area) [$\mathrm{N\,m^{-2}}$]
θ	deformation angle
ξ	ridge clustering function
F	cumulative distribution function (CDF)
f	probability density function (PDF)
$\mathbb{Z}$	set of all integers
$\mathbb{R}$	set of all real numbers
∇	2-D nabla operator (only x and y components)
∇_3	3-D nabla operator

List of Figures

List of Tables

Bibliography

Aagaard, K., and E. C. Carmack, The Role of Sea Ice and Other Fresh Water in the Arctic Circulation, *J. Geophys. Res., 94*(C10), 14,485–14,498, 1989.

Aitchison, J., and J. A. C. Brown, *The Lognormal Distribution,* 176 pp., Cambridge University Press, 1957.

Alexandrov, V. Y., T. Martin, J. Kolatschek, H. Eicken, M. Kreyscher, and A. P. Makshtas, Sea ice circulation in the Laptev Sea and ice export to the Arctic Ocean: Results from satellite remote sensing and numerical modeling, *J. Geophys. Res., 105,* 17,143–17,159, 2000.

AMAP, *AMAP Assessment Report: Arctic Pollution Issues. Arctic Monitoring and Assessment Programme (AMAP),* xii + 859 pp., Oslo, Norway, 1998.

Amundrud, T. L., H. Melling, and R. G. Ingram, Geometrical constraints on the evolution of ridged sea ice, *J. Geophys. Res., 109,* C06005, doi:10.1029/2003JC002251, 2004.

Andreas, E. L., and B. A. Cash, Convective heat transfer over wintertime leads and polynyas, *J. Geophys. Res., 104*(C11), 25,721–25,734, 1999.

Arfeuille, G., L. A. Mysak, and L.-B. Tremblay, Simulation of the interannual variability of the wind-driven Arctic sea-ice cover during 1958–1998, *Clim. Dyn., 16,* 107–121, 2000.

Arya, S. P. S., Contribution of Form Drag on Pressure Ridges to the Air Stress on Arctic Sea Ice, *J. Geophys. Res., 78*(30), 7092–7099, 1973.

Axell, L., B. Cheng, J. Haapala, T. Vihma, and K. Wang, Ridging module parameterisation by analysed ridging data and second version of models, *EU Project IRIS (EVK3-CT-2002-00083), Deliverable D21, Internal report,* Swedish Meteorological and Hydrological Institute, Norrköping, Sweden, 2005.

Belchansky, G. I., D. C. Douglas, and N. G. Platonov, Spatial and temporal variations in the age structure of Arctic sea ice, *Geophys. Res. Lett., 32,* L18504, doi:10.1029/2005GL023976, 2005.

Belkin, I. M., S. Levitus, and J. Antonov, "Great Salinity Anomalies" in the North Atlantic, *Progr. Oceanogr., 41*(1), 1–68, 1998.

Bjørgo, E., O. M. Johannessen, and M. W. Miles, Analysis of merged SMMR-SSM/I time series of Arctic and Antarctic sea ice parameters 1978–1995, *Geophys. Res. Lett., 24*(4), 413–416, 1997.

Brümmer, B., S. Thiemann, and A. Kirchgäßner, A cyclone statistics for the Arctic based on European Centre re-analysis data, *Meteorol. Atmos. Phys., 75*, 233–250, 2000.

Brümmer, B., G. Müller, B. Affeld, R. Gerdes, M. Karcher, and F. Kauker, Cyclones over Fram Strait: impact on sea ice and variability, *Polar Research, 20*(2), 147–152, 2001.

Carmack, E. C., The Arctic Ocean's freshwater budget: Sources, storage and export, in *The Freshwater Budget of the Arctic Ocean*, edited by E. L. Lewis, pp. 91–126, NATO ASI Series 2: Environmental Security, vol. 70, Kluwer Academic Publishers, Dordrecht, Netherlands, 2000.

Cavalieri, D. J., and S. Häkkinen, Arctic climate and atmospheric planetary waves, *Geophys. Res. Lett., 28*(5), 791–794, 2001.

Cavalieri, D. J., P. Gloersen, C. L. Parkinson, J. C. Comiso, and H. J. Zwally, Observed Hemispheric Asymmetry in Global Sea Ice Changes, *Science, 278*, 1104–1106, 1997.

Chapman, W. L., and J. E. Walsh, Recent Variations of Sea Ice and Air Temperature in High Latitudes, *Bull. Am. Met. Soc., 74*(1), 33–47, 1993.

Colony, R., and A. S. Thorndike, Sea Ice Motion as a Drunkard's Walk, *J. Geophys. Res., 90*(C1), 965–974, 1985.

Comiso, J. C., Satellite-observed variability and trend in sea-ice extent, surface temperature, albedo and clouds in the Arctic, *Ann. Glaciol., 33*, 457–473, 2001.

Comiso, J. C., A rapidly declining perennial sea ice cover in the Arctic, *Geophys. Res. Lett., 29*(20), 1956, doi:10.1029/2002GL01565, 2002.

Comiso, J. C., Abrupt decline in the Arctic winter sea ice cover, *Geophys. Res. Lett., 33*, L18504, doi:10.1029/2006GL027341, 2006.

Comiso, J. C., and C. L. Parkinson, Satellite-observed changes in the Arctic, *Phys. Today, 57*(8), 38–44, 2004.

212

Coon, M. D., A Review of AIDJEX modelling, in *Sea Ice Processes and Models*, edited by R. S. Pritchard, pp. 12–27, Univ. Washington Press, Seattle, W.A., USA, 1980.

Courant, R., K. Friedrichs, and H. Lewy, Über die partiellen Differenzengleichungen der mathematischen Physik, *Mathematische Annalen*, *100*(1), 32–74, 1928.

Crow, E. L., and K. Shimizu (Eds.), *Lognormal Distributions: Theory and Applications*, xvi + 387 pp., Marcel Dekker, Inc., New York, 1988.

Cuny, J., P. B. Rhines, and R. Kwok, Davis Strait volume, freshwater and heat fluxes, *Deep-Sea Res. I*, *52*(3), 519–542, 2005.

Curry, J. A., J. L. Schramm, and E. E. Ebert, Sea Ice-Albedo Climate Feedback Mechanism, *J. Climate*, *8*(2), 240–247, 1995.

Davis, N. R., and P. Wadhams, A statistical analysis of Arctic pressure ridge morphology, *J. Geophys. Res.*, *100*(C6), 10,915–10,925, 1995.

Deser, C., On the Teleconnectivity of the "Arctic Oscillation", *Geophys. Res. Lett.*, *27*(6), 779–782, 2000.

Dickson, R. R., J. Meincke, and S.-A. Malmberg, The "Great Salinity Anomaly" in the northern North Atlantic 1968–1982, *Progr. Oceanogr.*, *20*, 103–151, 1988.

Dierking, W., Laser profiling of the ice surface topography during the Winter Weddell Gyre Study 1992, *J. Geophys. Res.*, *100*(C3), 4807–4820, 1995.

Ebert, E. E., and J. A. Curry, An intermediate one-dimensional thermodynamic sea ice model for investigating ice-atmosphere interactions, *J. Geophys. Res.*, *98*(C6), 10,085–10,109, 1993.

Eicken, H., From the Microscopic, to the Macroscopic, to the Regional Scale: Growth, Microstructure and Properties of Sea Ice, in *Sea Ice: An Introduction to its Physics, Chemistry, Biology and Geology*, edited by D. N. Thomas and G. S. Dieckmann, pp. 22–81, Blackwell Science Ltd., 2003.

Emery, W. J., and R. E. Thomson, *Data Analysis Methods in Physical Oceanography, Second and revised edition*, xvi+638 pp., Elsevier Science B.V., Amsterdam, Netherlands, 2001.

Emery, W. J., C. W. Fowler, and J. A. Maslanik, Satellite-derived maps of Arctic and Antarctic sea ice motion: 1988 to 1994, *Geophys. Res. Lett.*, *24*(8), 897–900, 1997.

Ezraty, R., and J. F. Piollé, Sea-ice drift in the central Arctic combining QuikSCAT and SSM/I sea ice drift data – User's manual (v1.0), *Tech. rep.*, CERSAT-IFREMER, 2004.

Fetterer, F., and N. Untersteiner, Observations of melt ponds on Arctic sea ice, *J. Geophys. Res., 103*(C11), 24,821–24,835, 1998.

Fischer, H., Comparison of an optimized dynamic-thermodynamic sea ice model with observations in the Weddell Sea, Reports on Polar and Marine Research, vol. 166, Alfred Wegener Institute, Bremerhaven, Germany, 1995.

Fissel, D. B., J. R. Marko, and H. Melling, Upward looking ice profiler sonar instruments for ice thickness and topography measurements, *Oceans '04 MTS/IEEE Techno-Oceans '04, 3,* 1638–1643, doi:10.1109/OCEANS.2004.1406369, 2004.

Flato, G. M., and R. D. Brown, Variability and climate sensitivity of landfast Arctic sea ice, *J. Geophys. Res., 101*(C11), 25,767–25,777, 1996.

Flato, G. M., and W. D. Hibler, III., An initial numerical investigation of the extent of sea ice ridging, *Ann. Glaciol., 15,* 31–36, 1991.

Flato, G. M., and W. D. Hibler, III., Ridging and strength in modelling the thickness distribution of Arctic sea ice, *J. Geophys. Res., 100*(C9), 18,611–18,626, 1995.

Fowler, C., Polar Pathfinder Daily 25 km EASE-Grid Sea Ice Motion Vectors (Digital media), *Tech. rep.*, Boulder, CO, USA: National Snow and Ice Data Center, 2003.

Fritzsch, B., Arbeitsbericht zur Mitarbeit am Projekt ENVOC, *Tech. rep.*, Alfred Wegener Institute, Bremerhaven, Germany, 2001.

Garbrecht, T., C. Lüppkes, J. Hartmann, and M. Wolff, Atmospheric drag coefficients over sea ice — validation of a parameterisation concept, *Tellus, 54 A,* 205–219, 2002.

Gray, J. M. N. T., and P. D. Killworth, Sea Ice Ridging Schemes, *J. Phys. Oceanogr., 26*(11), 2420–2428, 1996.

Gray, J. M. N. T., and L. W. Morland, A two-dimensional model for the dynamics of sea ice, *Philos. Trans. R. Soc., London Ser. A, 347,* 21–290, 1994.

Gudkovich, Z. M., Relation of the ice drift in the Arctic Basin to ice conditions in Soviet Arctic seas (in russian), *Tr. Okeanogr. Kom. Akad. Nauk. SSSR, 11,* 14–21, 1961.

Haapala, J., On the modelling of ice-thickness redistribution, *J. Glaciol., 46*(154), 427–437, 2000.

Haapala, J., N. Lönnroth, and A. Stössel, A numerical study of open water formation in sea ice, *J. Geophys. Res., 110,* C09011, doi:10.1029/2003JC002200, 2005.

Haas, C., EM ice thickness measurements during GreenICE 2004 field campaign, *Tech. rep.,* EU project GreenICE (EVK2-2001-00280), Alfred Wegener Institute, Bremerhaven, Germany, 2004a.

Haas, C., Late-summer sea ice thickness variability in the Arctic Transpolar Drift 1991–2001 derived from ground-based electromagnetic sounding, *Geophys. Res. Lett., 31,* L09402, doi:10.1029/2003GL019394, 2004b.

Häkkinen, S., An Arctic source for the Great Salinity Anomaly: A simulation of the Arctic ice-ocean system for 1955–1975, *J. Geophys. Res., 98*(C9), 16,397–16,419, 1998.

Harder, M., Dynamics, roughness and age of Arctic sea ice — Numerical investigations with a large-scale model, Reports on Polar Research, vol. 203, Alfred Wegener Institute, Bremerhaven, Germany, 1996.

Harder, M., Roughness, age and drift trajectories of sea ice in large-scale simulations and their use in model verifications, *Ann. Glaciol., 25,* 237–240, 1997.

Harder, M., and P. Lemke, Modelling the Extent of Sea Ice Ridging in the Weddel Sea, in *The Polar Oceans and Their Role in Shaping the Global Environment, Geophys. Monogr.,* vol. 85, edited by O. M. Johannessen, R. D. Muench, and J. E. Overland, pp. 187–197, Amer. Geophys. Union, 1994.

Harder, M., P. Lemke, and M. Hilmer, Simulation of sea ice transport through Fram Strait: Natural variability and sensitivity to forcing, *J. Geophys. Res., 103*(C3), 5595–5606, 1998.

Hibler, W. D., III., Removal of aircraft altitide variations from laser profiles of the Arctic ice pack, *J. Geophys. Res., 77*(36), 7190–7195, 1972.

Hibler, W. D., III., Characterization of cold-regions terrain using airborne laser profilometry, *J. Glaciol., 15*(73), 329–347, 1975.

Hibler, W. D., III., A dynamic-thermodynamic sea ice model, *J. Phys. Oceanogr., 9*(4), 815–846, 1979.

Hibler, W. D., III., Modeling a Variable Thickness Sea Ice Cover, *Month. Weather Rev., 108*(12), 1943–1973, 1980.

Hibler, W. D., III., The role of sea ice dynamics in modeling CO_2 increases, in *Climate Processes and Climate Sensitivity, Geophys. Monogr.*, vol. 29, edited by J. E. Hansen and T. Tikahashi, pp. 238–253, Amer. Geophys. Union, 1984.

Hibler, W. D., III., and K. Bryan, A diagnostic ice-ocean model, *J. Phys. Oceanogr., 17*(7), 987–1015, 1987.

Hibler, W. D., III., and G. M. Flato, Sea Ice Models, in *Climate System Modeling*, edited by K. E. Trenberth, pp. 413–436, Cambridge University Press, 1992.

Hilmer, M., A model study of Arctic sea ice variability, Berichte aus dem Institut f. Meereskunde, vol. 320, Institut f. Meereskunde, 2001.

Hilmer, M., and T. Jung, Evidence for a recent change in the link between the North Atlantic Oscillation and Arctic sea ice export, *Geophys. Res. Lett., 27*(7), 989–992, 2000.

Hilmer, M., and P. Lemke, On the Decrease of Arctic Sea Ice Volume, *Geophys. Res. Lett., 27*(22), 3751–3754, 2000.

Hilmer, M., M. Harder, and P. Lemke, Sea ice transport: a highly variable link between Arctic and North Atlantic, *Geophys. Res. Lett., 25*(17), 3359–3362, 1998.

Holloway, G., F. Dupont, E. Golubeva, S. Häkkinen, E. Hunke, M. Jin, M. Karcher, F. Kauker, M. Maltrud, M. A. M. Maqueda, W. Maslowski, G. Platov, D. Stark, M. Steele, T. Suzuki, J. Wang, and J. Zhang, Water properties and circulation in Arctic Ocean models, *J. Geophys. Res., 112*(C4), C04S03, doi:10.1029/2006JC003642, 2007.

Hopkins, M. A., On the ridging of intact lead ice, *J. Geophys. Res., 99*(C8), 16,351–16,360, 1994.

Hopkins, M. A., Four stages of pressure ridging, *J. Geophys. Res., 103*(C10), 21,883–21,891, 1998.

Hopkins, M. A., and W. D. Hibler, III., On the ridging of a thin sheet of lead ice, *Ann. Glaciol., 15*, 81–86, 1991.

Hopkins, M. A., W. D. Hibler, III., and G. M. Flato, On the numerical simulation of the sea ice ridging process, *J. Geophys. Res., 96*(C3), 4809–4820, 1991.

Hoyland, K. V., Simulations of the consolidation process in first-year sea ice ridges, *Cold Reg. Sci. Technol., 34*, 143–158, 2002.

Hunke, E. C., and J. K. Dukowicz, An Elastic-Viscous-Plastic Model for Sea Ice Dynamics, *J. Phys. Oceanogr., 27*, 1849–1867, 1997.

Hurrell, J. W., Decadal trends in the North Atlantic Oscillation: Regional temperatures and precipitation, *Science, 269*, 676–679, 1995.

Jacobsson, M., Hypsometry and volume of the Arctic Ocean and its constituent seas, *Geochem. Geophys. Geosyst., 3*(5), doi:10.1029/2001GC000302, 2002.

Johannessen, O. M., E. V. Shalina, and M. W. Miles, Satellite Evidence for an Arctic Sea Ice Cover in Transformation, *Science, 286*, 1937–1939, 1999.

Johannessen, O. M., L. Bengtsson, M. W. Miles, S. I. Kuzmina, V. A. Semenov, G. V. Alekseev, A. Nagurnyi, V. F. Zakharov, L. P. Bobylev, L. H. Pettersson, K. Hasselmann, and H. P. Cattle, Arctic climate change: observed and modeled temperature and sea-ice variability, *Tellus, 56 A*, 328–341, 2004.

Kalnay, E., M. Kanamitsu, R. Kistler, W. Collins, D. Deaven, L. Gandin, M. Iredell, S. Saha, G. White, J. Woolen, Y. Zhu, M. Chelliah, W. Ebisuzaki, W. Higgins, J. Janowiak, K. C. Mo, C. Ropelewski, J. Wang, A. Leetmaa, R. Reynolds, R. Jenne, and D. Josephs, The NCEP/NCAR 40-Year Reanalysis Project, *Bull. Am. Met. Soc., 77*(3), 437–471, 1996.

Karcher, M., R. Gerdes, F. Kauker, and C. Köberle, Arctic warming: Evolution and spreading of the 1990s warm event in the Nordic seas and the Arctic Ocean, *J. Geophys. Res., 108*(C2), 3034, doi:10.1029/2001JC001265, 2003.

Ketchum, R. D., Jr., Airborne laser profiling of the Arctic pack ice, *Remote Sens. Environ., 2*, 41–52, 1971.

Key, J. R., and A. S. McLaren, Periodicities and keel spacings in the under-ice draft distribution, *Cold Reg. Sci. Technol., 16*, 1–10, 1989.

Kimura, N., and M. Wakatsuchi, Relationship between sea-ice motion and geostrophic wind in the Northern Hemisphere, *Geophys. Res. Lett., 27*(22), 3735–3738, 2000.

Kistler, R., E. Kalnay, W. Collins, S. Saha, G. White, J. Woollen, M. Chelliah, W. Ebiszuzaki, M. Kanamitsu, V. Kousky, H. van den Dool, R. Jenne, and M. Fiorino, The NCEP/NCAR 50-year reanalysis, *Bull. Am. Met. Soc., 82*(2), 247–267, 2001.

König-Langlo, G., and E. Augstein, Parameterization of the downward longwave radiation at the earth's surface in polar regions, *Meteorol. Zeitschr., N.F.3.Jg.*(H.6), 343–347, 1994.

Kovacs, A., On pressured sea ice, in *Sea Ice*, edited by T. Karlsson, Proceedings of the International Sea Ice Conference, Reykjavik, Iceland, May 10–13, pp. 276–295, 1971.

Kreyscher, M., Dynamics of Arctic sea ice — Validation of different rheology schemes for the use in climate models, Reports on Polar Research, vol. 291, Alfred Wegener Institute, 1998.

Kreyscher, M., M. Harder, P. Lemke, and G. M. Flato, Results of the Sea Ice Model Intercomparison Project: Evaluation of sea ice rheology schemes for use in climate simulations, *J. Geophys. Res.*, *105*(C5), 11,299–11,320, 2000.

Krishfield, R. A., and D. K. Perovich, Spatial and temporal variability of oceanic heat flux to the Arctic ice pack, *J. Geophys. Res.*, *110*, C07021, doi:10.1029/2004JC002293, 2005.

Kwok, R., Recent Changes in Arctic Ocean Sea Ice Motion Associated with the North Atlantic Oscillation, *Geophys. Res. Lett.*, *27*(6), 775–778, 2000.

Kwok, R., Variability of Nares Strait ice flux, *Geophys. Res. Lett.*, *32*, L24502, doi:10.1029/2005GL024768, 2005.

Kwok, R., and D. A. Rothrock, Variability of Fram Strait ice flux and the North Atlantic Oscillation, *J. Geophys. Res.*, *104*(C3), 5177–5189, 1999.

Kwok, R., A. Schweiger, D. A. Rothrock, S. Pang, and C. Kottmeier, Sea ice motion from satellite passive microwave imagery assessed with ERS SAR and buoy motions, *J. Geophys. Res.*, *103*(C4), 8191–8214, 1998.

Kwok, R., G. F. Cunningham, and S. S. Pang, Fram Strait sea ice outflow, *J. Geophys. Res.*, *109*, C01009, doi:10.1029/2003JC001785, 2004.

Laevastu, T., Factors affecting the temperature of the surface layer of the sea, *Comment. Phys. Math.*, *25*(1), 1960.

Laine, V., Arctic sea ice regional albedo variability and trends, 1982–1998, *J. Geophys. Res.*, *109*, C06027, doi:10.1029/2003JC001818, 2004.

Lemke, P., A coupled one-dimensional sea ice-ocean model, *J. Geophys. Res.*, *92*(C12), 13,164–13,172, 1987.

Lemke, P., W. B. Owens, and W. D. Hibler, III., A coupled sea ice-mixed layer-pycnoclyne model for the Weddell Sea, *J. Geophys. Res.*, *95*(C6), 9513–9525, 1990.

Lensu, M., The Evolution of Ridged Ice Fields, M-Series Reports, vol. 280, Helsinki University of Technology, Ship Laboratory, Helsinki, Finland, 2003a.

Lensu, M., Conservation equations for ridging parameters, Parts 1 & 2, *EU Project IRIS (EVK3-CT-2002-00083), Deliverable D5, Parts 2 & 3, Internal report*, Helsinki University of Technology, Ship Laboratory, Helsinki, Finland, 2003b.

Lensu, M., A simulation method for the generation of a ridged ice cover with realistic clustering properties, *EU Project IRIS (EVK3-CT-2002-00083), Deliverable D12, Part 3, Internal report*, Helsinki University of Technology, Ship Laboratory, Helsinki, Finland, 2003c.

Lensu, M., The estimation of clustering effect using simulated profiles of ridged ice cover, *EU Project IRIS (EVK3-CT-2002-00083), Deliverable D10, Part 2, Internal report*, Helsinki University of Technology, Ship Laboratory, Helsinki, Finland, 2004.

Lensu, M., B. Cheng, and L. Axell, The first implementation of ridging to the sea ice forecast models of FIMR and SMHI, *EU Project IRIS (EVK3-CT-2002-00083), Deliverable D10, Part 1, Internal report*, Helsinki University of Technology, Ship Laboratory, Helsinki, Finland, 2003.

Leppäranta, M., On the drift and deformation of sea ice fields in the Bothnian Bay, *Tech. Rep. No. 29*, Winter Navigation Research Board, Helsinki, Finland, 1980.

Leppäranta, M., The Dynamics of Sea Ice, in *Physics of Ice-Covered Seas, vol. 1*, edited by M. Leppäranta, pp. 305–342, Helsinki University Press, 1998.

Leppäranta, M., M. Lensu, P. Kosloff, and B. Veitch, The life story of a first-year sea ice ridge, *Cold Reg. Sci. Technol., 23*, 279–290, 1995.

Lewis, J. E., M. Leppäranta, and H. Granberg, Statistical properties of sea ice surface topography in the Baltic Sea, *Tellus, 45 A*, 127–142, 1993.

Lieser, J. L., A Numerical Model for Short-term Sea Ice Forecasting in the Arctic, Reports on Polar and Marine Research, vol. 485, Alfred Wegener Institute, Bremerhaven, Germany, 2004.

Lieser, J. L., Sea ice conditions in the northern North Atlantic in 2003 and 2004, *Reports on Polar and Marine Research, vol. 504*, Alfred Wegener Institute, Bremerhaven, Germany, 2005.

Light, B., H. Eicken, G. A. Maykut, and T. C. Grenfell, The effect of included particulates on the spectral albedo of sea ice, *J. Geophys. Res., 103*(C12), 27,739–27,752, 1998.

Lindsay, R. W., and J. Zhang, The Thinning of Arctic Sea Ice, 1988–2003: Have We Passed a Tipping Point?, *J. Climate*, *18*(22), 4879–4894, 2005.

Lüpkes, C., J. Hartmann, G. Birnbaum, W. Cohrs, M. Yelland, R. Pascal, T. Spieß, and M. Buschmann, Convection over Arctic Leads (COAL), in *The Expedition ARKTIS XIX/1 a, b and XIX/2 of the RV "Polarstern" in 2003*, edited by U. Schauer and G. Kattner, pp. 47–62, Reports on Polar and Marine Research, vol. 481, Alfred Wegener Institute, Bremerhaven, Germany, 2004.

Martin, T., Spatial and Temporal Variability of Arctic Sea Ice Dynamics, Diploma thesis, Institut f. Meereskunde, Kiel, Germany, 2003.

Martin, T., Comparison of different ridge formation models of Arctic sea ice with observations from laser profiling, *Ann. Glaciol.*, *44*, 403–410, 2006.

Martin, T., and R. Gerdes, Sea ice drift variability in Arctic Ocean Model Intercomparison Project models and observations, *J. Geophys. Res.*, *112*(C4), C04S10, doi:10.1029/2006JC003617, 2007.

Martin, T., and T. Martin, Anomalies of sea-ice transports in the Arctic, *Ann. Glaciol.*, *44*, 310–316, 2006.

Maslanik, J., T. Agnew, M. Drinkwater, W. Emery, C. Fowler, R. Kwok, and A. Liu, Summary of ice-motion mapping using passive microwave data (NSIDC Special Publication 8), *Tech. rep.*, National Snow and Ice Data Center, Boulder, CO, 1998.

Maykut, G. A., Energy exchange over young sea ice in the central Arctic, *J. Geophys. Res.*, *83*(C7), 3646–3658, 1978.

Maykut, G. A., The surface heat and mass balance, in *The Geophysics of Sea Ice*, edited by N. Untersteiner, pp. 395–463, NATO ASI Series B: Physics, vol. 146, Plenum Press, New York, N.Y., USA, 1986.

Maykut, G. A., and M. G. McPhee, Solar heating of the Arctic mixed layer, *J. Geophys. Res.*, *100*(C12), 24,691–24,703, 1995.

Maykut, G. A., and N. Untersteiner, Some results from a time dependent thermodynamic model of sea ice, *J. Geophys. Res.*, *76*(6), 1550–1575, 1971.

McCabe, G. J., M. P. Clark, and M. C. Serreze, Trends in Northern Hemisphere Surface Cyclone Frequency and Intensity, *J. Climate*, *14*, 2763–2768, 2001.

McPhee, M. G., Ice-Ocean Momentum Transfer for the AIDJEX Ice Model, *AIDJEX Bull.*, *29*, 93–111, 1975.

McPhee, M. G., The Effect of the Oceanic Boundary Layer on the Mean Drift of Pack Ice: Application of a Simple Model, *J. Phys. Oceanogr.*, *9*, 388–400, 1979.

McPhee, M. G., An analysis of pack ice drift in summer, in *Sea Ice Processes and Models*, edited by R. S. Pritchard, pp. 62–75, Univ. Washington Press, Seattle, W.A., USA, 1980.

Meier, W., J. Stroeve, F. Fetterer, and K. Knowles, Reductions in Arctic Sea Ice Cover No Longer Limited to Summer, *EOS, Transactions*, *86*(36), 326, doi:10.1029/2005EO360003, 2005.

Melling, H., and D. A. Riedel, The underside topography of sea ice over the continetal shelf of the Beaufort Sea in the winter 1990, *J. Geophys. Res.*, *100*(C7), 13,641–13,653, 1995.

Melling, H., and D. A. Riedel, Development of seasonal pack ice in the Beaufort Sea during the winter of 1991–1992, *J. Geophys. Res.*, *101*(C5), 11,975–11,992, 1996.

Melling, H., P. H. Johnsto, and D. A. Riedel, Measurements of the Underside Topography of Sea Ice by Moored Subsea Sonar, *J. Atmos. Oceanic Technol.*, *12*(3), 589–602, 1995.

Mellor, G. L., and L. H. Kantha, An ice-ocean coupled model, *J. Geophys. Res.*, *94*, 10,937–10,954, 1989.

Mellor, M., Mechanical behavior of sea ice, in *The Geophysica of Sea Ice*, edited by N. Untersteiner, pp. 165–281, NATO ASI Series B: Physics, vol. 146, Plenum Press, New York, N.Y., USA, 1986.

Mesinger, F., and A. Arakawa, Numerical methods used in atmospheric models, Global Atmospheric Research Program Publication Series, vol. 17, WMO, 1976.

Mock, S. J., A. D. Hartwell, and W. D. Hibler, III., Spatial Aspects of Pressure Ridge Statistics, *J. Geophys. Res.*, *77*(30), 5945–5953, 1972.

Nansen, F., *Fridtjof Nansen's "Farthest North" — The Norwegian Polar Expedition 1893–1896, vol. I and II*, 480+456 pp., Georges Newnes Ltd., 1898.

Nghiem, S. V., Y. Chao, G. Neumann, P. Li, D. K. Perovich, and T. Street, Depletion of perennial sea ice in the East Arctic Ocean, *Geophys. Res. Lett.*, *33*, L17501, doi:10.1029/2006GL027198, 2006.

Nortala-Hoikkanen, A., K. Riska, O. Salmela, and G. Wilkman, Methods to map ice conditions, measure ice properties and quantify ice features, *Hydrotechnical Construction, 28*(3), 180–188, doi:10.1007/BF01545936, 1994.

NSIDC, Sea Ice Decline Intensifies, Joint press release of NSIDC, NASA and Univ. Washington, `http://www-nsidc.colorado.edu/news/press/20050928_trendscontinue.html`, 2005.

Ortmeyer, M., and I. G. Rigor, International Arctic Buoy Program Data Report 2003, Technical Memorandum APL-UW TM 2-04, *Tech. rep.*, Applied Physics Laboratory, University of Washington, Seattle, WA, 2004.

Overland, J. E., and R. L. Colony, Geostrophic drag coefficients for the central Arctic derived from Soviet drifting station data, *Tellus, 46 A*, 75–85, 1994.

Overland, J. E., and K. L. Davidson, Geostrophic drag coefficients over sea ice, *Tellus, 44 A*, 66–54, 1992.

Owens, W., and P. Lemke, Sensitivity studies with a sea ice-mixed layer-pycnocline model in the Weddell Sea, *J. Geophys. Res., 95*(C6), 9527–9538, 1990.

Parkinson, C. L., and W. M. Washington, A large-scale numerical model of sea ice, *J. Geophys. Res., 84*(C1), 311–337, 1979.

Parkinson, C. L., D. J. Cavalieri, P. Gloerson, H. J. Zwally, and J. C. Comiso, Arctic sea ice extents, areas, and trends, 1978–1996, *J. Geophys. Res., 104*(C9), 20,837–20,856, 1999.

Parmeter, R. R., A Model of Simple Rafting in Sea Ice, *J. Geophys. Res., 80*(15), 1948–1952, 1975.

Parmeter, R. R., and M. D. Coon, Mechanical models of ridging in the Arctic sea ice cover, *AIDJEX Bull., 19*, 59–112, 1973.

Perovich, D. K., The Optical Properties of Sea Ice, *vol. 96-1*, U.S. Army Corps of Eng., Cold Reg. Res. Eng. Lab., Hanover, NH, USA, 1996.

Perovich, D. K., and G. A. Maykut, Solar Heating of a Stratified Ocean in the Presence of a Static Ice Cover, *J. Geophys. Res., 95*(C10), 18,233–18,245, 1990.

Pichler, H., *Dynamik der Atmosphäre*, 572 pp., 3. aktual. Aufl., Spektrum Akad. Verl., Heidelberg, 1997.

Press, W. H., S. A. Teukolsky, W. T. Vetterling, and B. P. Flannery, *Numerical Recipes in Fortran 77, Second Edition, The Art of Scientific Computing, Reprint with corrections 2003*, xxxi + 933 pp., Cambridge University Press, 1992.

Proshutinsky, A., and M. A. Johnson, Two circulation regimes of the wind driven Arctic Ocean, *J. Geophys. Res., 102*, 12,493–12,514, 1997.

Proshutinsky, A., R. H. Bourke, and F. A. McLaughlin, The role of the Beaufort Gyre in Arctic climate variability: Seasonal to decadal climate scales, *Geophys. Res. Lett., 29*, 2100, doi:10.1029/2002GL015847, 2002.

Richter-Menge, J. A., and K. F. Jones, The tensile strength of first-year sea ice, *J. Glaciol., 39*(133), 609–618, 1993.

Rigor, I. G., and J. M. Wallace, Variations in the age of Arctic sea-ice and summer sea ice extent, *Geophys. Res. Lett., 31*, L09401, doi:10.1029/2004GL019492, 2004.

Rigor, I. G., J. M. Wallace, and R. L. Colony, Response of Sea Ice to the Arctic Oscillation, *J. Climate, 15*(18), 2648–2663, 2002.

Rothrock, D. A., The energetics of plastic deformation of pack ice by ridging, *J. Geophys. Res., 80*(33), 4514–4519, 1975.

Rothrock, D. A., Y. Yu, and G. Maykut, Thinning of the Arctic Sea-Ice Cover, *Geophys. Res. Lett., 26*(23), 3469–3472, 1999.

Rothrock, D. A., J. Zhang, and Y. Yu, The Arctic ice thickness anomaly of the 1990s: A consistent view from observations and models, *J. Geophys. Res., 108*(C3), 3083, doi:10.1029/2001JC001208, 2003.

Schauer, U., and G. Kattner, The Expedition ARKTIS XIX/1 a, b and XIX/2 of the RV "Polarstern" in 2003, *Reports on Polar and Marine Research, vol. 481*, Alfred Wegener Institute, Bremerhaven, Germany, 2004.

Schlosser, P., B. Ekwurzel, S. Khatiwala, B. Newton, W. Maslowski, and S. Pfirman, Trace studies of the Arctic freshwater budget, in *The Freshwater Budget of the Arctic Ocean*, edited by E. L. Lewis, pp. 453–478, NATO ASI Series 2: Environmental Security, vol. 70, Kluwer Academic Publishers, Dordrecht, Netherlands, 2000.

Schramm, J. L., G. M. Flato, and J. A. Curry, Toward the modeling of enhanced basal melting in ridge keels, *J. Geophys. Res., 105*(C6), 14,081–14,092, 2000.

Schröder, D., Wirkung von Zyklonen auf das Meereis in der Framstraße: Modellrechnungen und Beobachtungen, Ph.D. thesis, Universität Hamburg, FB Geowissenschaften, Hamburg, Germany, 2005.

Schulkes, R. M. S. M., A note on the evolution equations for the area fraction and the thickness of a floating ice cover, *J. Geophys. Res., 100*(C3), 5021–5024, 1995.

Schuster, S., and C. Haas, Laser profiling of pressure ridges, in *Polarstern ARKTIS XVII/2, Cruise Report: AMORE 2001*, edited by J. Thiede, pp. 67–69, Reports on Polar and Marine Research, vol. 421, Alfred Wegener Institute, Bremerhaven, Germany, 2002.

Semtner, A. J., A model for the thermodynamic growth of sea ice in numerical investigations of climate, *J. Phys. Oceanogr., 6*(3), 379–389, 1976.

Serreze, M. C., Climatological Aspects of Cyclone Development and Decay in the Arctic, *Atmos.-Ocean, 33*(1), 1–23, 1995.

Serreze, M. C., and R. G. Barry, Synoptic Activity in the Arctic Basin, 1979–85, *J. Climate, 1*, 1276–1295, 1988.

Serreze, M. C., J. E. Box, R. G. Barry, and J. E. Walsh, Characteristics of Arctic Synoptic Activity, 1952–1989, *Meteorol. Atmos. Phys., 51*, 147–164, 1993.

Serreze, M. C., J. A. Maslanik, T. A. Scambos, F. Fetterer, J. Stroeve, K. Knowles, C. Fowler, S. Drobot, R. G. Barry, and T. M. Haran, A record minimum Arctic sea ice extent and area in 2002, *Geophys. Res. Lett., 30*(3), 1110, doi:10.1029/2002GL016406, 2003.

Shinohara, Y. A., A Redistribution Function Applicable to a Dynamic Model of Sea Ice, *J. Geophys. Res., 95*(C8), 13,423–13,432, 1990.

Smith, D., Coefficients for sea surface wind stress, heat flux, and wind profiles as a function of wind speed and surface temperature, *J. Geophys. Res., 93*(C12), 15,647–15,467, 1988.

Smith, D. M., Recent increase in the length of the melt season of perennial Arctic sea ice, *Geophys. Res. Lett., 25*(5), 655–658, 1998.

Smolarkiewicz, P. K., A simple positive definite advection scheme with small implicit diffusion, *Month. Weather Rev., 111*, 479–486, 1983.

Steele, M., and T. Boyd, Retreat of the cold halocline layer in the Arctic Ocean, *J. Geophys. Res., 103*(C5), 10,419–10,435, 1998.

Steiner, N., Introduction of variable drag coefficients into sea-ice models, *Ann. Glaciol., 33*, 181–186, 2001.

224

Steiner, N., M. Harder, and P. Lemke, Sea-ice roughness and drag coefficients in a dynamic-thermodynamic sea-ice model for the Arctic, *Tellus, 51 A,* 964–978, 1999.

Storch, v., H., and F. W. Zwiers, *Statistical Analysis in Climate Research, First edition (corrected),* x+484 pp., Cambridge University Press, Cambridge, UK, 2001.

Stössel, A., and W. B. Owens, The Hamburg Sea-Ice Model, *Technical report, vol. 3,* Deutsches Klimarechenzentrum (DKRZ), Hamburg, Germany, 1992.

Stroeve, J. C., M. C. Serreze, F. Fetterer, T. Arbetter, W. Meier, J. Maslanik, and K. Knowles, Tracking the Arctic's shrinking ice cover: Another extreme September minimum in 2004, *Geophys. Res. Lett., 32,* L04501, doi:10.1029/2004GL021810, 2005.

Sturm, M., D. K. Perovich, and J. Holmgren, Thermal conductivity and heat transfer through the snow on the ice of the Beaufort Sea, *J. Geophys. Res., 107*(C10), 8043, doi:10.1029/2000JC000409, 2002.

Thompson, D. W. J., and J. M. Wallace, The Arctic Oscillation signature in the wintertime geopotential height and temperature fields, *Geophys. Res. Lett., 25,* 1297–1300, 1998.

Thompson, D. W. J., and J. M. Wallace, Annular Modes in the Extratropical Circulation. Part I: Month-to-Month Variability, *J. Climate, 13*(5), 1000–1016, 2000.

Thorndike, A. S., and R. Colony, Sea Ice Motion in Response to Geostrophic Winds, *J. Geophys. Res., 87*(C8), 5845–5852, 1982.

Thorndike, A. S., D. A. Rothrock, G. A. Maykut, and R. Colony, The Thickness Distribution of Sea Ice, *J. Geophys. Res., 80*(33), 4501–4513, 1975.

Timco, G. W., and R. P. Burden, An analysis of the shapes of sea ice ridges, *Cold Reg. Sci. Technol., 25,* 65–77, 1997.

Tomczak, M., and J. S. Godfrey, *Regional Oceanography: An Introduction,* pp. 89–111, Pergamon Press, 1994.

Tucker, W. B., III., D. S. Sodhi, and J. W. Govoni, Structure of first-year pressure ridge sails in the Prudhoe Bay region, in *The Alaskan Beaufort Sea: Ecosystems and Environment,* edited by P. W. Barnes, D. M. Shell, and E. Reimnitz, pp. 115–135, Academic Press, San Diego, CA, USA, 1984.

Untersteiner, N., On the mass and heat budget of Arctic sea ice, *Arch. Meteorol. Geophys. Bioklimatol., A*(12), 151–182, 1961.

Untersteiner, N., AIDJEX Review, in *Sea Ice Processes and Models*, edited by R. S. Pritchard, pp. 3–11, Univ. Washington Press, Seattle, W.A., USA, 1980.

Vinje, T., Physical Environment Western Barents Sea: Drift, Composition, Morphilogy and Distribution of the Sea Ice Fields in the Barents Sea, Norsk Polarinstitutt Skrifter No. 179 C, Oslo, Norway, 1985.

Vinje, T., Dynamics and morphology of the Barents Sea ice field, in *POAC '87*, edited by W. M. Sackinger and M. O. Jeffries, Proc. 9th Intl. Conf. Port and Ocean Engineering under Arctic Conditions, vol. 1, Geophys. Inst., Univ. Alaska, Fairbanks, pp. 263–268, 1988.

Vinje, T., Fram Strait Ice Fluxes and Atmospheric Circulation: 1950–2000, *J. Climate, 14*, 3508–3517, 2001.

Vinje, T., N. Nordlund, and A. Kvambekk, Monitoring Ice Thickness in Fram Strait, *J. Geophys. Res., 103*(C5), 10,437–10,450, 1998.

Vinnikov, K. Y., A. Robock, R. J. Stouffer, J. E. Walsh, C. L. Parkinson, D. J. Cavalieri, J. F. B. Mitchell, D. Garrett, and V. F. Zakharov, Global warming and northern hemisphere sea ice extent, *Science, 286*, 1934–1937, 1999.

Vowinkel, E., and S. Orvig, The climate of the North Polar Basin, in *World Survey of Climatology, vol. 14: Climates of the polar regions*, edited by S. Orvig, pp. 401–424, Elsevier, New York, 1970.

Wadhams, P., Characteristics of deep pressure ridges in the Arctic Ocean, in *POAC '77*, edited by D. B. Muggeridge, Proc. 4th Intl. Conf. Port and Ocean Engineering under Arctic Conditions, Memorial Univ., St. Johns, Nfld., pp. 544–555, 1978.

Wadhams, P., A comparison of sonar and laser profiles along corresponding tracks in the Arctic Ocean, in *Sea Ice Processes and Models*, edited by R. S. Pritchard, pp. 283–299, Univ. Washington Press, Seattle, W.A., USA, 1980.

Wadhams, P., Sea-ice topography of the Arctic Ocean in the region 70°W to 25°E, *Philos. Trans. R. Soc., London Ser. A, 302*(1464), 45–85, 1981.

Wadhams, P., *Ice in the ocean*, xi + 351 pp., Gordon and Breach Science Publishers, 2000.

Wadhams, P., and T. Davy, On the Spacing and Draft Distributions for Pressure Ridge Keels, *J. Geophys. Res., 91*(C9), 10,697–10,708, 1986.

Wadhams, P., and J. R. Horne, An analysis of ice profiles obtained by submarine in the Beaufort Sea, *J. Glaciol., 25*(93), 401–424, 1980.

Wadhams, P., J. P. Wilkinson, and A. Kaletzky, Sidescan Sonar Imagery of the Winter Marginal Ice Zone Obtained from an AUV, *J. Atmos. Oceanic Technol.*, *21*(9), 1462–1470, 2004.

Walsh, J. E., and W. L. Chapman, 20th-century sea-ice variations from observational data, *Ann. Glaciol.*, *33*, 444–448, 2001.

Walsh, J. E., W. L. Chapman, and T. L. Shy, Recent Decrease of Sea Level Pressure in the Central Arctic, *J. Climate*, 9, 480–486, 1996.

Weeks, W. F., Groth Conditions and the Structure and Properties of Sea Ice, in *Physics of Ice-Covered Seas, vol. 1*, edited by M. Leppärante, pp. 25–104, Helsinki University Printing House, Helsinki, Finland, 1998.

Weeks, W. F., and A. Kovacs, On pressure ridges, *Tech. rep.*, U.S. Army Corps of Eng., Cold Reg. Res. Eng. Lab., Hanover, NH, USA, 1970.

Weeks, W. F., A. Kovacs, and W. D. Hibler, III., Pressure ridge characteristics in the Arctic coastal environment, in *POAC '71*, edited by S. S. Wetteland and P. Bruun, Proc. 1st Intl. Conf. Port and Ocean Engineering under Arctic Conditions, Tech. Univ. Norway, Trondheim, pp. 152–183, 1971.

Weiss, J., and D. Marsan, Scale properties of sea ice deformation and fracturing, *C. R. Physique*, *5*, 735–751, doi:10.1016/j.crhy.2004.09.005, 2004.

Wilks, D. S., *Statistical Methods in Atmospheric Sciences: An Introduction*, xi+464 pp., Academic Press, San Diego, CA, USA, 1995.

Williams, E., C. Swithinbank, and G. de Q. Robin, A submarine sonar study of Arctic pack ice, *J. Glaciol.*, *15*(73), 349–362, 1975.

WMO, *WMO Sea-Ice Nomenclature*, World Meteorological Organization, Secretariat of the WMO, Geneva, Switzerland, 5. ed., 1989.

Woodgate, R. A., and K. Aagaard, Revising the Bering Strait freshwater flux into the Arctic Ocean, *Geophys. Res. Lett.*, *32*, L02602, doi:10.1029/2004GL021747, 2005.

Yen, Y. C., Review of the thermal properties of snow, ice and sea ice, *Tech. Rep. 81-10, 27pp*, U.S. Army Corps of Eng., Cold Reg. Res. Eng. Lab., Hanover, NH, USA, 1981.

Zhang, J., D. Rothrock, and M. Steele, Recent Changes in Arctic Sea Ice: The Interplay between Ice Dynamics and Thermodynamics, *J. Climate, 17*, 2300–2317, 2000.

Bibliography

Zhang, X., J. E. Walsh, J. Zhang, U. Bhatt, and M. Ikeda, Climatology and Inter-annual Variability of Arctic Cyclone Activity: 1948–2002, *J. Climate, 17*, 2300–2317, 2004.

Zillman, J. W., *A study of some aspects of radiation and heat budgets of the southern hemisphere oceans, Meteorological study*, vol. 26, 526 pp., Bureau of Meteorology, Dept. of the Interior, Canberra, Australia, 1972.

Zyryanov, D., and V. N. Smirnov, Nonlinear behavior of the arctic ice ridge system, Geophys. Res. Abstr., vol. 8, 02001, 2006 SRef-ID: 1607-7962/gra/EGU06-A-02001, EGU, 2006.

Acknowledgements

My sincere thanks I give to Prof. Dr. Peter Lemke for offering the opportunity of a PhD study at the AWI, supporting my work at any time during its evolution and the final comments rounding off the thesis.

I thank Prof. Dr. Klaus Dethloff for reviewing my thesis.

I am very grateful to my supervisor Dr. Christian Haas for introducing me to the world of sea ice and offering so many opportunities to present and discuss my work at international workshops and conferences. I enjoyed the countless scientific discussions we had.

I particularly would like to thank Prof. Dr. Rüdiger Gerdes for initiating our study on sea ice drift and introducing me to the AOMIP community. I enjoyed the straight and deliberate way of scientific working with him.

Special thanks go to my Finnish colleagues Jari Haapala and Mikko Lensu. Mikko patiently explained to me his view on ridge modelling in the very beginning of my own work and Jari supported my work with fruitful discussions and encouragement during an important phase of my PhD.

Furthermore, I would like to thank my fantastic colleagues of the Sea Ice Physics group and namely Frank, Jan, Jill, Katja, Martin, Michael K., Michael S. and Ralph (sorry, I couldn't list you all) for their support, ideas, corrections, sympathy, humour, ...; you all really made it an enjoyable time.

My greatest gratitude goes to my girlfriend Joke for her invaluable and never-ending encouragement and patience.

I also would like to thank my parents, who never stopped to believe in me to accomplish what I began to do.

The End

Heft-Nr. 540/2006 – „Seafloor analysis based on multibeam bathymetry and backscatter data", by Andreas Beyer.

Heft-Nr. 541/2006 – „The Exchange of Energy, Water and Carbon Dioxide between Wet Arctic Tundra and the Atmosphere at the Lena River Delta, Northern Siberia", by Lars Kutzbach.

Heft-Nr. 542/2007 – „Identification of seafloor provinces - specific applications at the deep-sea Håkon Mosby Mud Volcano and the North Sea", by Kerstin Jerosch.

Heft-Nr. 543/2007 – „Farming in a High Energy Environment: Potentials and Constraints of Sustainable Offshore Aquaculture in the German Bight (North Sea)", by Bela Hieronymus Buck.

Heft-Nr. 544/2007 – „The Expeditions ARKTIS XX/1 and XX/2 of the Research Vessel 'Polarstern' in 2004", edited by Gereon Budéus and Peter Lemke.

Heft-Nr. 545/2007 – „Lakustrine Sedimente als Archive des spätquartären Umweltwandels in der Amery-Oase, Ostantarktis", von Nadja Hultzsch.

Heft-Nr. 546/2007 – „Detaillierte Biomarkeruntersuchungen an Sedimentkernen von ODP-Leg 177", von Petra Weller.

Heft-Nr. 547/2007 – „Development of a novel balloon-borne optical sonde for the measurement of ozone and other stratospheric trace gases", von Mareile Wolff.

Heft-Nr. 548/2007 – „Holocene and Last Glacial Maximum (paleo-)productivity off Morocco. Evidence from benthic foramini-fera and stable carbon isotopes", by Astrid Eberwein.

Heft-Nr. 549/2007 – „11th International Conference on the Physics and Chemistry of Ice (PCI-2006). Bremerhaven, Germany, 23-28 July 2006. Abstracts", edited by Frank Wilhelms and Werner F. Kuhs.

Heft-Nr. 550/2007 – „Expeditions in Siberia in 2005", edited by Lutz Schirrmeister.

Heft-Nr. 551/2007 – „The Expeditions ANTARKTIS-XXII/1 and XXII/2 of the Research Vessel 'Polarstern' in 2004/2005", edited by Saad El Naggar, Gerhard Dieckmann, Christian Haas, Michael Schröder and Michael Spindler.

Heft-Nr. 552/2007 – „Spatial distribution of snow accumulation and snowpack properties in Dronning Maud Land, Antarctica: Observational techniques and methods for surface mass-balance assessments of polar ice sheets", by Gerit Rotschky.

Heft-Nr. 553/2007 – „Helicopter Electromagnetic sea ice thickness estimation: An induction method in the centimetre scale", by Andreas Pfaffling.

Heft-Nr. 554/2007 – „Late Quaternary environment of Central Yakutia (NE Siberia): Signals in frozen ground and terrestrial sediments", by Steffen Popp.

Heft-Nr. 555/2007 – „Bestimmung verschiedener Eisklassen durch statistische Analyse der Rauigkeit von Meereis", von Carola von Saldern.

Heft-Nr. 556/2007 – „The Expedition ANTARKTIS-XXIII/1 of the Research Vessel „Polarstern" in 2005", edited by Michiel Rutgers van der Loeff.

Heft-Nr. 557/2007 – „The Expedition ANTARKTIS-XXIII/4 of the Research Vessel „Polarstern" in 2006", edited by Karsten Gohl.

Heft-Nr. 558/2007 – „The Expedition ANTARKTIS-XXIII/3 of the Research Vessel „Polarstern" in 2006", edited by Christine Provost.

Heft-Nr. 559/2007 – „Determination of Sea Ice Surface Elevation with Laser and Radar Altimetry and Comparison with Ice Thickness Data Sets in the Arctic and Antarctic", by Sibylle Göbell.

Heft-Nr. 560/2007 – „Steps of Foundation of Institutionalized Antarctic Research. Proceedings of the 1st SCAR Workshop on the History of Antarctic Research. Bavarian Academy of Sciences and Humanities, Munich (Germany), 2-3 June, 2005", edited by Cornelia Lüdecke.

Heft-Nr. 561/2007 – „Anwendung des stratifizierten Krigings auf ERS-1 und ERS-2 Radaraltimeterdaten zur Untersuchung von Eishöhenänderungen im Lambert Gletscher/Amery Eisschelf-System, Ostantarktis", von Ralf Stosius.

Heft-Nr. 562/2007 – „Tolerance limits and survival potential of methanogenic archaea from Siberian permafrost under extreme living conditions", by Daria Morozova.

Heft-Nr. 563/2007 – „Arctic Sea Ice Dynamics: Drift and Ridging in Numerical Models and Observations", by Torge Martin